National Library of Canada
Canadian Theses Service
Ottawa, Canada
K1A 0N4

Bibliothèque nationale du Canada
Services des thèses canadiennes

CANADIAN THESES

THÈSES CANADIENNES

NOTICE

The quality of this microfiche is heavily dependent upon the quality of the original thesis submitted for microfilming. Every effort has been made to ensure the highest quality of reproduction possible.

If pages are missing, contact the university which granted the degree.

Some pages may have indistinct print especially if the original pages were typed with a poor typewriter ribbon or if the university sent us an inferior photocopy.

Previously copyrighted materials (journal articles, published tests, etc.) are not filmed.

Reproduction in full or in part of this film is governed by the Canadian Copyright Act, R.S.C. 1970, c. C-30.

AVIS

La qualité de cette microfiche dépend grandement de la qualité de la thèse soumise au microfilmage. Nous avons tout fait pour assurer une qualité supérieure de reproduction.

S'il manque des pages, veuillez communiquer avec l'université qui a conféré le grade.

La qualité d'impression de certaines pages peut laisser à désirer, surtout si les pages originales ont été dactylographiées à l'aide d'un ruban usé ou si l'université nous a fait parvenir une photocopie de qualité inférieure.

Les documents qui font déjà l'objet d'un droit d'auteur (articles de revue, examens publiés, etc.) ne sont pas microfilmés.

La reproduction, même partielle, de ce microfilm est soumise à la Loi canadienne sur le droit d'auteur, SRC 1970, c. C-30.

THIS DISSERTATION
HAS BEEN MICROFILMED
EXACTLY AS RECEIVED

LA THÈSE A ÉTÉ
MICROFILMÉE TELLE QUE
NOUS L'AVONS REÇUE

NL-339 (r.86/06)

Canada

Laser Studies of the Photophysics of Humic Substances

Joan F. Power

A Thesis
in
The Department
of
Chemistry

Presented in Partial Fulfillment of the Requirements
for the Degree of Doctor of Philosophy at
Concordia University
Montréal, Québec, Canada

August 1986

ISBN 0-315-35559-X

ABSTRACT

Laser Studies of the Photophysics of Humic Substances

Joan F. Power
Concordia University, 1986

Two aspects of the photophysics of humic substances were studied in the course of this work. The first used time resolved emission and flash photolysis techniques to determine the transient species formed under near UV irradiation of a well characterised humic substance. The second involved the use of a steady state thermooptic technique for the determination of weak absorbances of dissolved humic materials.

Laser flash photolysis studies were carried out at 355 nm with resolution from 20 ps to greater than 100 microseconds. The principal components of transient absorption were, for the well characterised humic substance standard, Armadale fulvic acid : a solvated electron with a lifetime of 1 - 2 microseconds (pH 7), a radical ion species with a lifetime of 1 - 15 microseconds and a long lived component with a lifetime in excess of 100 microseconds. The solvated electron was identified on the basis of its absorption spectrum which showed a maximum near 700 nm, its sensitivity to N_2O, and its rate constants for bimolecular quenching by O_2, H^+ and Cu^{2+}. The radical species had an absorption spectrum with a maximum near 480-510 nm. It

appeared concurrent with the electron at 20 ps past excitation. The third, longest lived component had a broad featureless absorption spectrum and was assigned to the triplet states of the humic material. Emission lifetime measurements at 355 nm gave a three component model for emission gave a three component model for emission with lifetimes as follows: (i) 100-200 ps (ii) 2-3 ns and (iii) 6-8 ns.

A thermal lens spectrometer was designed and constructed incorporating a photodiode array detection system. The spectrometer was operated mainly as a mode-mismatched instrument. The mode-mismatched intensity profiles observed in the detector plane were analysed by diffraction theory. Fourier techniques were developed for the analysis of mode-mismatched intensity profiles. The detection limit for the spectrometer was an absorbance of 2-4 x 10^{-5} at 50 mW of laser power, in the absence of beam profile analysis.

Thermal lensing was applied to measurements of humic substance concentrations at natural water levels. The thermal lens signal was found to be insensitive to light scattered by large particulates added to samples of dissolved humic material. Thermal lens studies of a series of natural organic carbon samples yielded a quadratic relationship between the absorptivity of a sample and its carbon content, for a given E4/E6 ratio. This observation was explained by the formation of intraparticle electron donor/acceptor complexes, and supplies a general model for interpreting the photophysics of humic substances.

Dedication

The work is dedicated to my parents, whose support and encouragement over the past four years has made this work possible.

Acknowledgements

The author wishes to thank Dr. C.H. Langford for his supervision and guidance in the course of this work. Thanks are also extended to Dr. R. Lesage for his work on the single photon counting measurements, to Mr. Paul Cahill for his technical support in the construction of the thermal lens instrument and to Mr. Don Gutzman for his practical assistance.

Contents

Chapter Page

Index of Figures

Index of Tables

List of Symbols

Symbol	Description
α	copper binding fraction (fraction of binding sites covered) (Chapter 2)
α	thermal diffusivity
α	absorption coefficient in cm^{-1} (p 191-8)
α	fractional absorption (equations 5-1 to 5-17)
α_s	attenuation coefficient due to scattering (cm^{-1})
α_d	degree of dimerisation
α_1	dummy variable
α_2	dummy variable
a	aperture width for thermal lens element
a_s	sample absorption coefficient in $(g/l)^{-1}$ cm^{-1}
a_m	absorption coefficient of monomer
a_d	absorption coefficient of dimer
A	absorbance
A,B,C,D	elements of A,B,C,D ray transformation matrix
ΔA	transient absorption
a,b	regression coefficients in equation 5-18

A_n	amplitude contribution of a fluorescence lifetime component
A_m	monomer absorbance
A_d	dimer absorbance
A_0	a constant proportional to the electric field amplitude
B	a constant proportional to the electric field amplitude, U_0
C_p	specific heat at constant pressure
%C	% weight carbon content by elemental analysis
c	fractional carbon content
c_s	wt/vol concentration of sample
	Dirac delta function
dn/dT	temperature coefficient of refractive index
dV_0	Volume increment $dV_0=dx_0dy_0dz_0$
E	enhancement factor for thermal lensing over conventional spectrophotometry
E4/E6	(classical definition) ratio of sample absorbance at 465nm and 665 nm
E4/E6	(this work) ratio of sample absorbance at 458nm and 600 nm.
ϵ	absorption coefficient of sample
f	focal length
f	discrete frequency (Chapter 4)
f(t)	time dependent focal length of a thermal lens

k_q	bimolecular quenching rate constant in
k_0	decay lifetime for transient absorption signals in the absence of quenching
k_{obs}	observed first order decay constant in s^{-1}
λ	wavelength
l	cell path length
m^s	slope of thermal lens calibration curve for fluorescent sample
m^r	slope of thermal lens calibration curve for non-luminescent reference
$[M]$	monomer concentration
$[M_2]$	dimer concentration
$[M^{2+}]$	divalent metal ion concentration
m	discrete frequency increment (Chapter 4)
n_0	refractive index in sample medium
$n(r,t)$	refractive index distribution in time and radial coordinate
n	number of dimensions (equations 3-12)
$p_a(r)$	an aperture function: $p_a(r) = \begin{matrix} 1 & \text{if } r < a \\ 0 & \text{if } r > a \end{matrix}$
$\bar{p}_a(r)$	the complement of $p_a(r)$: $\bar{p}_a(r) = \begin{matrix} 0 & \text{if } r < a \\ 1 & \text{if } r > a \end{matrix}$
P or P_l	laser power
P_{th}	power degraded to heat by relaxation
P_f	power emitted as fluorescence
P_t	transmitted power
φ_f	quantum yield for fluorescence
	quantum yield for thermal processes
φ_e	quantum yield for electron ejection
	optical path length

$f(\infty)$	focal length of a steady state thermal lens
F	fractional loss in beam power due to fluorescence
F	Fresnel integral
$G(r-r_0, t-t_0)$	Green's function with respect to time and spatial coordinates
$\tilde{G}(k_s, t-t_0)$	Fourier transform of Green's function with respect to spatial coordinates
$\tilde{\tilde{G}}(k_s, \omega)$	Fourier transform of Green's function with respect to time and spatial coordinates
$I_0(r)$	modified Bessel function of order zero in equation 3-17
I_0	center intensity of laser beam (TEM(0,0)) in absence of a thermal lens
$I(t=\infty)$	center intensity of a TEM(0,0) laser beam in the presence of a thermal lens
$\tilde{I}_0(jk)$	Fourier transform of beam profile spatial signal at t = 0.
$\tilde{I}_\infty(jk)$	Fourier transform of beam profile spatial signal at t =
I	intensity of laser beam
j	
$J_0(r)$	Bessel function of order zero
k	wave number
K	thermal conductivity
k_s	spatial frequency vector
k_1	spatial frequency - x coordinate
k_2	spatial frequency - y coordinate
k_3	spatial frequency - z coordinate
K_d	equilibrium constant for dimerization

ν_l	laser frequency
$\langle\nu\rangle$	mean emission frequency
Q or Q(r)	radial heat source distribution function
$\tilde{q}$	complex radius of curvature of Gaussian laser beam
$\tilde{q}_p$	complex radius of curvature of Gaussian beam in the presence of a thermal lens
[q]	quencher concentration
r	radial coordinate
ρ	density
R	radius of phase front of Gaussian laser beam
r_0	spatial position of source
t	time coordinate
t_0	time position of source
T_0	ambient temperature
ΔT	temperature distribution in sample
θ	angular polar coordinate
θ_0	angular polar coordinate for source
t_c	time constant for lens formation
τ	decay lifetime for excited species
$U, \tilde{U}$ or U_0	electric field amplitude
$U(t-t_0)$	unit step function
ω_l	spot radius of TEM(0,0) laser beam
ω_0	spot radius of TEM(0,0) beam at beam waist
ω	time frequency (Chapter 4)
ω_l^*	instantaneous spatial frequency (x coordinate)

ω_2^*	instantaneous spatial frequency (y coordinate)
x, y, z	Cartesian coordinates
x_0, y_0, z_0	source position in Cartesian coordinates
z_1	z coordinate - distance from the sample to the laser beam waist
z_2	z coordinate - distance from the sample cell to the detector
z_c	confocal distance of beam

Chapter 1

Introduction

The role of the humic substances in the aquatic environment is of central importance to the regulation of the composition of natural waters. Humic materials, through their complexing capacity for cations (1-7) contribute to the control of the pH of natural systems. Humic materials are also known to play an important role in the speciation of metal ions in the aquatic environment (1) : ultimately, they may control both the uptake of metal ions by living organisms and the toxicity of the metal ions available by the selective complexation of the different ionic species present. Much work (8-16) on the photochemistry of natural waters has demonstrated that under sunlight irradiation, waters containing humic substances generate a wide variety of reactive intermediates and radicals. The photochemically generated species have been shown to be effective in bringing about the degradation of dissolved organic waste materials such as pesticides (14,15) in aquatic systems. Humic substances, therefore, participate in the dual action of chemical and photochemical regulation of a natural system's composition.

The general character of humic substances is of an extremely heterogeneous mixture (1,17,18). The humic materials represent the refractory fraction of the byproducts of living organisms that have undergone extensive degradation in the environment. Their origin is traceable to plant degradation and the synthetic activity of microorganisms (7). An important source of humic materials in the freshwater environment is soil runoff (1).

The extreme complexity of humic substances prevents the assignment of a precise chemical structure to account for their properties. The most general practices include classification of the various types of humic materials according to the isolation and fractionation proceedures (7), or according to their macromolecular properties such as molecular weight or particle size (19,20). Other properties useful for providing classification include carbon and/or oxygen content and total acidity of the material (1,21).

The photophysics of humic substances is of great interest from two points of view. The first point of view is mechanistic : the diversity of the photochemistry observed in natural waters has led to the requirement for a more detailed understanding of the elementary steps by which excited humic chromophores yield reactive states and intermediates. The second point of view is methodological : the chemical and physical properties of environmental humic substances are frequently monitored by such classical methods as fluorescence and absorption spectrometry (21,22). An important requirement for environmental studies is the availability of probes which are capable of providing high measurement sensitivity in the presence of light scattering matrices.

The approach of this work has been the study of the photophysics of dissolved humic materials from these two points of view. The first approach has motivated the laser flash photolysis and time resolved emission studies of Chapter 2. While the flash photolysis work of Chapter 2 is not the first study of its kind(23,24), it is the first to employ such a broad timescale of observation (picoseconds to microseconds). It is also the first study of a well characterised model humic material for which the physical and chemical properties have been established (2-6,17,18). The objective of the flash photolysis and time resolved emission work has been to determine the generation and decay of transient species and possible precursor states to the reactive intermediates which have been already detected in natural waters.

The second aspect of this work has been methodologically oriented. The objective has been the application of laser thermal lensing, a sensitive thermooptic technique for the measurement of weak absorbances (25-27), to the direct measurement of humic substance concentrations and properties in natural samples, without pretreatment or preconcentration steps. In addition, this project has pursued the development of novel detection schemes in thermal lensing. The thermal lens effect has been, to a major extent, studied for its own sake in the course of this work. Two chapters have been devoted to reporting theoretical and instrumental thermal lens developments (Chapter 3 and 4).

Chapter 5 reports the application of thermal lensing to a series of natural organic materials and demonstrates a solution to some of the technical problems posed by environmental water samples requiring the measurement of weak absorbances. The thermal lens technique is shown to exhibit high sensitivity in the visible : a region of the spectrum that has generally been regarded as inaccessible for the direct study of environmental materials because of their low visible absorptivity (21). Finally, thermal lensing has been evaluated for the direct determination of the absolute quantum yield of natural organic materials, in the hope of providing an alternative to conventional methods of spectrofluorimetry (22) in the study of humic substances.

Chapter 2

Laser Flash Photolysis and Time Resolved Emission Studies of a Well Characterised Soil Humic Substance

In recent years, appreciable information has been accumulated on the photochemical activity of dissolved humic substances in natural waters with the objective of laying the groundwork for understanding the photoprocesses occurring in the aquatic environment. The role played by dissolved humic substances in aquatic photochemistry promises to be a complex one. The character of the humic or " refractory organic " material dissolved in freshwater systems is that of a complex mixture of phenol carboxylate and refractory carbohydrate fragments (7,17,28). It represents the fraction of natural products remaining after the final stages of degradation of molecules originating from living systems. These organic materials are colloidal in nature, and are chiefly responsible for the yellow-brown coloration of natural waters. In the environment, they harvest solar energy and initiate photochemistry. It has been argued that this is mainly by means of indirect mechanisms of energy transfer (8) since the wavelengths readily available from the solar spectrum were generally considered too long to cause direct phototransformation of the humic substrate.

A number of recent studies have demonstrated the presence of a variety of oxidants and free radical species in irradiated humic waters. Such studies are typically carried out under broadband or sunlight irradiation and involve the analysis of the photodecomposition products of well characterised photochemical probes.

A good example is the detection of singlet oxygen, reported by Zepp et al. (10) in the sunlight irradiation of a series of humic water samples. Singlet oxygen is an excited form of O_2 which is commonly sensitised by excited triplet states of a variety of organic chromophores. The formation is summarised by the scheme :

$$^{1}HS_{0} \xrightarrow{h\nu} {}^{1}HS_{1} \xrightarrow{isc} {}^{3}HS_{1}$$

$$^{3}O_{2} + {}^{3}HS_{1} \longrightarrow {}^{1}HS_{0} + {}^{1}O_{2}$$

In this scheme, humic substance chromophores ($^{1}HS_{0}$) are excited to the first singlet state, on the absorption of light, and intersystem cross to the triplet ($^{3}HS_{1}$), which sensitises the formation of $^{1}O_{2}$ from its triplet ground state, $^{3}O_{2}$. $^{1}O_{2}$ adds readily to conjugated systems in a manner analogous to the Diels-Alder reaction (29) to produce peroxidic reaction products. The work of Zepp et al. involved both sunlight and near UV irradiation (370 nnm) of solutions containing humic substances and 2,5 dimethyl furan (DMF), a well characterised singlet oxygen acceptor. Product analysis verified the production of singlet oxygen : this finding was further supported by studies showing inhibition of the photooxidation reaction in the prescence of known singlet oxygen inhibitors. The environmental importance of these results arises because of the reactivity of singlet oxygen for a variety of olefins and sulfides, and in some cases, because of its potential toxicity. In particular, the water soluble pesticide cis-resmethrin, a furan derivative, is expected to exhibit a high reactivity for singlet oxygen (13).

A more recent example of a reactive form of oxygen found in the irradiation of humic waters is superoxide ion, observed by Baxter and Carey (12). It is formed photochemically by the reduction of dissolved oxygen:

$$O_2 + e^- \longrightarrow O_2^-$$

This species is of interest environmentally because it may provide a mechanism for the photodechlorination of chlorinated organic compounds in sunlight irradiated humic waters. An example could be provided by the photoinduced decomposition of methoxychlor (a DDT analog), (14) observed in irradiated humic waters. A mechanism involving singlet oxygen has been effectively ruled out in this case. The possible importance of a superoxide route is further suggested in a product analysis indicating the reactivity of DDT for synthetically generated O_2^- (30).

Superoxide is also interesting because it may explain the formation of hydrogen peroxide observed in humic waters (15):

$$2O_2^- + H_2O \longrightarrow O_2 + HO_2^- + OH^-$$

$$2HO_2^- \longrightarrow 2OH^- + O_2$$

$$HO_2^- + H^+ \rightleftharpoons H_2O_2$$

Dismutation of the H_2O_2 results in the formation of hydroxyl radical , $OH^\cdot$, another transient species observed in humic waters (13,16) :

$$H_2O_2 \xrightarrow{h\nu} 2OH^\cdot$$

Recent work by Bolton et al (31) on the photolysis of benzoquinone in water, has demonstrated the direct formation of benzoquinone radicals and $OH^\cdot$. This may be a relevant process in humic waters because of the compositional importance of quinoid chromophores to humic materials (9,17).

It is clear from these reaction schemes that the action of superoxide may promote photodecomposition processes via initiation of free radical reactions as well as by direct routes. Distinction among mechanisms is likely to prove complicated owing to the variety of pathways observed for reactive intermediates in these situations.

The participation of organic free radicals is a further topic of importance in humic water photochemistry. Irradiated solutions of humic substances have been shown to contain enhanced concentrations of free radical oxidants such as RO· in addition to OH· (13). The participation of radicals has been invoked to explain the photoreductive dissolution of colloidal iron oxides in the presence of dissolved humic substances as reported by Waite and Morel (32) :

$$HS \xrightarrow{h\nu} HS\cdot$$

$$HS\cdot + M^{n+} \longrightarrow M^{(n-1)+} + HS$$

It is clear from this brief survey that a variety of interesting and environmentally important photoreactions occur in irradiated humic waters. The multiplicity of potential reaction pathways and the difficculty of distinguishing among them has given rise to a need for more detailed photophysical information. The formation kinetics of states parent to the transient intermediates, their lifetimes and quenching behavior have become the subject of investigation relatively recently (23,24). Strategies for obtaining basic photophysical information may involve steady state photolysis or the use of flash photolysis techniques which yield time resolved information.

The second approach has been recently applied in studies reported by Fischer et al. (23,24) in which a series of natural water samples was irradiated in the near UV with pulses from a nanosecond laser (Nd:YAG third harmonic wavelength : 355 nm). The authors were able to resolve two components of transient absorption common to all of the samples studied : a component with maximum absorption at 475 nm and a lifetime of several microseconds and a signal near 700 nm which was attributed to a solvated electron on the basis of its absorption spectrum and sensitivity to N_2O. It was believed, on the basis of experiments with oxygen, and with triplet acceptor probes (which partially quenched the transient) that the 475 nm species was assignable to triplet states of the humic substance. However, experiments with photooxidation probes also demonstrated a composite nature to the 475 nm transient absorption which suggested a connection with free radical generation. Owing to a lack of early (and later) time resolution in their experiments (33), it was not possible to eliminate conclusively these ambiguites in the interpretation.

In this work, we have chosen a well characterised humic substance as a model for the naturally occurring materials. The sample, Armadale fulvic acid, is a soil extract which has been extensively studied by numerous authors (2-6,17,18,20), and has been prepared in a form which is unambiguous with respect to protonation state and metal ion content (3,4,8). The possibility of relating changes in the observed photophysics to the physicochemical properties of the sample becomes realisable. In addition, we have undertaken flash photolysis studies on timescales ranging from picoseconds, where the transient states appear, to nanoseconds and microseconds where their decays are observed. In this way, the evolution of the transient species over the entire timescale may be observed, and a link may be established between the signals observed in each domain. The objective has been to locate possible precursors to the transient intermediates observed in humic waters and to obtain information on the pathways for their formation and decay.

The Armadale Sample

The study of a well characterised humic material has been a point of departure of this work from previous work in the field. A large volume of information has been accumulated on the Armadale sample first isolated by Hansen and Schnitzer (17) from the Bh horizon of a P.E.I. podzol. The properties of the material relevant to this study are summarised in this section along with pertinent data.

The definition of the terms " humic " and " fulvic " acids are clarified with reference to the fractionation techniques used to isolate them. The scheme depicted in Figure 1 indicates that these definitions are operational, based on the solubilities of the various fractions contained in a soil sample. The total organic matter present in the soil is first classified into humic and non-humic substances. The non-humic fraction consists of the fragments of biopolymers such as polysaccharides, proteins and lignins, which have not undergone extensive degradation in the soil. The humic substances represent the fraction of materials remaining after the non-humics have been extensively decomposed leaving smaller fragments with relatively few functional units. Humic substances are removed from the soil by alkaline extraction (7) to yield the subfractions : fulvic acid (soluble in acid and alkali), humic acid (soluble in alkali - insoluble in acid) and humin (insoluble in both acid and alkali). The fulvic fraction is the most oxygenated, and

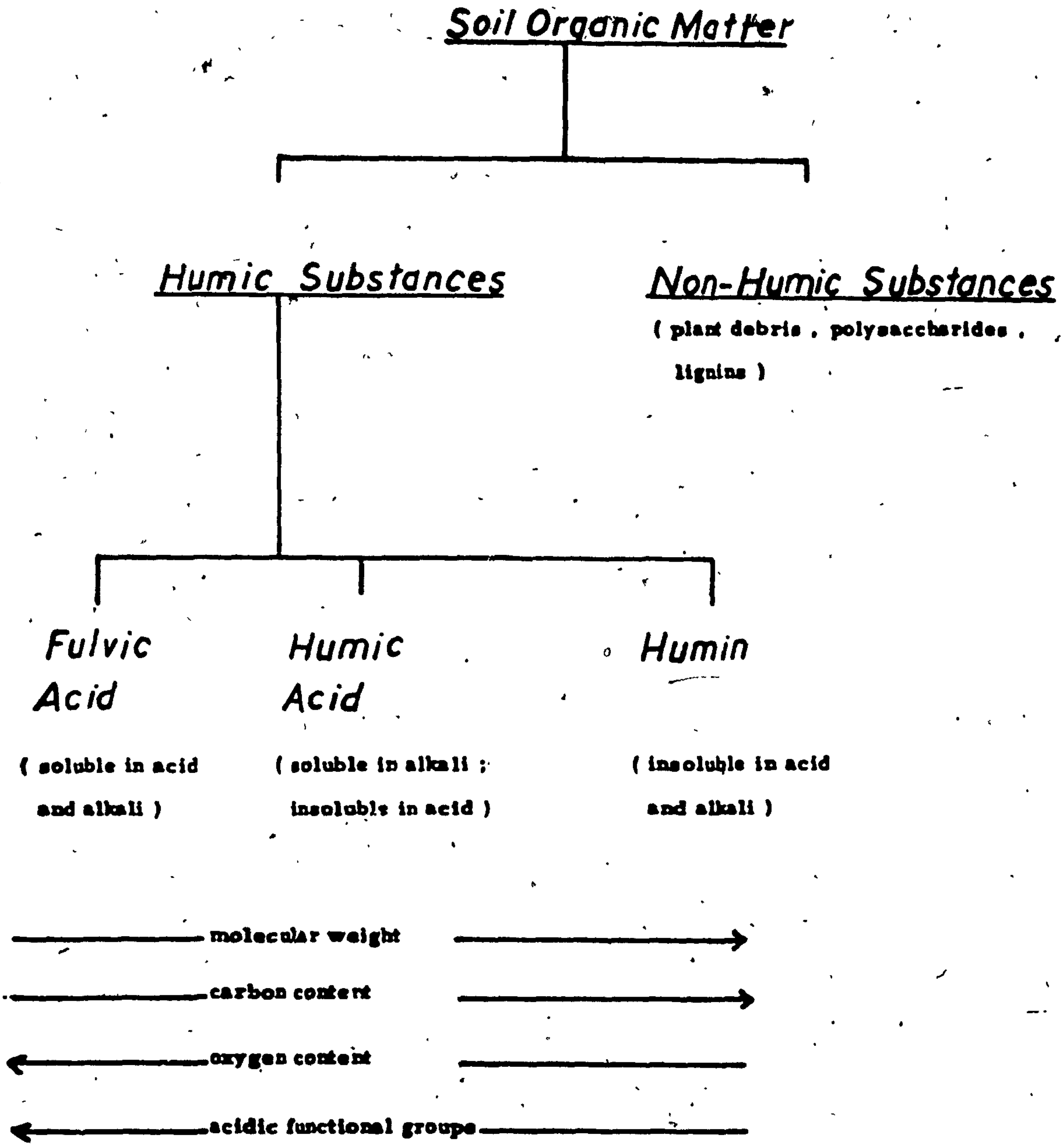

Figure 1 : Scheme for classification of soil organic fractions

contains the highest content of acidic functional groups. It also occupies the lowest range of molecular weight of the three classes of humic substances.

In addition to the alkaline extraction, Armadale fulvic acid has been further refined through extensive ion exchange for removal of metals. The end product is a fully protonated material free of bound cations. Hence Armadale fulvic acid is a natural fraction but it is not a raw material.

One may at this point question the choice of a soil derived material as a model for the organic matter dissolved in inland lakes and streams. In freshwaters, as in the soil, the organic matter present is classified into categories based on origin and operational definition. Dissolved organic material is first classified as " pedogenic " or "aquogenic" depending upon whether it had its origin in the soil or the aquatic environment. Each of these categories is further subdivided into " refractory " or " non-refractory " material. " Refractory " organic material consists of dissolved humic substances while the " non - refractory " portion consists of the undegraded fragments of biomolecules in direct correspondence with the " non-humic " fraction in the soil(1).

In most freshwater systems (1), 70-80 % of the dissolved organic material consists of refractory organic material (ROM), most of which is pedogenic or soil derived (PROM). Up to 70 % of this fraction consists of dissolved fulvic material. A recent review by Buffle (1) compared the properties of soil fulvic acids and PROM and showed striking similarities in the properties of both fractions with respect to molecular weight range, elemental composition, and distribution of acidic functional groups. This comparison, then, supports the Armadale sample as a relevant model for the naturally occuring materials. Unlike aquatic materials, it is available in reasonable quantity.

Functional Group Analysis

Schnitzer (7,17) has determined through titration, derivatization and degradative proceedures, the following distribution of functional groups in the sample: 3.3 meq/g phenolics; 7.7 meq/g carboxylate; 3.6 meq/g aliphatic alcohol; 0.6 meq/g quinone. NMR studies confirm this analysis.

Elemental Analysis

Results yielded %wt content as follows for the current batch of material (34): C = 49.52% ; N=0.58% ; H=4.6% ; Metal ion content (determined by atomic absorption) is less than 10 mmole/g .

Titrimetric Properties

Armadale FA has been characterised by acidometric titration by Gamble (18) . His results yielded equivalence points of 4.99 and 7.74 mmol/g FA for the sample, based on the Gran's function method. These equivalence points are repoducible to within 2 % between separate batches of the material (4). Gamble has interpreted the equilibrium binding function as follows: the first phase of the titration involves the deprotonation of salicylate structures which represent the most acidic sites on the material. These structures are deprotonated after the addition of 3 meq / g FA of titrant. The second phase of the titration (to 3-5 meq / g FA) involves deprotonation of monomeric carboxyl groups and other carboxylate structures whose acidity constants are relatively insensitive to conformational changes in the fulvic "polymer ". The final phase of the titration (5-6.5 meq. / gFA) yields data showing strong electrolyte effects, indicating structural sensitivity of the acidity constants. This is typical of polymeric carboxylic acid functionalities.

Molecular Weight Range

The value assumed in this work is the number average figure of 951 g/mol as determined by vapor phase osmometry (17). The weight average values are significantly larger (20). The material is polydisperse.

Metal Binding Properties

Copper ion loadings have been determined by Lee (3). The binding capacity of the sample for Cu^{2+} was determined to be 4.7 mmol/gFA at pH6 and concentrations of 100 mg/l FA. The binding capacity of the sample decreases as a function of decreasing fulvic acid concentration, decreasing pH and increasing concentration of supporting electrolyte. The binding capacity at 10 mg/l FA is 3.3 mmol/gFA at pH 6. These results were obtained in the absence of background electrolyte.

Experimental Section

Materials and Methods of Preparation

Armadale fulvic acid, prepared by the method of Hansen and Schnitzer (17) was generously supplied by P. Aysola, Chemistry Dept., Concordia University.

Fulvic acid stock solutions were prepared in Millipore ultrapure water (ionic conductivity 13 $M\Omega$- cm) or glass distilled water which had previously been adjusted to pH 2. Stock solutions were prepared and discarded on a weekly basis as recommended by Underdown (4), and protected from exposure to light. Stock concentrations were 400-500 mg/l of FA.

Samples for fluorescence lifetime studies or flash photolysis were prepared by dilution of the stocks. pH adjustments were made with 0.1 M HCl and NaOH, to a precision of ± 0.15 units. This proceedure was adopted to minimise the ionic strength increase required by the use of buffers. The FA concentration was 200-250 mg/l, for the flash photolysis experiments, and was chosen to satisfy the requirements of the flash kinetic spectrometers (0.5 units / 2mm). Samples for fluorescence lifetime measurements were prepared at 50 mg/l of FA. In these experiments the ash content of the materials was treated as an integral component of the sample. FA solutions were unfiltered in all cases.

Stock solutions of metal ions were prepared directly from reagent grade $CuCl_2$ and $NiCl_2$. $ZnCl_2$ was prepared from the metal (analytical grade pellets). The copper content of the salts was checked by iodometric titration (35) and found to be within 1 % of the formula weight.

Values of the copper binding for the Armadale sample were obtained from the binding curves reported by Lee (3). Experiments were carried out over a range of copper binding fractions, α , from $\alpha = 0$ to $\alpha = 1.00$.

FA solutions were aerated for absorption experiments run in the picosecond and early nanosecond domain. Later nanosecond experiments were run on samples which were deaerated with N_2 or Ar. Fluorescence measurements were run in both modes but were found to be insensitive to the effects of O_2.

Instrumentation

Absorbance measurements were made on a Perkin Elmer 552 UV-Visible Spectrophotometer or a Beckmann Acta MVI Spectrophotometer. The wavelength was 355 nm. Absorbance measurements were made in 1 cm or 1mm glass cells. Conventional fluorescence measurements were made on a Perkin-Elmer 1450B Spectrofluorimeter in a 1 cm quartz cell.

Flash Kinetic Spectrometers :

Picosecond Domain

Experiments were conducted on the picosecond spectrometer located at the Canadian Center for Picosecond Laser Flash Photolysis, Concordia University, Montreal. All spectra were recorded with the cooperation of Dr. D. Sharma, head of laser operations.

Excitation was supplied as 20 - 30 ps pulses from a passively modelocked Nd:YAG laser (Quantel). The 3rd harmonic of the Nd:YAG system was used for sample irradiation, with a wavelength of 355 nm. The pulse energy throughout was approximately 3 mJ. Probe pulses were obtained over the range from 410-650 nm by stimulated Raman scattering from D_2O .The detection system consisted of a double monochromator and an optical multichannel analyser (PAR) interfaced to a PDP 11 laboratory computer. Spectra were obtained at delays from 20-100 ps and over the range from 500 ps - 10 ns .Each spectrum was the average of 8-10 shots.

The geometry for detection of the transient absorption signals was a collinear configuration in which pump and probe irradiation volumes were aligned coaxially. A block diagram of the system is shown in Figure 2a.

Nanosecond Flash Kinetic Spectrometer

Flash photolysis experiments in the nanosecond domain were conducted on the flash kinetic spectrometer located at

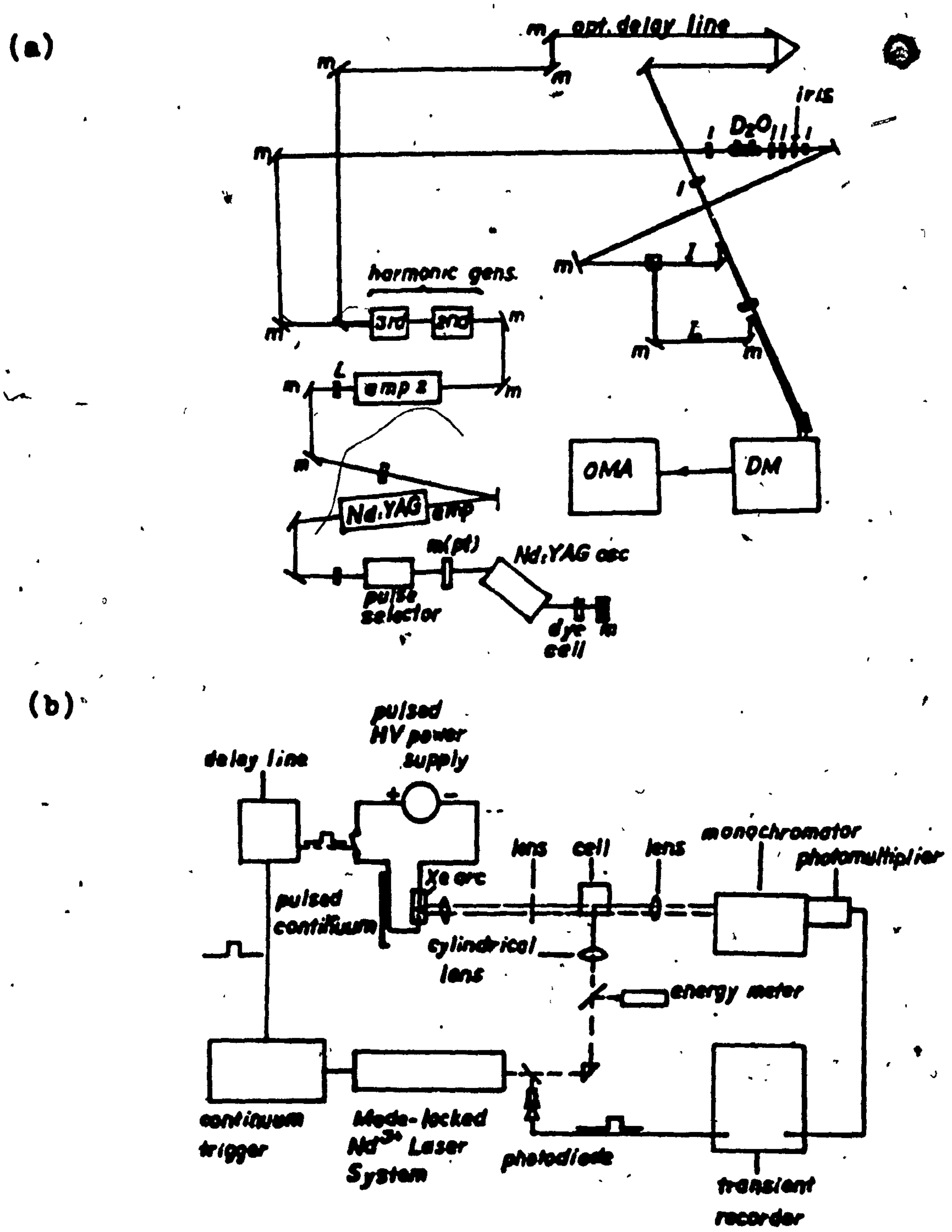

Figure 2 : Block diagrams of (a) the flash kinetic spectrometer located at the Canadian Center for Picosecond Laser Flash Photolysis (b) the nanosecond flash kinetic spectrometer located at CNRS Laboratoire de Chimie Physique A , Universite de Bordeaux I.

Bordeaux I, Talence, France.

Source excitation was obtained from a passively mode-locked Nd:YAG laser system (Quantel). The pulse width was 300 ps at the third harmonic wavelength (355 nm), with a range of pulse energies from 10-30 mJ. Continuum probe light was supplied by a pulsed Xe arc source (200 W) with a discharge period of 10 microsec. In experiments involving long microsecond observation times, the Xe arc was operated with continuous illumination and the laser discharge was initiated manually. The spectrometer utilised a perpendicular detection geometry (Figure 3), in which the continuum probe intersected the irradiation volume at right angles. The detection system consisted of a monochromator and a photomultiplier tube (RCA IP28). The photomultiplier output was monitored by a transient recorder (Tecktronix 7912 AD) with a time resolution of 5 ns. The transient recorder was interfaced to a microcomputer (HP 85) for data analysis under routines written in Basic. A block diagram of the spectrometer is shown in Figure 2b.

Irradiation Geometries

The picosecond domain experiments utilised a coaxial detection geometry in which the probe and excitation pulses overlapped in the irradiation zone. By contrast, nanosecond domain experiments used the perpendicular irradiation geometry of Figure 3. The excitation pulse was introduced into a side face of the photolysis cell. The continuum radiation was directed into the cell at right angles via a 2

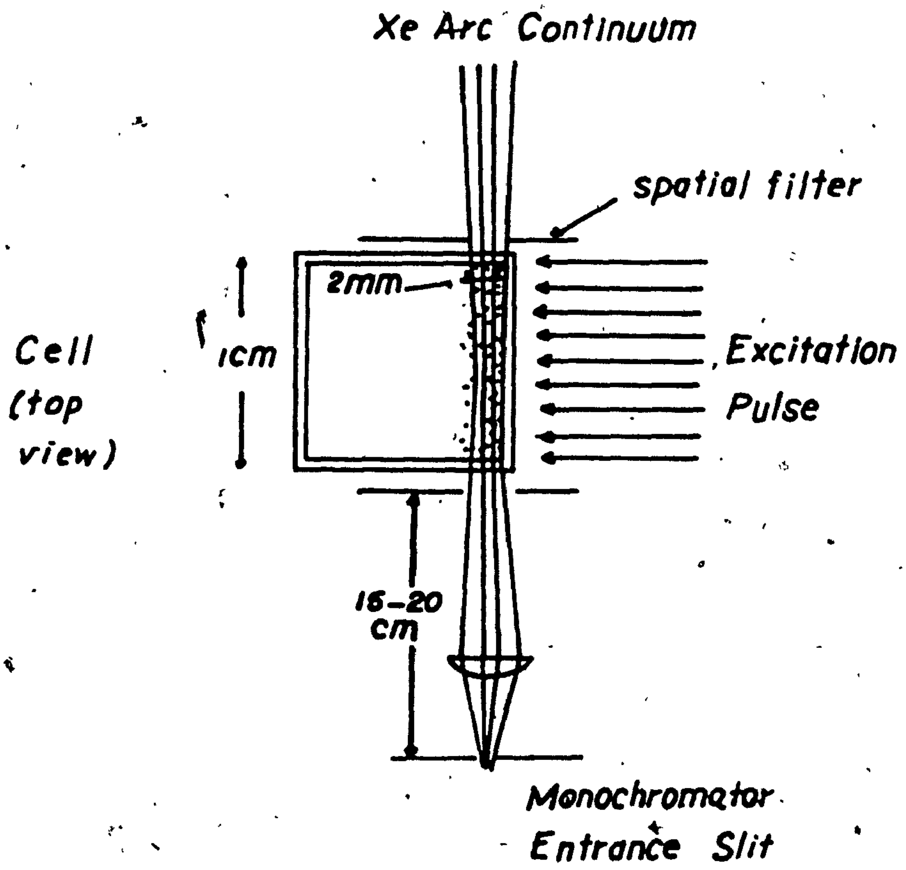

Figure 3 : Schematic of the irradiation geometry for the nanosecond flash kinetic spectrometer showing perpendicular detection scheme .

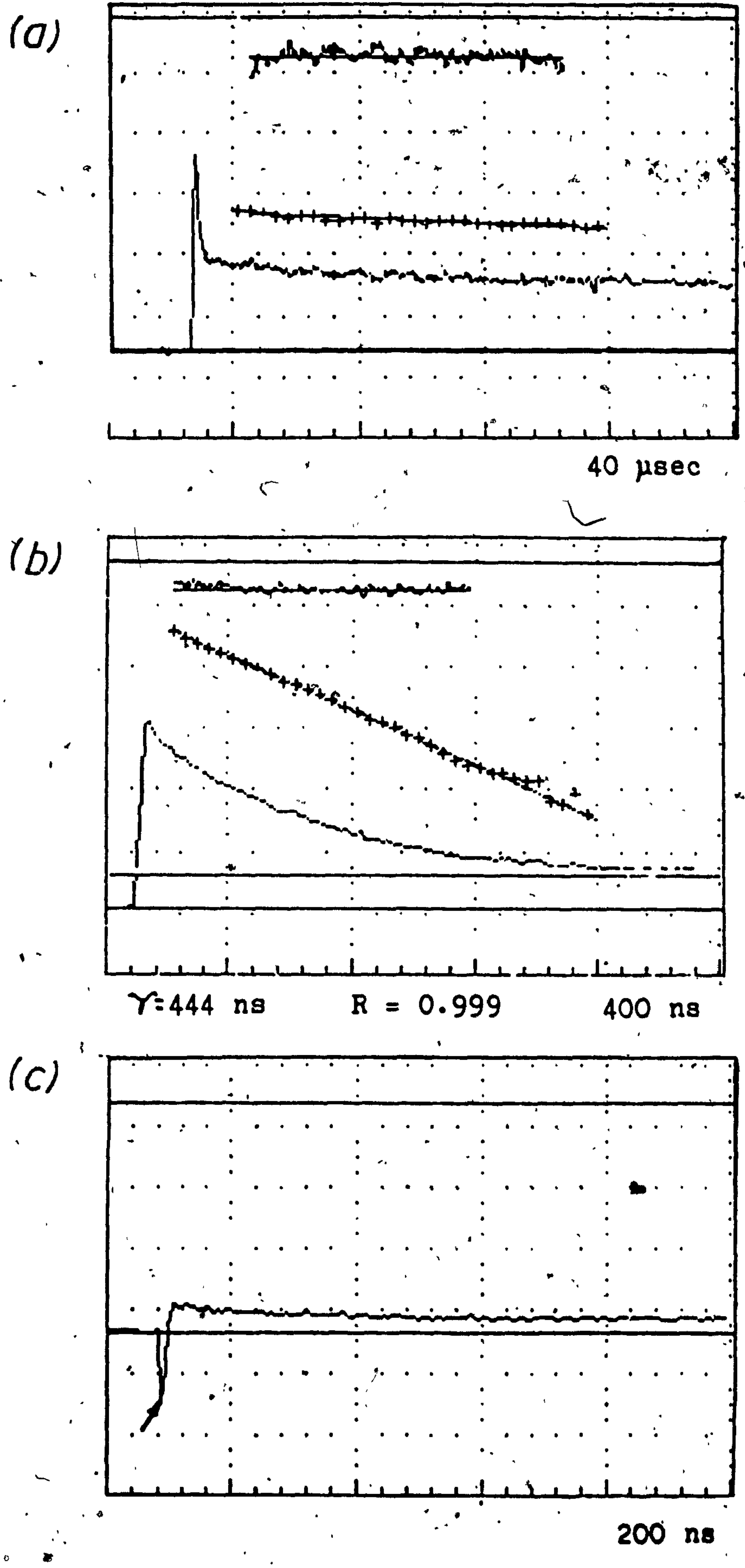

Figure 4: Kinetic profiles obtained from the nanosecond spectrometer. (a) long time scale trace for FA/pH7,showing "black residue"; observation wavelength was 600nm. (b) kinetic analysis of solvated electron decay at 675 nm in presence of 10% O_2 (pH 7). (c) signal observed at 480 nm. Arrow indicates strong emission pulse excited at 355 nm.Samples (a) and (c) were N_2 degassed.

mm slot in the cell holder. The probe radiation emerging from the cell was then focused onto the monochromator entrance slits at a distance of 10-20 cm.

The sensitivity of the perpendicular geometry depends critically on the overlapping of a 2 mm irradiation path with the intersecting probe beam. The design assumes a homogeneous spatial distribution of excited species over the 2mm irradiation path. Highly absorbing samples produce a narrow, inhomogeneous spatial distribution of excited states so that the probe beam traverses a path containing a large section of the irradiation volume unaffected by the excitation pulse. The nanosecond apparatus was designed to photolyse samples with ground state absorbances of $A = 1.00\ cm^{-1}$. The low signal levels initially observed for dissolved FA required the absorbance to be raised to $A = 2.5\ cm^{-1}$. The AFA concentrations were approximately 250 mg/l, which matched the sample concentrations used in the picosecond experiments. However, large absorbance values produced inhomogeneities in the excited state distribution so that it was neccessary to reduce the width of the probe beam section to 1 mm and use high excitation power (20-30 mJ).The coaxial design used in the picosecond instrument yielded a much higher detection sensitivity.

Two additional problems were associated with the perpendicular design. The first was a problem of intense, short lived fluorescence, produced by the photolysis pulse. The pulse of fluorescence effectively "blinded" the photomultiplier tube for up to 100 ns after the passage of the photolysing pulse and prevented study of the earliest (50 ns) decay components (see Figure 4). This problem most likely arose from the relatively close spacing between the photolysis cell and the entrance to the monochromator (Figure 4).

The second problem was encountered in the long time domain (t > 10 microsec) and involved interference due to photothermal deflection effects in the sample. The diffusion of heat at long times after excitation produces a thermal gradient in the sample (which may also in part be due to an uneven spatial distribution of excited species in the sample in the initial flash). The thermal and/or concentration gradients may produce a deflection of the probe beam (36,37) and an apparent reduction in its intensity observed at the detector. Experiments with oxygen quenching of the longest lived transient absorption signals have demonstrated that they are not artifacts of these phenomena. However, the photothermal interference makes it impossible to determine where to place the signal baseline. No kinetic analysis of the longest signal components was therefore possible.

Fluorescence Lifetime Determinations : Instrumentation

In the picosecond/early nanosecond domain, measurements were made on an instrument located at the Canadian Center for Picosecond Laser Flash Photolysis, Concordia University, Montreal. Excitation was obtained from the passively mode-locked Nd:YAG laser mentioned above with a pulse width of 30 ps. The irradiation wavelength was 355 nm (third harmonic) and the pulse energy was 3 + 0.25 mJ. The detection system consisted of a streak camera (Hammamatsu). The cell path for irradiation was 2mm. An integrated emission was monitored above 435 nm.

Nanosecond domain experiments were carried out at L'Universite du Québec à Trois Rivières by Dr. R. Lesage. The apparatus was a Photochemical Research Associates single photon counting emission spectrometer. The wavelengths of excitation and of observation for emission were 350 and 500 nm, respectively. Emission lifetime data were deconvoluted and fitted to three exponentials under propreitary software.

Results Section

Kinetic Overview of the Observed Phototransients

The observed kinetic behavior for the photolysis of the Armadale sample may be summarised by the kinetic map shown in Figure 5. Temporally, the scheme is divided into four components of which two may be assigned.

The most striking feature of these results is the formation of a solvated electron (component II). This signal has a characteristic absorption spectrum which maximises near 700 nm, and a lifetime which increases with pH. Based on its quenching behavior in the presence of N_2O, copper and dissolved oxygen, as reported in the next section, its identity has been conclusively verified. Concurrent with the formation of the solvated electron, a transient absorption signal arose with a maximum at 450-510 nm. Its lifetime range (1-15 microseconds) and spectrum match the signal observed by Fischer et al. (23). Our experiments present strong evidence that this signal is linked to the solvated electron. A third less obvious feature of the kinetics is the presence of a strong featureless background absorption signal with a lifetime in excess of 100 microseconds. This signal, which has been independently verified, is dubbed " the black residue " because of its very broad featureless absorption. It has been studied in the presence of quenchers and its growth in the early time domain has been recorded. Quenching of the signal by O_2 (in the

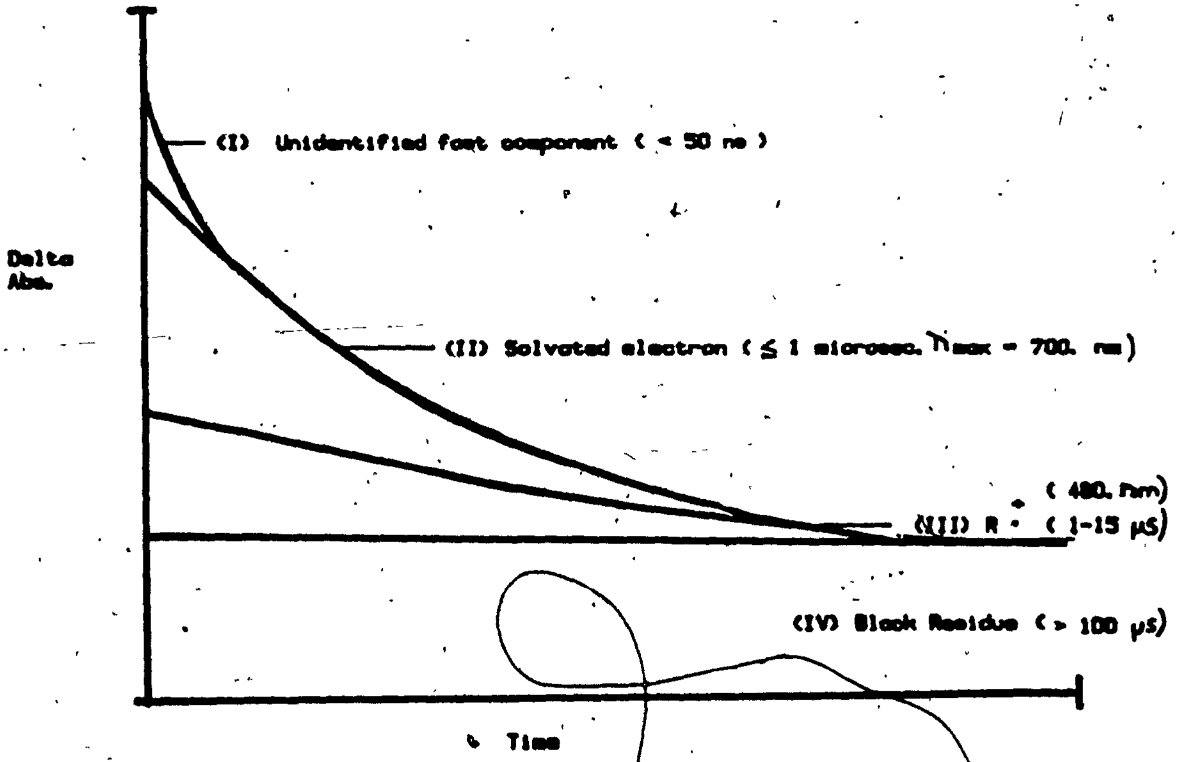

Figure 5 : Schematic " map " of the transient species observed in the nanosecond flash photolysis of Armadale fulvic acid .

microsecond domain) has demonstrated that this signal is not an experimental artifact. Finally a fourth component of transient absorption was observed, with a lifetime of approximately 50 ns. It has remained unidentified owing to the technical problems mentioned in the previous section which make this time domain fall between our two spectrometer systems.

Time resolved spectra for components II–IV are reported at t = 200 ns for fulvic acid samples at pH 4 and 7 in the presence and absence of N_2O (Figure 6a,b). As expected, the 650–700 nm transient absorption was quenched by N_2O, which acts as an electron scavenger (38):

$$N_2O + e^- + H_2O \longrightarrow OH^{\cdot} + N_2 + OH^-$$

Based on the solubility of N_2O in aqueous solution and the Stern-Volmer equation, the lifetime of the solvated electron is less than 200 ps so that the 650 -700 nm spectral feature does not appear in the spectrum recorded at 200 ns. The residual spectra clearly indicate the presence of a transient absorption signal with a maximum at about 440–480 nm, and a featureless " background " absorption on which the signal is superimposed.

The growth of these features may be observed in the picosecond domain. Transient absorption spectra recorded as early as 20 ps show the presence of both the 480 nm and 650–700 nm components at this early time, implying concurrent formation on the timescale of the excitation pulse. The third

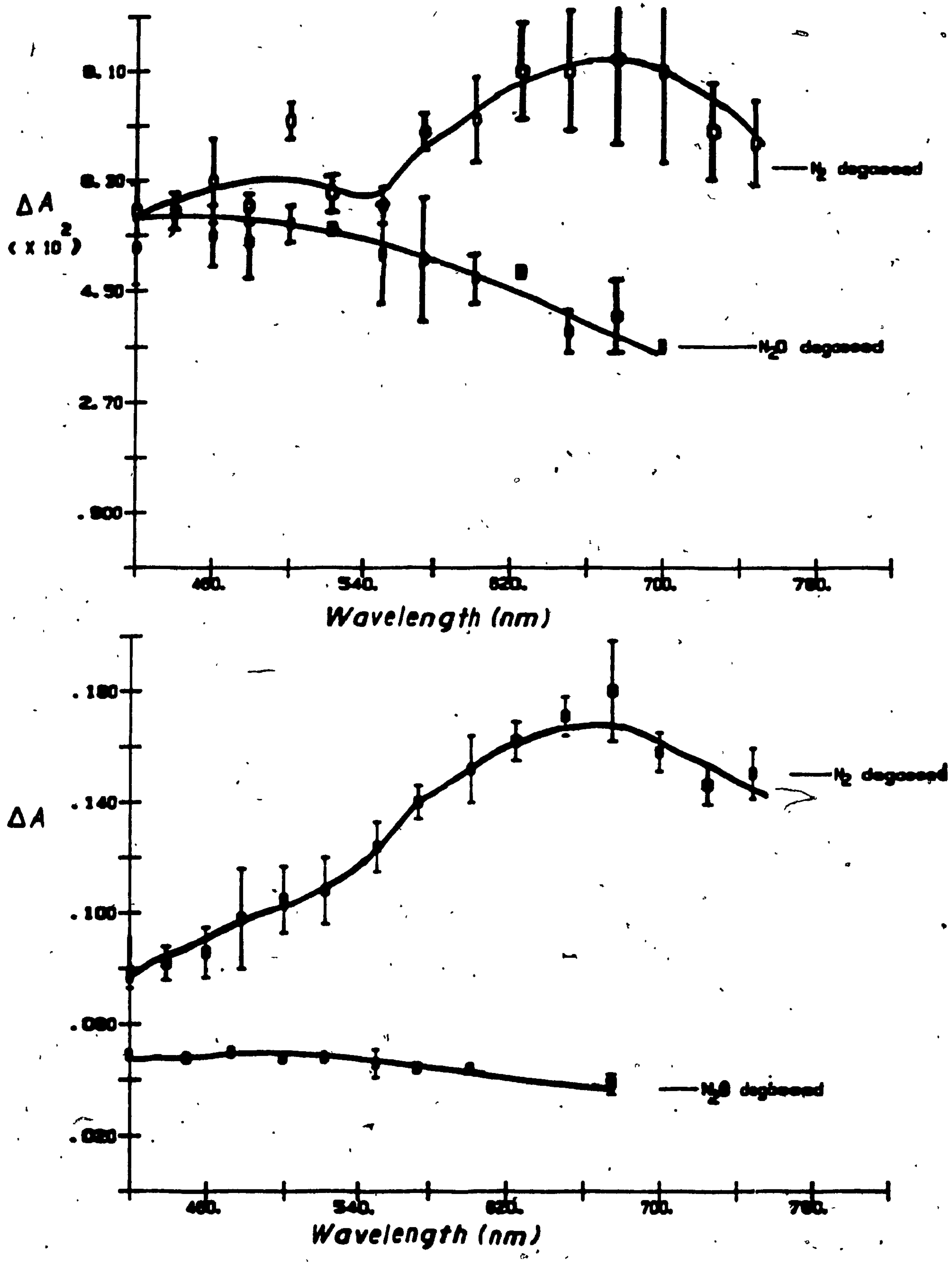

Figure 6 : Transient absorption spectra observed for Armadale FA showing the effect of N_2O on signals . Spectra were recorded 200 ns after excitation with a 300 ps pulse. (a) pH 4 (b) pH 7 . Pulse energy was 30 mJ .

component, The "black residue " emerges several nanoseconds following excitation and is not apparently, a primary species like the other two.

Formation and Decay of the Solvated Electron

Figure 7 shows excited state spectra recorded at t = 20 ps after excitation for FA at various pH's. This time corresponds to the width of the excitation pulse. It is clear that the 480 nm transient and solvated electron appear concurrently within the pulse width.

The early appearance of the solvated electron is in agreement with measurements by picosecond spectroscopy (39,40) which indicated the appearance of the 700 nm spectrum at times as early as 10 ps after excitation. The formation of the solvated electron in metal free FA solutions is essentially complete within the passage of the photolysis pulse. Further growth in the signal from t > 20 ps to t = 10 ns seems to be entirely due to the " black residue (BR) " component.

The fast formation of the solvated electron persists over the pH range from 2 - 7. The situation becomes more complicated in the presence of bound metal ions. The addition of millimolar amounts of copper (II) to the FA solutions has the effect of quenching the solvated electron formation at 20

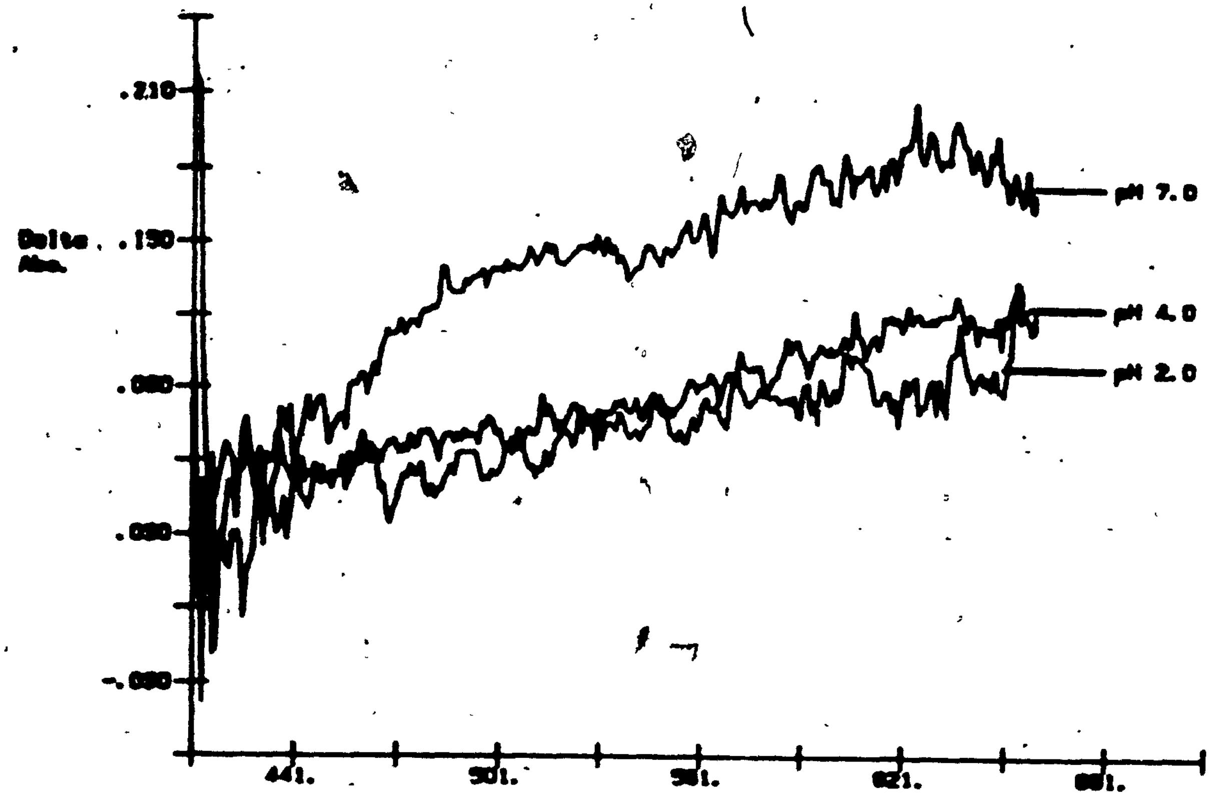

Figure 7 : Transient absorption spectra of Armadale FA recorded at t = 20 ps . Pulse energy was 2.5 mJ .

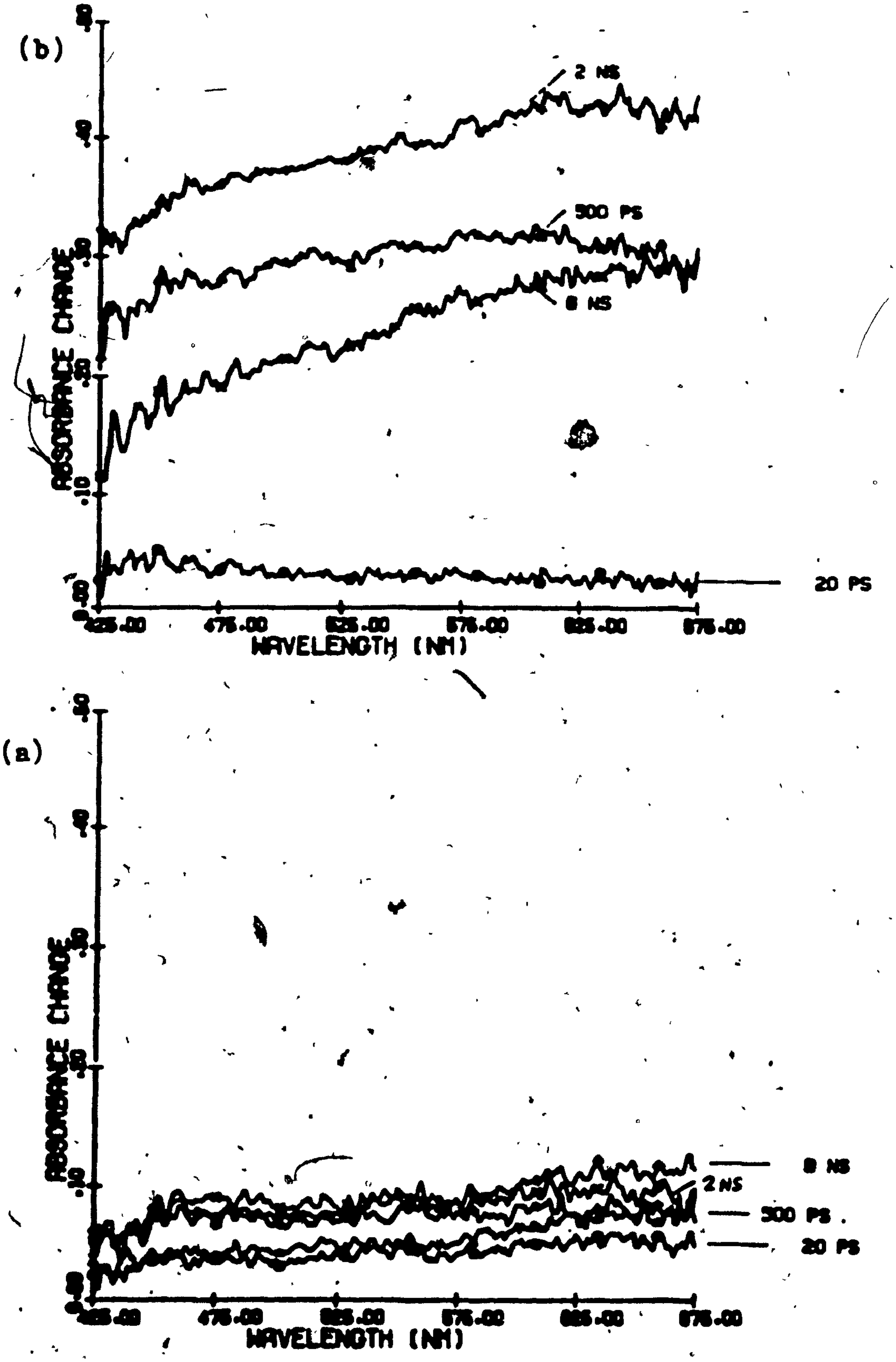

Figure 8 : Transient absorption spectra of Armadale FA samples containing sufficient copper to occupy (a) 40 % of binding sites (b) 100 % of binding sites . [FA] = 100 ppm , pH = 6.0 .

the effect of quenching the solvated electron formation at 20 ps (Figure 8a,b). At later times (2 - 8 ns), the 650-700 nm spectrum seems to emerge. The late arrival of this feature is quite pronounced in the samples containing enough copper to occupy all of the binding sites. The explanation might be based on changes in the aggregation state of the materials that occur at high copper loadings (4). Photoionisation may be occurring in the interior of the FA aggregates. Diffusion times in the interior of such aggregates would probably be greater than in water, delaying the appearance of the 700 nm spectrum(40).

The formation yield for the solvated electron in the nanosecond regime was studied as a function of the pulse energy (Figure 9). A linear plot of transient absorption was obtained over the range from 10 to 50 mJ per pulse indicating monophotonic formation processes. No saturation of the transient absorption signal was observed, even at the highest energies available from the laser system. The monophotonic formation of e^-_{solv} suggests that the process could be environmentally relevant. 355 nm photons are available in sunlight.

This result may seem surprising in view of the rather long irradiation wavelengths used in the experiments (355 nm). However, from the early work of Joschek and Grossweiner (41) on the flash photolysis of a series of phenol derivatives and compounds structurally related to components of fulvic acid, it was observed that solvated electrons were released by monophotonic processes. Furthermore, it was

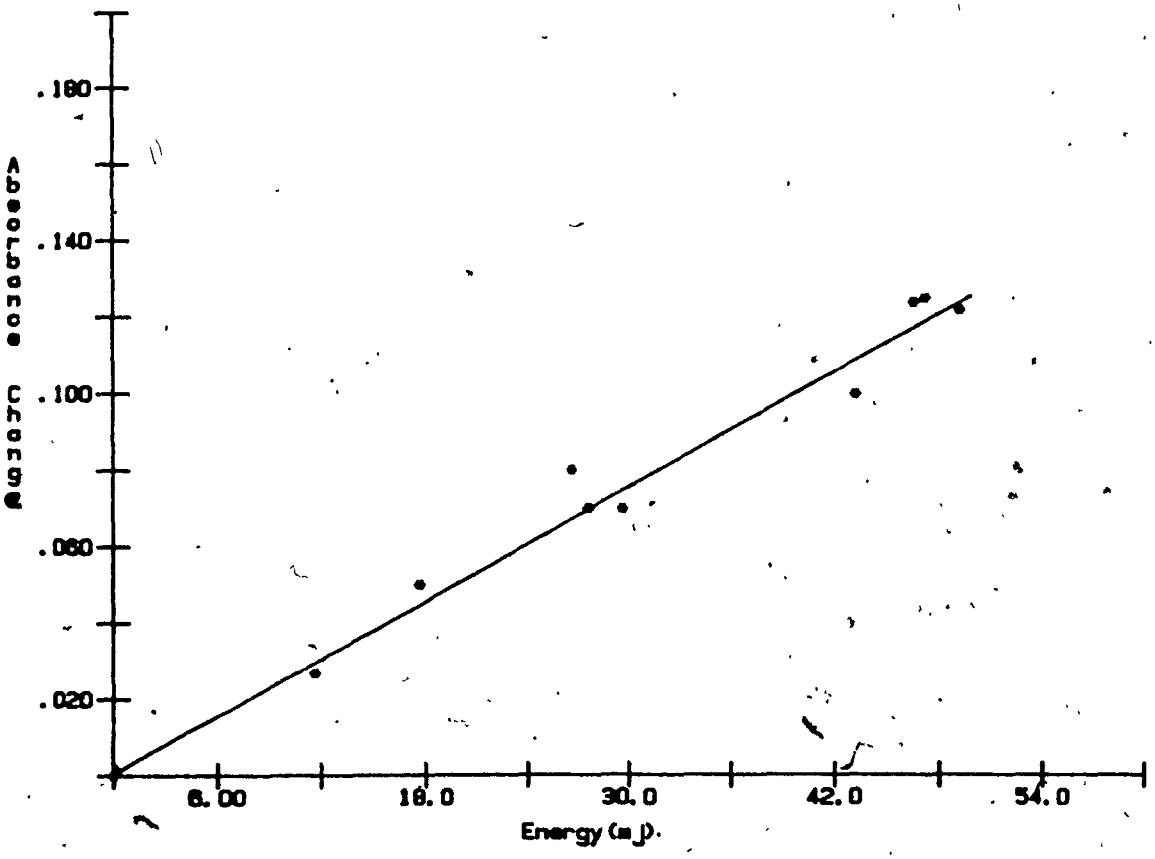

Figure 9 : Plot of transient absorption signal vs pulse energy for the solvated electron , observed at t = 500 ns after excitation . Observation wavelength was 675 nm .

observed that the ejection processes were even more efficient from the lowest lying excited singlet states of the chromophores (at wavelengths of 300 nm or greater) than from the higher energy S_2 states located from 250-300 nm. The suggestion of these authors was that electron release occurred via a charge transfer to solvent (CTTS) state populated via the ring system. More recent mechanistic work (42) supports this assignment. Electron release from S_2 states has also been shown to occur following a mechanism of direct photoionisation. The process of electron ejection may also be biphotonic in some cases (42). Consequently the low energy release of solvated electrons from humic materials seems to be consistent with known mechanisms.

Estimations of the formation yield for the solvated electron at early times have been made directly from time resolved absorption spectra recorded at 20 ps and the molar absorptivity for the solvated electron supplied by the National Bureau of Standards (43). At t = 25° C and 675 nm the value was $1.4 \times 10^4\ M^{-1}cm^{-1}$. The volume of irradiation for the sample was approximately 2×10^{-5} l based on the dimensions of the laser pulse at the cell. The values of for the formation yield are reported in Table 1. The efficient release of the electron indicates that the process may be environmentally relevant.

The decay of the solvated electron signal was studied in

Table 1

Quantum Yields for Formation of the Solvated Electron at 20 ps

pH	A_{355}	E_{pulse} (mJ)	ΔA_{20ps}	φ_e
2.0	0.512	2.43	0.07	0.09
4.0	0.495	2.98	0.13	0.15
7.0	0.561	2.52	0.16	0.20

the nanosecond regime, and its quenching behavior was examined in the presence of dissolved Cu^{2+}, O_2 and H^+. Quenching rate constants were evaluated for the 650-700 nm transient by means of a Stern-Volmer analysis. The resultant values of k_q are reported in Table 2.

For the quenchers studied, the following bimolecular reactions are anticipated :

$$O_2 + e^- \longrightarrow O_2^-$$

This process directly predicts the formation of superoxide, as observed by Baxter and Carey (12).

For copper quenching :

$$Cu^{2+} + e^- \longrightarrow Cu^+$$

This process predicts the direct photoreduction of metal ions in solution, potentially explaining the photoreductive dissolution of iron(III) colloids in irradiated humic waters (32).

For proton quenching, H_2 is liberated :

$$H^+ + e^- \longrightarrow H^\cdot$$

$$2H^\cdot \longrightarrow H_2$$

The rate of reaction of solvated electrons with the free acceptors mentioned is near the diffusion limit as seen from

Table 2

Summary of Flash Photolysis Kinetic Measurements for Armadale Fulvic Acid Under Laser Excitation at 355 nm

Transient Studied	λ_{max}	τ_{obs}*	Quencher	k_q (x 10^{10} $M^{-1}s^{-1}$)
solvated electron	675 nm	1140ns (pH 7)	O_2	1.2 (lit. 2.0)
			Cu^{2+} (pH 6)	1.6 (lit. 3.3)
			N_2O	>.1 (lit. 0.9)
		480 ns (pH 4)	H^+	1.2 (lit. 2.1)
		530 ns (pH 7)	0.1 M NaCl	
radical	475 nm	3.9 us (pH 4)	-	-
"black residue"	broad (featureless)	>100 us	Cu^{2+} (pH 6)	5 x **
			Ni^{2+}	2 x **
			Zn^{2+}	1.4 x **
			O_2 (pH 7)	2 x **

Literature values are from reference 44.

* Samples were run in degassed solutions .

** This figure represents the ratio of the signal amplitudes observed in the absence and prescence of 10^{-3} M quencher ,at 100 usec after excitation.

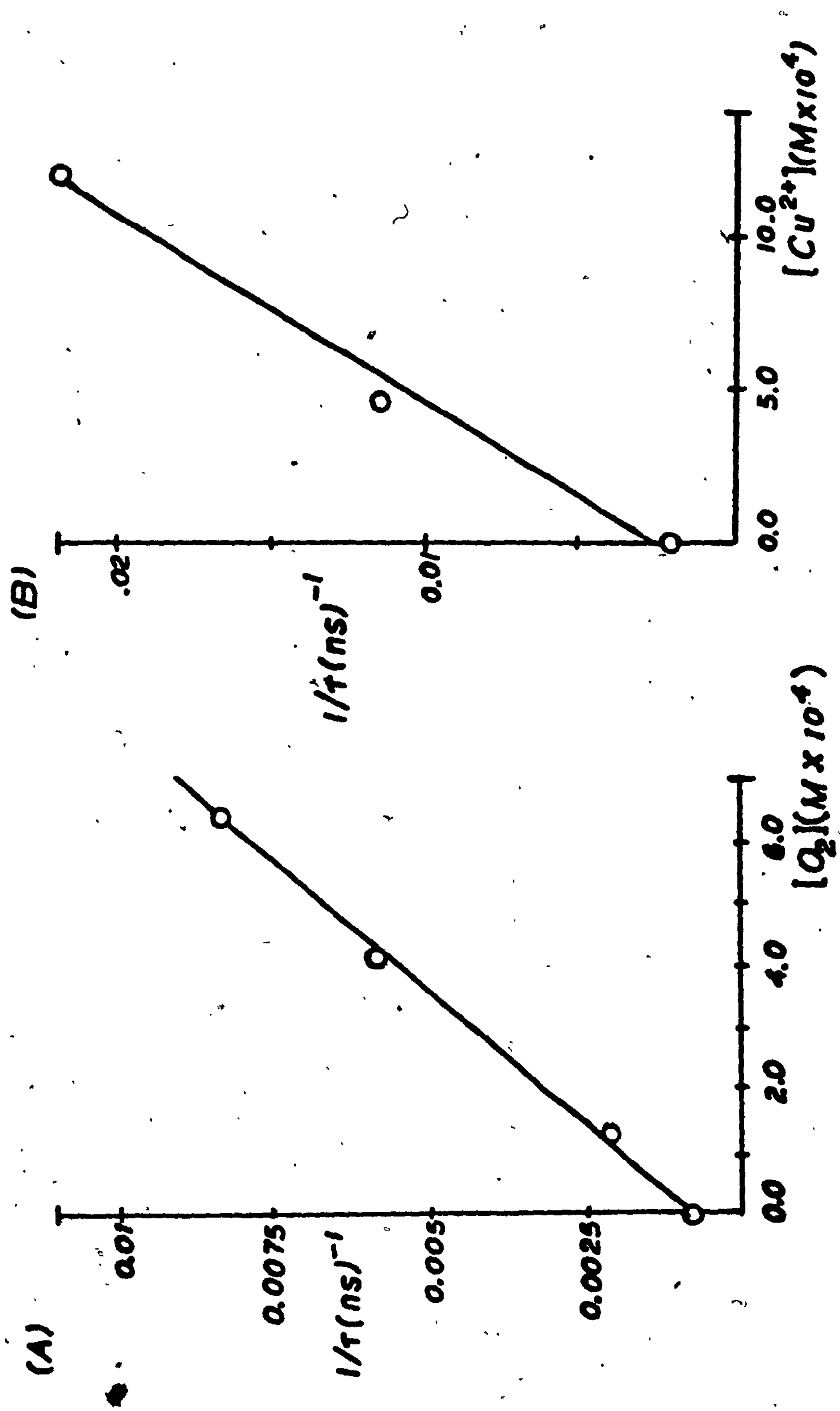

Figure 10 : Stern-Volmer data for quenching of the solvated electron (a) oxygen quenching (b) quenching by copper(II) . Observation wavelength was 600 nm .

the literature values reported in Table 2. The data show good agreement with this range of reaction rates although the specific values of the experimental quenching rate constants are low. While part of the difference may be attributed to inherent imprecision in the estimates of k_q, it also appears likely that the observed rate constants reflect a reduction in the quenching rate due to binding of the quenchers to the humic material. The k_q values estimated in Table 2 assumed that the quenchers were available as free species. In fact, a significant fraction of the bound Cu^{2+} could have a reduced reactivity for the electron; the activity of quenchers is perhaps reduced in the presence of the humic material. Alternatively, if a significant fraction of the electron generating sites are located in the interior of the humic aggregates, the diffusion coefficients for the quenchers may be significantly reduced relative to the value in water. Diffusion of the electron into the bulk solvent may be slowed so that the recombination reaction with free quenchers is inhibited.

Finally, the question of the recombination of the electron with the humic substrate is addressed. From early flash photolysis work on solvated electron generation in phenols and cresols (45) the lifetime for the electron was observed to be 25 microseconds in deaerated aqueous solution. The relatively large value of the lifetime observed for the electron indicated a low reactivity for the radicals formed from the parent species. In the present experiments, the much shorter lifetime observed for e^-_{solv} (approximately 1 microsecond) indicates that recombination with the humic material itself is a major route for capture of the electron. The rate constant for quenching by the humic substance is estimated from the Stern-Volmer equation:

$$k_{obs} = k_0 + k_q[\ Q\ ] \qquad (2\text{-}1)$$

In this case, [FA] = [Q] = 2.5×10^{-4} M. If $k_{obs} = 1 \times 10^6\ s^{-1}$, and the k_0 value for the electron (as observed in the presence of the cresols)is $4 \times 10^4\ s^{-1}$ then $k_q = 4 \times 10^9\ M^{-1}\ s^{-1}$ suggesting recombination at rates approaching the diffusion limit. A range of reactivities for the electron could also be accounted for by a variety of benzenecarboxylic acid structures commonly found in fulvic acids (17,21,28) (Table 3). The recombination reaction of the solvated electron with the humic substance could potentially supply structural information on the humic materials. This is because conformational changes in the humic "polymer" could change the observed quenching rate constant for e^-_{solv} by varying the availability of recombination sites on the material. This effect may explain the decreases in the lifetime of the solvated electron observed in the presence of 0.1 M NaCl (Table 2).

Table 3

Rate Constants for Recombination of the Solvated Electron with Aryl Acids *

Structure	k_q (M^{-1} s^{-1})
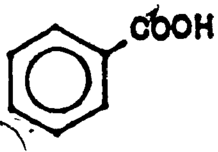	2×10^{10} M^{-1} s^{-1}
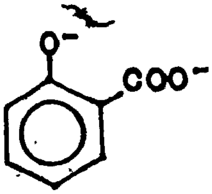	2×10^{10} M^{-1} s^{-1}
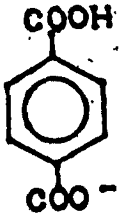	8×10^{9} M^{-1} s^{-1}
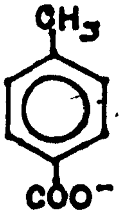	2×10^{9} M^{-1} s^{-1}

* Rate data were obtained from reference 46.

Radical Coproducts

The early time spectra recorded in Figure 7 contain, in addition to the 700 nm transient absorption, evidence of a second species with a peak at 475 nm. The early formation of this species concurrent with the formation of the solvated electron seems to indicate that it is a radical/cation species associated with the generating site for the electron. Further evidence that the two signals are linked is indicated by a spectrum recorded with excitation at 530 nm (2nd harmonic Nd:YAG) showing absence of both features.

If this assignment is correct, it is well supported by past work on the formation of solvated electrons in phenols and related compounds (41). A variety of the radical coproducts generated with release of an electron exhibited spectra with absorption maxima between 400-500 nm.

Some potential candidates for radical co-products are presented here. The general features of the electron/radical generating processes appear to be as follows (41,47,48) :

1. Phenolic compounds when irradiated efficiently yield solvated electrons and phenoxyl radicals :

$$C_6H_5OH \xrightarrow{-H^+} C_6H_5O\cdot \; + \; e^-$$

2. Anisoles and related methoxy benzenes yielded radicals of the phenoxymethyl type, with accompanying loss of a proton :

$$C_6H_5\ OCH_3 \xrightarrow{-H^+} C_6\ OCH_2\cdot \; + \; e^-$$

3. Phenoxy acids yield the phenoxymethyl radical via loss of

CO_2 at the terminal carbon (41) :

$$C_6H_5\ O\ CH_2\ COO^- \xrightarrow{-H^+} C_6H_5\ O\ \dot{C}H\ COO^- + e^-$$

$$C_6H_5\ O\ \dot{C}H\ COO^- \xrightarrow{+H^+} C_6H_5\ O\ CH_2^{\cdot} + CO_2$$

Both types of radicals show broad absorption from 350 - 500 nm.

Oxygen quenching behavior is quite different for the two species. Phenoxyl radicals are insensitive to oxygen and persist to times greater than 100 microsec. The phenoxymethyl radical is readily quenched by O_2 and posseses lifetimes of 25 microsec or less. The 480 nm spectral feature observed at 1 microsec seems to be readily explainable in terms of this species. Phenoxyl radicals would probably contribute to a component of the " black residue " signal on the basis of their long lifetimes.

On the basis of typical absorptivities for the radical photolysis products of phenols (45), the value of $1 \times 10^4\ M^{-1}\ cm^{-1}$ was assumed. This value was used to approximate an initial formation yield for the radical product at 20 ps. From the known values for the molar absorptivity of e^- solv at 675 nm and 475 nm the electron spectrum was subtracted from the 20 ps spectrum recorded at pH 7. Based on the residual absorption signal at 480 nm, the pulse energy and the volume of irradiation, the calculated quantum yield value was approximately 0.1 which matches the formation yield for the electron. This further suggests a link between the two signals.

The " Black Residue " : Formation and Quenching Behavior

The third early time domain component of interest is the " black residue " spectral feature. This transient is observed to form with a time constant of about 2 ns after a 1-2 ns induction period. The growth kinetics of " BR " have been observed by subtracting the 20 ps transient spectrum from spectra recorded at later times. The differential spectra obtained are broad, nearly flat envelopes which reach a maximum intensity within 6-10 ns of excitation (Figure 12). The kinetic profile of Figure 13 further illustrates the situation. The data of Figure 13 seem to suggest that the feature begins to decay past 10 ns, but unfortunately, it was not possible to directly follow the decay kinetics past this point (see experimental section).

Because of the " black " spectral signature, a link is suggested with the signal observed at times past 10 microsec (see Figure 11). The microsecond BR signal was studied with respect to proton, oxygen and metal ion quenching behavior. A kinetic analysis of the data was not possible owing to the very weak signal levels involved over the long time period and the potential intereference of photothermal artifacts.

The intensity of the "BR" signal was found to be approximately linear with the pulse energy, indicating monophotonic formation processes. The signal was found to be strongly quenched by O_2, H^+ and bound metal ions such as Cu^{2+}, Ni^{2+}, and Zn^{2+}. Plots of the relative signal magnitude

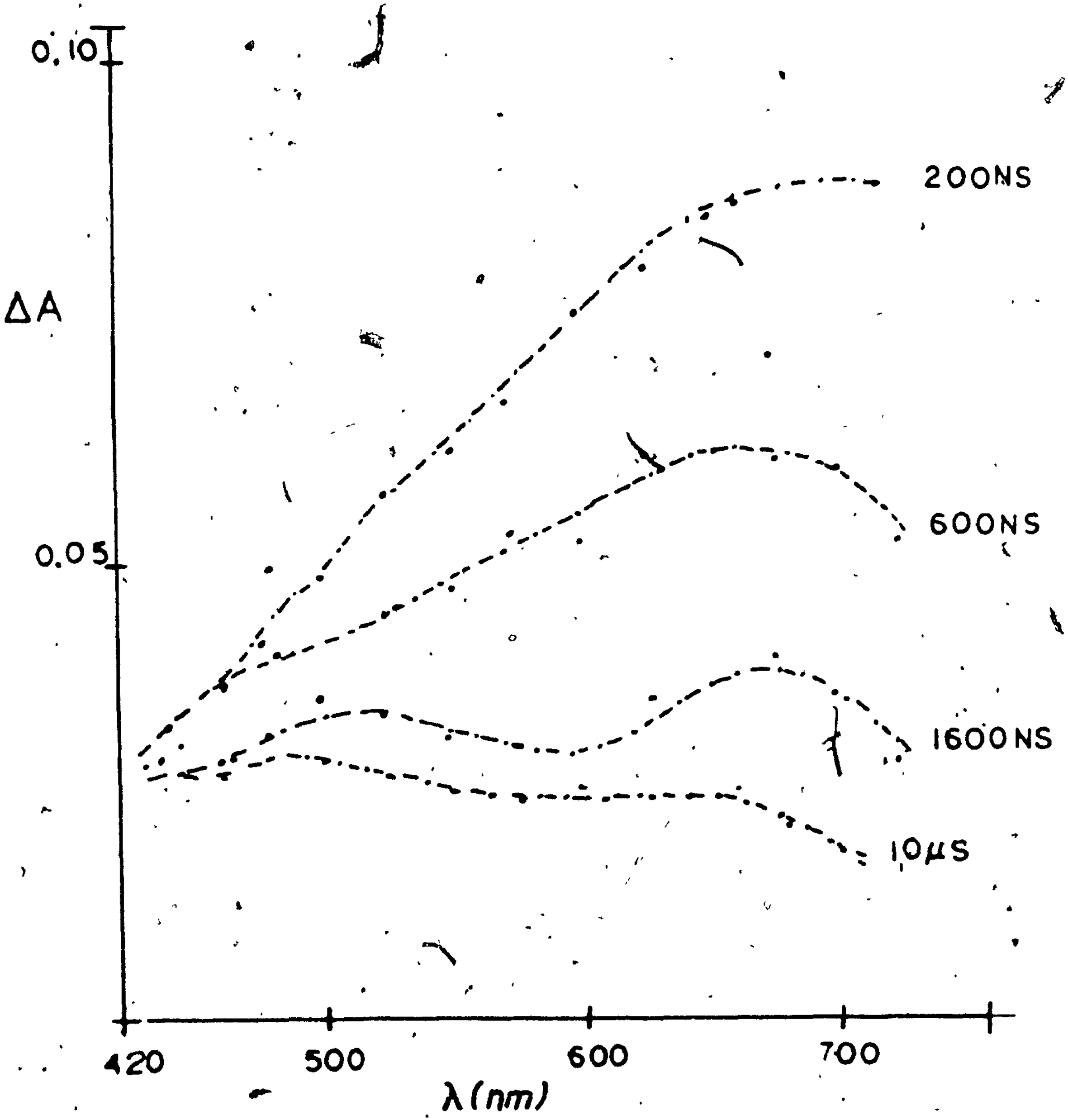

Figure 11 • Time resolved Spectrum of Armadale FA in the nanosecond regime showing prescence of the "black residue" at 10 microseconds.

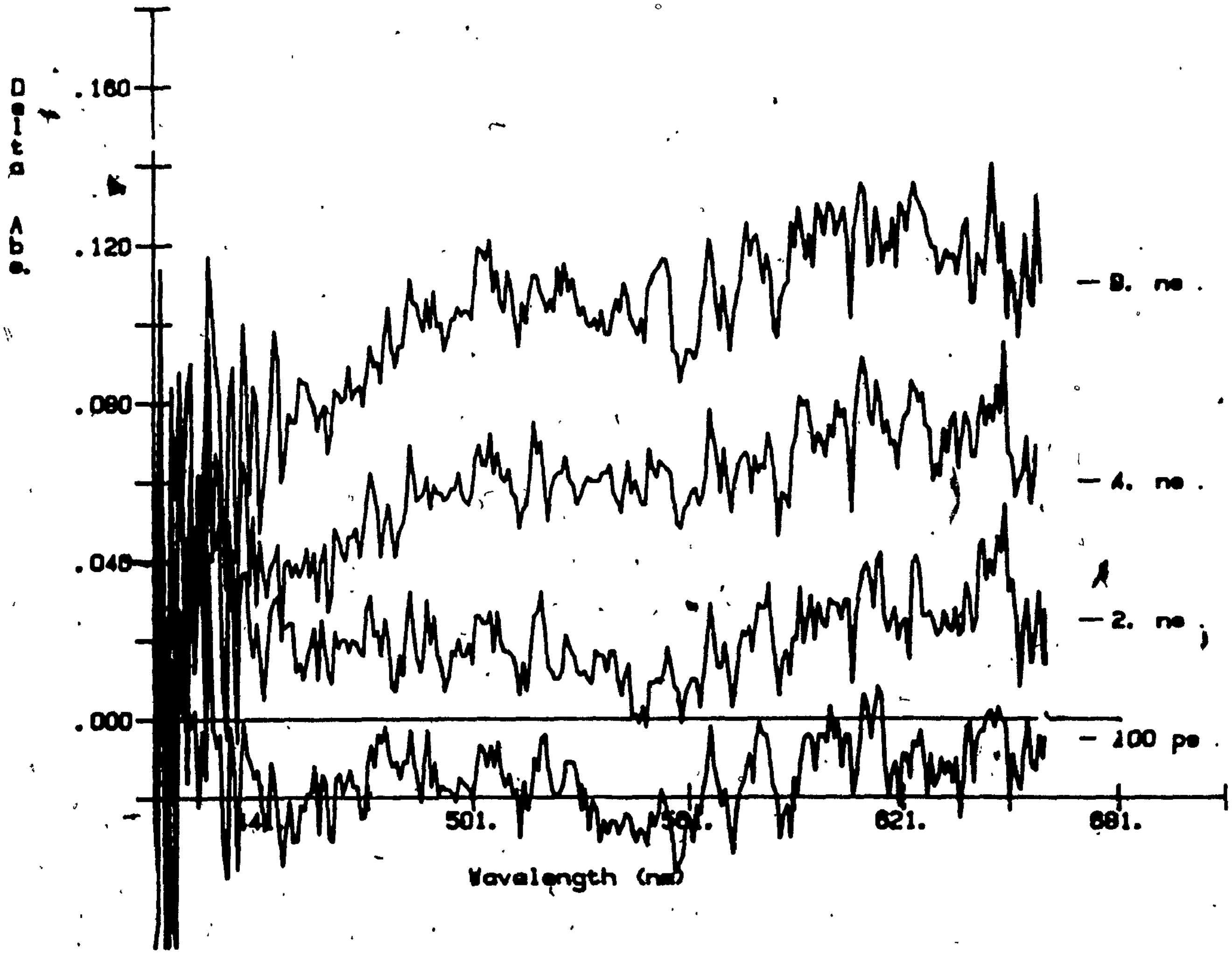

Figure 12 : Differential spectra of Armadale FA at early times showing the growth of the "black residue" component. The spectrum recorded at 20 ps was subtracted from spectra recorded at later times . $E_{pulse} = 3.0$ mJ .

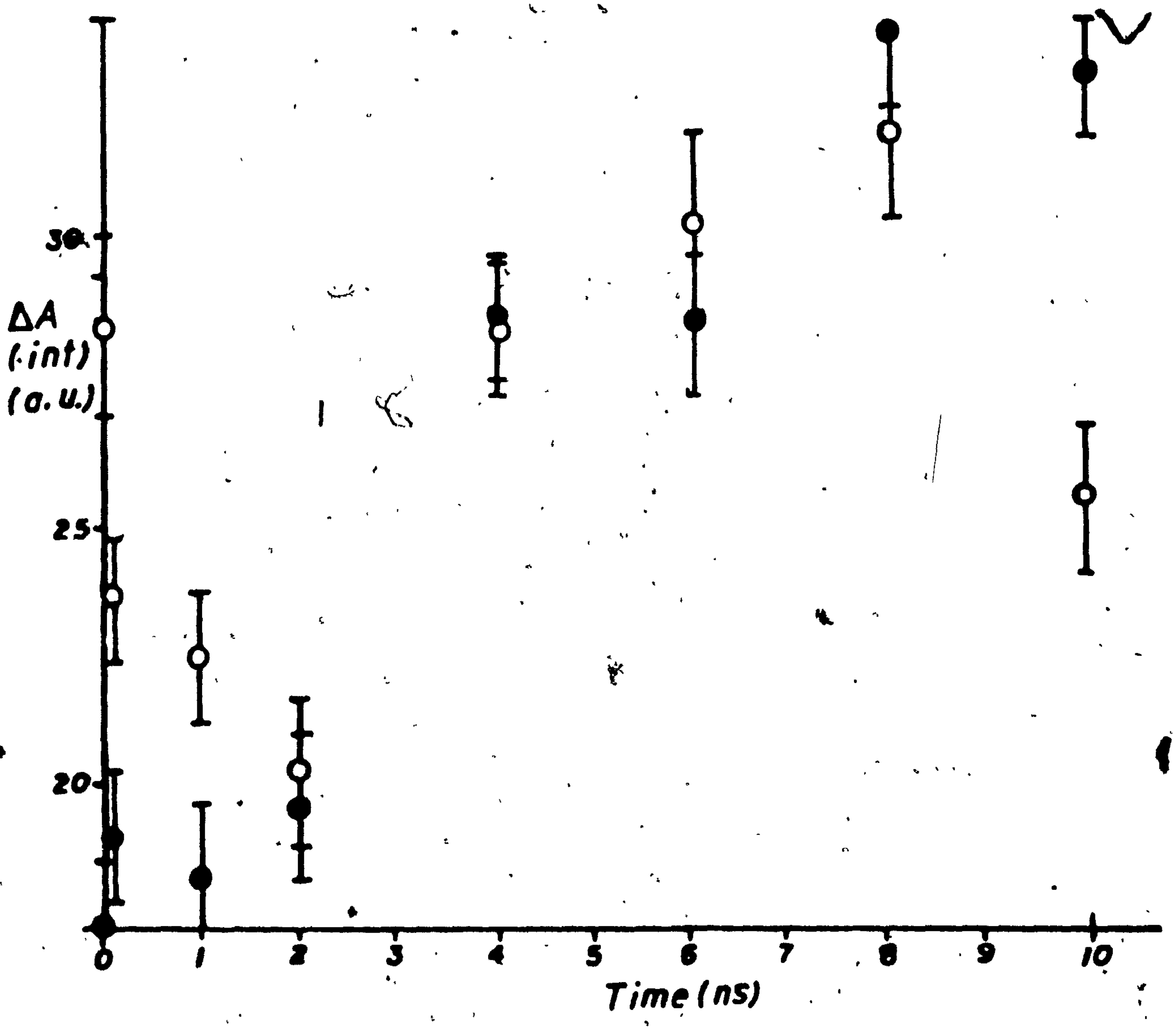

Figure 13 : Integrated absorption signal vs time profile at early times. Transient absorption spectra were integrated over the wavelength range from 510-580 nm and normalised to a pulse energy of 2.8 mJ. ○ = pH 4. ● = pH 7.

versus concentration of metal ion quencher are reported in Figure 14. In the figure, the parameter " %Q " represents the percentage of total BR signal intensity remaining in the presence of given concentrations, [M^{2+}], of metal ion quenchers. (It is defined as %Q = (A([M^{2+}]) / A ([M^{2+}] = 0)) x 100, where A is the magnitude of the transient absorption signal at the observation time t.) Weakly binding cations such as Zn^{2+} had a slight quenching effect. In the case of the metal ions, the quenching seemed to depend on the order of binding strengths of the ions: $Cu^{2+} > Ni^{2+} > Zn^{2+}$. This behavior is similar to the patterns of fluorescence quenching observed in humic substances (4,5,49). Furthermore, the quenching process is clearly independent of aggregation state : quenching by Cu^{2+} is essentially complete in samples containing sufficient copper to complex about 30 % of the binding sites. The ordering of the metal ion quenching effects matched observations reported by Fischer et al (23,24) for the 475 nm transient reported. Their results indicated static quenching of the " 475 nm " transient, believed here to be a composite signal consisting of a superimposed radical transient and BR component. On the timescale of observation of their experiments, quenching of BR would yield a decrease in signal intensity without any change in lifetime. This description matches the reported observations (23).

The early BR component behaves very differently with respect to copper ion induced aggregation. At low copper loadings (Figure 8) the growth of the BR signal is

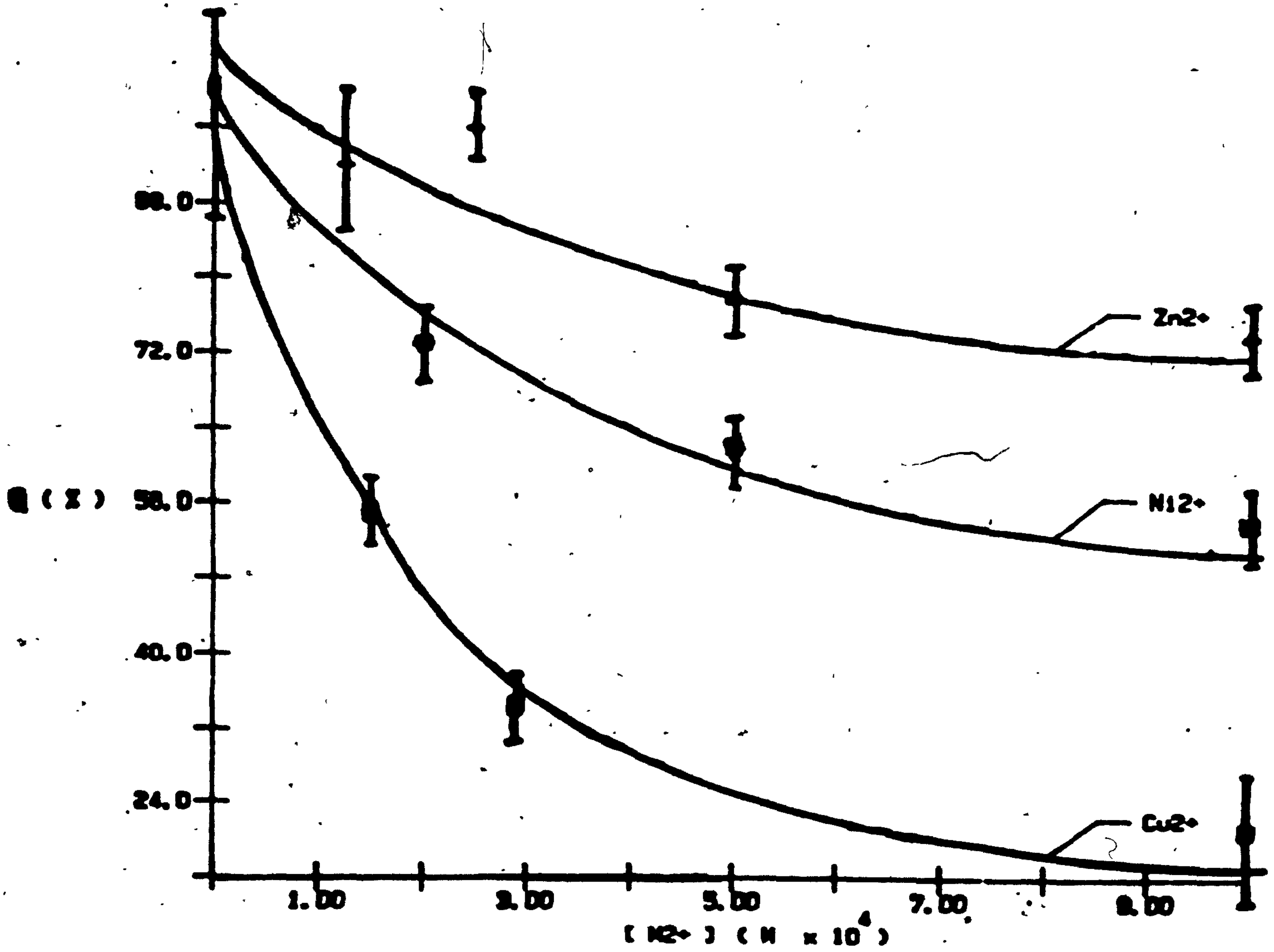

Figure 14 : Metal ion quenching of the "black residue" signal observed at 100 microseconds past excitation and 480 nm. Sample pH was 6 . E_{pulse} : 30 mJ .

accelerated (relative to metal free samples), while the growth at long wavelengths appears to be suppressed. In the presence of sufficient copper(II) to induce aggregation (3,4) very large increases in signal intensity were observed for BR, along with an acceleration in the growth of the signal. The signal appears to have maximised at or before 2 ns and has decayed significantly by 8 ns. It is possible that the early BR transient observed in these experiments is a precursor to the BR signals observed at times greater than 1 microsec.

It is tempting to assign the BR states as triplet states based on a number of features related to the results of other workers. In a series of steady state irradiations of humic solutions, Zepp et al. (50) determined the distribution of triplet energies in a series of humic water samples under broadband and sunlight irradiation. The observed distribution was very broad and centered at 250 KJ/mole (equivalent absorption wavelength : 465nm), with about half of the triplet states observed at energies lower than the mean value. This broad distribution of energies is consistent with the " black " spectral signature of BR. Oxygen sensitivity of the microsecond BR signal was observed in these experiments and is consistent with a triplet assignment (although we could not evaluate a quenching rate constant). An additional piece of evidence was provided by Fischer et al. (23) in their triplet quenching experiments on the reported "475 nm" transient. Their results demonstrated that a signal with triplet character is present at times coincident with the BR signal in the present experiments.

The growth features of the BR signal at early times also suggest a possible connection with fluorescence processes. This point is discussed in detail in relation to emission lifetimes in the next section.

On the basis of the present data, it is not possible to directly determine which components of the long timescale BR signal arise from triplet states and which components arise from the contribution of radicals. The production of phenoxyl radicals accompanying the solvated electron generation predicts a long lived component of transient absorption with a lifetime greater than 100 usec. The component, would, in addition, be insensitive to O_2. Such a component may be possibly observed here as the unquenched portion of the black residue signal.

Finally, it should be emphasised that the nanosecond apparatus used for this survey of the very long lived components was not optimum for studies in this range. Ideally, further work should be carried out using a microsecond apparatus, with an irradiation geometry which is less susceptible to photothermal artifacts. Some caution must be attached to the microsecond results observed in these experiments because of the possibility of these artifacts contributing at low signal levels.

Fluorescence Lifetime Studies

Fulvic acid fluorescence lifetime studies were carried out in the picosecond and nanosecond domains with excitation at 355 nm. The emission data were recorded at 500 nm for the nanosecond experiments, while for the picosecond experiments, the integrated emission above 435 nm was monitored using filters. Emission could be represented by a three component model : a fast component is observed with a lifetime of about 300 ps or less, a middle component with a lifetime of 1-3 ns, and a relatively weak, long lived component with a lifetime of 6-8 ns (Tables 4 and 5).

The third component makes a very small contribution to the total signal at any time, t. However, it is a dominant contributor to the steady state signal observed in conventional fluorimetry because its integrated contribution ($I(t) \cdot \tau$) to the quantum yield is large. This weak 3rd component contributes about 1-5 % of the total signal amplitude at any time,t. For this reason, it could only be observed in the later nanosecond domain on the single photon counting apparatus. The detection system in the (PRA) spectrometer is logarithmic and is capable of recording over 4 decades of signal intensity. In Figure 15, the signal at 40 ns exceeds the pulse residual by one decade of response, indicating the presence of a true emission signal.

The short time domain signals reported in Table 4 should be disregarded because they lie within the envelope of the excitation flash provided by the single photon counting apparatus. The subnanosecond components are better represented by the values reported in Table 5. These data were recorded with streak camera detection.The recording of emission profiles was initially made on several timescales with resolution varying from 4.35 ps/datum to 26.66 ps/datum. The weak 6 - 8 ns component is essentially invisible in these measurements because the streak camera records signal intensities linearly. The weakest components are effectively " buried " by the stronger emissions. Data were approximated on the 26.66 ps/datum timescale to two exponentials (there is effectively no accuracy in the longest lived component on this timescale).The data required no deconvolution because the pulse width was only 30 ps. Depending on the timescale of observation, the distribution of components shifts somewhat due to a difference in the weighting of the values : data resolved on short timescales emphasise short lived emission components at the expense of large errors ir the longest components, while data recorded on the longer timescales tend to average the shorter components. The variation in results recorded on different timescales is consistent with the mixture nature (7,17) of the fulvic material which predicts a continuum of emission lifetime components (2, 18).

The three exponentials probably represent the minimum set of parameters neccessary to describe an even more complex decay envelope.The approach adopted in this work is to consider three distinct regions of emission decays: (I) <= 300 ps (II) 1-3 ns (III) 5 ns or greater,

Table 4 : Emission Lifetime Data for Armadale FA by Single Photon Counting Measurements

Sample pH	Sweep (total ns)	A_N	τ_N	Integrated Lifetime Contribution (%)
pH 2	45 ns	0.74	680 + 74 ps	32 %
		0.21	3.1 + 0.2 ns	42 %
		0.05	8.0 + 0.2 ns	26 %
pH 4	25 ns	0.86	80 + 0.0 ps	15 %
		0.10	1.8 + 0.2 ns	37 %
		0.04	6.5 + 0.3 ns	48 %
pH 7	25 ns	0.88	100 + 0.0 ps	20 %
		0.09	1.9 + 0.2 ns	38 %
		0.03	6.8 + 0.3 ns	42 %
pH 4	200 ns	0.87	1.8 + 0.07 ns	62 %
		0.125	7.5 + 0.2 ns	37 %
		0.001	38.7 + 5 ns	1.5 %
pH 7	200 ns	0.88	1.9 + ns	63 %
		0.12	8.2 + ns	37 %
		<0.001	48. + ns	-

Table 5 : Emission Lifetime Measurements with Streak Camera Detection

Sample pH	A_N	τ_N	Integrated Lifetime Contribution (%)
pH 2	0.71	180 ps	17 %
	0.29	2.2 ns	83 %
pH 4	0.73	180 ps	23 %
	0.27	1.6 ns	77 %
pH 6	0.69	280 ps	19 %
	0.31	2.7 ns	81 %
pH 7	0.85	300 ps	34 %
	0.14	3.5 ns	66 %

Sample concentration was 50 ppm FA .

Excitation wavelength : 355 nm

Wavelength region of observation : 435 - 650 nm (integrated emission)

Sweep : 6900 ps total

Pulse energy : 3.0 + 0.3 mJ

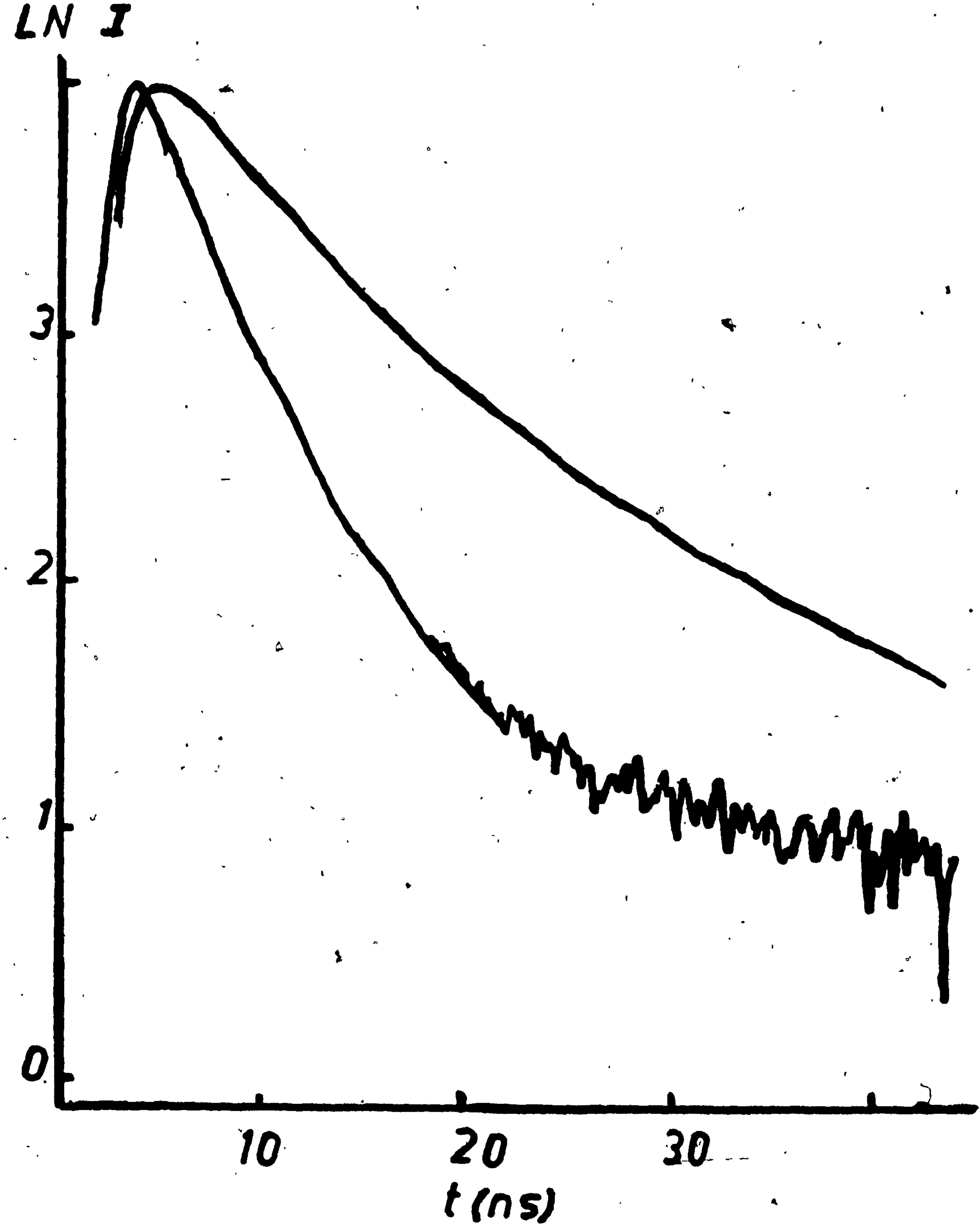

Figure 15 : Nanosecond domain emission decay profile for Armadale FA recorded by single photon counting technique . Lower curve : lamp profile . Upper curve : emission profile of sample . Excitation wavelength was 355 nm . Observation wavlength was 500 nm . [FA] = 50.0 ppm at pH 2 .

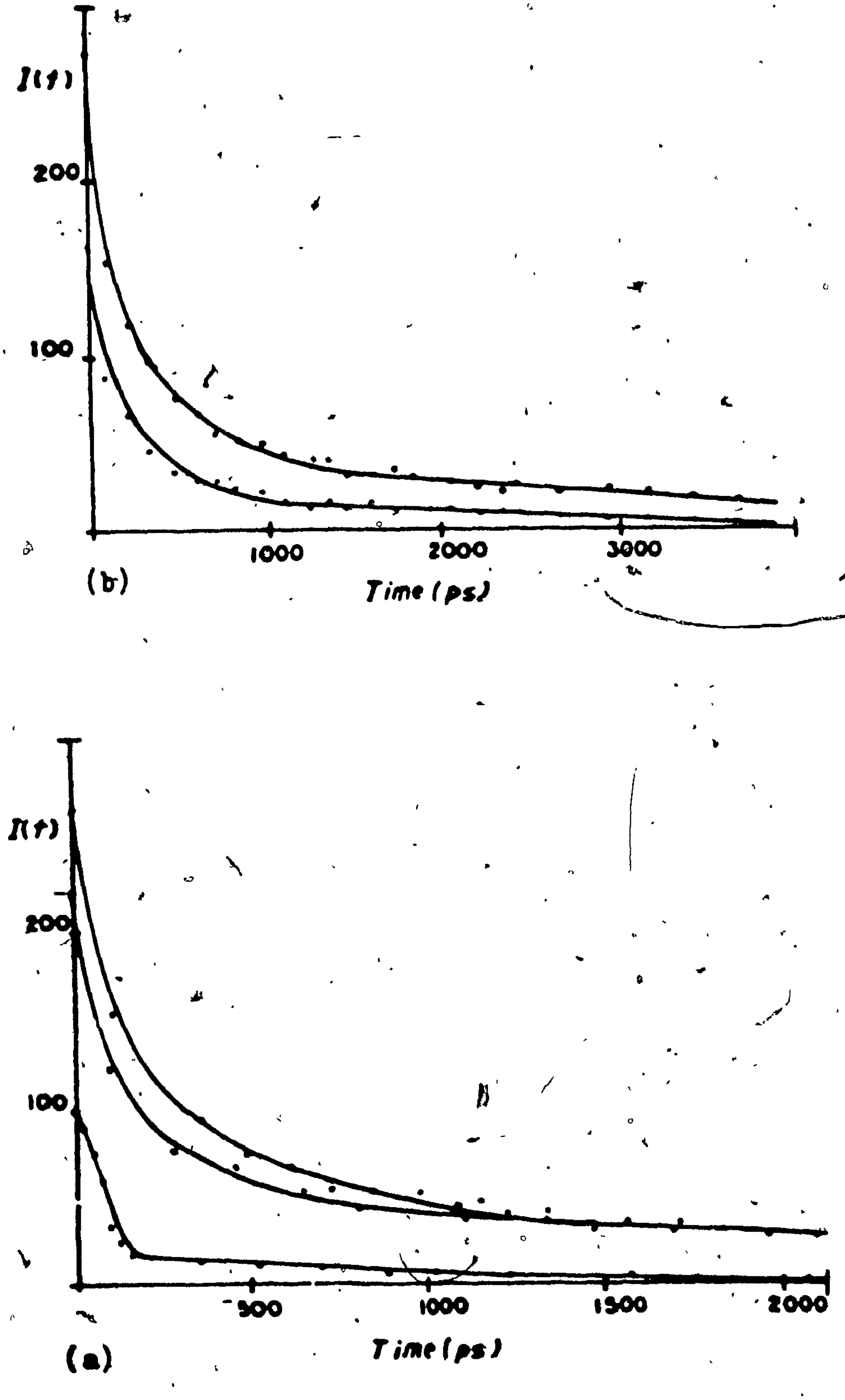

Figure 16: Emission decay profiles observed with streak camera detection . (a) effect of pH . Upper curve : PA at pH 6 ; lower curve : PA at pH 2 . (b) effect of copper(II) loading for 50.0 ppm PA solutions at pH 6. Upper curve : = 0 ; middle curve : α = 0.4 ; bottom curve : α > 1.0.

and to interpret the quenching behavior in terms of the effects observed over these ranges.

The ranges of emission decays are generally consistent with the work of previous authors, notably, Lappen and Seitz (51) and Fischer et al. (23,24). In the work of Lappen and Seitz, emission data were subjected to a biexponential fit and yielded two components of emission at 1 ns and 6 ns, with an intensity ratio of 5:1, approximately matching the signal intensity ratios observed here. On the other hand, the results of Fischer et al. (23) indicated a 3 ns emission lifetime. In their experiments, excitation was carried out with 300 ps pulses (at 337 nm, N_2 excitation) but the observation timescale was not specified. It is possible that the early picosecond components were entirely missed due to a lack of time resolution in their apparatus. At the same time, it is clear that the streak camera results of the present work would have missed the longest component (6-8 ns), were it not for the information yiel[illegible]d by the single photon counting experiments.

The emission decays were examined first for pH effects. Figure 16a shows the effect of pH quenching on the picosecond / early nanosecond scale. The effect of pH seems to be primarily static : the relative contributions of the short and long lifetime components are unchanged over the range [illegible]H studied, while the magnitude of quenching is generally consistent with the work of Underdown (4), in which steady state fluorescence was reduced by a factor of about 2 over the pH range from 2 to 6.

The effect of metal ion binding is probably of greater interest. Sufficient Cu^{2+} to fully bind to the FA complexation sites was added to solution at pH 6. The results, shown in Figure 16b, indicated a strong static quenching effect of both the 100-200 ps component and the component at 1-3 ns. The 1-3 ns component is very strongly affected. This case may be contrasted with the effects observed when approximately 30 % of the binding sites are covered (Figure 16b, middle curve). At the low copper coverage, the 1-3 ns emission is practically unaffected while the picosecond component shows a reduction in amplitude of only about 20 %. These results appear to indicate that the 1-3 ns component is sensitive to the aggregation state of the fulvic material, in contrast with the results of Underdown, whose work showed fluorescence quenching to be independent of metal ion induced aggregation effects (4).

A comparison of the present results with Underdown's steady state experiments (4) is in order.In that work, the 480 nm fluorescence emission (excited at 355 nm) was monitored at pH 6. It was found that metal ion quenching of fluorescence was nearly complete prior to the onset of aggregation. A close look at his data indicated that at 2 mmol added Cu^{2+}/g FA, 60 % of the fluorescence was quenched (the FA concentration was 100 mg/l).Addition of Cu^{2+} past 2 mmol/g FA caused further quenching but to a much more gradual extent : the plots of fluorescence intensity vs added Cu^{2+} leveled off. For the picosecond domain experiments reported in the present work, observed quenching effects were slight from 0 - 1.5 mmol added Cu^{2+} /g FA. Most of the observed quenching of the emission in the present experiments involved the 1-3 ns component and occurred at high copper loadings. This observation could be readily explained if at low copper loadings, the 6-8 ns component, mainly, was effected, while at high Cu^{2+} loadings, the 1-3 ns component was strongly affected. (The 6-8 ns component was effectively invisible in the streak camera recordings).The 1-3 ns component contributes about 40 % of the integrated total emission in these experiments which matches the levels of steady-state emission remaining at 2 mmol Cu^{2+}/g FA in Underdown's experiments. At copper loadings greater than 2mmol/g FA, light scattering begins to increase with added Cu^{2+},indicating the onset of particle growth. If the 1-3 ns emission observed in the present experiments is quenched by processes associated with particle growth, then it could remain unquenched at copper loadings from 0 to 2 mmol/g FA and yield a sufficiently low integrated fluorescence intensity to account for the observed steady state signal levels. The 1-3 ns component is not completely quenched at full copper loadings : the residual emission appears to match the level of unquenched fluorescence signals observed by Underdown. Consequently, a case could be made for linking the 1-3 ns signal to fulvic acid particle size.

The connection between particle growth and the 1-3 ns emission component may provide a link between the fluorescence and transient absorption processes. The early " black residue " component showed a strong enhancement concurrent with copper ion induced aggregation. At low copper coverage, BR was hardly affected, although there was evidence for its accelerated growth in the early time domain. The 1-2 ns induction period for the appearance of BR was effectively eliminated in the presence of copper(II). The enhanced growth of the BR signal might be explained by an enhancement in the rate of intersystem crossing promoted by bound copper(II), because of its paramagnetic properties. Furthermore, the enhancement of BR at times as early as 500 ps matches the observed decrease in the 100-200 ps emission component (Figure 16b). Finally, the decrease in the 1-3 ns emission component, apparently as the result of aggregation , is matched by a large enhancement of BR states.

A Polymer Model for Humic Substance Photophysics

A major challenge to natural water photochemistry has been to determine the nature of the chromophores participating in the generation of reactive intermediates in natural waters (8). The light absorbing functional groups in natural waters have been referred to as " unknown photoactive chromphores " (UPC's) because their apparent heterogeneity has made it difficcult to identify specific processes occurring at the molecular level.

Extensive degradative studies and functional group analyses of Armadale fulvic acid (7,17) have yielded a structure for the material which is highly aromatic, consisting largely of phenol carboxylate fragments. Components of lakewater humic substances are generally lower in molecular weight, but consist of phenolic fragments of essentially similar functionality to soil FA (1,9,17,21) .In addition, the high content of acidic and phenolic functionalities will ensure an interdependence of the chemical and physical properties of the materials : changes in the ionisation or aggregation state of the FA will therefore affect the environment of the chromophores and consequently their absorbance and fluorescence properties (4).

In the present experiments, photolysis of the materials was carried out at 355 nm. Near this wavelength, fluorescence emission is most efficient relative to the available photon flux (22), rather than at the shortest wavelengths where the absorption clearly maximises. In addition, current experiments show an efficient yield of solvated electron formation at very low energies, even below the typical range of S_1 energies reported by Joschek and Grossweiner (41) for many phenolic structures

If the phenol carboxylate structures identified in the degradative studies (17) are to be considered as candidates to account for the photochemical activity of the sample, some mechanism must be available for populating the S_1 states of the phenolic chromophores. However, a brief survey of the absorption properties of a variety of phenolic and phenol carboxylate compounds (21) showed few examples with any significant absorption at 355 nm. A summary of some of these model fragments is presented in Table 6. Chromophores containing quinoid structures mainly, seem to absorb efficiently at the photolysis wavelengths of 355 nm (9). There does, however, exist an alternative mechanism for populating the phenolic chromophores at 355 nm. Recent work in polymer photophysics (53) has shown that in a variety of synthetic polymers containing aromatic functional units, the formation of excimers dominates the fluorescence properties of the materials. In aromatic systems, excimers form when high densities of chromophores are irradiated (54). In these situations the excimers arise due to a face-to-face overlap of the aromatic rings in the excited state (Figure 17) with a spacing of about 10 Å. Excimer fluorescence is very broad and red shifted relative to the monomer fluorescence spectrum

Table 6

A Survey of the Absorption Properties of Some Model Chromophores for Humic Substances

Compound	λ_{max} (nm)	Absorptivity at 355 nm (approx) $M^{-1}cm^{-1}$	Solvent
o-p-m-cresol	275	0	MeOH
catechol	290	0	MeOH
benzoic acid	275	0	MeOH
hydroquinone	290	0	MeOH
phenylacetic acid	265	0	MeOH
p-benzoquinone	300	0	MeOH
2,5,bis p-methoxy phenoxy p-benzoquinone	350-379	2500	MeOH
2,5 dihydroxy p-benzoquinone	290	0	MeOH
2,5 di t-butyl p-benzoquinone	300	0	MeOH
tetramethyl benzoquinone	280	0	MeOH
phenyl p-benzoquinone	375	600	in HCl/MeOH
		0	in neutral MeOH
2,6 dihydroxy -3,5 dimethyl p-benzoquinone	338	$>10^4$	basic MeOH
		0	neutral MeOH

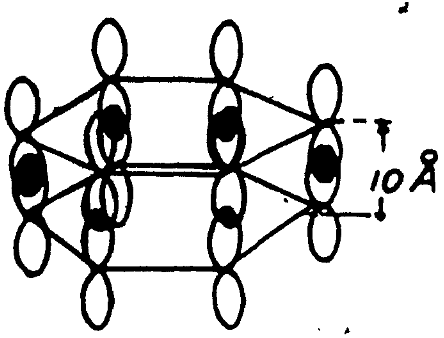

Figure 17 : Geometry for excimer formation in aromatic systems .

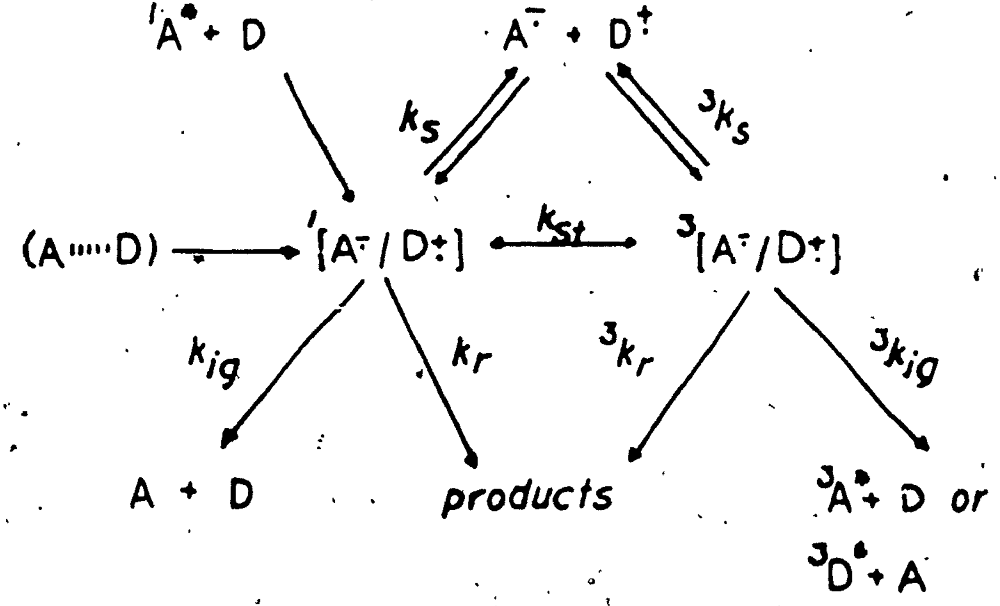

Figure 18 : Electron donor/acceptor complexes : scheme for formation and decay in aromatic systems (reference 54) .

(54). It has served as a sensitive probe of the changes in conformation and of aggregation states of linear synthetic polymers (55).

Closely related to excimer formation has been the formation of ground state dimers (56,57,58) posessing the geometry exhibited by excimers in the excited state. When irradiated, the dimer states may yield a fluorescence indistinguishable from excimer fluorescence. The presence of these dimers in the ground state may shift the absorption spectrum as much as 50-100 nm to the red (56,57).

If the chromophores forming an excited pair complex are not identical, the result is an exciplex or excited state donor/acceptor complex. The formation of exciplexes is usually accompanied by a transfer of charge in the excited state (54). The exciplexes may then separate to yield radical ion pairs or intersystem cross to form triplet exciplexes. The situation is described in Figure 18. Highly polar complexes do not usually fluoresce.

How far do these considerations apply to humic substances ? First of all, humic substances are known to form donor/acceptor complexes with substances such p-phenylene diamine and chloranil (59). Secondly, if phenols or phthalic acids may be invoked as models for some of the structural components of fulvic acids, then some good examples of these phenomena are reported in the literature. In cresols and related alkylphenol derivatives (56) both the formation of excimers and ground state dimers have been demonstrated. Concentrated solutions of substituted alkylphenols were shown to contain new long wavelength components in the absorption spectrum. The states arising from the long wavelength components yielded excimer fluorescence, as expected, for the face-to-face alignment of the aromatic rings. Ground state dimers and accompanying " excimer " fluorescence have been observed in polyethylene terephthalate (58) which also contains structural units similar to fulvic acid. An even more convincing analog is Bisphenol A resin (57) in which the uncured (monomeric) material exhibited only narrowband short wavelength fluorescence and absorption in solution. Addition of hardener to Bisphenol A resulted in a red shift of the ground state absorption and fluorescence spectra by as much as 50 nm. Triplet excimer formation in Bisphenol A resins has also been verified at 480 nm. The excimers formed in these resins apparently did not arise from any component of the amine hardeners used in the curing process.

The excimer/dimer/exciplex model provided by polymer photophysics is helpful in explaining the fluorescence properties of humic substances in general. The fluorescence of humic substances is most efficiently excited between 350-400 nm, rather than at shorter wavelengths where the ground state absorption is the greatest. The broad fluorescence emission also lies well beyond the range of fluorescence of many phenol carboxylate model compounds, as pointed out by Buffle et al (21). If the fluorescent emissions from fulvic acid are due to a series of " excimer "states the irradiation of the long wavelength dimer states will be a more efficient

Table 7

Excimers Observed in the Literature Containing Functional Groups Relevant to the Structure of Fulvic Acid

Compound (nm)	Absorption Maximum Wavelength (nm)		Emission Maximum Wavelength	
	monomer	dimer("excimer")	monomer	excimer
poly-para-phenylene diacrylic acid (in solution) (ref. 55)	-	-	383	470
Bisphenol A diglycidyl ether resin (in solution) (ref. 57)	275	330-350	405	460
p-cresol (in solution) (ref. 56)	280	300	310	350
polyethylene terephthalate (ref. 58,60)	-	-	325	400

route for the excitation of fluorescence. This is because emission from the excimer states may require absorption of ground state conformations close to the excimer geometry (56,57) : this is especially true where the lifetime of the monomer unit is short compared with the time required for diffusional encounter. It seems likely that the humic substances, because they are aggregates, provide many possibilities for achieving these conformations, since the chromophore density is very high within aggregates (1). This point may be confirmed by the fact that at high DOC levels (> 100 mg/l), significant red shifts in the wavelengths of absorption and emission are observed in humic substances (21).

In a system as complicated as a humic substance, conclusions concerning the photophysics must be drawn conservatively. However, some general interpretations could be made here in consideration of the polymer photophysical model outlined in the previous section.

It is clear that the photochemistry initiated in the near UV originates mainly from the lowest singlet states of the excited aromatic chromophores. The most likely small-molecule candidates to account for the near UV absorption of Armadale FA are structures containing quinoid chromophores (9). Another possible pathway is presented via the population of excited dimer states, and donor/acceptor complexes as already discussed. This pathway would implicate the direct participation of phenol carboxylate moities whose near UV absorptivity is otherwise low (Table 6), but which are known, for example, to efficiently yield solvated electrons via their S_1 states (41). A possible route for electron ejection by a donor/acceptor complex might be presented by the irradiation of a weakly associated chromophore pair. Water molecules hydrogen bonded to the chromophores could assist in the solvation of the electron and bring about prompt photoionisation :

$$nH_2O\cdots[\,D\cdots A\,]\xrightarrow{h\nu}D^+ + A + e^-$$

Such a process could be of sufficiently low energy to be monophotonic.

The charge separation involved in the above process would require the electron releasing state to be non-fluorescent (54). This would predict the absence of a direct connection between the fluorescent states observed for the humic substance and the electron releasing states. Absolute quantum yields for emission for the Armadale sample (evaluated in Chapter 5) were shown to be nearly an order of magnitude lower than the formation yield of the electron at 20 ps. Although the evidence is not conclusive, this observation is consistent with separate excitation pathways for the electron releasing states and the fluorescent states. Based on the donor/acceptor model, the fluorescent states would be of lower polarity than the electron releasing states (54) so that much less charge separation occurs in the excited state. The formation of free radicals from both the singlet and triplet states of the excited complex (Figure 18) is also predicted.

The model raises some interesting questions on the nature of the " triplet " species observed in these experiments. The " black residue " seems to be the likely candidate to account for the triplet states of the humic substance. Both the 1-3 ns emission lifetime component and the BR component observed at t < 10 ns show sensitivity to the change in aggregation brought on by added Cu^{2+}. The large enhancement in BR transient absorption, brought on at high copper loadings suggests the additional possibility that this component could be a triplet exciplex.

In previous work on the photophysics of humic substances (23,24) correlations were made between experimental variables, such as carbon content, ground state absorbance, and fluorescence intensity of the sample, and the magnitude of the 475 nm transient. The present donor/acceptor model predicts that properties such as absorbance and fluorescence are determined by the chromophore density of the material, which is probably related to the carbon content of the sample as well (Chapter 5). If the 475 nm transient, itself, arises from a donor/acceptor complex, then a direct relationship naturally arises between the magnitude of the transient absorption signal and all sample properties which are relatable to the chromophore density of the material.

The donor/acceptor model recommended here provides a holistic approach to the photochemistry of humic substances (59). It supplies a potential means of interrelating the photochemical and physicochemical properties of dissolved humic materials. It is not the intention of the author to denigrate the success of the small molecule approach adopted by other workers in the field but to point out a valid alternative explanation for the observed photochemistry. Verification of the proposed model is beyond the scope of the present survey : confirmation of the model would require quantitative titrimetric experiments to be conducted on the transient species reported here, with the results interpreted in conjunction with a variety of conventional probes.

In conclusion, if the formation of excimers and dimer states is invoked to explain chromophore interactions in humic materials, a mechanism is provided which explains the long wavelengths associated with absorption and emission by the materials and the broadness of the spectra. In addition, the model provides a potential explanation for the effects of aggregation and conformational changes on the observed optical properties of humic substances.The model also implicates the participation of phenol carboxylate functional groups in the photophysical scheme, and supplies a potential means of interrelating the physicochemical and photochemical properties of dissolved humic substances.

Chapter 3

Theory and Design Equations for A Laser Thermal Lens Spectrometer

The theory of the thermal lens effect presents an apparent departure from the central issue of this thesis, since it bears no direct relation to the photophysical investigations of Chapters 2 and 5. However, as a second major objective of this work, a laser thermal lens spectrometer was designed and constructed for trace analysis and application to natural water analysis. It is difficult to work meaningfully with the equations of thermal lensing without an understanding of their origins. In addition, the use of beam imaging detectors in thermal lensing (as incorporated in the spectrometer design of Chapter 4) presents additional opportunities for the development of spatial signal analysis techniques. Because the analysis techniques reported in Chapter 4 have their basis in diffraction theory and physical optics, their theoretical foundation has been presented in this chapter, in addition to the background theory of the thermal lens effect.

The Phenomenon of Thermal Lensing

Laser thermal lensing is a novel and sensitive technique for the determination of the absorbance of weakly absorbing media. The effect was first discovered in 1964 by Gordon et al (25) in the course of a series of laser Raman experiments. Introduction of an absorbing sample into their laser cavity was found to produce a time dependent change in the laser power. In addition, the presence of the sample was found to cause mode changes in the cavity, and under certain conditions, to inhibit laser action completely.

A detailed analysis of their results led the authors to conclude that their observations could be explained by thermally induced refractive index changes in the sample. The observed pattern of refractive index gradients indicated that the phenomenon they were observing was, in fact, a lens, produced thermally in the sample. Hence, the name " thermal lensing " arose to describe the effect.

The thermal lens effect may be observed by much simpler instrumental arrangements than the intracavity experiments of Gordon et al. (25). The beam from a laser cavity may be focused to a waist by a converging lens and directed into a cell containing a weakly absorbing liquid. The lowest order mode of most laser cavities posesses a Gaussian transverse intensity profile (TEM (0,0); Figure(19). Hence, the absorption profile of the sample, spatially, will follow the intensity profile. If a sample is chosen which

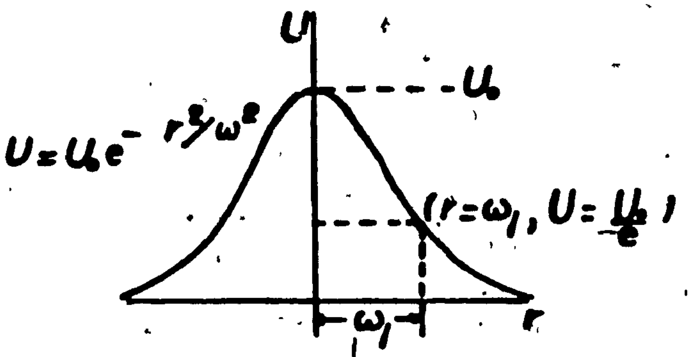

Figure 19 : Transverse field amplitude distribution for a TEM(0,0) laser beam , showing mode pattern (U(r)) and spot size (ω_1) . (see reference 81) .

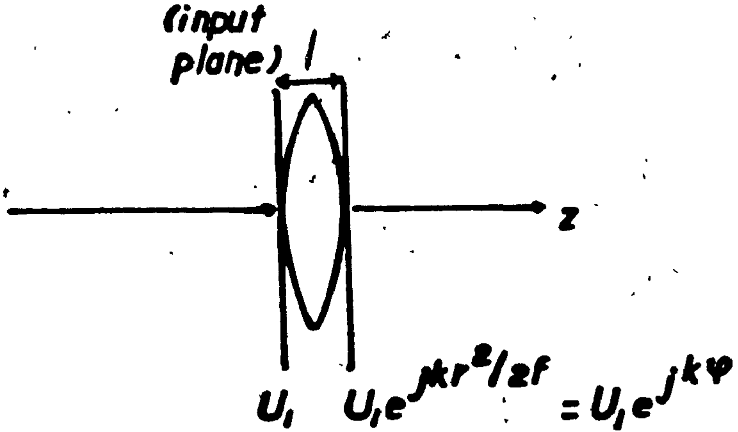

Figure 20 : Behavior of a thin lens as a phase multiplier (reference 64) .

dissipates the absorbed energy from the beam as heat (through relaxation of its excited states) a transverse thermal gradient is set up in the sample across the region illuminated by the beam. This thermal gradient induces a continuous change in the refractive index of the medium, which causes the lens-like behavior. A finite amount of time is required for a balance to be established between the rate of heat introduced into the sample by absorption from the laser beam, and the rate of heat lost to the medium by conduction. Hence, both transient and steady-state thermal lens behavior is observed .The thermal lens effect, therefore, arises due to the deposition of small quantities of heat in the sample and may be used as a thermal monitor of absorbance. The heat dissipated in the sample causes refractive index changes by changing the density of the sample. Increasing the absorbance causes a steepening of the thermal gradient in the sample, resulting in a steepened refractive index gradient and consequent shortening of the focal length of the induced thermal lens. The relative strength of the thermal lens formed depends on the temperature coefficient of the sample's refractive index, dn/dT. This property is negative for most liquids with the result that a diverging lens usually forms in liquid samples (61). The technique has been applied successfully, as well, to absorbance measurements in solids (62) and gases (63).

Preliminary Modelling of the Thermal Lens Effect

The first question to be solved in the theoretical modelling of the thermal lens element concerns the relationship between the sample's refractive index variations induced by the absorption of laser radiation, and the lens-like behavior observed .

It is well known from physical optics that ideal thin lenses behave as quadratic phase multipliers (64). The effect of the lens is to multiply the front of an incident wave by a factor of the form $e^{-jk\varphi}$ where $\varphi = \frac{r^2}{2f}$, k is the wave number, and f is the focal length of the lens. The phase of the incident wavefront varies quadratically with distance in the plane transverse to the axis of propagation (Figure 20). The optical pathlength, φ , travelled in any transparent medium (65) is given by 3-1 where n(r,t), is the refractive index distribution about the axis of propagation,z, and l is the distance travelled in the medium (Figure 20):

$$\varphi_f = (n(r,t) - n_0)\,l \qquad (3\text{-}1)$$

The refractive index distribution, n(r,t), will also vary with time because of the time growth of the thermal gradient. It is determined from the temperature distribution, Δ T(r,t) and temperature coefficient of refractive index, dn/dT, via the Taylor series expansion (66):

$$n(r,t) = n_0 + \frac{dn}{dt}\Delta T(r,t) \qquad (3\text{-}2)$$

(n_0 is the refractive index of the medium at the beam center).

The temperature distribution, $\Delta T(r,t)$, is available from a solution of the heat conduction equation, as shown in the next section of this chapter. It can be seen from that derivation that the distribution, $\Delta T(r,t)$, approximates to a quadratic expression in r for small heating effects near the beam center. The quadratic phase factor obtained is equivalent to the expression $\frac{r^2}{2f}$ for an ideal thin lens. Consequently the thermal "lens" behavior may be demonstrated.

Solution of the Heat Conduction Equation: Determination of $\Delta T(r,t)$

The temperature distribution $\Delta T(r,t)$, is obtained from a solution of the heat conduction equation for a cylindrical heat source with a Gaussian transverse intensity distribution:

$$\nabla^2(\Delta T) - \frac{1}{\alpha}\frac{\partial(\Delta T)}{\partial t} = -\frac{Q}{K} \qquad (3\text{-}3)$$

$$\dot{Q} = \begin{cases} 0 \text{ if } & t=0 \\ Be^{-2r^2/\omega_l^2} \text{ if } & t>0 \end{cases} \qquad (3\text{-}3a)$$

where K is the thermal conductivity, and α is the thermal diffusivity of the medium, defined as $\alpha = \frac{K}{\rho C_p}$. Equation 3-3 is obtained directly from the Fourier law of heat conduction and the first law of thermodynamics, applied to a control

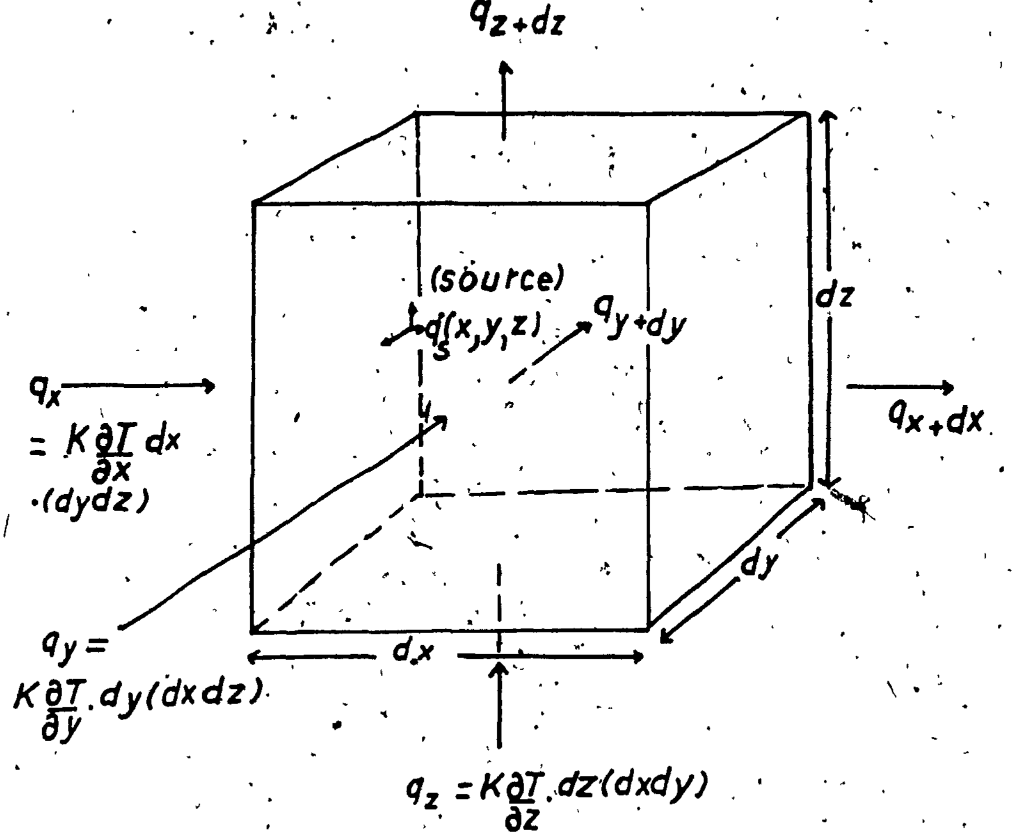

first law for control volume: $\dot{E}_{in} - \dot{E}_{out} + \dot{E}_{srce} = \dot{E}_{stored}$

$\dot{E}_{stored} = \rho C_p \frac{\partial T}{\partial t} dxdydz$; $\dot{E}_{srce} = \dot{q}_s$

$\dot{E}_{in} - \dot{E}_{out} = (q_x + q_y + q_z) - (q_{x+dx} + q_{y+dy} + q_{z+dz}) = K\nabla^2 T(dxdy.dz)$

$\therefore \underline{\nabla^2 T + \dot{q}_s/K = (\rho C_p/K)\,\partial T/\partial t}$

Figure 21 : Derivation of the heat conduction equation in Cartesian coordinates showing the conservation of energy for a control volume of dimensions dx , dy , dz . (reference 67)

volume in the sample medium (67) (Figure 21). The solution of 3-3 is complicated by the prescence of the source term Q(r,t)/K. An immediate problem is that the time and spatial variables do not separate. However, a solution is available via the appropriate Green's function, which is a standard technique for solving inhomogeneous differential equations (68,69,70).

The Green's function for a system is a function ,G, which gives the system's response for a unit impulsive source located at any point in time or space (Figure 22).The Green's function for heat conduction is obtained from :

$$\nabla^2 G - \frac{1}{\alpha}\frac{\partial G}{\partial t} = -\frac{1}{K}\delta(r-r_0)\delta(t-t_0) \qquad (3\text{-}4)$$

where δ is the Dirac delta function. The variables r_0 and t_0 correspond to the position of the impulsive source in space and time, and are taken as independent variables of G.

The solution of $\Delta T(r,t)$ from equation 3-3 is given simply by the convolution of the source $Q(r_0)/K$ and the Green's function (effectively the system's impulse response) obtained from 3-4 (70):

$$\Delta T(r,t) = \int_0^t dt_0 \iiint G(r-r_0, t-t_0)\dot{Q}(r_0, t_0)\,dV_0 \qquad (3\text{-}5)$$

The Green's function in equation 3-4 may be obtained from a Fourier transform technique (71). The volume Fourier transform of both sides of equation 3-4 is given by (72) :

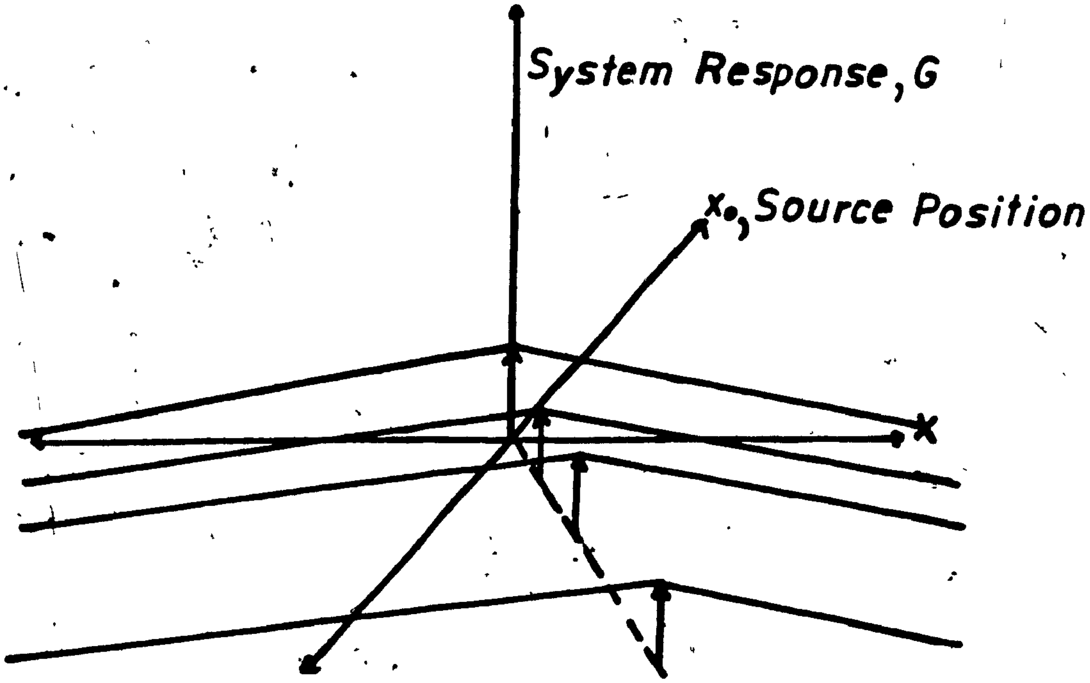

Figure 22 : Illustration of the Green's function for a simple one dimensional system . The function G is the envelope of impulse responses for all source positions , r_0 . (reference 68) .

$$e^{-jk_S r_0}\tilde{G}(k_S,t-t_0)=\iiint e^{-jk_S r}e^{-jk_S r_0}G(r-r_0,t-t_0)\,dV \qquad (3\text{-}6)$$

note that k is a spatial frequency vector : $k_S = \hat{i}k_1 + \hat{j}k_2 + \hat{k}k_3$

and $(r-r_0) = \hat{i}(x-x_0) + \hat{j}(y-y_0) + \hat{k}(z-z_0)$

where i,j,k are unit vectors. The inverse transform is given by :

$$G(r-r_0,t-t_0)=\frac{1}{(2\pi)^3}\iiint e^{+jk_S r}\left(e^{-jk_S r_0}\tilde{G}(k_S,t-t_0)\right)dk_1\,dk_2\,dk_3 \qquad (3\text{-}7)$$

From the standard properties of Fourier transforms (72,73) equation 3-4 transforms to :

$$k_S^2\,\tilde{G}(k_S,t-t_0)-\frac{1}{\alpha}\,\frac{\partial\tilde{G}}{\partial t}(k_S,t-t_0) = -\frac{1}{K}\delta(t-t_0) \qquad (3\text{-}8)$$

Fourier transformation with respect to the time variable gives :

$$-k_S^2\,\tilde{\tilde{G}}(k_S,\omega)-\frac{j\omega}{\alpha}\tilde{\tilde{G}}(k_S,\omega) = -\frac{1}{K} \qquad (3\text{-}9)$$

(note that a double tilde $\approx$ is used to indicate Fourier transformation with respect to both the time and spatial variables.)

With rearrangement, 3-9 yields :

$$\tilde{\tilde{G}}(k_S,\omega) = \frac{1/K}{j\frac{\omega}{\alpha}+k_S^2} \qquad (3\text{-}10)$$

transformation of $e^{-j\omega t_0}\tilde{\tilde{G}}(k_S,\omega)$ with respect to time gives :

$$\tilde{G}(k_S,t-t_0) = \frac{\alpha}{K}\,e^{-\alpha k_S^2(t-t_0)}\,U(t-t_0) \qquad (3\text{-}11)$$

where $U(t-t_0)$ is the unit step function.

The task of finding G consists from this point, in finding the inverse transform of $e^{-jk_s r_0}\tilde{G}(k_s, t-t_0)$ as :

$$G(r-r_0, t-t_0) = \frac{1}{(\sqrt{2\pi})^n}\iiint e^{-jk_s r} \cdot \frac{\alpha}{K} \cdot e^{-\alpha k_s^2 (t-t_0)}\, U(t-t_0)\, e^{-jk_s r_0}\, dk_1\, dk_2\, dk_3 \qquad \text{3-12)}$$

where n is the number of spatial dimensions. The integral in 3-12 was solved (75) to yield, in Cartesian coordinates and two spatial dimensions :

$$G(r-r_0, t-t_0) = \frac{1}{4\pi K(t-t_0)}\, e^{-(r-r_0)^2/4\alpha(t-t_0)} \qquad (\text{ 3-13 })$$

$$t > t_0$$

For cylindrical symmetry equation 3-13 is converted to polar coordinates. With a heat source applied at $t_0 = 0$, and from the reciprocity principle (74) equation 3-13 becomes :

$$G(r-r_0, t) = \frac{1}{4\pi K t_0}\, e^{-(r^2+r_0^2)/4\alpha t_0}\, e^{-rr_0\cos(\theta-\theta_0)/2\alpha t_0}$$

(3-14)

Because of the circular symmetry, the angular part of the Green's function is integrated with respect to θ

$$G(r-r_0, t) = \frac{1}{4\pi K t}\, e^{-(r^2+r_0^2)/4\alpha t}\int e^{-rr_0\cos(\theta-\theta_0)/2\alpha t}\, d\theta_0$$

(3-15)

This expression can be further simplified from the properties of Bessel functions (75):

$$J_0(r) = \frac{1}{2\pi}\int_0^{2\pi} e^{-jr\cos(\theta-\xi)}\,d\theta \tag{3-16}$$

since the argument in 3-16 is real, we use (76):

$$J_0(jr) = I_0(r) \tag{3-17}$$

where $I_O(r)$ is a modified Bessel function of order zero, so that:

$$G(r-r_0,t) = \frac{1}{2Kt}\, e^{-(r^2+r_0^2)/4\alpha t}\, I_0\left(\frac{rr_0}{2\alpha t}\right) \tag{3-18}$$

The integral in 3-5 is solved by convolution of $Q(r_O)$ with $G(r-r_O,\ t-t_O)$:

$$\Delta T(r,t) = \frac{B}{2K}\int_0^t dt_0 \int_0^\infty \frac{e}{t_0}^{-2r_0^2/\omega_1^2} e^{-(r^2+r_0^2)/4\alpha t_0}\, I\left(\frac{rr_0}{2\alpha t_0}\right) r_0\,dr_0 \tag{3-19}$$

The next step is the separation of variables: factors containing r_O and r_O^2 are separated from factors which do not contain the variable. $\Delta T(r,t)$ becomes:

$$\Delta T(r,t) = \frac{B}{2K}\int_0^t \frac{dt_0}{t_0}\cdot e^{-r^2/4\alpha t_0} \iiint e^{-2r_0^2/\omega_1^2}\, e^{-r_0^2/4\alpha t_0}\, I_0\left(\frac{rr_0}{2\alpha t_0}\right) dV_0 \tag{3-20}$$

The spatial part of 3-20 is solved by means of an identity involving the Bessel function (77):

$$\int_0^\infty e^{-a^2r_0^2} J_0(br_0)\, r_0\,dr_0 = \frac{e^{-b^2/4a^2}}{2a^2} \tag{3-21}$$

If $a^2 = \left(\frac{2}{\omega_1^2} + \frac{1}{4\alpha t_0}\right)$ and $b = \frac{ir}{2\alpha t_0}$

the final result is:

$$\int_0^\infty e^{-\left(\frac{2}{\omega_1^2}+\frac{1}{4\alpha t_0}\right)r_0^2} I\left(\frac{r r_0}{2\alpha t_0}\right) r_0 \, dr_0 = e^{r^2\omega_1^2/4\alpha t_0(8\alpha t_0+\omega_1^2)} \cdot \frac{2\alpha t_0 \omega_1^2}{(\omega_1^2+8\alpha t_0)} \qquad (3\text{-}22)$$

The integration of 3-22 is evaluated with respect to the time coordinate after rearrangement of 3-22 (25). With the substitutions; $y = \left(\frac{1}{\omega_1^2+8\alpha t_0}\right)^{-1}$

and $dt_0 = -dy/8\alpha y^2$

the time integral in 3-20 transforms to:

$$\Delta T(r,t) = -\frac{B\omega_1^2}{8K}\int_{1/\omega_1^2}^{1/(8\alpha t_0+\omega_1^2)} e^{-2r^2 y}\frac{dy}{y} \qquad (3\text{-}23)$$

The result is a set of exponential integrals:

$$\Delta T(r,t) = \frac{B\omega_1^2}{8K}\left[Ei\left(-\frac{2r^2}{\omega_1^2}\right) - Ei\left(-\frac{2r^2}{\omega_1^2+8\alpha t}\right)\right] \qquad (3\text{-}24)$$

where Ei(x) is the exponential integral (78):

$$Ei(x) = \int_x^\infty \frac{e^{-t}}{t}\,dt$$

The temperature distribution in the sample, $\Delta T(r,t)$, given by equation 3-25 is the basis for all theoretical descriptions of thermal lensing. The distribution is shown in Figure 23 as a function of radius at different times after sample exposure to the heating beam.

For small values of the argument x, the exponential

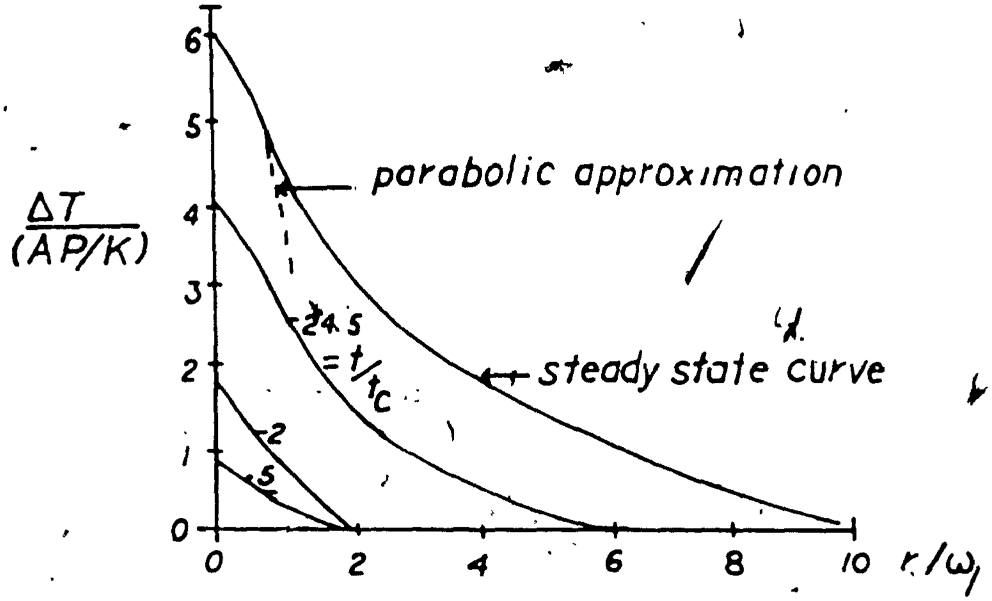

Figure 23 : Temperature profile in sample medium heated by Gaussian cylindrical source. $\Delta T(r,t)$ as obtained from equation 3-24 . (reference 25) .

integral may be approximated by the following series (79):

$$Ei(x) = \ln \gamma x + \sum_{m=1}^{\infty} \frac{x^m}{m\,m!} \qquad (3\text{-}25)$$

where γ = 1.71.......

If the first two terms in the series are retained, then the resulting expression for $\Delta T(r,t)$ is :

$$\Delta T(r,t) = \frac{B\omega_l^2}{8K}\left[\ln\left(1+\frac{8\alpha t}{\omega_l^2}\right) - \frac{16\alpha t}{(\omega_l^2+8\alpha t)}\left(\frac{r^2}{\omega_l^2}\right)\right] \qquad (3\text{-}26)$$

One further modification is neccessary before using (3-26) to generate n(r,t). The factor $\frac{B\omega_l^2}{8K}$ must be expressed in terms of the laser power, P, which is the experimentally measureable quantity, rather than B. The heat density of the laser source in this problem is given by (25):

$$\dot{Q}(r) = 0.24\,P(r)\epsilon \qquad (3\text{-}28)$$

where P(r) is the heat density of the source, $\dot{Q}(r)$ is as given in equation 3-3a, and ϵ is the sample absorptivity. If the laser power, P, is expressed in Joules and the heat source in calories, then the expression is divided by a conversion factor of 0.24 = (1.987cal/ 8.314 J), which appears in the original derivation.

Consequently, if we integrate P(r) over all space :

$$P \cong \iint P(r)\,dr = \int_0^{2\pi}\int_0^{\infty} \frac{Be^{-2r^2/\omega_l^2}}{0.\text{[illegible]}\epsilon}\, r\,dr\,d\theta \qquad (3\text{-}28)$$

so that $P = \pi B\omega_1^2/0.48\epsilon$

and $\omega_1^2 = \frac{0.48\epsilon P}{\pi}$

Consequently :

$$\Delta T(r,t) = \frac{0.06\epsilon P}{\pi K}\left[\ln\left(1+\frac{8\alpha t}{\omega_1^2}\right) = \frac{16\alpha t}{\omega_1^2+8\alpha t}\left(\frac{r^2}{\omega_1^2}\right)\right] \quad (3\text{-}29)$$

In the original derivation, the authors (25) pointed out that this equation suffers the defect that an infinite response is predicted for $f\ \infty$, that is, no steady state is ever reached in 3-29. This arises from the assumption that heat conduction occurs in an infinite medium. It does not affect the expression for the focal length, as will be seen shortly. A steady state expression for ΔT(r,t) is useful and has been derived assuming that the boundary conditions are T = 0 for r = a (where a is the radius of the sample cell) The result is:

$$\Delta T(r,t) = \frac{0.06\epsilon P}{\pi K}\left\{\ln\left(\frac{2\gamma a^2}{\omega_1^2}\right) - \frac{2r^2}{\omega_1^2}\right\} \quad (3\text{-}30)$$

where the details of the derivation have been omitted. From the temperature distribution of 3-31 and the series expansion of 3-2, we can evaluate:

$$n(r,t) = n_0 - \frac{dn}{dT}\left[\frac{0.06P\epsilon}{\pi K}\left(\frac{16\alpha t}{\omega_1^2+8\alpha t}\right)\left(\frac{r^2}{\omega_1^2}\right)\right] \quad (3\text{-}31)$$

The logarithmic term in 3-29 has been neglected in this expression because it has no radial dependence. Its product with the small valued parameter dn/dT is small.

Equation 3-31 has the parabolic form: $n(r) = n_0(1 - \beta r^2)$

where

$$\beta = -\frac{dn}{dT} \cdot \frac{1}{n_0} \cdot \frac{0.06\epsilon P}{\pi K} \cdot \left(\frac{16\alpha}{\omega_1^2 + 8\alpha t}\right) \cdot \frac{1}{\omega_1^2} \tag{3-32}$$

Returning, finally, to equation 3-1, the optical path length distribution yielded by the sample will be:

$$\varphi = n_0 l - \frac{dn}{dT} \cdot \frac{0.06\epsilon P}{\pi K}\left(\frac{16\alpha t}{\omega_1^2 + 8\alpha t}\right)\frac{r^2}{\omega_1^2} \cdot l \tag{3-33}$$

from which

$$\frac{1}{f(t)} = \frac{dn}{dT} \cdot \frac{0.24AP}{\pi K} \cdot \left(\frac{8\alpha t}{\omega_1^2 + 8\alpha t}\right) \cdot \frac{1}{\omega_1^2} \tag{3-33a}$$

With rearrangement of 3-33a, the focal length, f(t), may be written in the form:

$$f(t) = f_\infty(1 + t_c/2t) \tag{3-34}$$

where t_c is a characteristic time constant for formation of the thermal lens, and f_∞ is the steady state focal length of the thermal lens:

$$f_\infty = \frac{K\pi\omega_1^2}{0.24AP(dn/dT)} \tag{3-35}$$

$$t_c = \omega_1^2/4\alpha \tag{3-35b}$$

Equations 3-33 to 3-35 predict a lens-like behavior for the medium because of the quadratic variation of the refractive index with radial distance from the beam axis. The parabolic approximation is indicated in Figure 23. For radial values far from the beam center, however, more terms in the series expansion for the exponential integral must be included in equation 3-25. The temperature distribution " flattens " at longer distances from the beam axis, producing aberration in the lens element. The theoretical treatment of lens aberration has been developed in detail by Sheldon et al. (66) but is not pursued here.

The Thermal-Lens Effect : Detection

A simple scheme for detection of the thermal lens effect is diagrammed in Figure 24. A TEM(0,0) laser beam with a transverse Gaussian intensity distribution is focused to a waist by means of a converging lens. A cell containing an absorbing liquid is placed at a point slightly past the waist. The beam forms the lens in the cell via thermally induced refractive index changes following light absorption. Because the dn/dT factor is negative for most liquids the lens formed is assumed to be a diverging lens. The effect of the diverging lens is to expand the laser beam and increase its spot radius (80,81). The center of the beam is sampled at the detector which is most simply a pinhole and photodiode placed in the far field region of the beam. The signal is measured at the detector as a drop in the photocurrent of the photodiode, corresponding to a drop in the center intensity of the beam.

The simple scheme depicted in Figure 24a is adequate for many applications of thermal lensing, but suffers from the disadvantage that a burden of high performance is placed on the laser forming the thermal lens. This is because optical noise (often at levels as high as 1 % RMS) in the laser will limit the levels of signal detection. A better scheme is to use a dual beam configuration (82) (Figure 24b) in which a low powered, highly stable, probe laser detects the lens effect, and a high powered, noisier pump laser forms the lens. Because the lens response is slow (milliseconds to

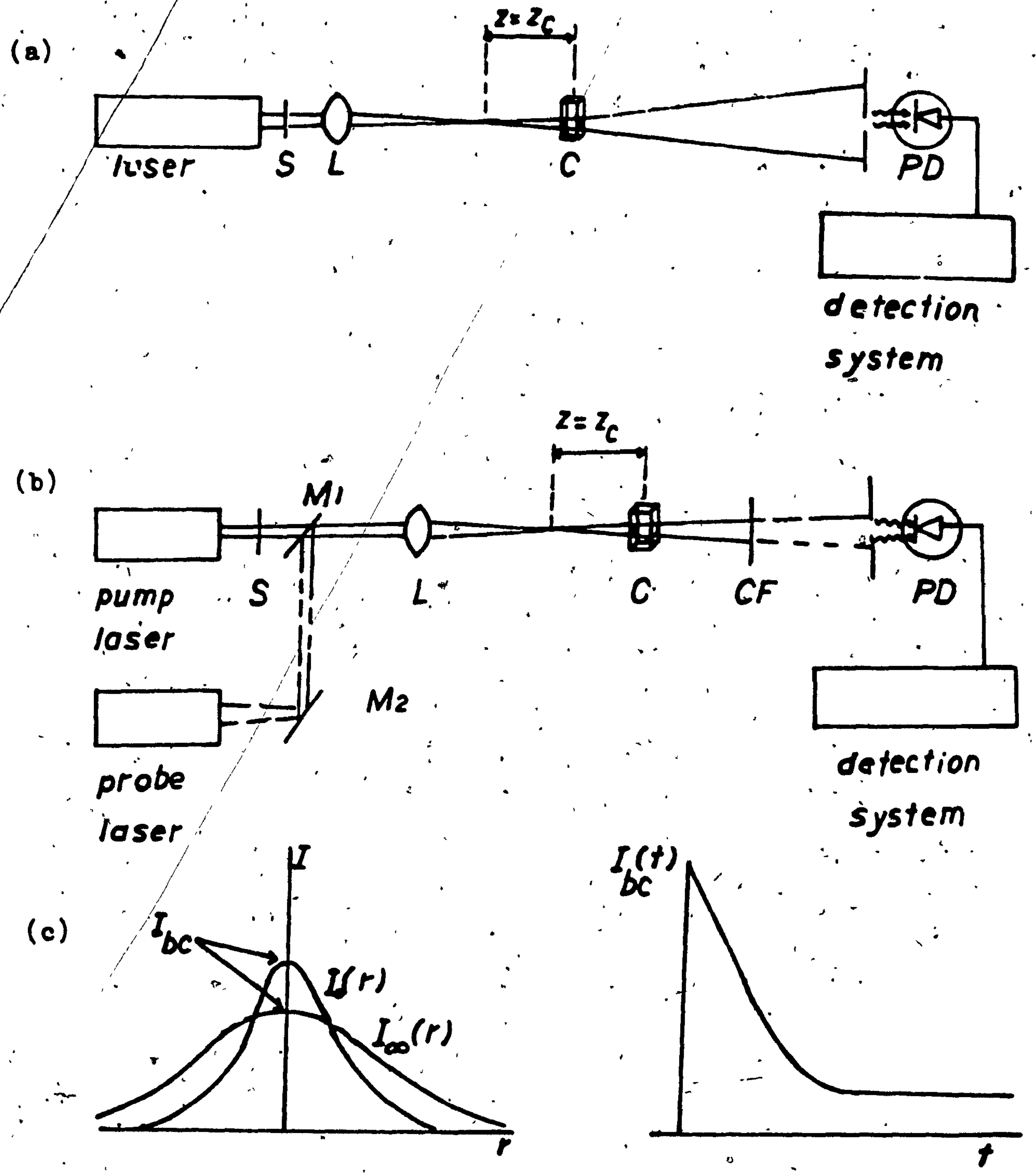

Figure 24 : Schemes for experimental detection of the thermal lens effect . (a) single beam experiment (b) dual beam (mode-matched) experiment . (c) observed signals for thermal defocusing . In a,b : S = shutter, L=lens , C = sample cell , PD = photodiode , CF= color filter , M1,M2 are partially transmitting mirrors .

seconds depending on the solvent thermal parameters in equation 3-35a,b the dual beam detection scheme is relatively insensitive to the high frequency optical noise in the pump laser. The use of dye lasers to supply the pump radiation ensures tunability of the excitation beam over a wide range of wavelength, without the requirement for high stability. Low power ,state-of-the-art Helium Neon lasers with output stabilities of better then 0.1 % are readily available at low cost, to supply the probe beam.

While the detection schemes of Figures 24a and b demonstrate detection of the thermal lens effect, they provide no information on the optimisation of alignment for maximum sensitivity of signal detection nor do they yield any relationship between the absorbance of the sample and the signal observed at the detector. In order to obtain this information it is neccessary to consider the properties of Gaussian laser beams and derive the appropiate expressions from geometrical optics (81) and/or diffraction theory.

The mode patterns of most laser resonator cavities consist of a series of Gaussian intensity distributions of increasingly higher order (80,81) and are described by a set of Hermite or Laguerre Polynomials. The equations of thermal lensing assume lens formation by the lowest order (0,0) mode which has an electric field amplitude distribution of the form (81):

$$U(x,y,z) = \frac{U_0}{\omega_l} e^{-jkr^2/2\tilde{q}} \cdot e^{jkz} \qquad (3\text{-}36)$$

where $K = 2\pi/\lambda$, the wavenumber and the factor $\tilde{q}$ represents a complex radius of curvature for the wave:

$$\frac{1}{\tilde{q}} = \frac{1}{R} + \frac{jk}{2\omega_l^2} \qquad (3\text{-}37)$$

$\tilde{q}$ is determined by the wavefront radius, R, and the spot radius of the laser beam, ω_l, both of which are functions of the propagation distance, z. The situation is clarified by referring to a diagram of the beam propagation (81) (Figure 25).

Figure 25 shows the propagation behavior of a focused Gaussian laser beam. The beam propagates to form a waist, indicated by z = 0 in the Figure. The waist may be located inside the laser cavity or it may be formed externally by means of a converging lens (not shown in the diagram). At the waist, the phase fronts are planar ($R = \infty$) and the spot size, ω_l, is a minimum. As the wave propagates foreward (left to right in the diagram) the spot size increases, and the phase front curvature decreases, until the confocal point of the beam is reached. At the confocal point ($z = z_c$) the curvature of the phase front is a minimum, while the spot size inceases to $\sqrt{2}\omega_0$ (ω_0 is the spot radius at the waist).Because the spot area is given by $2\pi\omega_c^2$ at the confocal point, the beam area has increased by a factor of 2, which means that the power density of the beam has dropped to half the value at the waist. For this reason, the confocal

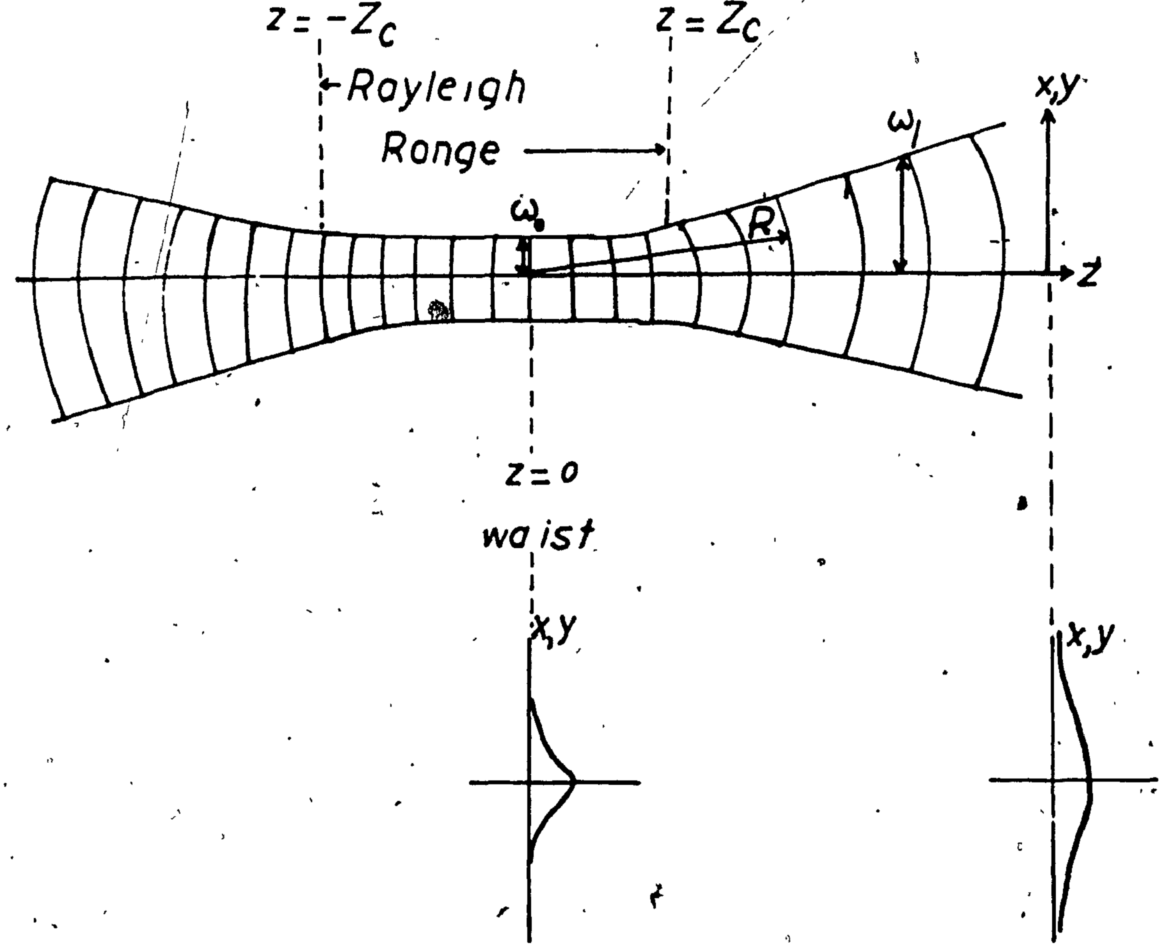

Figure 25 : Schematic description of the propagation of a Gaussian laser beam (reference 81) showing phase fronts , beam divergence and intensity profiles.

point may be regarded as a " half power point " for the beam. There is an identical confocal point on the left hand side of the waist in the figure The region between the two confocal points is referred to as the " Rayleigh Range" for the beam (81) and defines a region of effective collimation of the beam.

Past the confocal point, the beam continues to propagate with R and ω_1 increasing as a function of distance. In the far field both R and ω_1 increase nearly linearly with distance, z. As z approaches infinity, the beam wavefront approaches a plane waveform.

The effect of distance on R and ω_1 is given by (81):

$$R(z) = z + \left(\frac{\pi\omega_0^2}{\lambda}\right)^2 \frac{1}{z} \qquad (\ 3\text{-}38a\ )$$

$$\omega_1(z) = \omega_0\sqrt{1+\left(\frac{\lambda z}{\pi\omega_0^2}\right)^2} \qquad (\ 3\text{-}38b\ )$$

Differentiation of both expressions with respect to z yields minima at $z = z_c$ and $z = 0$, respectively, while at large values of z. $R(z) \sim z$ and $\omega_1(z) \sim \frac{\lambda z}{\pi\omega_o}$ as discussed. The value of the analysis presented here is that once λ, z, ω_o^2 are known, ω_1 and R may be computed to yield $\tilde{q}$ in equation 3-37. That is, once the wavefront dimensions are known, the exact form of the Gaussian profile is known from 3-36.

Gaussian spherical waves obey geometrical optics because they have the property that they propagate as spherical waves while retaining their Gaussian transverse profile (80,81). This means that the ray transformation matrices may be used to describe the transformation of $\tilde{q}$ through optical systems.

The transformation by an optical element of the complex radius, $\tilde{q}$, and its slope $\tilde{q}'$, are expressed in general matrix form (81) as :

$$\begin{bmatrix} \tilde{q}_2 \\ \tilde{q}_2' \end{bmatrix} = \begin{bmatrix} A & B \\ C & D \end{bmatrix} \begin{bmatrix} \tilde{q}_1 \\ \tilde{q}_1' \end{bmatrix} \qquad (3\text{-}39)$$

The optical element producing the transformation may be a lens, a mirror, or even free space. The matrix elements A,B,C,D are obtained from geometrical optics using a small angle (paraxial) ray analysis (examples are listed in Table 8). By multiplying a sequence of these matrices together, one follows the transformation of a Gaussian beam through an optical system, element by element :

$$\begin{bmatrix} \tilde{q}_2 \\ \tilde{q}_2' \end{bmatrix} = \begin{bmatrix} A_n & B_n \\ C_n & D_n \end{bmatrix} \begin{bmatrix} A_m & B_m \\ C_m & D_m \end{bmatrix} \begin{bmatrix} A_L & B_L \\ C_L & D_L \end{bmatrix} \cdots \begin{bmatrix} A_1 & B_1 \\ C_1 & D_1 \end{bmatrix} \begin{bmatrix} \tilde{q}_1 \\ \tilde{q}_1' \end{bmatrix} \qquad (3\text{-}40)$$

In order to analyse the optical system used for thermal lens detection in Figure 24, three matrices are required: (a) a matrix describing free propagation of the beam from the waist position (arbitrarily defined as $z = 0$) to the cell at $z = z_1$ (b) a matrix describing the thermal lens (modelled as a diverging lens) and (c) another " free space " matrix for propagation of the beam from $z = z_1$ to $z = z_2$ (the detector plane) .

The total transformation is described by:

Table 8

Paraxial Ray Matrices for Selected Optical Elements
(references 80,81)

Element	**System Matrix**
1. Free Space 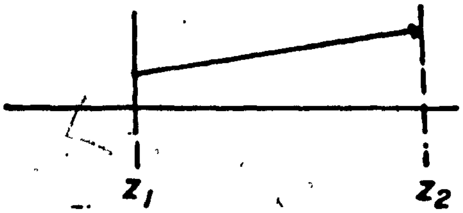 	$\begin{bmatrix} 1 & L \\ 0 & 1 \end{bmatrix}$
2. Thin lens of focal length , f 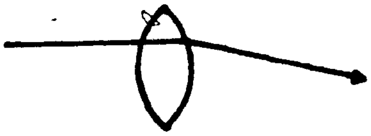 f > 0 (converging lens) f < 0 (diverging lens)	$\begin{bmatrix} 1 & 0 \\ -1/f & 1 \end{bmatrix}$
3. Curved dielectric interface 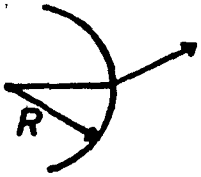 	$\begin{bmatrix} 1 & 0 \\ \frac{n_2-n_1}{n_2 R} & \frac{n_1}{n_2} \end{bmatrix}$

$$\begin{bmatrix}\tilde{q}_2\\ \tilde{q}_2'\end{bmatrix}=\begin{bmatrix}1 & z_2\\ 0 & 1\end{bmatrix}\begin{bmatrix}1 & 0\\ -1/f(t) & 1\end{bmatrix}\begin{bmatrix}1 & z_1\\ 0 & 1\end{bmatrix}\begin{bmatrix}\tilde{q}_1\\ \tilde{q}_1'\end{bmatrix} \qquad (3\text{-}41)$$

It can be shown from inversion of equation 3-37 and differentiation with respect to z that $\frac{d\tilde{q}}{dz} = \tilde{q}' = 1$ for all z. With the complex radius at the input plane equal to q_0, we obtain, in general:

$$\tilde{q}_1 = A\tilde{q}_0 + B$$

and

$$1 = C\tilde{q}_0 + D$$

so that overall,

$$\tilde{q}_1 = \frac{A\tilde{q}_0 + B}{C\tilde{q}_0 + D} \qquad (3\text{-}42)$$

which, from equations 3-38a,b ultimately gives:

$$R = \frac{A^2 Z_c^2 + B}{ACZ_c^2 + BD} \qquad (3\text{-}43a)$$

$$\omega_1 = \frac{\lambda}{\pi}\left[\frac{A^2 Z_c^2 + B^2}{(AD - BC)Z_c}\right] \qquad (3\text{-}43b)$$

The values of A and B obtained from 3-41 are substituted into 3-43a,b to obtain an expression for the spot size observed in the detector plane:

$$\omega_1^2 = \frac{\omega_0^2}{Z_c^2}\left(\left(1 - \frac{Z_2}{f(t)}\right)^2 + \left(Z_1 - \frac{Z_1 Z_2}{f(t)}\right) + Z_2^2\right) \qquad (3\text{-}44)$$

here f(t) is the time-dependent focal length of the thermal lens, computed earlier in equation 3-34. The effect of the thermal lens on the beam maximises in the far field so that $z_2 \ggg z_1$. Consequently

$$\omega_1^2 = Z_2^2 \omega_0^2 \left(\frac{1}{f(t)^2} + \left(1 - \frac{Z_1}{f(t)} \right)^2 \frac{1}{Z_c} \right) \qquad (3\text{-}45)$$

The signal observed in a thermal lens experiment is the relative change in the spot size, before and after lens formation. For steady state thermal lenses:

$$\frac{\omega_1^2(t=\infty) - \omega_1^2(t=0)}{\omega_1^2(t=0)} = \frac{\Delta\omega^2}{\omega_1^2(t=0)} \qquad (3\text{-}46)$$

Before the lens forms, we have the condition f(t = 0) = ∞ so that from E3-45, while in the prescence of a steady state thermal lens, $f(\infty)$ is obtainable directly from equation 3-35a. Substitution of these expressions into 3-45 yields an expression for the detector signal :

$$\frac{\Delta\omega^2}{\omega^2(t=0)} = \frac{-2.303 P (dn/dT) A}{\lambda K} \left(\frac{2 Z_1 Z_c}{Z_c^2 + Z_1^2} \right) \qquad (3\text{-}47)$$

This expression is derived from 3-45, and neglects terms in $1/f(\infty)^2$ because for weak thermal lenses, $f(\infty)$ is large and these terms don't contribute. Equation 3-47 is the basic working equation of experimental thermal lensing and predicts both the nature of the detected signal and the effect of cell positioning on measured sensitivity of the effect.

It is not neccessary to actually measure the spot size at the detector because the intensity of the beam is inversely proportional to the spot area (81); if I is the beam center intensity then

$I = \frac{2}{\pi}\frac{A_0}{\omega_1^2}$ where A_0 is a constant.

Consequently, a measurement of $\Delta I/I(t=\infty)$ will be equivalent to the measurement of 3-46, where $\Delta I = I(t=0) - I(t=\infty)$.

For the remainder of this chapter, and throughout Chapter 4, the notations I_0 and I_∞ are used to indicate $I(t=0)$ and $I(t=\infty)$.

The bracketed term in 3-47 predicts a position dependence for the lens effect which is diagrammed in Figure 2 6. The position dependence is Lorentzian about the beam waist. Assuming that the thermal lens is a diverging lens (liquid sample) the lens may produce thermal focusing of the beam, if placed ahead of the beam waist (position a) or thermal defocusing if placed past the waist (position b). The effect of the diverging lens is to increase the rate of expansion of the phase front radius, R, with distance, z. If the lens is placed at the waist, the phase fronts are planar, no further expansion is possible and the lens has no effect on the beam propagation. Hence $\frac{\Delta I}{I_\infty}$ is zero. Maximum effects are observed for cell placement at either of the confocal points because R is a minimum at $+z_c$. Consequently, maximum thermal focusing is observed at $-z_c$ and maximum thermal defocusing is observed at $+z_c$. Once past the confocal points $Z_1 = Z_c$, the spot radius, ω_1, rapidly increases with distance. If the same beam is used to form and detect the thermal lens, there is a drastic loss in

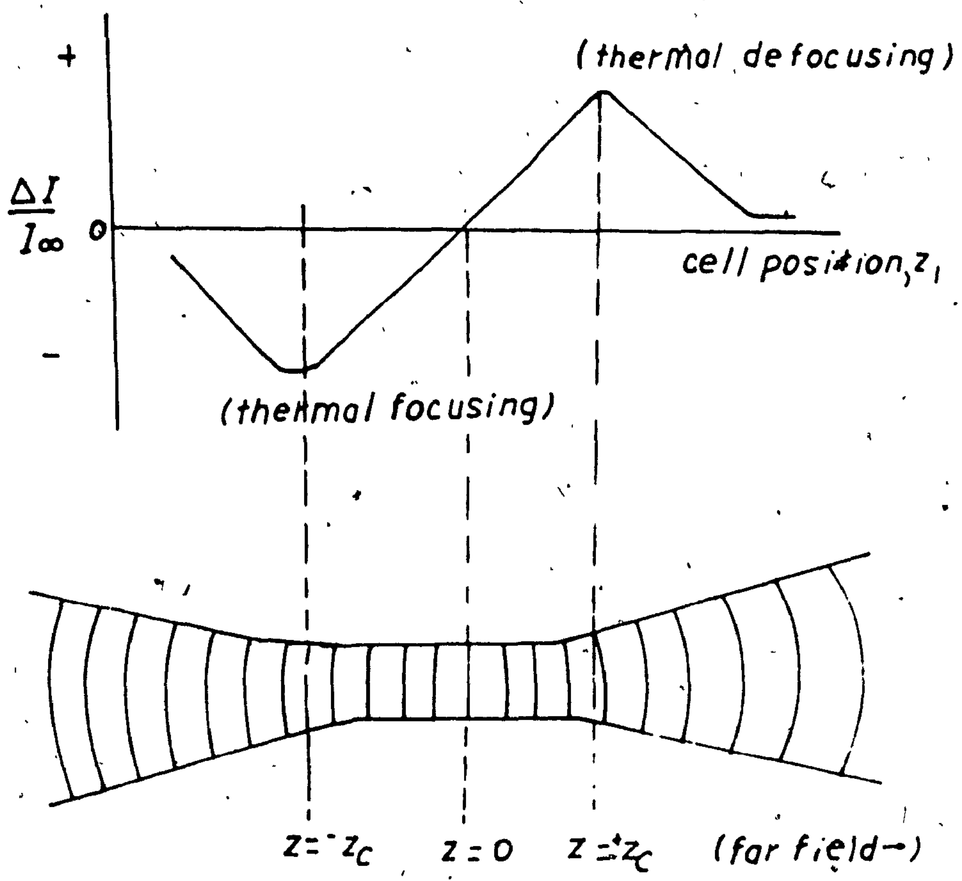

Figure 26 : Position dependence of thermal lens signal about the beam waist (references 26 , 27).

sensitivity past z_c due to expansion of the beam (with a corresponding increase in $f(\infty)$).

In summary, equation 3-47 predicts that the best compromise between sensitivity losses due to spot radius increases, and sensitivity losses due to planarity of the phase fronts, is achieved with cell placement at the confocal points of the beam forming the lens.

If two separate beams are used to form and probe the thermal lens, equation 3-47 is still valid provided the beams have matched waist positions and confocal points. If this condition is met, the two beams will propagate essentially coincidently over all space (81). Maintenance of these conditions is called " mode-matching " because the complex radii of curvature of the two beams are effectively matched.

Equation 3-47 yields a relation between the sample properties and the detector signal. We assume that the sample consists of a solution containing absorbing solutes. The collection of factors $-P(dn/dT)/\lambda K$ defines a factor E (83), which represents the sensitivity enhancement of thermal lensing over conventional absorption spectrophotometry. Consequently, we can recast 3-47 in the form :

$$\frac{\Delta I}{I_\infty} = 2.303EA\left(\frac{2z_1z_c}{z_c^2+z_1^2}\right) \qquad (3\text{-}48)$$

which for cell placement at the confocal point of the beam yields $z = z_c$ and :

$$\frac{\Delta I}{I_\infty} = 2.303\,EA \qquad (3\text{-}49)$$

The assumption made in deriving 3-49 is that the thermal lens effect is weak, which applies for dilute samples. Consequently, the values of dn/dT and K will be dominated by the properties of the solvent, while the absorbance, A, is dominated by the solute. Equations 3-47 to 3-49, in addition, establish that a linear relationship is predicted between the thermal lens signal and the sample absorbance for weak thermal lenses.

At sufficiently high sample absorbances, the focal length of the thermal lens shortens significantly with the consequence that terms in $1/f^2(\infty)$ are no longer negligible in 3-45. Retaining these terms in 3-45 gives :

$$\frac{\Delta I}{I_\infty} = 2.303EA + \frac{(2.303EA)^2}{2} \qquad (3\text{-}50)$$

Consequently, for strong thermal lenses, equation 3-50 predicts a parabolic relationship between the thermal lens response and the absorbance. This curvature arises directly from the fact that the approximations behind 3-47 are inaccurate when $f^2(\infty) \sim (Z_1^2 + Z_C^2)$. It in no way includes the effects of aberration of the lens element formed in the sample by distortions in the refractive index profile. In equation 3-50 we are still dealing with an ideal thin lens although a partial saturation effect has set in at high enough A .

The problem of lens aberration has been addressed by Sheldon et al.(66), and requires a solution by diffraction theory. However, the effect of their analysis produced the only major experimental consequence that signal optimisation is achieved for cell placement at $z = \sqrt{3} \cdot z_c$ rather then at $z = z_c$. The shape of the sigmoid curve predicted by their analysis is similar to that of 3-49 . Qualitatively , the interpretation of the optimization of cell positioning is the same .

Finally, up to this point, very little has been mentioned regarding the time dependent thermal lens effect. This has been the case because the spectrometer design and experiments of Chapter 4 have involved the observation of steady state thermal lenses. Time resolved thermal lens signals involve the full expression for f(t) in 3-45. The time dependent equation equivalent to 3-50 is given by (83,84):

$$I(t) = I_0 \left[1 + \frac{2.303EA}{1 + t_c/2t} + \frac{1}{2}\left(\frac{2.303EA}{1 + t_c/2t} \right)^2 \right]^{-1} \qquad (3\text{-}51)$$

The form of the signal development with time is shown in Figure 24 (inset). For $t \ll t_c$, the drop in the beam power is approximately linear with time. The signal quickly saturates after $t > t_c$ and steady state lens formation is approached .

Dual Beam Mode-Mismatched Laser Thermal Lensing

From the analysis presented in 3-47 and Figure 27, it is clear that the conventional single beam or dual beam mode-matched thermal lens experiment is carried out in compromised conditions (85-88). In theory maximum thermal lens formation is available at the waist of the pump beam. However, no thermal lens effect is detectable at the beam waist because of the flatness of the phase fronts.

If on the other hand, the optical alignment were arranged so that the cell were placed at the waist of the pump beam yet at the confocal point of the probe beam, the sensitivity would be potentially doubled. However if these conditions were maintained, the beams would be mismatched, with the radius of the probe beam being larger than that of the pump beam in the cell .This possibility is not accounted for in 3-45 to 3-47 .

Mode-mismatched thermal lensing was first reported as an analytical technique by Ishibashi et al (86). The sensitivity enhancement reported in their experiments was approximately 2 over conventional mode-matched experiments, as expected from spot size considerations. Later authors have reported theories (87,88), to account for the optimisation of cell positioning, and to establish signal linearity for the effect. These theories establish that the mode-mismatched experiment is analytically useful, and confirm the results of experiment.

The size mismatch between the pump and probe beams has the additional consequence that the Gaussian profile of the probe beam is destroyed. Early experiments in our laboratories with beam imaging detection (Chapter 4) have demonstrated that in the prescence of a thermal lens, a mismatched probe beam refracts to form an annular interference pattern in the detector plane .An annulus forms in the beam profile as the result of the interference of two sections of the probe beam, as diagrammed in Figure 27. The inner section of the beam passes through the lens element and is refracted while the outer section is unaffected by the lens. Both beams then propagate to the detector plane. The effect of the lens is to increase the rate of expansion of the inner section of the probe beam. The expanding inner section interferes with the unrefracted outer section, forming an interference pattern related to the aperture radius, a, and the lens element .

Because the experiments reported in this work used beam imaging detection, it has been of interest to determine, theoretically, the shape of the beam profile observed at the detector in mode-matched thermal lensing. Additional interest arises because of the results of Chapter 4, which show that the Fourier magnitude spectra of mode-mismatched beam profiles contain sideband components related to the prescence of the lens. The side band signals show enhanced sensitivity to lens formation over the conventional measurements. Therefore, a theory which is capable of predicting the shape of the Fourier spectrum is desirable to

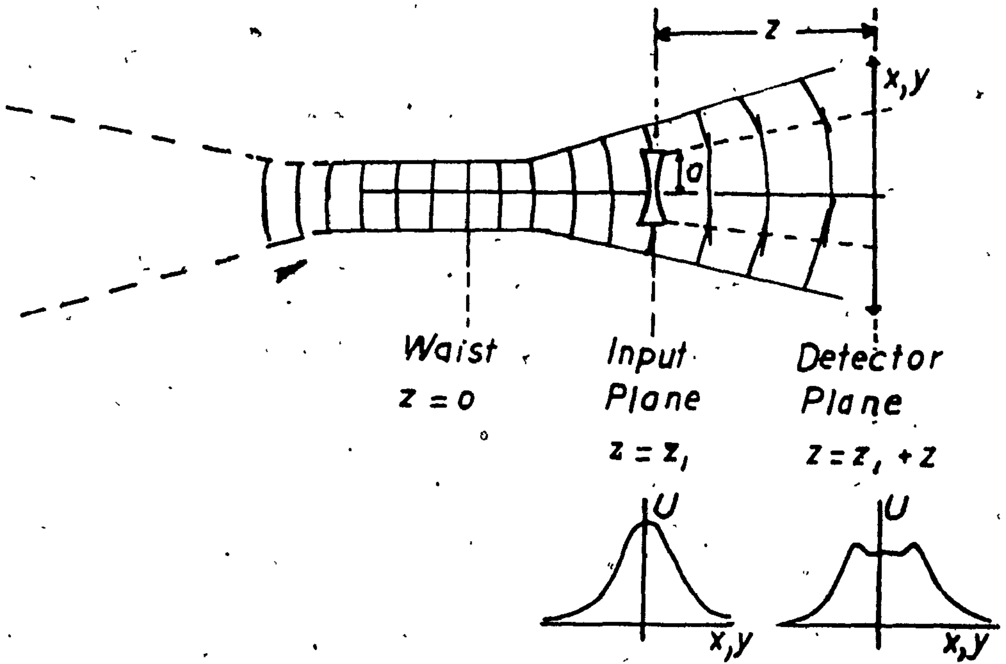

Figure 27 : Mode-mismatched thermal lens signal : formation of an annular interference pattern in the detector plane .

establish the analytical usefulness of the technique as a means of measuring weak absorbances .

The simplest case is to model the thermal lens as an ideal thin lens of finite aperture, a, placed in the path of a larger unrefracted probe beam. The shape of the probe beam profile at the detector is solved by diffraction theory (81,89), assuming the Fresnel approximation holds (89).

At the left face of the lens in Figure 28, the transverse field amplitude is :

$$\vec{U} = \sqrt{\frac{2}{\pi}}\,\frac{U_0}{\omega_1}\,e^{-\frac{jk}{2\tilde{q}_1}r^2} \qquad (3\text{-}52)$$

At the right hand surface of the lens, the light field amplitude is :

$$U_1 = \sqrt{\frac{2}{\pi}}\,\frac{U_0}{\omega_1}\,e^{-\frac{jk}{2\tilde{q}_1}r^2}\left(e^{-\frac{jk}{2f}r^2}\,p_a(r) + \bar{p}_a(r)\right) \qquad (3\text{-}53)$$

where $$p_a(r) = \begin{cases} 1 & \text{if } r \leq a \\ 0 & \text{if } r > a \end{cases}$$

For a wavefront incident on the lens aperture (r <= a) the lens multiplies the incident waveform by the quadratic phase factor $\frac{kr^2}{2f}$. Outside the aperture, (r > a) the wavefront is unaffected, and multiplied by unity.

Fresnel diffraction (89) predicts that the beam profile in the detector plane is obtained via the 2 dimensional convolution :

$$U_d(x,y,z) = U_1 \ast\ast \frac{j e^{-jkz}}{z\lambda}\,e^{-\frac{jk}{2z}r^2} \qquad (3\text{-}54)$$

where

the factor $e^{-j\frac{k}{2z}r^2}$ may be regarded as an impulse response or point spread for free space.

The integral to be solved (81,89) is :

$$U_d(x,y,z)=\frac{je^{-jkz}}{z\lambda}\iint_{-\infty}^{\infty}\tilde{U}_1(x_0,y_0)\,e^{-j\frac{k}{2z}\cdot((x-x_0)^2+(y-y_0)^2)}\,dx_0\,dy_0 \qquad (3\text{-}55)$$

It is best to evaulate 3-54 by splitting the beam into two sections and evaluating them separately :

I (inner section) :

$$U_d^I= U_1 e^{-j\frac{k}{2F}r^2}P_a(r) ** j\frac{e^{-jkz}}{2z\lambda}e^{-j\frac{k}{2z}r^2} \qquad (3\text{-}56a)$$

O (outer section) :

$$U_d^0 = U_1\bar{p}_a(r) ** j\frac{e^{-jkz}}{2z\lambda}e^{-j\frac{k}{2z}r^2} \qquad (3\text{-}56b)$$

At the detector, the observed signal is $U_d = U_d^{outer} + U_d^{inner}$

For the inner section, we evaluate :

$$U_d^i(x,y,z)=\frac{je^{-jkz}}{2z\lambda}\sqrt{\frac{2}{\pi}}\,\frac{U_0}{\omega_1}\iint_{-\infty}^{\infty}e^{-j\frac{k}{2}\left(\frac{1}{q}+\frac{1}{f}\right)(x_0^2+y_0^2)}\,e^{-j\frac{k}{2z}((x-x_0)^2+(y-y_0)^2)}\,p_a(x_0,y_0)\,dx_0\,dy_0 \qquad (3\text{-}57)$$

If we expand the terms in the exponent in 3-57 and abbreviate $\frac{1}{q_p}=\frac{1}{q}+\frac{1}{f}+\frac{1}{z}$:

$$U_d^i(x,y,z)=\frac{je^{-jkz}}{2z\lambda}\sqrt{\frac{2}{\pi}}\,\frac{U_0}{\omega_1}\,e^{-j\frac{k}{2z}(x^2+y^2)}\int_{-a}^{a}e^{-j\frac{k}{2q_p}x_0^2}\,e^{-j\frac{kxx_0}{z}}\,dx_0\int_{-a}^{a}e^{-j\frac{k}{2q_p}y_0^2}\,e^{-j\frac{kyy_0}{z}}\,dy_0 \qquad (3\text{-}58)$$

With the substitutions : $\alpha_1=\alpha_2=\frac{k}{2q_p}$

$$\omega_1^* = -\frac{kx}{z} \; ; \quad \omega_2^* = -\frac{ky}{z}$$

3-58 is directly recognisable as a two dimensional Fourier transform (67) :

$$U_d^i(x,y,z) = \frac{je^{-jkz}}{2z\lambda}\sqrt{\frac{2}{\pi}}\,\frac{U_0}{\omega_1}\,e^{-j\frac{k}{2z}r^2}\int_{-\infty}^{\infty} e^{-j\omega_1^* x_0}\, e^{-j\alpha_1 x_0^2}\, p_a(x_0)\,dx_0$$

$$\cdot \int_{\infty}^{\infty} e^{-j\omega_2^* y_0}\, e^{-j\alpha_1 y_0^2}\, p_a(y_0)\,dy_0 \qquad (3\text{-}59)$$

The transform has solutions available directly in terms of a set of Fresnel integrals (67) . For y = 0 , the transverse intensity profile observed in the x dimension at the detector is : for $\frac{1}{a} = \frac{1}{q_1} + \frac{1}{f} + \frac{1}{z}$:

$$U_d^i(x,y,z) = j\sqrt{\frac{2}{\pi}}\,\frac{U_0\; e^{-jkz}}{\omega_1 z\left(\frac{1}{a}+\frac{1}{z}\right)}\quad F(\sqrt{\alpha_1}a)\, e^{-\frac{jk\,r^2}{2(a+z)}} \cdot \qquad (3\text{-}60)$$

$$\cdot \left\{ F\!\left(\sqrt{\alpha_1}a + \frac{kx}{2z\sqrt{\alpha_1}}\right) + F\!\left(\sqrt{\alpha_1}a - \frac{kx}{2z\sqrt{\alpha_1}}\right)\right\}$$

For the outer annulus , the detector signal is obtained from Babinet's principle (89) , which states

$$U_d = U_d^0 + U_d^i \qquad (3\text{-}61)$$

In the abscence of the lens :

$$U_d^i(x,y,z) = \frac{je^{-jkz}}{2z\lambda}\sqrt{\frac{2}{\pi}}\,\frac{U_0}{\omega_1}\iint_{-\infty}^{\infty} e^{-\frac{jk}{2q}(x_0^2+y_0^2)}\, e^{-\frac{jk}{2z}((x-x_0)^2+(y-y_0)^2}\,dx_0\,dy_0$$

$$(3\text{-}62)$$

Solution of the diffraction integral in the absence of the lens yields :

$$U_d = \sqrt{\frac{2}{\pi}}\, \frac{e^{-jkz}\, U_o}{\omega_1 z\left(\frac{1}{q_1} + \frac{1}{z}\right)} \cdot e^{-\frac{jkr^2}{2(q_1+z)}} \qquad (3\text{-}63)$$

The inner section of the beam from r = 0 to r = a is , in the abscence of the lens , given by :

$$U_d^i(x,y,z)(\text{no lens}) = j\,\frac{e^{jkz}\, U_o}{\omega_1 z\left(\frac{1}{q_1} + \frac{1}{z}\right)} \cdot \sqrt{\frac{2}{\pi}}\; e^{-\frac{jk\,r^2}{2(q+z)}} \cdot F(\sqrt{\alpha_1}a) \qquad (3\text{-}64)$$

$$\cdot \left\{ F\left(\sqrt{\alpha_2}a - \frac{kx}{2z\sqrt{\alpha_2}}\right) + F\left(\sqrt{\alpha_2}a + \frac{kx}{2z\sqrt{\alpha_2}}\right) \right\}$$

where

$$\alpha_2 = -\frac{k}{2}\left(\frac{1}{q} + \frac{1}{z}\right)$$

Equation 3-63 is readily obtainable from 3-60 by assuming that f = ∞ (infinitely weak lens)

From Babinet's principle , in the absence of the lens (3-61), the expression for the outer annulus is :

$$U_d^{o} = \sqrt{\frac{\pi}{2}}\; e^{-jkz}\, \frac{U_o}{\omega_1 z\left(\frac{1}{q} + \frac{1}{z}\right)}\; e^{-\frac{jk}{2}\cdot\frac{r^2}{(q+z)}} \left\{ 1 - \frac{j4}{\pi} F(\sqrt{\alpha_2}a) . \right. \qquad (3\text{-}65)$$

$$\left. \left\{ F\left(\sqrt{\alpha_2}a - \frac{kx}{2z\sqrt{\alpha_2}}\right) + F\left(\sqrt{\alpha_2}a + \frac{kx}{2z\sqrt{\alpha_2}}\right) \right\} \right\}$$

It is clear from equations 3-58 to 3-65 that the discontinuities introduced by the finite aperture of the lens produce complexities in the mathematical description of the effect. While it is not practical to directly fit observed beam profiles to these equations, they may be used to numerically generate theoretical profiles and Fourier spectra for comparison with the experimental results.

The theoretical treatment outlined here may be criticised on the grounds that it takes no account of the aberrations present in the thermal lens element at non-negligible distances from the beam axis (66). While the theory is certainly greatly simplified, there is evidence in the experiments of Chapter 4 to indicate that the refractive index profile " flattens " at relatively short distances from the beam axis, indicating a large mismatch in the pump and probe beam radii. In these experiments there is probably poor spatial resolution of the lens element near the beam center so that a detailed description of the aberrations is probably unimportant. Moreover, the primary feature of interest in the beam profile is the mismatch discontinuity, and its behavior with respect to sample properties. Experimental investigations of mode-mismatched thermal lensing follow in the next chapter.

Chapter 4 : A Laser Thermal Lens Spectrometer for Natural Organic Matter Analysis

As described in the previous chapter, it has already been seen that the thermal lens technique is a potentially simple and effective means of measuring very weak absorbances. Thermal lens instrumentation, while simple in principle, suffers two main technical drawbacks in application which have probably impeded the development of commercially available spectrometers. The first of these drawbacks is the requirement for the high powered CW laser systems needed to supply the pump beam. While it has been demonstrated that inexpensive, low powered helium/neon lasers perform adequately in some circumstances, these sources have no wavelength tunability, and are restricted to use with samples having high absorptivity in the red. The other problem with the classic thermal lens experiments (using pinhole / photodiode combinations for detection) is the large optical path neccessary for observation of the signal. Classic CW thermal lensing requires signal measurements to be made at the beam center in the far field region. These requirements may be met with optical path lengths in excess of 5 meters (90). The long optical path produces a signal which is very sensitive to vibration and drifts in alignment , so that any attempts at packaging this design commercially will be prohibitively wasteful of space and require vibration isolation of the optical bench.

The first of these limitations may perhaps await the availability of low cost solid state visible laser sources (91) if a commercial steady state spectrometer is to be developed. A low cost pulsed dye laser system is commercially available* and could successfully function as a source in a pulsed thermal lens spectrometer. The use of pulsed lasers in thermal lensing has been reported by Miyaishi et al (92). However, the detection limits reported with pulsed excitation ($E = 20\ \mu J$; $A=7\times10^{-4}\ cm^{-1}$ in CCl_4) were much poorer than detection limits available with CW systems, even in organic solvents where enhancements are typically high. The use of pulsed lasers with energies of less than 100 µJ per pulse will probably not compete effectively with low cost solid state CW systems as they become available.

The second technical limitation of conventional thermal lensing, that of the long optical path required for signal measurement, may be solved by placing an imaging detector in the near field of the probe laser beam. Such a detector will record an entire cross section of the probe beam (rather than simply the center intensity) and enable the user to fit the spatial data to a theoretically known mode pattern for the recorded beam profiles. The use of a photodiode array in thermal lensing has already been reported by Ishibashi et al (85,93) and has been demonstrated to improve analytical detection limits somewhat. Here ,it is also suggested that such detectors permit measurement of thermal lens signals in the near field with a reduction in the optical path length by as much as an order of magnitude.

* PRA Nitromite, Photochemical Research Associates

In the course of this work, a CW dual beam thermal lens spectrometer has been designed and constructed, incorporating a photodiode array detection system. The dual beam design of this system also permits the implementation of mode-mismatched thermal lensing. In this chapter, the interference patterns detected in mode-matched LTL are analysed in the spatial frequency domain and are utilised for the analysis of low concentration samples. This type of analysis, otherwise inaccessible, is made possible through the use of a photodiode array detection system.

Mark I LTL Spectrometer

The first phase in the development of the CW spectrometer was the evaluation of the photodiode array as a detector, with the objective of reducing the optical path for signal measurement. The ultimate objective, of course, was the attainment of a minimum detection limit for the technique.

The prototype photodiode array spectrometer initially constructed (here referred to simply as LTL I) was built from low cost, readily available components. The objectives of the first design were to rapidly implement and evaluate the new detection system prior to the refinement and design of a more permanent system. The configuration of the system prior to LTL I was as a single beam instrument following the conventional designs described in Chapter 3. The single beam spectrometer was successfully developed and applied by our group to the trace analysis of Fe(II), sulfur dioxide (94) and formaldehyde (95). Reported here are the design details of the evaluation prototype. A block diagram of LTL I is shown in Figure 28 . The pump beam signal is supplied by a CW argon ion laser (Coherent CR6 Supergraphite Ion) equipped with a model 590 dye laser head. The dye laser is operated using Rhodamine 6G which permits tunability of the pump wavelength over the range of 550 to 632 nm, so that the yellow to red region of the visible is covered. The blue to green wavelengths are also readily available (457.8 , 488, 496.5, 514 nm). Output powers up to 6W and 1W are available

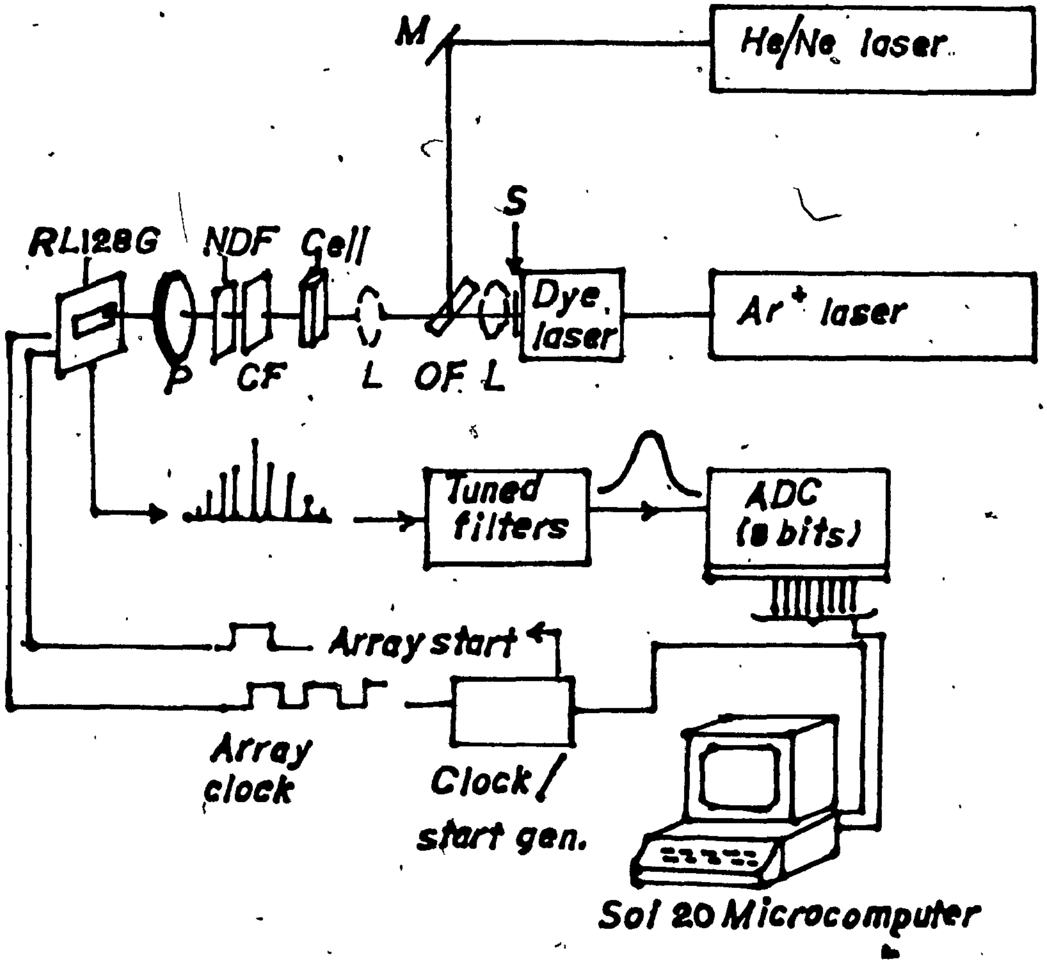

Figure 28 : Block diagram of LTL I thermal lens spectrometer system.

from the argon and dye lasers, respectively.

The probe beam is obtained from a 10 mW Spectraphysics helium/neon laser with an output stability of about 1 %. The probe beam is reflected off mirror M and directed onto an optical flat (OF) where it is combined with the pump beam from the argon laser. The beam from the argon system is passed through a converging lens (L) (f=23 cm) and the optical flat, to the cell, consisting of a 1 cm square glass cuvette. The optical flat reflects less than 1 % of the incident probe power, and is chosen as a simple means of attenuating the 10 mW signal prior to detection. The optical flat was chosen with a thickness of approximately 10 mm to eliminate the interference patterns associated with thin plates, which would otherwise distort the Gaussian profile of the beam (this point is discussed in more detail in later sections of this chapter).

It is possible to operate the spectrometer in both the mode-matched and mode-mismatched configurations, depending on the placement of the converging lens. In the case of mode-matched operation, the lens is placed after the optical flat; both pump and probe beams are focused to approximately the same waist position and the cell is placed at one confocal distance from the waist. For higher sensitivity, mode-mismatched operation is adopted, in which the cell is placed at the waist of the pump beam, while the probe beam remains unfocused. Once past the cell, the pump beam is attenuated and separated from the probe by the combination of a neutral density filter (NDF) and color filter (CF). The intensity of the probe beam is made adjustable by means of a gelatin polariser placed directly in the path of the beam.

The probe beam profile was detected in the near field by means of a photodiode array containing 128 or 256 elements (the 256 element array was interchangeable with the smaller device) mounted horizontally in the beam path (RL128G or 256G). The device recorded the transverse intensity profile of the probe beam. In this case, the probe beam diameter was less than the width of the array, so that no focusing optics were required to reduce it to the detector dimensions. The photodiodes in the array were sequentially read out by on chip circuitry. The array was supported by a current amplifier system (Reticon RC 301) whose output consisted of a train of amplitude modulated spikes. The intensity of each spike was proportional to the photocurrent integrated by a corresponding photodiode in the array (over the integration period of the device). The signal was filtered in several stages of active filters to remove the carrier (the spikes). The filtered signal was then digitised by a system of analog to digital converters and logged by an on-line microcomputer system (SOL 20, Processor Technology Corp.), at a rate of 30 KHz. The converter resolution was 8 bits. The digital output was reported to an ASR 33 teletype as a series of intensities, each intensity corresponding to the average reading of a group of photodiodes (Appendix A contains the details of the interface operation).

Used in conjunction with a 256 element array, at a clock rate of 100 KHz, the program logged 83 data points and 17 baseline points for a total of 100 points per scan. The logged data stored in the Sol 20, in early experiments, were reported directly to the teletype under control of the Sol operating system. In later experiments, the Sol 20 was linked to an IBM PC which was used for real-time data processing. Data from the Sol were reported to the IBM system via an RS232 interface under control of programs written in 8080 assembler and IBM BASICA.

The Photodiode Array Detector

The detector used in both versions of the spectrometer was a Reticon G Series line scanner equipped with an RC301 current amplifier board. An overview of their basic operation is presented here.

The Reticon G series devices (96) are a family of linear photodiode arrays which are integrated for self scanning operation. A "G" series device consists of a row of 128, 256 or 512 silicon photodiodes with a width of 15 microns and a center to center spacing of 25 microns. The array is sealed beneath an Si substrate on the surface of an integrated circuit containing the readout electronics. The array is sealed beneath a silica window, so that the device's spectral response covers the visible and near IR with the response curve maximising near 800 nm. The sensitivity of the device is close to optimum in the present application, where the probe beam wavelength is the 632 nm

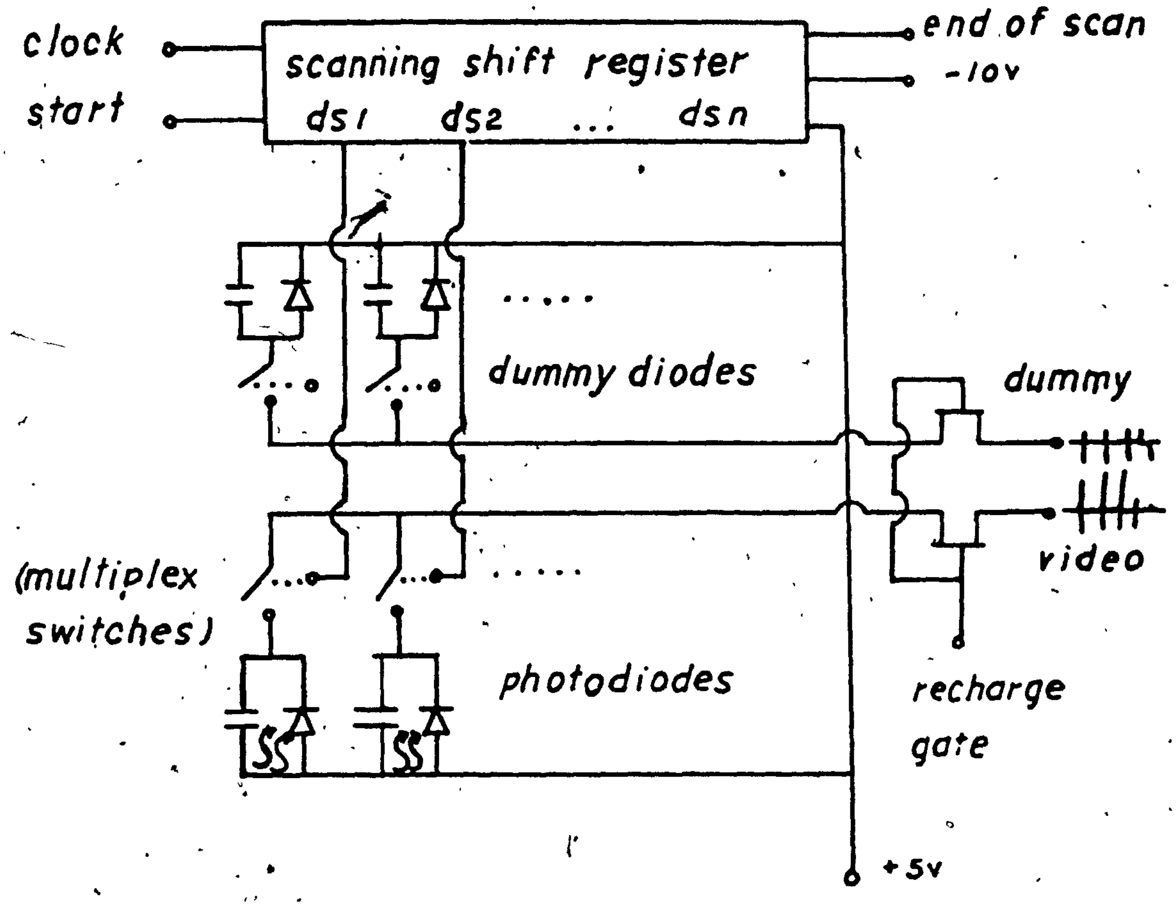

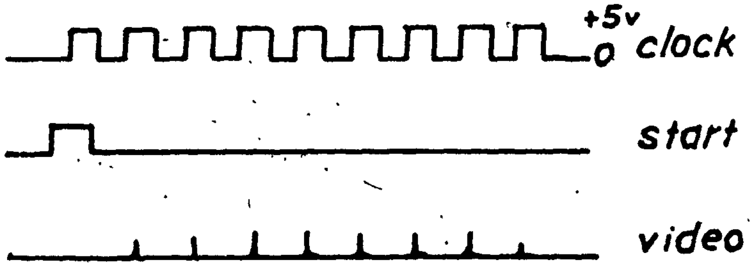

Figure 29 : Equivalent circuit for G series line scanners (reference 96).

line of the helium/neon laser.

In measurement of the light intensity incident on the photodiodes, the G series arrays behave as charge storage devices. An on chip shift register samples a linear array of cells (Figure 29) : each cell consists of a photodiode and associated storage capacitance. As a diode is exposed to light, it conducts, causing a photocurrent to flow in the cell. A storage capacitor is connected across each photodiode. Each capacitor is initially charged to +5v at the start of a readout sequence. As the photodiode is illuminated, photocurrent depletes the charge on the cell storage capacitor. When the scanning shift register closes the MOS switch associated with the cell, the cell capicitance is recharged to the supply voltage and a pulse of current appears on the video recharge line. The intensity of the current pulse is proportional to the amount of photocurrent integrated by the cell capacitance.

In the course of reading out a photodiode, switching transients appear on the recharge line. These transients are eliminated by means of a set of dummy cells that are read out simultaneously with the cells containing the photodiodes. The output of the dummy line contains only the switching transients so that differential amplification of the signal trains from the dummy and video recharge lines allows for recovery of a " clean " video signal.

The dummy and video lines are accessed via a set of analog switches which are biased " ON " by applying a negative voltage to the recharge gate (see equivalent circuit, Figure 29). The direct amplification of the recharge line signals is the measurement strategy adopted by the RC301 current amplifier support circuitry. Another measurement strategy is possible, however, in which signals from the dummy and video recharge lines are buffered by means of on chip amplifiers.The second design strategy is adopted by the more advanced RC100B motherboard system used in LTL II.

Evaluation of Instrument Performance

Evaluation of the performance of the spectrometers was achieved by preparing solutions of known absorption and recording calibration curves of thermal lens response (as $\frac{\Delta I}{I_\infty}$) vs concentration or absorbance of the standard. Absorption standards for thermal lensing were prepared by dilution of concentrated stock solutions of accurately known absorbance (A $\sim$ 0.100 cm^{-1}). The range of absorbances for the thermal lens standards was 7×10^{-5} - 0.010 cm^{-1} at the source wavelength of 488 nm.

For the evaluation of LTL I, Armadale fulvic acid in distilled water was used as the absorbance standard at 488 nm. (A few experiments at 600 nm used aqueous $CuSO_4$ as the standard). For LTL II, evaluation was made using aqueous $CoSO_4$. The preparation and spectrometer calibration procedures have been described in detail in Chapter 5 and are not repeated here.

Performance of the Instrument : LTL I

The thermal lens response of LTL I was determined by measurement of the peak heights obtained from photodiode array data. Some typical beam profiles obtained from the system are shown in Figure 30 a and b. The profiles shown in (a) indicate the effects of thermal defocusing on the probe beam. As the lens forms, the probe beam drops in intensity and broadens out. In the case of the mode-mismatched geometry (Figure 30(b)) thermal defocusing produces an annular intensity pattern due to the interference of two sections of the beam : a refracted inner section which passes through the thermal lens. and an unrefracted outer section which is unaffected by its presence (see Chapter 3 and the last section of this chapter).

The presence of distortions from the Gaussian distribution and of interference patterns in the I_O intensity profiles of Figure 30 a,b are well known phenomena associated with photodiode array signals (85). These interferences are caused by defects in the surfaces of the optical components and multiple reflections caused by thin plate optical elements placed in the beam path. A careful alignment of the beam optics is required to minimise these effects, since they increase directly as the number of components placed in the beam path (Figure 31). These interferences have been termed " spatial noise " although they are not noise in the true sense. As seen shortly, the effect of "spatial noise " on the measured detection limit

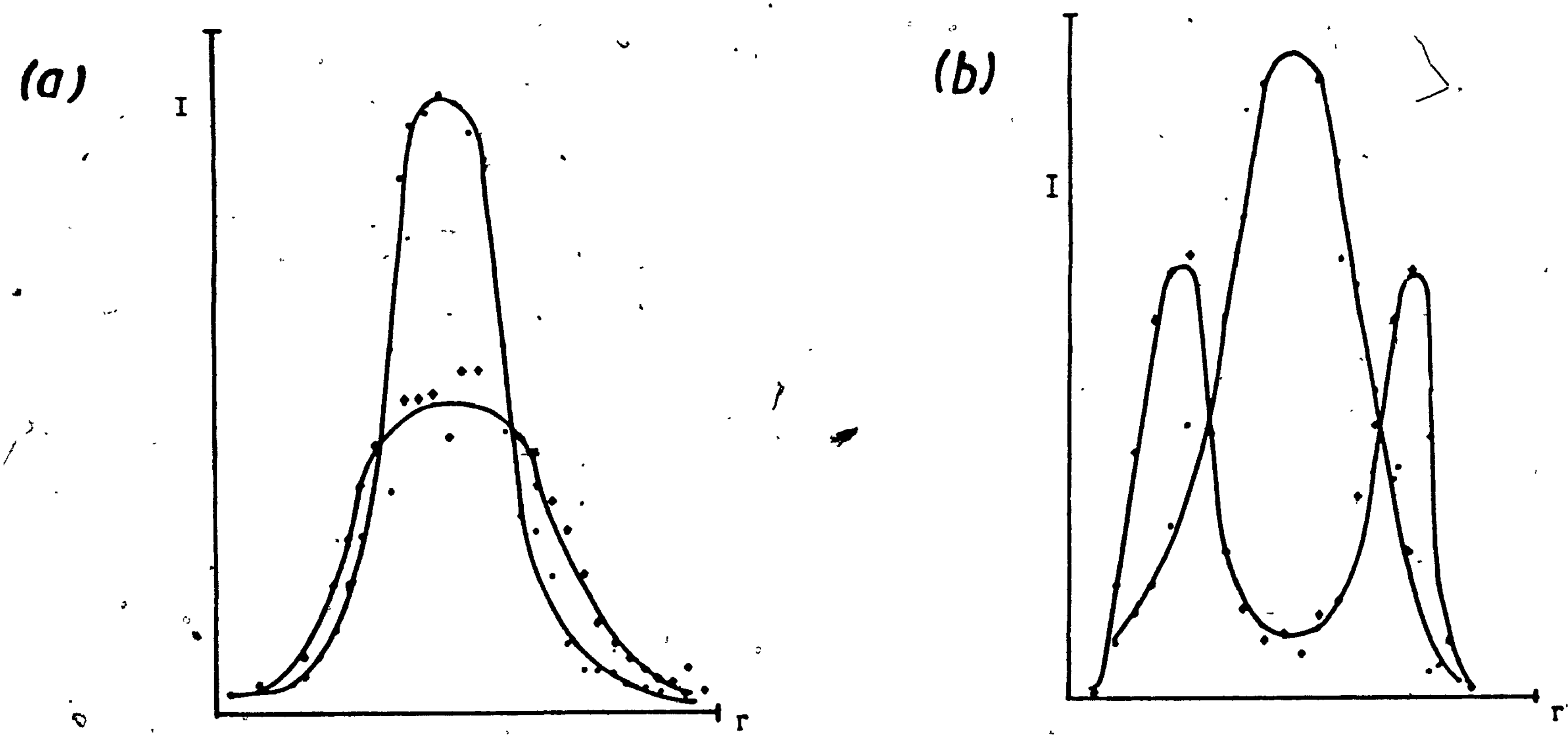

Figure 30 : Detector recordings of beam profiles for thermal defocusing effect (a) mode-matched thermal lens signal (sample was Armadale fulvic acid , 2 ppm , P = 125 mW ; excitation wavelength was 488 nm. (b) mode-mismatched thermal lens signal (sample was $CuSO_4$ with an absorbance of 0.015/cm. P = 50 mW ; excitation wavelength was 600 nm).

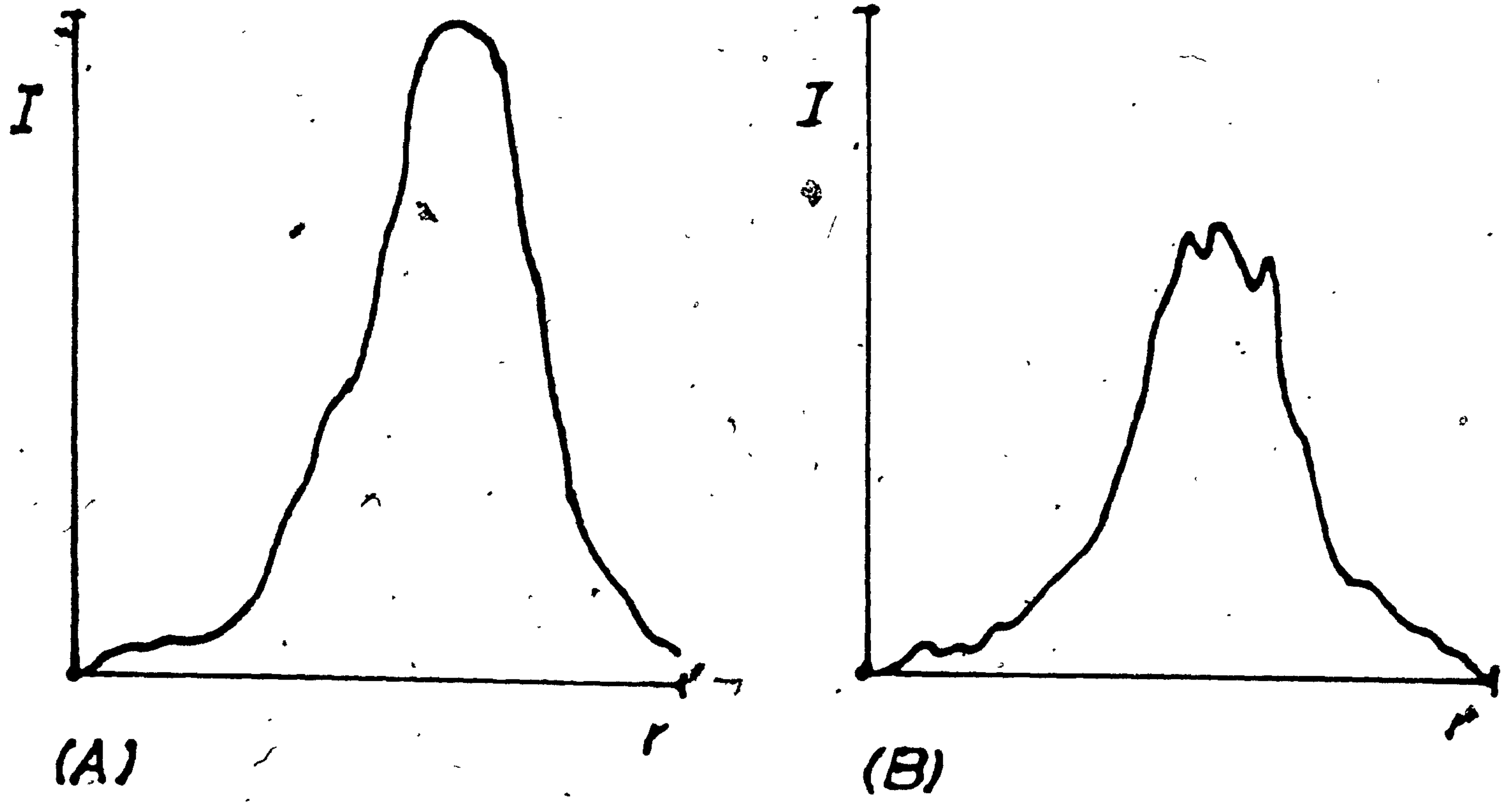

Figure 31 : Effect of adding optical elements on shape of imaged beam profile. Beam profile contacting (a) mirror, optical flat and polariser (b) elements ofa plus a lens, cell and color filter.

depends on the stability of these interferences over time.

Calibration curves of instrument response versus calculated absorbance (from known concentrations of analyte and from Beer's law) were prepared and are reported in Figure 32. The instrument was calibrated with aqueous solutions of Armadale fulvic acid over the pH range from 5 - 8. The instrument measured steady state thermal lens signals (with cell exposures of 3 seconds). The relationships between $\frac{\Delta I}{I_\infty}$ and concentration (or absorbance) were approximately linear (0.985 < R < 0.99) at $\frac{\Delta I}{I_\infty}$ values below 0.30. Above this range, the thermal lens signal obeys a parabolic relationship with concentration as discussed in Chapter 3. This arises because the simplified optical equations originally derived for infinitely weak thermal lenses no longer hold.

The instrument response curves of Figure 32 were determined over a range of beam powers in the mode-matched geometry (beam power in these experiments was measured at the cell). At a beam power of 120 mW, the enhancement factor E = 18 was obtained. In water, with 488 nm excitation, it was possible to detect fulvic acid absorbances as low as 1×10^{-4} on this instrument based on the I.U.P.A.C. definition of detection limit, in which the minimum detectable concentration or absorbance is that value at which the measured instrumental signal is twice the the standard deviation of the blank (97).

An apparent limitation on the instrument performance in

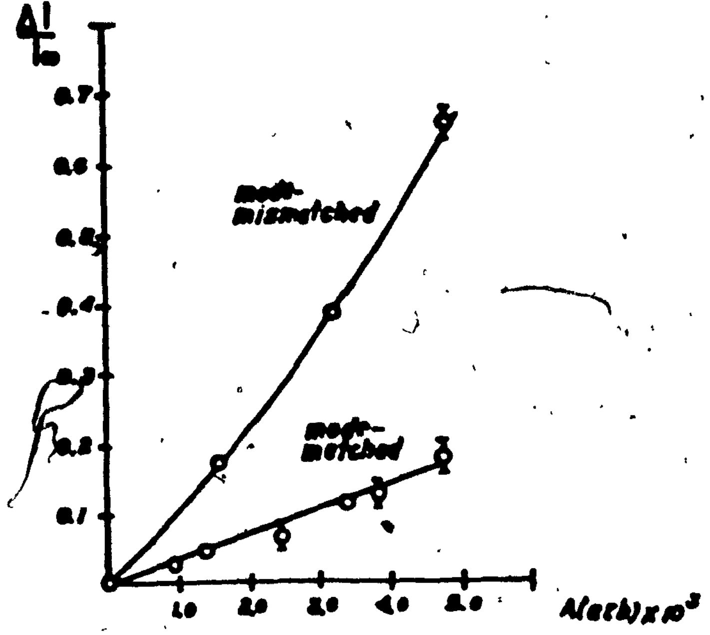

Figure 33 : Comparison of the sensitivities obtainable with mode-mismatched (E = 48) and mode-matched (E = 16) alignments. For both cases: wavelength was 488 nm (all line) and P = 100 mW.

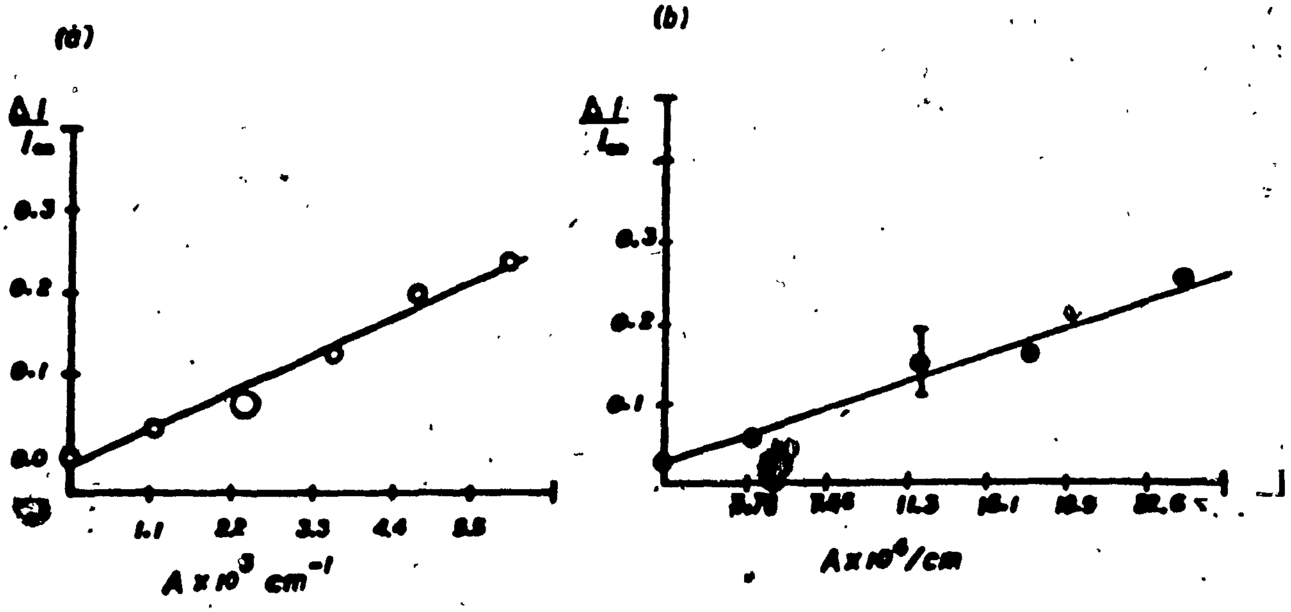

Figure 32 : Calibration curves of $\Delta I / I_\infty$ vs absorbance for Armadale fulvic acid on LTL I spectrometer system. (a) mode-matched thermal lens signal; P = 120 mW; (b) Mode-mismatched signal : P = 100 mW. Excitation wavelength was 488 nm. Enhancement factors were 18 for (a) and 51 for (b).

the mode-matched configuration was a lack of resettability of the optical alignment. It was neccessary to realign the probe beam optics on a daily basis due to pointing instabilities in the helium/neon laser. In the case of the dye laser, daily alignment of the cavity optics was neccessary to obtain optimum output. The tight coaxial alignment of the pump and probe beams in the mode-matched configuration was especially sensitive to small errors in positioning so that the enhancement factor could vary by as much as 40 % from one day's run to the next, at a given power. Results recorded within a single day's run provided a valid indication of the instrument's detection capabilities : a comparison of absolute readings from one day's run to the next was not, however, meaningful without standardization. The variation of sensitivity with alignment set no true limit on the detection capabilities of the instrument because these relatively small losses in sensitivity due to misalignment could be easily compensated by increasing the beam power. In the case of the calibration standards used, their absorption properties are known to be stable under the experimental conditions. Any changes in the instrument response from one day's run to the next are therefore not attributable to chemical factors. While it is theoretically possible to compute the absorbance of a sample directly from a thermal lens measurement, such calculations require an accurate knowledge of the thermooptic properties of the sample and a detailed knowledge of the precise alignment geometry of the instrument. Both factors are usually unavailable so that it is inadvisable to attempt to measure absolute " absorbance" in preference to values determined by direct standardisation (83). Consequently, the practical use of a thermal lens instrument as an absorption spectrometer requires, as a first step, calibration of the instrument with a standard of known absorbance (with the same solvent in which the analyte is determined).

Calibration curves have been prepared for the mode-mismatched alignment, in addition to the conventional alignment just discussed. In the mode-mismatched geometry, the probe beam is unfocused (or loosely focused) so that the alignment of the pump and probe beam is greatly facilitated (86). The mode-mismatched configuration exhibited a sensitivity enhancement of 2-3 over the conventional alignment (Figure 33). However, the mismatched geometry destroys the Gaussian profile of the beam as the lens forms so that the analysis reported below does not apply .

In mode-matched experiments, Gaussian fitting of the profiles was undertaken in order to determine if any improvement could be made in the detection limit. The beam profile data were fitted to an equation of the form in which (85):

$$\mu = \frac{\sum I \cdot r}{\sum I} \qquad (4\text{-}1)$$

$$\omega^2 = \frac{\sum I \cdot r^2}{\sum I} \qquad (4\text{-}2)$$

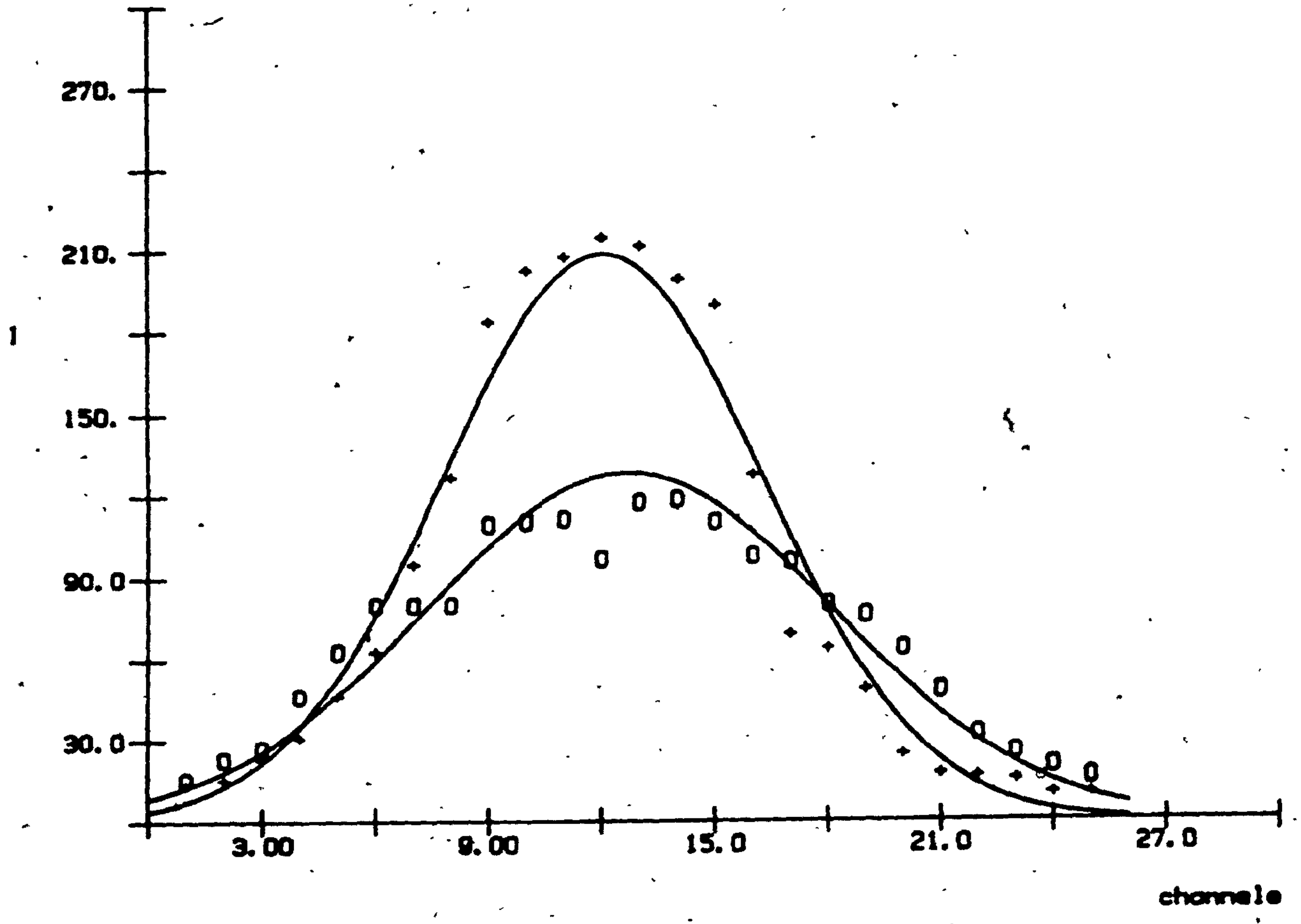

Figure 34: Gaussian fitting of beam profile data for (+) t=0 and (0) t= ∞ data. Gaussian parameters were obtained from equations 4-1 to 4-3.

$$I_0 = \frac{1}{\sqrt{2\pi}} \frac{\sum I}{\omega_1} \qquad (4\text{-}3)$$

Examples of the Gaussian fitting technique applied to the beam profile data are shown in Figure 34. While it is not clear from these data, the work of previous authors (85) has shown that the Gaussian parameters obtained from fitting are functions of the range of data fitted. The fitting of beam profiles using data points too close to the beam center tended to emphasise the optical interferences at the beam center, while the inclusion of data too far from the beam center weighted the fitted signal too much to the beam edge (85). For data obtained in the presence of a thermal lens, the observed detection limit depended critically on the fitting region chosen for the array data. Beam profile data fitted from the wrong range actually increased the observed detection limit by a factor of 2-4 (85).

In the mode-matched experiments with LTL I, no significant improvement was found using Gaussian fitting, over the single point measurement made at the beam center. This suggested that the primary sources of noise in these experiments were time dependent and systematic.

This point underlines the character of the data required if spatial averaging of the beam profile is to be effective. The requirement for successful ($1 / \sqrt{N}$) reduction of noise is that the averaged signal be stationary : the mean value and standard deviation of every data point in the array must not vary with time (98). This requirement is definately violated if the beam intensity profile changes shape over time. The requirement for spatial stability of the beam is very severe : fast acquisitions of $\frac{\Delta I}{I_\infty}$ signals (on timescales faster than the spatial fluctuations) will not yield spatially stationary data. Every time the beam distorts spatially, the Gaussian beam parameters shift slightly and change the computed value of $\frac{\Delta I}{I_\infty}$. This behavior, observed in our experiments, has been discussed by Jansen and Harris (93) to explain the relatively poor performance of photodiode arrays as averagers of spatial noise. To date, the best detection limit improvements by Gaussian beam profile analysis have been by factors of 2-4 over single diode averaging (85,93). The $1/\sqrt{N}$ improvement has not yet been realised by this technique.

The specific sources of "spatial noise " went largely unidentified in the development of LTL I. The identification and elimination of these spatial noise problems was essential for the success of LTL II. Even with the limited readout resolution of the LTL I detection system, the main limits on sensitivity were directly traceable to instabilities in the probe laser and to a number of sources of uncompensated spatial noise in the optical system. The solution to these problems is described in the next section of this chapter.

LTL II : Description

A second, upgraded version of the spectrometer has been developed, incorporating a number of improvements in design over LTL I. The block diagram is shown in Figure 35.

The basic optical design of LTL II is similar to the early version, except that the new design was exclusively mode-mismatched. The helium/neon probe laser was upgraded to a Siemens/PRA model 250 with a stability rating of 0.1 %. It was neccessary to shield the probe laser from external air currents to realise this level of stability.The optical path of the probe laser was shielded by means of a dust baffle, which was built around all of the optical components. The size of the dust cabinet was sufficiently large for convenient operation of the instrument (alignment of optics and cell manipulation) but otherwise was kept to a minimum to reduce the circulation of air currents and dust in the interior of the case. The sample cell used in LTL II was a fixed flow-through cell with a cylindrical design (Figure 35 - inset). This design was chosen for its immunity to turbulence associated with convection disturbances in the cell (99). The spectrometer was run in the steady state mode, as with LTL I, with cell exposures of 1-3 seconds.

Improvement of the detector signal quality was achieved by upgrading the detector electronic support to the Reticon RC100B motherboard system. The output is supplied as a sample and hold signal and requires no further processing (other than level matching) prior to digitisation. Further

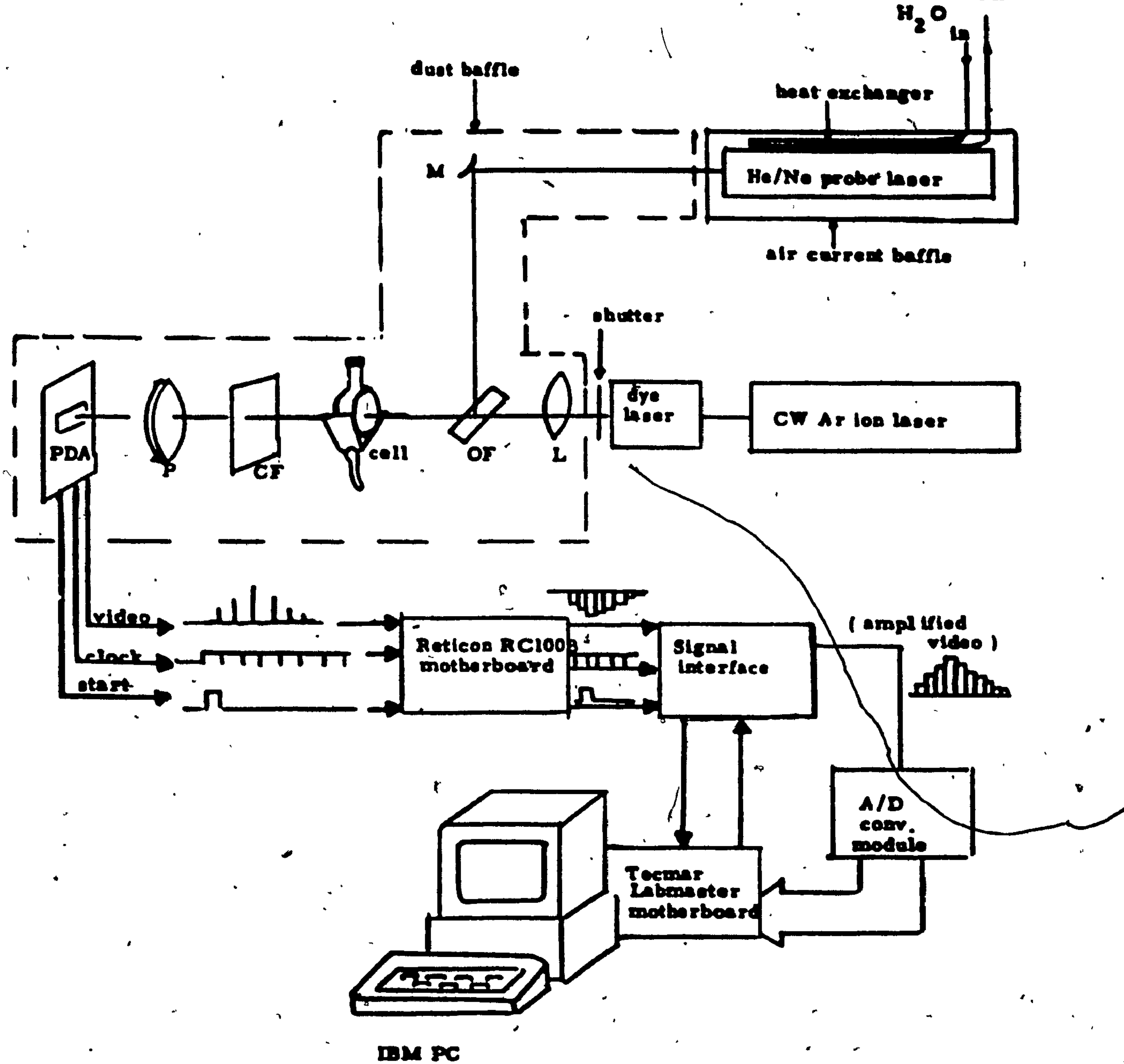

Figure 35: Block diagram of LTL II thermal lens spectrometer system.

resolution and speed have been added to the electronics as the result of incorporating a Tecmar Labmaster Data Acquisition Module into the system design. The Labmaster system provides a major improvement in readout resolution (12 bits) as compared with LTL I.

Finally the computer system has been upgraded to an IBM PC which provides fast acquisition and access to a variety of high level languages for data analysis. In this work, data acquisition routines were written at the machine level (8088 instruction set) while the data analysis was carried out under programs written in Asyst *. Under software control, data acquisition is converter limited (40 KHz) and 100 profiles of the array are averaged for the I_0 and I readings. As configured, the software and signal interface will support a 128, 256 or 512 element array.

Data Acquisition Hardware and Interface

The current version of the spectrometer is equipped with a Tecmar Labmaster Data acquisition system (Tecmar Corp., Cleveland, Ohio). The system contains with a DAS 5712 acquisition module which permits analog to digital conversion rates as high as 40 KHz. The Labmaster system is interfaced to an IBM personal computer as a memory mapped device, so that its data ports are accessed by 8088 memory reference instructions. The Labmaster comprises a two board system. A motherboard is directly interfaced to the IEEE 488

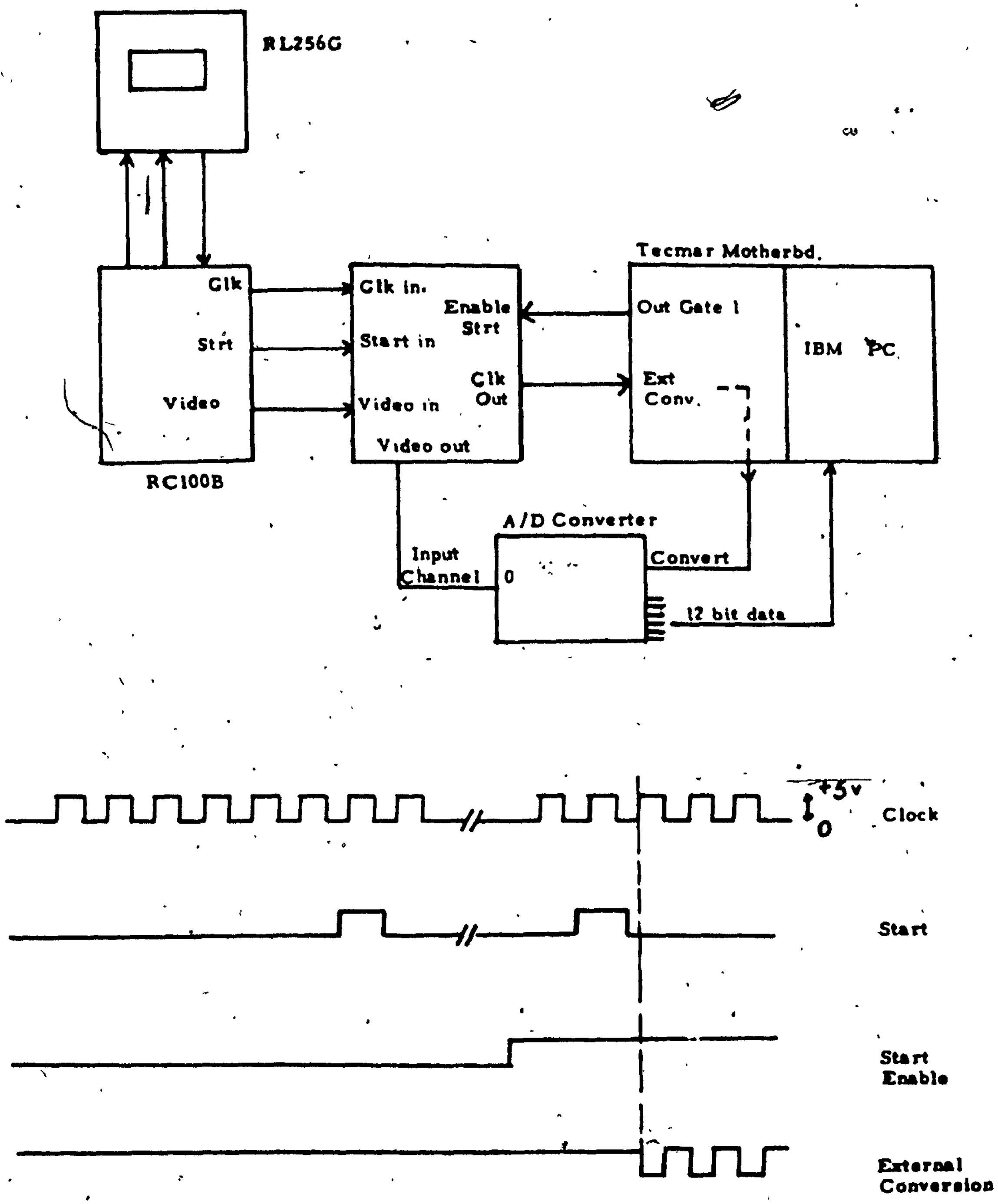

Figure 36: Block diagram of LTL II Data Acquisition Interface

bus. A daughter board, containing the data acquisition module is located externally to the PC and cabled to the motherboard. This second board contains an analog multiplexer which allows conversion of data from selectable sources. External signals are directly connected to the daughter board via 40 connector ribbon cable.

LTL II uses pipelined analog to digital conversion of data from the interface to ensure converter limited acquisition rates. Conversions are initiated externally from the clock pulse train supplied by the Reticon motherboard circuitry via the "external start conversion" channel of the Labmaster daughter board.. For maxiumum conversion speed, the strobing of channels of the analog multiplexer is suppressed : only the channel containing the amplified detector signal is converted. In order to minimise gain requirements for amplification of the array signal prior to conversion, a unipolar input on the analog to digital converter with a 0 to 10 V range was selected. The digital output is unsigned 12 bit integer data (with single ended inputs selected). It should be noted that the DT 5712 does not contain a programmable gain option so that matching of signal levels to the converter input range must be achieved by user supplied hardware. With the Labmaster configured as described, the recognition of external data conversion requests is enabled by software. The status flags indicating completion of conversion, busy condition, or overrun condition on the ADC are read by the device handler . Details concerning the jumpering of the Tecmar daughterboard module for selection of acquisition options, of the switch settings on the motherboard and of the acquisition software, are reported in Appendix B.

The signal interface designed for LTL II synchronised the computer initiated data acquisition sequences with the scanning and readout sequences of the array. The design reported here was adopted to minimise timing and synchronisation complexity by allowing the Reticon line scanner to function autonomously. The relationships governing data acquisition may be understood from the timing diagram of Figure 36 . The Reticon motherboard is jumpered for internal clock and start operation so that clock and start pulses are continuously supplied at regular intervals to the signal interface. The interface initially disables the "external start conversion" line of the ADC. When the the IBM system is ready to initiate a data acquisition cycle, it drives the " start enable " line high. The next start pulse supplied by the Reticon system is then latched by the signal interface and used to gate the clock train into the external conversion channel of the Labmaster system. These clock pulses are thus used to synchronously initiate analog to digital conversions of the video line pulses. Once conversions are enabled, the computer logs a linear array of data points up to 128K in length. The switch settings on the Reticon motherboard are preset to provide 16 baseline points at the end of every readout of the array. Each scan of the array supplies 256 points. The conversion format and specifications for the interface and data acquisition cycles are summarised in Table 9.

LTL II : Instrument Performance and Noise Analysis

A schematic of the noise sources encountered in laser thermal lensing is shown in Figure 37. It is assumed that the detector is a photodiode array, and that the spectrometer is a dual beam instrument. In the figure, the time dependent thermal lens element is modelled as a low pass filter L(f), while the helium neon probe beam is considered to supply the input signal I_0. The input noise sources add to I_0 at the summing points $\sum_{1-3}$, while the output noise adds at $\sum_{4-5}$.

In the absence of the lens, the noise sources are as follows :

(a) thermal fluctuation noise : occurring inside the helium/neon laser tube. This is probably due to convection set up within the plasma. Thermal fluctuations limit the long timescale stability of the probe laser output (at $t > 1$ sec). They also affect the spatial intensity distribution of the beam. These effects may, furthermore, may contribute systematic error if the plasma tube is ventilated and cooled by external air currents.

(b) optical noise in the probe laser system : this noise dominates at $t < 1$ sec and is "white" in character.

(c) "path noise" : encountered by the beam as it travels

Table 9

Specifications for Reticon/Labmaster Interface

No. bytes per scan : 528 (includes baseline)

Maximum conversion rate of ADC : 40 KHz

Input rate of software : 40 KHz

Readout time of array at 40 KHz Rate : 12.4 msec (512 diodes)

No. of baseline points logged between scans : 16

Total acquisition time under software : 3.5 sec (for 127 KB of data)

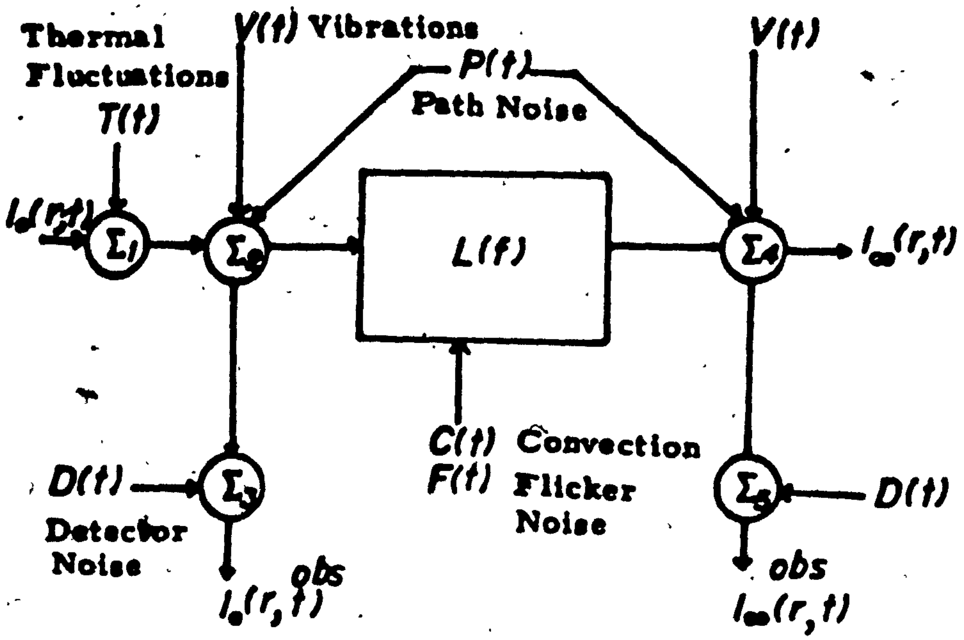

Figure 37 :Schematic diagram of noise sources in LTL II system.

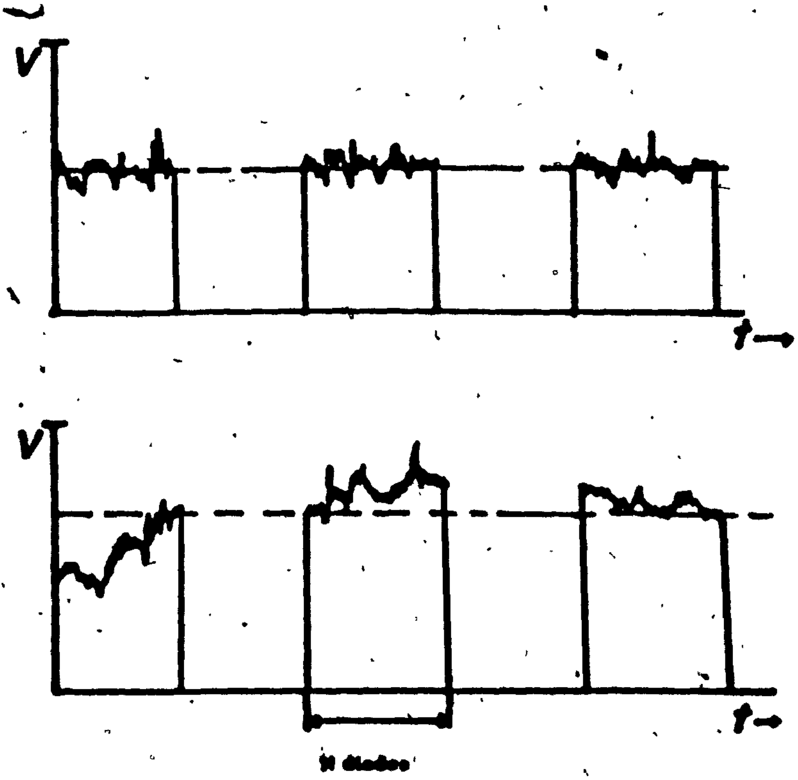

Figure 38: Electronic interferences in photodiode array background signal : effect on readout sequence. upper trace: high frequency noise; lower trace: low frequency noise.

through the optical system. Dust circulating in the beam path causes time dependent light scattering. Air currents circulating in the beam bring about slight changes in the refractive index of the optical path and measureable fluctuations in the beam profile observed at the detector. Both of these effects contribute at low frequency (0.1 - 0.01 Hz).

(d) vibration noise : causing motion of the detector relative to the source. Vibration dominates on the short term (t < 1 sec) and is usually statistical, although it may have systematic components.

(e) cell position error : this effect arises from variations in the positioning of optical components placed in the beam path.

(f) detector noise :

(i) electronic noise : The photodiode array readout sequence is a serial process noise in the readout or detection circuitry translates effectively to spatial noise because the time varying electronic noise pattern is superimposed on the spatial pattern read out of the array. As long as the frequency spectrum of the noise contains no major components significantly below the scan repetition frequency of the array, the noise will average spatially. Low frequency electronic noise is a much more serious problem because it introduces a time varying background into the recorded profiles which is averageable over time, but not over the spatial coordinates of the array.

(ii) quantum noise : aside from the usual shot noise encountered with single photodiodes, linear photodiode arrays encounter additional complications due to the overlap of responses of adjacent pixels (96) . Light falling between any two adjacent pixels has a 50% chance of being integrated by one element or the other. If there is a large difference in the light intensity striking any two photodiodes, there is a large jitter in the integrated signal due to the effect of the partitioning of incident photons between one diode and the other (100). The jitter effect increases as the difference in the intensity between any two diodes. The result is a noise effect which varies with the spatial intensity distribution of the imaged signal.

Additional noise sources are encountered in the presence of the lens. These could be termed " lens formation noises " because they affect the measured signal by varying the extent of lens formation :

(a) convection in the samples : due to the heating of the sample during cell exposure.

(b) power fluctuations in the pump laser over long time periods

(c) flicker noise caused by errors in the shuttering of the beam. Instabilities in the choppers or shuttering used to gate the pump beam into the sample cell directly affect the extent of lens formation by introducing errors in the timing of the cell exposure.

In the design of LTL II, it was neccessary to take special precautions to eliminate various sources of spatial noise present. Even if the measurement interval for the thermal lens signal is short, long term variations in the beam profile still limit improvement by spatial analysis. The consequence is that the thermal lens signal averages over time, while spatial averaging yields only a slight improvement in signal reproducibility.

Because LTL II was a steady state instrument (capturing signals on a timescale of seconds) the effects of spatial noise were quite apparent once the once stability rating of the probe laser was upgraded to the nominal value of 0.1 % (for the Siemens/PRA model 250). Measurements made on the upgraded probe laser system showed no initial improvement over the LTL I measurements. Two major spatial noise problems were identified and corrected in order to achieve the manufacturer's rating. The first was a "path noise" problem caused by circulation of dust and air currents in the beam path. The problem was corrected by encasing the probe beam path in a dust cabinet made of transparent polystyrene panels (101). The second problem, that of thermal fluctuations in the laser system, was even more severe. The helium/neon system was cooled via ventilation holes in the tube chasis. Air currents circulating through these holes produced a time dependent transverse intensity variation in the output beam, on a timescale of seconds. The problem was corrected by building a polystyrene case over the tube chassis to shield the probe laser from these external influences. Cooling was maintained by clamping a heat exchanger to the tube chassis and circulating cold water through it (Figure 35). With these measures taken, the beam stability was greatly improved, so that stabilities of 0.1 % were achievable over the time period of formation of the steady state thermal lens. However, thermal fluctuations still contributed a major source of beam variation over long timescales.

The problem of cell positioning error was eliminated by using a fixed, flow-through cell, used in previous experiments. In the early experiments with LTL I using a movable cell, correlation coefficients for instrumental calibration curves were between 0.985 and 0.99. LTL I used a square cell with a conventional spectrophotometer cell holder. In later experiments, a movable cylindrical cell was used, but the particular cell used did not index correctly on the cell holder. The calibration curves obtained with this arrangement were effectively non-linear (R < 0.985). Adoption of the fixed, flow-through cell design improved the linearity of the calibration curves yielding correlation coefficients of 0.999 or better (Figure 38).

The effects of detector noise were investigated on both short and long timescales to determine the contribution, if any, to the measured thermal lens signal. The shorter timescale of 0 - 500 msec was chosen because thermal fluctuations make a minor contribution to the beam instability in this regime.

The stability of the " dark " array signal was first examined with respect to time variations in the signal integrated by a single photodiode in the array. It was found that the signal baseline stability was + 1.5 bits (3.5 mV on 10 V full scale for the analog to digital converter). Over time on a single pixel, the baseline noise averaged as $1/\sqrt{S}$ for S scans, so that over the 100 scans of the array logged in a steady state experiment, the baseline noise falls below the readout resolution of the converter. Electronic noise originating in the level matching amplifier (see schematic, Appendix B) and the input noise in the converter were found to be negligible as the result of tests carried out over timescales less than 500 msec with the signal inputs grounded. The noise in the baseline therefore most likely originated in the line scanner IC or the Reticon support circuitry.

The spatial integral of the "dark" photodiode array signal was monitored over time on the short and long timescales. On the short (< 500 msec) timescale the integral of the array scan averaged over time as $1/\sqrt{S}$ as observed for a single pixel, 0.1%. However, the % stability of the spatial integral, calculated as $\sum I(r)$, was the same as that obtained for a single photodiode. This observation indicates that the array background signal fluctuates systematically over time from scan to scan, which is possibly indicative of low frequency electronic inteference (Figure 39). Interestingly, it was found that over sets of 100 replicates of the array scans, the noise reduction was better than 1/ S, suggesting that the low frequency effects were averaged, and that spatial averaging was becoming effective as the systematic background fluctuations were reduced.

As a check on the spectral content of the background signal, a series of Fourier magnitude spectra was recorded for replicates of the background signal over timescales of less than 500 msec and over time periods of seconds. The spectral distributions of the individual scans showed high noise levels (2%). Averaging the spectra over 100 replicates reduced the amplitude variation by better than $1/\sqrt{S}$. This, again, could indicate that the time dependent variations had been reduced to a significant extent. Background frequency spectra averaged over long periods showed no further noise improvements. However, the long term signal stability was better than 0.02 %, even with very long acquisition intervals.

The next step in the analysis was to observe the effects of averaging on actual profiles from the probe laser. On the short term, the stability of the probe laser was found to be 1.6 bits (as standard deviation) which approximately matches the inherent noise of the detector. The noise in the beam center intensity was measured at a single photodiode, and found to average statistically as $1/\sqrt{N}$ over time. Gaussian fitting of the profiles on short timescales, to yield I_0 and I_∞ did not give estimates with improved stability indicating the ineffectiveness of spatial averaging even for data accumulated over short intervals. The low frequency components of Fourier magnitude spectra of these helium/neon profiles did not average over time as $1/\sqrt{S}$, indicating the presence of systematic short term changes in the spectral content of the beam profile. This behavior is quite different than for the " dark " signal whose Fourier spectra averaged over time. Therefore, it is probable that the short term spectral variations observed in the beam profiles were external and could have arisen from vibrations in the optical system, or perhaps even variations in the spatial homogeneity of the plasma discharge in the probe laser.

The effects of vibration noise in the optical train from building vibrations ,is partially compensated in this system by mounting the optical table on a set of foam pads. However even these isolation measures could have been inadequate. Correction of the problem is readily achieved if the vibrations are statistical and the profiles are averaged over 50-100 replicates. The steady state design of the current system compensates for this problem but places the measurement in a regime where thermal fluctuations dominate.

As the present experiments concentrated on the measurement of steady state thermal lenses ,the proceedure adopted was to average 100 replicates of the beam profile to obtain the I_0 reading, and 100 replicates for the I_∞ reading at steady state. Cell exposures of 1 sec were observed in early experiments. A close inspection of the signal showed that some residual lens growth took place as late as three seconds after the opening of the shutter. The longer exposures (3 seconds) had higher noise levels associated with them, probably because of convection in the sample associated with the longer irradiation period. For each sample ,the $\frac{\Delta I}{I_\infty}$ measurement was averaged over 6 replicates . The mean value of the array signal was computed from the beam profile data, and $\frac{\Delta I}{I_\infty}$ is calculated for data observed at the mean photodiode. Based on this proceedure, the minimum deectable signal was $\pm$ 0.0015 units of $\frac{\Delta I}{I_\infty}$. Ultimately, the limit on the stability of the probe laser in this regime is probably set by thermal fluctuations in the laser and in some cases, by convection. With an enhancement factor of 20.0, easily obtainable at 50 mW of excitation power (measured at the sample cell in this case), it was possible to detect absorbances as low as 2-4x10^{-5} cm^{-1}, with linearity of the calibration curves obtained up to 0.0025 cm^{-1}. This figure represents an order of magnitude improvement over the performance of LTL I. Furthermore, the use of the mode-mismatched geometry seems to have solved the problem of the non-uniformity of instrument response attending beam alignment. The calibration curves of Figures 39 a and b were recorded over several day's runs. With a minimum disturbance of the optical alignment between runs, the response is observed to be quite reproducible although daily standardisation is still recommended.

The results of this section indicate a solution of the second problem associated with conventional thermal lensing, that of the high power normally required for lens formation.

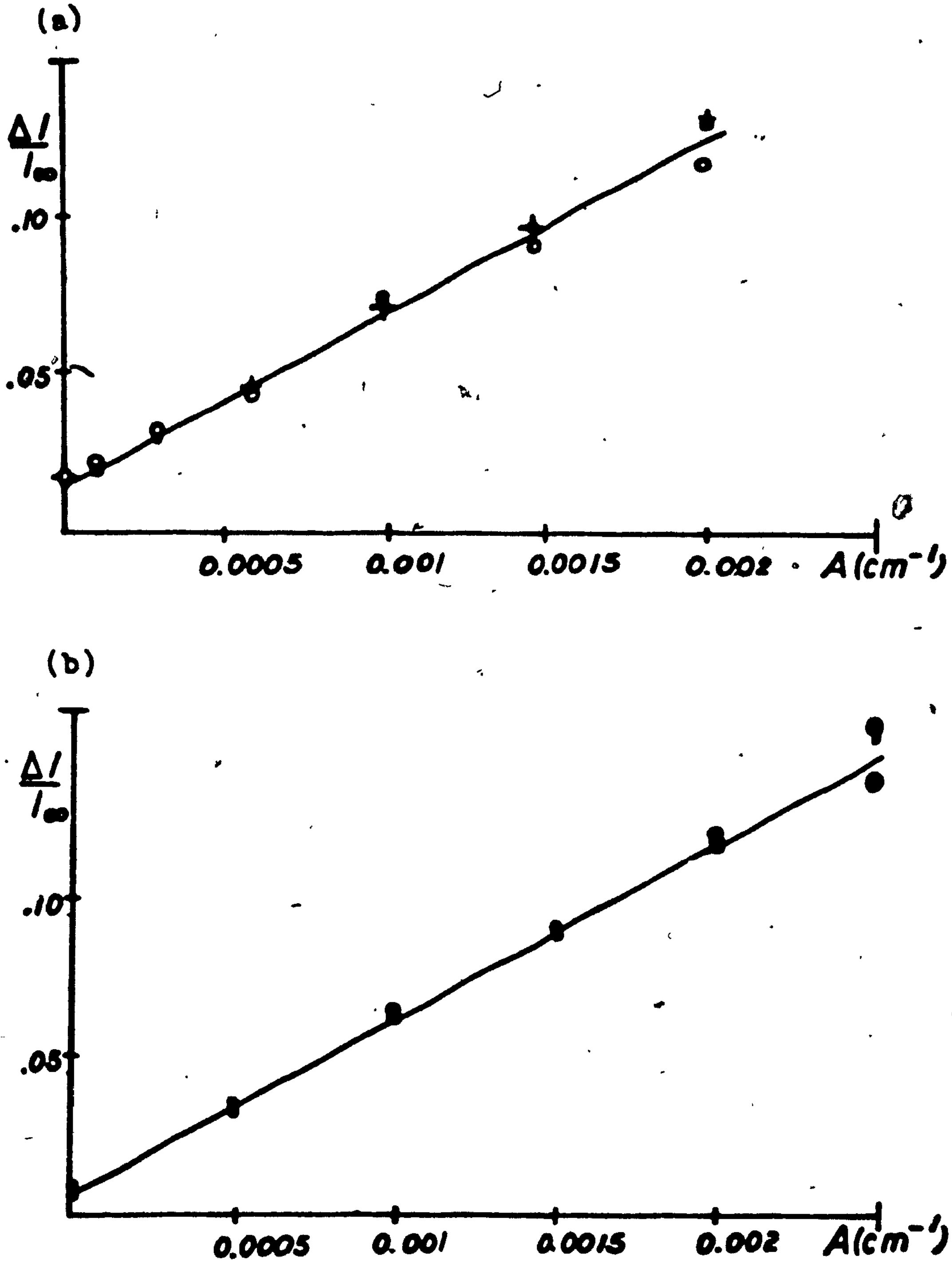

Figure 39: Calibration Curves of $\Delta I / I_\infty$ vs absorbance for $CoSO_4$(aq) on LTL II system. Data from several consecutive runs are superimposed. (a) P = 60 mW, excitation wavelength was 488 nm. (b) P = 50 mW, excitation wavelength was 458 nm.

Table 10

Summary of Instrument Response Parameters

LTL Spectrometer	Mark I	Mark II
A range for signal linearity	0 - 0.005 (100 mW) (mode matched) 0 - 0.0025 (100 mW) (mode-mismatched)	0-0.003 (50 mW) (mode-mismatched)
Wavelength	488 nm (or all line)	488 nm
Error in response (blank)	0.01 - 0.02	0.001 - 0.002
Enhancement factors	10-25 (mode-matched 120-180 mW 50 (mode-mismatched , 100 mW)	25-30 (mode-mismatched ,40-60 mW)
% Error in slopes of calibration curves	5-10 %	1-3 %
Linearity of calibration curves	R = 0.985 - 0.998	R = 0.998 or better
Detection limits as Absorbance (IUPAC)	2-4 x 10^{-4} cm-1	2-4 x 10^{-5} cm-1
as DOC	400-600 µg/l	40-60 µg/l

At beam powers as low as 50 mW, the required detection limit is low enough to carry out absorbance measurements on freshwater and sea water samples to levels approaching 50 ppb of dissolved organic carbon at 600 nm.

While the steady state design of LTL II has not yielded the hoped-for improvements promised by the stability of the upgraded probe laser, the identification and solution of the ~~spatial~~ noise problems has proven to be a neccessary prerequisite for the effective use of photodiode arrays as detectors in thermal lensing. The main limitation of LTL II has been that the long term thermal fluctuations override the benefits achieved by signal averaging over short times. The performance of LTL II could possibly be improved by switching to a transient mode of signal detection in which the lens signal is averaged over several hundred milliseconds. Such a proceedure would provide an order of magnitude improvement in signal stability, at a loss in sensitivity or enhancement factor, E. With the short term problems of vibration and background noise, however, it is still uncertain whether the spatial averaging technique would be fully effective and yield noise reductions proportional to $1/\sqrt{N}$.

Mode-Mismatched Thermal Lensing : Approaches to Signal Analysis

For the instrument performance so far reported, very little use was made of the photodiode array data per se other than to accurately locate the beam center by calculation. The problem posed by mode-mismatched thermal lensing is that the Gaussian profile of the probe beam is destroyed as the lens forms. The theoretical model of Chapter 3 indicates that the mathematical expression for the beam profile is too complicated to be dealt with by an analysis based on curve fitting. The results of the previous section, furthermore, seem to point to the undesirability of curve fitting proceedures in general, because of the stringent long term spatial stability requirements posed by beam imaging detection.

Because the spatial signal acquired in these experiments is biased (on a sample-to-sample basis) by spatial interferences, what is required is a strategy for eliminating any signal dependence on spatial noise. Three general strategies toward this end have been adopted and are reported here. The first involves the computation of a generalised frequency response function for the lens element and attempts to avoid the specific contributions of spatial noises in the input and output signals. The second approach uses a narrowband frequency-domain detection technique which avoids the frequency ranges associated with the spatial interferences.

Thermal Lens Detection by Computation of a Point-Spread

The simplest approach to handling the mode-mismatched array data was to model the lens as a filter stage which converts a beam profile with frequency spectrum $\hat{I}_0(jk)$ into $\hat{I}_\infty(jk)$ where k is the spatial frequency (Figure 40). The response function thus generated should be characteristic of the lens element only and would show gain or attenuation over a band of frequencies characterisic of the lens only for weak lenses, the unwanted spatial noise would be present to equal extents in $\hat{I}_0(jk)$ and $\hat{I}_\infty(jk)$ and would therefore have unity gain. Convolution of the lens response with an idealised Gaussian frequency distribution followed by inverse transformation could yield a " cleaned up " output signal with inverse tranformation to the spatial domain.

The technique was easily implemented using fast Fourier transform routines. The $I_0(r)$ profile was first fitted to a Gaussian profile in the spatial domain. Next, $I_\infty(r)$ and $I_0(r)$ were Fourier tranformed and the equivalent response function was obtained as $\hat{L}(jk) = \hat{I}_\infty(jk) / \hat{I}_0(jk)$. The Gaussian profile computed from $I_0(r)$ was then Fourier transformed and multiplied with the "lens transform", $\hat{L}(jk)$. Inverse transformation of the resulting product yielded an " $I_\infty(r)$ " beam profile which was the convolution of the lens response with an idealised Gaussian waveform. Finally $\Delta I/I_\infty$ was evaluated from the Gaussian waveform for I_0 and the convoluted waveform.

The lens response evaluated from the formation of a mode-mismatched thermal lens is shown in Figure 40. Figure 40(a) shows the magnitude plot of the lens response while (b) shows the phase plot. In both cases a series of side bands is quite evident which may possibly be related to the aperture of the thermal lens element. When convoluted with an idealised Gaussian lineshape, the lens response yields a signal as shown in Figure 41 for aqueous $CoSO_4$ ($A = 0.002$ cm^{-1}, $P = 50$ mW). While the signal is clearly free of "spatial noise " the observed enhancement factor is reduced by 40 % relative to a conventional beam center measurement. This result seems to suggest that the choice of a Gaussian profile in the convolution step has the effect of arbitrarily reducing the bandwidth of the input signal and missing some of the higher frequencies associated with the lens growth. The next step was to determine the effect of broadening the bandwidth of the input waveform by convoluting $\tilde{L}(jk)$ with Gaussian signals of increasingly narrowed peak width (in the frequency domain, the signal bandwidth broadens as the Gaussian linewidth is diminished.) The effect of increasing the $\tilde{I}_0$ signal bandwidth has the effect of increasing the magnitude of $\Delta I / I_\infty$. As the linewidth narrows, a " hole " develops in the center of the beam profile as is typical for a mode-mismatched thermal lens. However, an increasing distortion of the edges of the profile was observed suggesting that the frequency spectrum of the Gaussian signal experienced truncation error for very

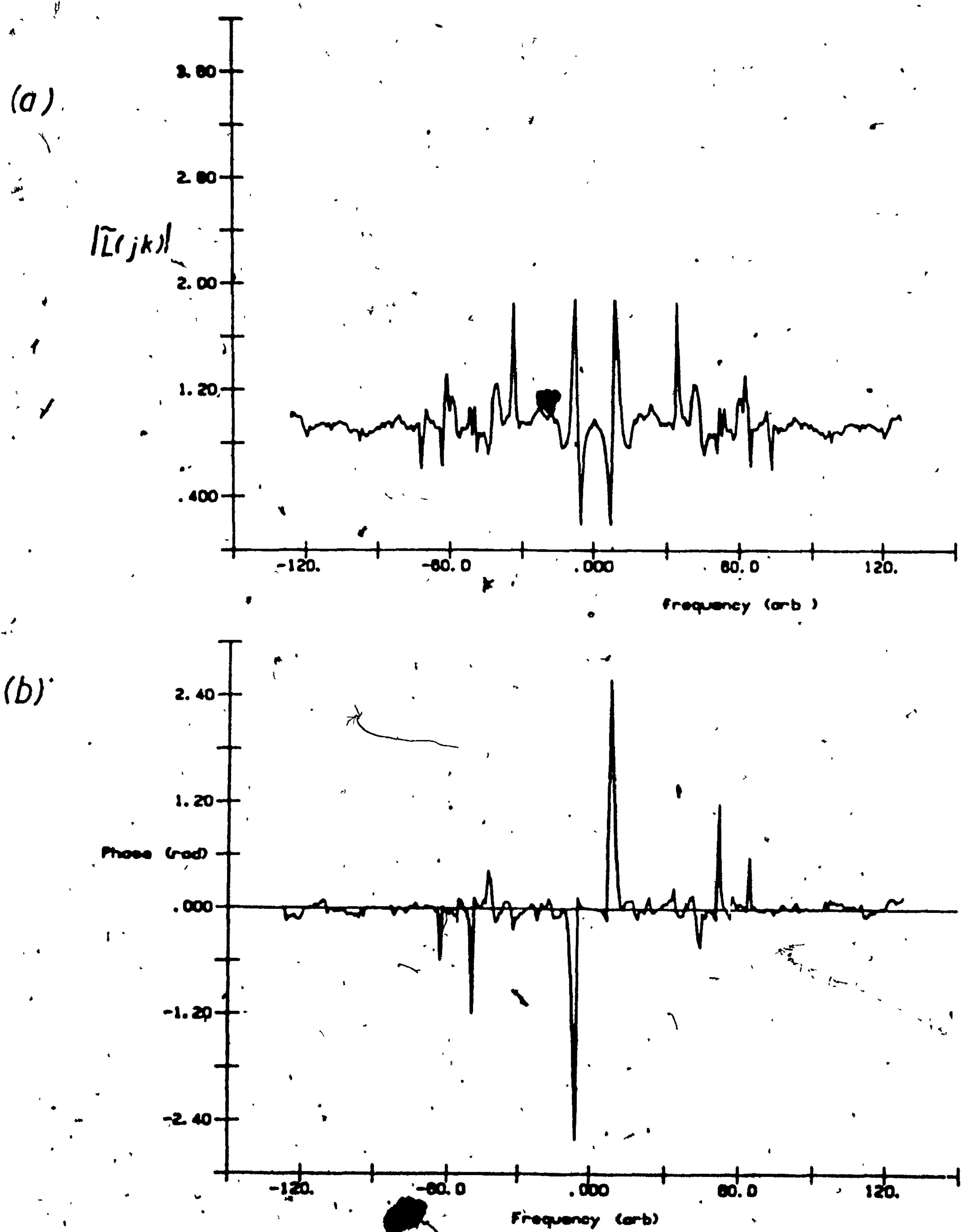

Figure 40: Frequency response function calculated for mode-mismatched thermal lens (a) magnitude signal (b) phase signal. Sample was $CoSO_4(aq)$ with an absorbance of 0.0025/cm. P = 50 mW ; excitation wavelength was 50 mW.

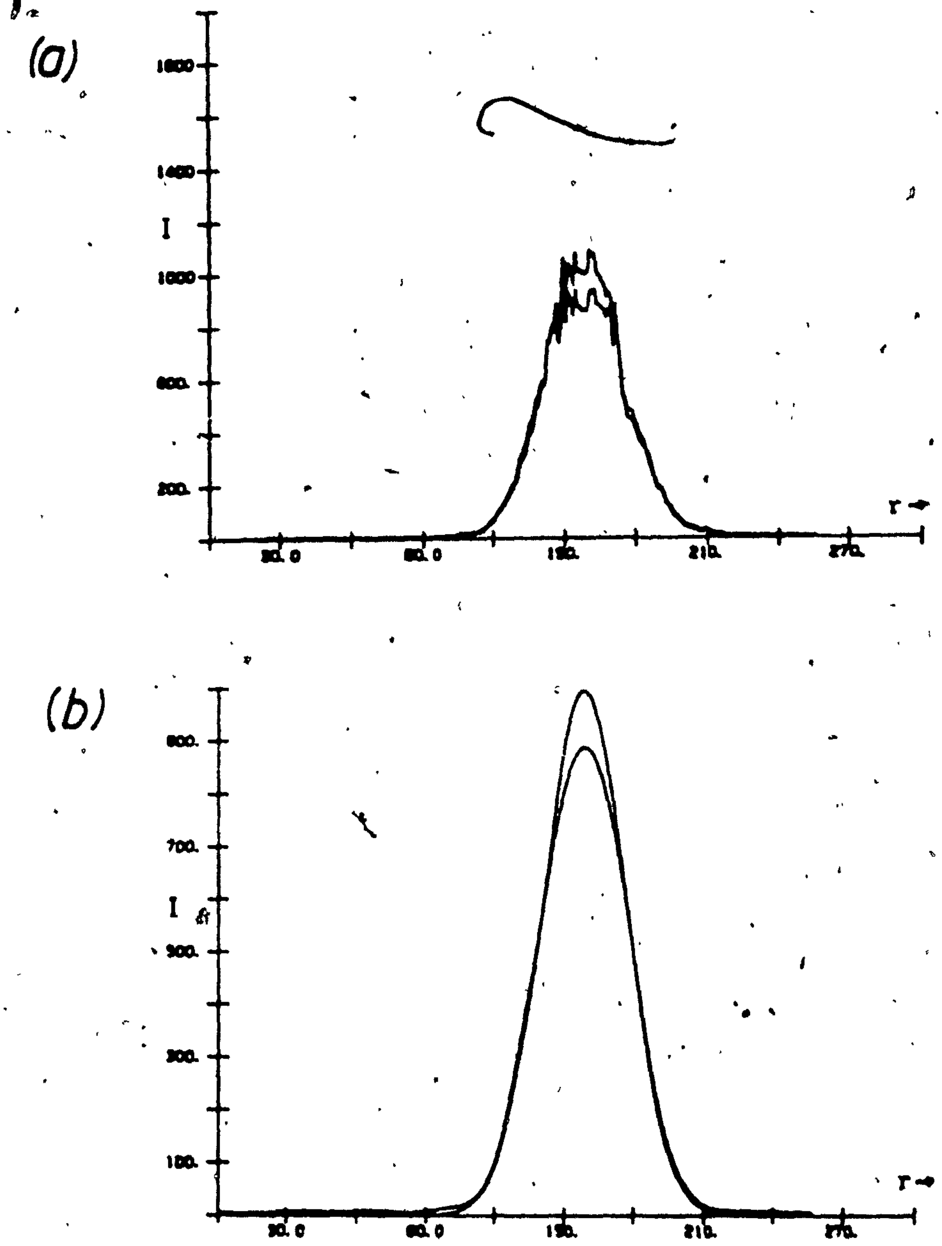

Figure 41: Application of the point spread method (a) unprocessed beam profiles (b) Gaussian signals convoluted with computed point spread. Sample was as per Figure 40.

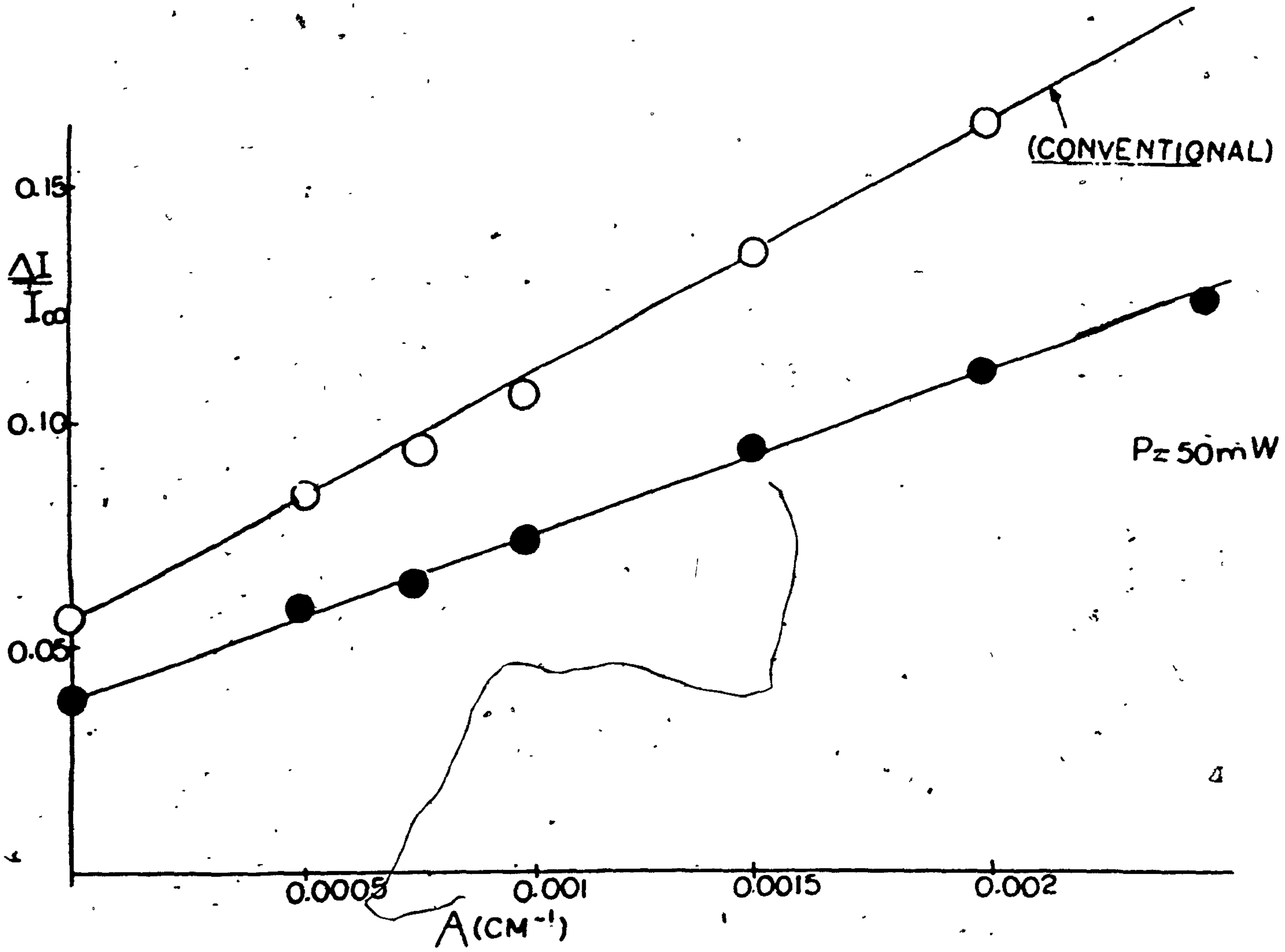

Figure 42: Calibration curves of $\Delta I/I_\infty$ vs absorbance for point spread method and for conventional thermal lens signal. ● = point spread data ; ○ = conventional data. Samples were $CoSO_4$(aq) at 50 mW of excitation power. Pump wavelength was 458 nm.

wide bandwidths. At the widest input bandwidths, the lens response signals approach the sensitivity of the beam center measurement : they never exceed or equal the sensitivity of the single point measurement.

Calibration curves of $\frac{\Delta I}{I_\infty}$ prepared for the lens response method indicated that the signals obtained are analytically useful (Figure 42). No loss of linearity is observed over the conventional $\Delta I / I_\infty$ technique. Stability tests on the helium/neon beam at steady state timescales, when analysed by this method indicate a gain in beam stability by a factor of about 2, so that the detection limit is not affected by the treatment. However, it is felt that the current steady state system does not provide a true test of the method's capabilities because the measurements were made on a timescale which included the effects of thermal fluctuations in the laser system, which can systematically change the frequency spectrum of I_0 relative to I_∞ over the measurement interval. The ideal application of this technique would probably be for transient signal detection assuming that early timescale sources of spatial noise could be eliminated (vibration, electronic interference). Successfully implemented, it could eliminate the requirement for high quality optical components in the spectrometer system, because of its immunity to spatial intereferences.

It should be mentioned as a final word of caution that the method is based on the calculation of an empirical point spread for the lens. Normally, in dealing with point spreads computed for optical systems containing lenses, the coordinates in the system's output plane must be scaled to account for possible effects of magnification by the lens (64). A potential problem with the proceedure carried out in thermal lensing is the possible introduction of new frequencies in the output spectrum that did not exist in the input spectrum. The computed point spread will then contain singularities (due to "division by zero " in the frequency domain). However, for weak thermal lenses and (ironically) for a sufficient bandwidth of spatial noise in the I_0 spectrum the singularity problem may be avoided. An additional assumption is, of course, that the spatial noise spectrum does not change systematically from I_0 to I_∞.

Thermal Lens Detection by Frequency Domain Analysis

An alternative approach to avoiding the "spatial noise" phenomenon present in imaged beam profiles is to use the narrow band detection of a frequency component or components in a regime which avoids the spatial noise. Consider, again, the distorted profiles obtained in mode-mismatched experiments. As the lens develops, discontinuities appear in the I_∞ profile at the edges of the lens element. The presence of these features produces the "hole" observed in the beam center. In the frequency domain, the growth of the features appears to be associated with a sideband component which develops in the (spatial) Fourier transform (magnitude spectrum). This section outlines the basic

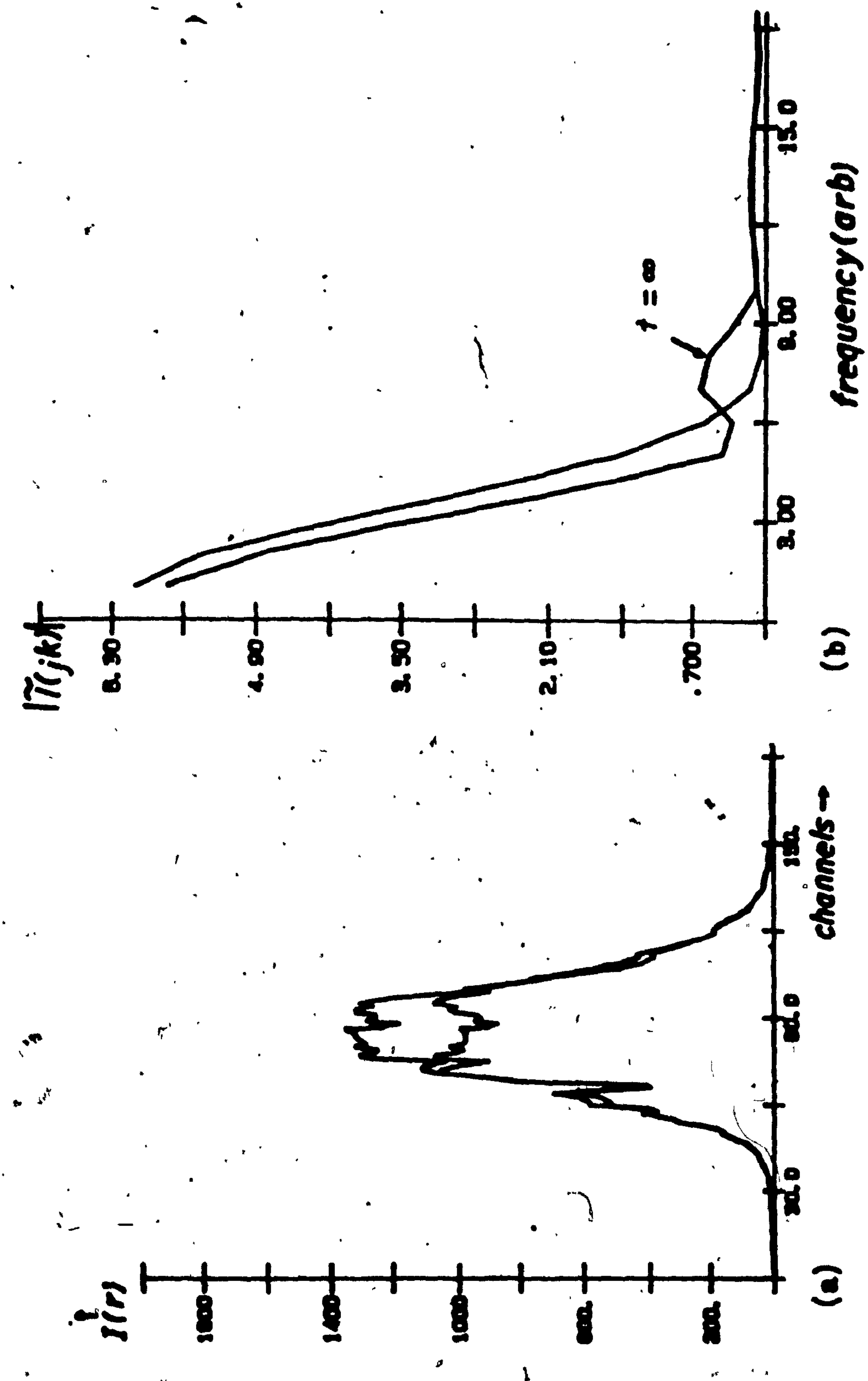

Figure 43: Beam profile of (a) mode-mismatched thermal lens signal and (b) corresponding Fourier spectrum showing sideband components in the frequency domain. Sample was CoSO$_4$(aq) with A = 0.0058/cm ; P = 50 mW.

behavior of the sideband component as the lens develops and examines the suitability of this signal for quantitative analysis.

The truncation of signal waveforms in the frequency domain has the well known consequence of producing "ringing" or damped sinusoidal oscillatory patterns into the time domain signal (102). The truncation of time domain signals, likewise, has the same effect in the freqency domain : the Fourier magnitude spectra of truncated time domain records contain sidebands related to the interval over which the truncation is made. In the case of the mode-mismatched lens signal, the discontinuous behavior of the space domain pattern contains sidebands apparently related to the aperture width ,a, of the thermal lens. The situation is diagrammed in Figure 43, which shows both the lens development and the sideband components of the frequency domain signal. The "frequency" scale of all figures reported in this section is expressed as a set of discrete frequencies:

$$f = m/NT \qquad (4-4)$$

where m = 0,1,2,3,.... N is the number of channels (in this case, N = 256 diodes) and T is the (spatial) sampling interval (T = 1 arbitrarily in this case).

The sideband components of Figure 43 are located in the range N = 6 to N = 10. The reciprocals of these frequencies correspond to the approximate dimensions of the lens aperture (20-30 diodes across).

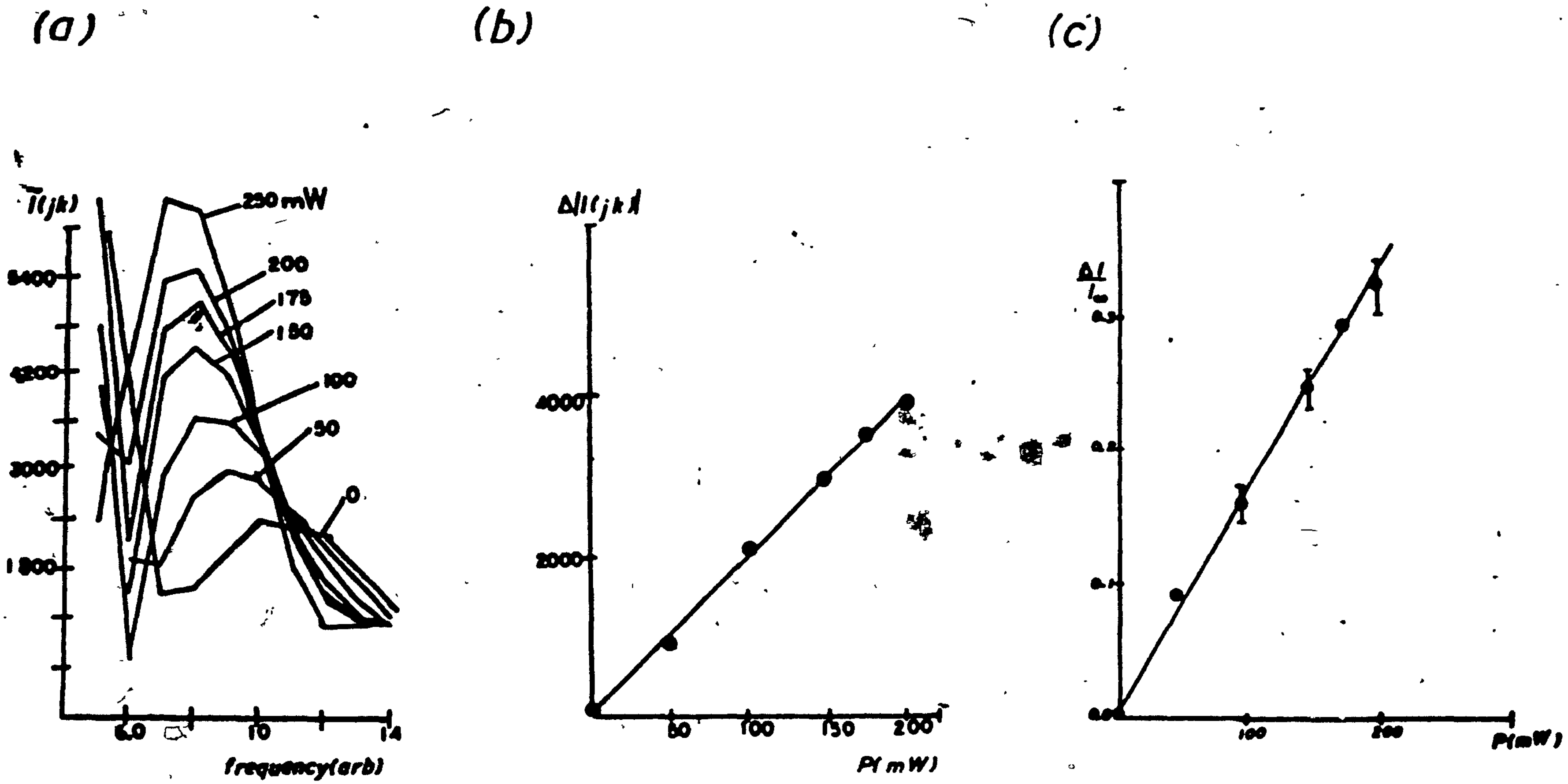

Figure 44: Effect of varying excitation power on the frequency spectrum of a mode-mismatched thermal lens (a) frequency spectra recorded at different beam powers (b) plots of $\Delta\bar{I}(jk)$ vs P for sideband component (c) plots of $\Delta I/I_\infty$ for same experiment. Sample was Armadale fulvic acid with absorbance A = 0.01/cm . Excitation wavelength was 600 nm.

The behavior of the aperture sidebands was next examined with respect to the extent of formation of the lens element. Figure 44 showsa segment of the frequency spectrum of an absorbing solution (Armadale fulvic acid - 5 x 10^{-6} M, A 0.01 cm^{-1}) irradiated at 600 nm. As the irradiation power was increased, a strong sideband developed over the range from f ~ 6 - 10 units. A plot of the sideband with beam power yielded a linear reltionship between the sideband intensity and the beam power (Figure 44). From this plot, the minimum power required to detect the thermal lens effect was found to be 500 microwatts compared with a value of 4.4 mW from a conventional $\Delta I / I_{\infty}$ plot (Figure 44c). This result suggested that the sideband could provide analytically useful signals.

The next step was to determine the dependence of the sideband on the sample absorbance. A set of Fourier transforms of I_{∞} profiles was acquired at a beam power of 100 mW for a set of highly absorbing samples (A = 0.00314 - 0.0251 cm^{-1}) (The absorber in this case was an adduct of formaldehyde and chromotropic acid in 10 % H_2SO_4, contributed by a colleague). The profiles of Figure 45 show the growth of the sideband as a function of increasing sample absorbance. As the lens growth becomes very strong, the sideband center shifts to slightly lower frequency. If the sideband is directly related to the lens aperture, then the shift is explained by the widening of the "hole" in the beam center of Figure 43 at very high power or absorbance. The

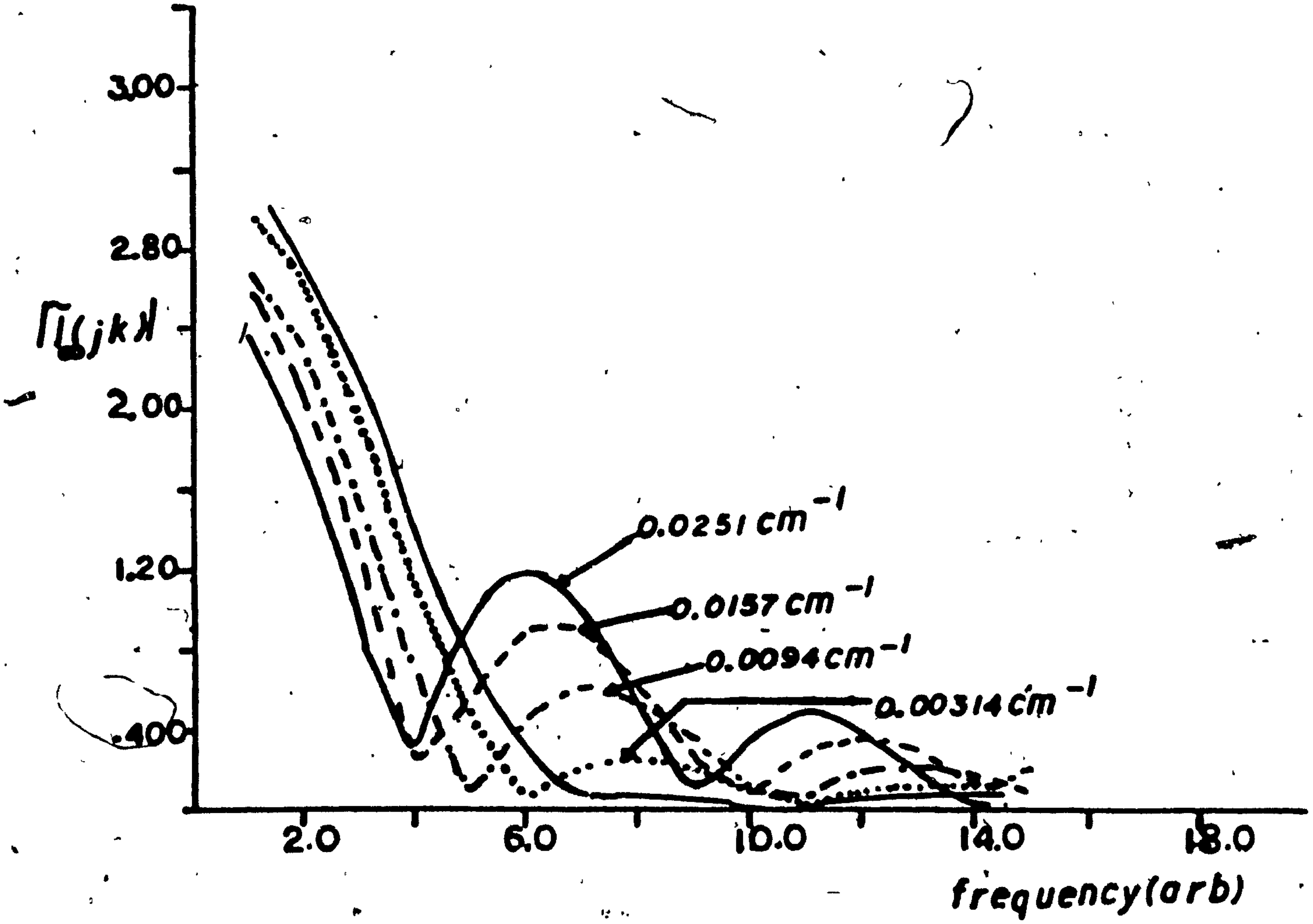

Figure 45: Effect of sample absorbance on frequency spectrum of a mode-mismatched thermal lens signal for a set of highly absorbing standards. P = 60 mW. Excitation wavelength was 600 nm.

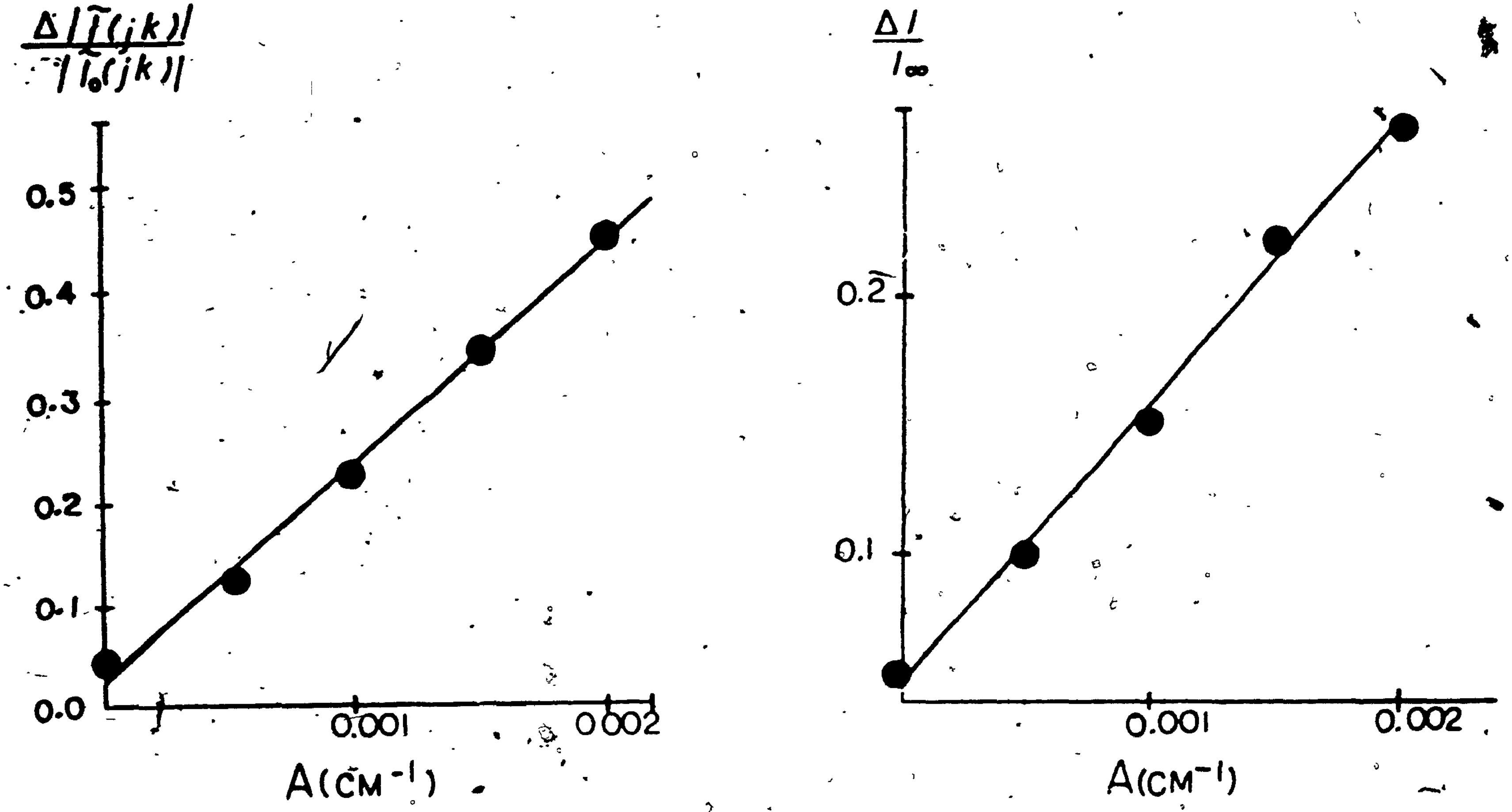

Figure 46: Comparative calibration curves of $\Delta|\tilde{I}(jk)|/|\tilde{I}_0(jk)|$ and $\Delta I/I_\infty$ vs absorbance for weakly absorbing $CoSO_4$(aq) standards. P = 50 mW ; Excitation wavelength was 458 nm.

widening develops because of the widening of the temperature profile $\Delta T(r,t)$, in the sample (Chapter 3). However, for weak thermal lenses, the sideband frequency appears to remain effectively constant.

Two approaches were taken to obtaining an analytical signal. The first was to plot $\Delta \tilde{I}(jk)$ as a function of absorbance or sample concentration. This approach appeared to be successful in the experiment which varied the irradiation power (in that case the probe beam profile is effectively constant in shape and intensity over the duration of the experiment). A better proceedure was to plot the fractional increase in $\tilde{I}(jk)$ as a function of concentration or sample absorbance. Figures 46a and b compare the signals obtained as $\frac{\Delta|\tilde{I}(jk)|}{|\tilde{I}(jk)|}$ and $\frac{\Delta I}{I_\infty}$ vs concentration for a set of $CoSO_4$ standards. The frequency domain technique in Figure 46b increased the thermal lens enhancement by a factor of 2 over the conventional $\frac{\Delta I}{I_\infty}$ method, with good signal linearity.

In general, the technique is very sensitive to the spectrometer alignment. Plots of $\frac{\Delta|\tilde{I}(jk)|}{|\tilde{I}(jk)|}$ will show varying sensitivity with the spatial frequency chosen to carry out the analysis. Figure 47 illustrates a case in point. For a spatial frequency at which $m = 9$ in 4-6, the shape of the calibration curve varied by a factor of 2 over the value obtained at $m = 8$. In some cases, a slightly negative intercept appears in the plots. This may reflect a component of thermal deflection present in the signals due to the off center alignment of the pump and probe beams, as is sometimes

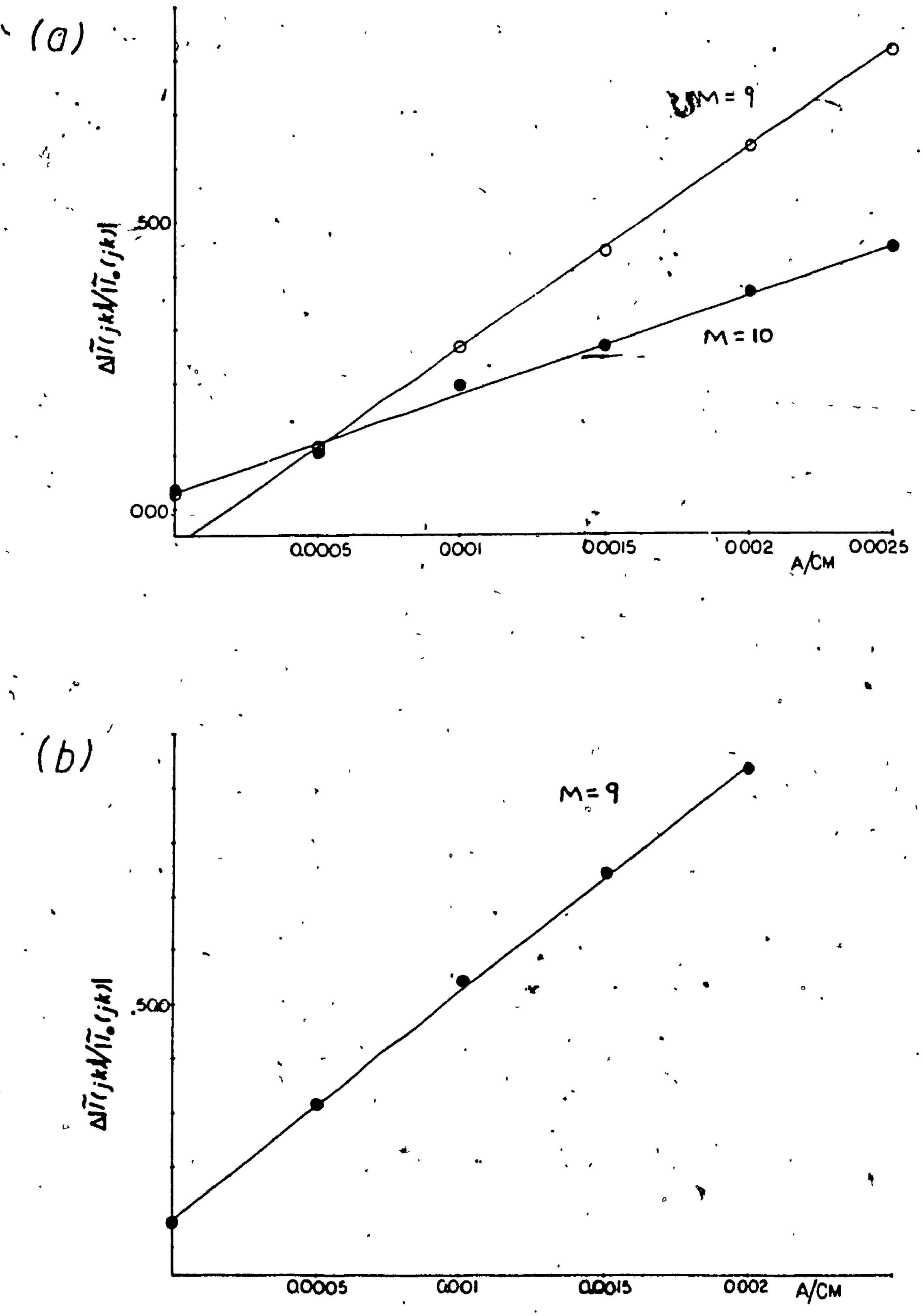

Figure 47: Calibration curves in the frequency domain showing the effect of sideband frequency on sensitivity of the analysis. Samples were $CoSO_4(aq)$. Excitation wavelength was 458 nm. Beam power was 50 mW.

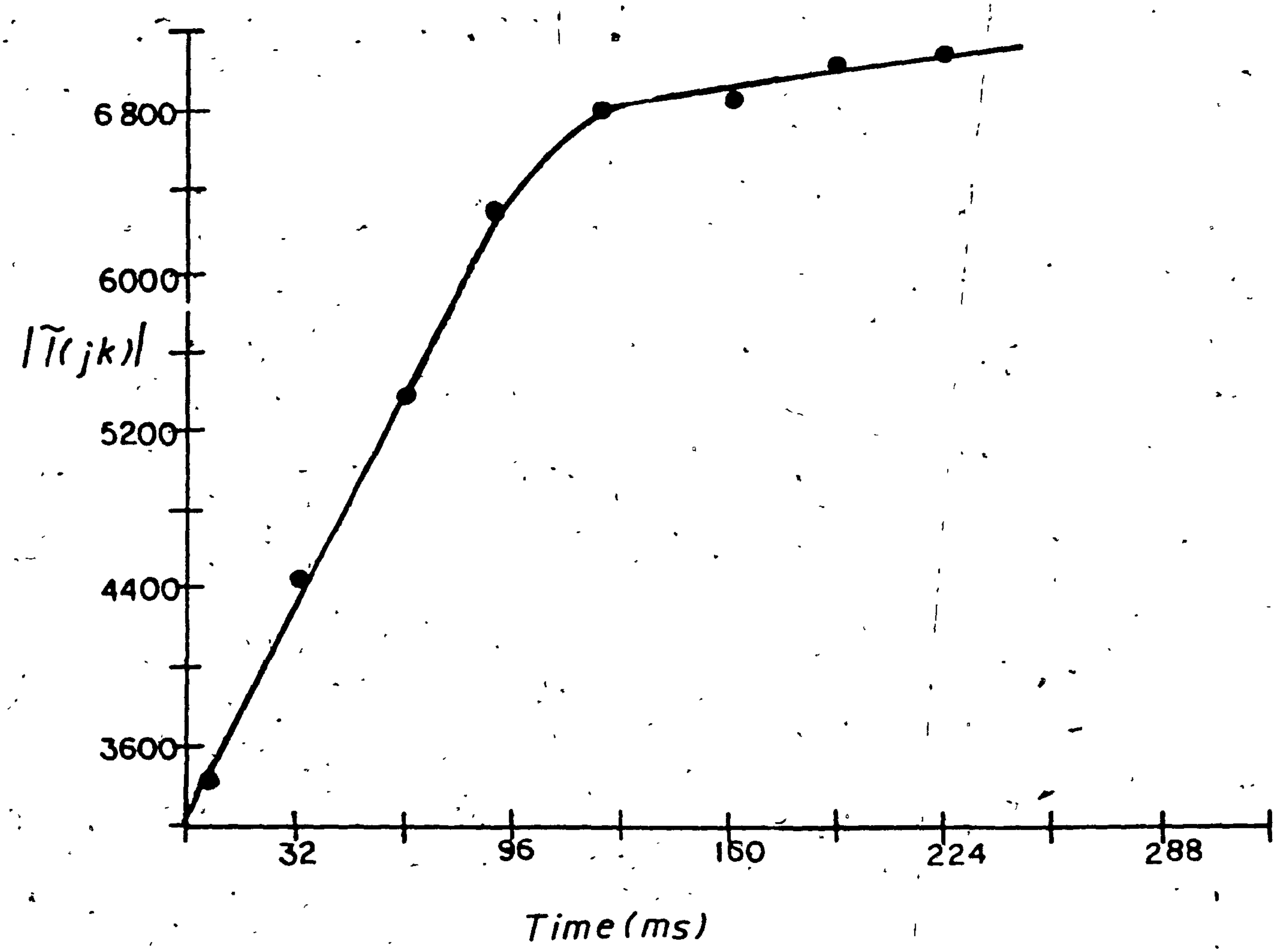

Figure 48: Time growth of sideband signal. Sample was Armadale FA (A = 0.01/cm) excited at 600 nm and a beam power of 100 mW.

observed in dual beam experiments (85).

The noise levels present in the frequency domain signals are variable and depend on the choice of spatial frequency for which the calibration curve is prepared. With favorable alignment, signal to noise enhancement factors as high as 7 have been observed with this technique (Figure 47). As was the case with the lens response measurements of the previous section, the experiments were carried out in a regime where thermal fluctuations in the probe laser, and possibly, convection in the samples, made important contributions to the background noise levels. These experiments, therefore, do not neccessarily constitute a true test of the method's capabilities. It would be of interest to average frequency domain signals on earlier time scales over the formation period of the lens. a time resolved plot of the growth of the sideband component is presented in Figure 48 ,showing achievement of a near steady state after about 100 msec of cell exposure to the heating beam. Signal growth at early times is nearly linear with time as is typical for conventional thermal lenses. The signal, then, appears to posess well behaved properties, which may, perhaps be explained by theory.

The evaluation of the theory of Chapter 3 (equations 3-60 to 3-65) is left to future work (103). However, the results of the present chapter indicate that the frequency domain signal provides a means of measuring weak absorbances with enhanced sensitivity in mode-mismatched thermal lensing.

Chapter 5

Absorbance Measurements on Dissolved Organic Materials at Natural Water Levels

The study and characterisation of the dissolved organic material present in natural water systems is of major importance for the understanding of the complex equilibria taking place in the aquatic environment. In particular, the details of metal ion speciation in natural situations are intimately linked to the character and quantity of organic material available to participate in complexation and redox reactions (1, 21).

Of the major classes of organic materials responsible for controlling metal ion speciation in the environment, the humic substances are known to play a major role in determining the availability of metal ions for uptake by living organisms (1). In part, this control is maintained via the complexing capability of humic substances, which has been shown to arise from the large quantity of salicylate (phenol carboxylate) and phthalate sites available on dissolved humic particles (17,18). Analytical methodologies which enable the measurement of concentrations of dissolved humic substances in water samples are therefore desirable as a means of evaluating the complexing capacity of a given sample for dissolved metal ions.

Measurements of dissolved organic carbon as humic substances are of additional interest in the study of natural water photochemistry. As already discussed in previous chapters, the photochemical activity of a natural water is experimentally relatable to the total concentration of organic carbon in a sample (11,23,104) and, indirectly, to the concentration of humic substances present. Consequently, the profiling of natural levels of organic and/or humic substances may eventually enable the mapping of the photochemical activity of natural water systems.

The problem of studying natural aquatic samples is underlined by the complexity of the chemical equilibria present in the environment and the perturbative nature of most of the analytical methodologies available in this area. As most humic materials are colloidal in nature (21), they may easily undergo such processes as aggregation or coagulation. If transition metals are present at sufficiently high concentration levels, there may be a significant change in the aggregation state of the materials (4). The presence in the sample of silica or suspended clay minerals may cause adsorption of the organic material on the surface of the sediments. Furthermore, some of these processes may be concentration dependent so that an apparently minor modification of the sample could strongly perturb the equilibria existing under natural conditions. Consequently, what are desired, ideally, in the study of these samples are nondestructive analytical techniques which require a minimum pretreatment of the samples prior to analysis, and which exhibit high sensitivity for dissolved organic materials.

The currently existing methodologies for measuring dissolved organic carbon and/or humic substance concentrations consist, classically of (a) destructive methods based on combustion of the sample followed by IR detection of evolved CO_2 and (b) optical methods such as UV absorption or fluorescence spectrometry, which indirectly evaluate dissolved organic carbon in terms of concentrations of humic substances (21). The combustion methods, which are destructive in character, provide an unambiguous measure of the integrated organic carbon content of the sample. They suffer limitations, however, including susceptibility to contamination by organic matter present in the laboratory environment. Optical techniques, on the other hand, offer some qualitative information on the character of the sample at the expense of ambiguity in the dissolved organic carbon (DOC) measurement. The primary disadvantage of conventional optical techniques is that they rely on the measurement of light transmitted from the sample, which makes them highly susceptible to interference from light scatttering from particulates suspended in the sample. Filtration of the sample prior to analysis is a requirement of these techniques. In some instances some of the humic particles themselves may contribute to the scattering matrix. In those cases, filtration would directly remove a fraction of the organic material under study.

Finally, a disadvantage of absorption spectrophotometry in particular, is its low sensitivity in the visible. The measurement of E4/E6 ratios, which has provided structural information on the humic fractions isolated from soils (105), has found no application in natural water studies for this reason (21).

The experiments reported in this chapter, had as their objective, the solution to problems encountered in the conventional optical analysis of natural samples, by laser thermal lensing. The approach of these experiments has been first to investigate the sensitivity of thermal lens signals to light scattering and the sensitivity obtainable with detection by this technique. In addition, thermal lensing has been evaluated for the measurement of the fluorescence yields of dissolved humic substances. The objective in this second case has been the evaluation of the thermal lens technique as an alternative means of obtaining fluorescence information on natural samples. This work has used Armadale fulvic acid as a model substance for environmental humic materials. A third direction of these photothermal experiments has been to demonstrate the use of thermal lensing as a means of measuring and interpreting E4/E6 ratios for a series of aquatic humic materials from different natural sources, thereby obtaining information of photophysical and structural interest on environmental samples.

Experimental Section

Materials and Methods

Natural organic carbon samples were generously contributed by Dr. J. Carey of the Canada Center for Inland Waters, Burlington, Ontario. The samples had been prepared as follows: natural waters from a series of locations in Southern Ontario were filtered through 0.7 micron glass fiber microfilters and pumped at 50 ml/min through a column of XAD-2 macroreticular resin. The columns were eluted with 0.1N NH_4OH in MeOH. Filtrates were collected and evaporated to dryness. The freeze dried samples were characterised by elemental analysis (Guelph Analytical Laboratories) with the results reported in Table 12.

Armadale fulvic acid was used as received from P. Aysola, Concordia University. The sample extraction proceedure has been described elsewhere in detail (4,17).

Concentrated stock solutions of the humic materials were prepared on a weekly basis at 100 - 400 mg/l. The samples were stored in the dark at pH 2-4. Preliminary tests have shown the absorbance of humic materials to be stable over several weeks (4). Dilute solutions for analysis by thermal lensing were prepared on a daily basis, immediately prior to analysis. All samples were protected from exposure to light.

Measurements of sample pH were carried out using a meter constructed by Concordia University Science Technical Services. The meter was calibrated using Fisher and Canlab

Standard Buffer Solutions. Adjustment of the sample pH was made by addition of 0.1 N KOH or HCl (reagent grade) or where indicated, in early experiments on light scattering, by addition of standard buffer solutions.

The solvent used was Nanopure H_2O (conductivity 18 MΩ-cm) for quantum yield experiments and E4/E6 measurements. Some early quantum yield measurements used double-deionized water as the solvent. Light scattering experiments used glass distilled H_2O as the solvent.

$CoSO_4$ was used as an absorbance standard at 458 nm. $CoSO_4 \cdot 7H_2O$ of unknown purity was recrystallised several times from hot water and EtOH. Its visible spectrum in 1 % H_2SO_4 (double distilled) showed good agreement with spectra obtained from the National Bureau of Standards. Anhydrous $CuSO_4$ (Baker reagent) was recrystallised from hot water. Spectra in 1 % H_2SO_4 also showed good agreement with NBS data (106).

Stock solutions of the transmission standards were prepared with absorbances of 0.1 cm^{-1}, as measured by visible spectrophotometry. Standards for thermal lensing of known absorbance were prepared by dilution of the stock.

SiO_2 for light scattering experiments, was obtained as sea sand. The sand was pre-washed in dilute chromic acid and thoroughly rinsed in distilled water. It was dried and ground to a fine powder in a mortar and pestle. 1-2 mg samples of SiO_2 were weighed out and added to 10 or 25 ml samples of dissolved fulvic acid. The sample pH was 5 - 7.

Procedures for cleaning glassware in these experiments involved soaking all glassware overnight in Decon decontaminant (BDH chemical) followed by thorough rinsing in double deionised water. Detergent traces were removed by a final rinse with 6M HNO_3 followed by double deionised water.

Apparatus

Visible absorption spectra of all samples were recorded on Perkin Elmer 552 UV-Visible spectrophotometer in a 1 cm glass cell. Fluorescence spectra were recorded on a Perkin-Elmer 1450B Spectrofluorimeter in a 1 cm quartz cell.

The thermal lens instrument used in these experiments has been descibed in detail in Chapter 4. The excitation source was a Coherent CR6 Supergraphite Ion laser equipped with a dye laser head (Coherent CR - 590) and operated using Rhodamine 6G. The excitation wavelengths were 458 nm for fluorescence quantum yield determinations, 458/600 nm for E4/E6 measurements, and 488 nm for early experiments involving light scattering. The light scattering experiments also used "all line " Argon ion excitation, consisting chiefly of 488 nm emission. The spectrometer was operated mainly in the mode-mismatched configuration although early experiments on light scattering used mode-matched alignment, and the earlier version of the spectrometer (LTL I).

For quantum yield and E4/E6 measurements, the spectrometer was calibrated using aqueous solutions of the absorbance standards $CoSO_4$ or $CuSO_4$. (The range of absorbances of the standards was 0.0005 - 0.002 cm^{-1}). Calibration curves of the thermal lens response vs absorbance were linear (R = 0.999) at both wavelengths over this range of absorbance. The spectrometer was aligned and calibrated on a daily basis. Thermal lens responses for the humic substance samples were directly converted to absorbance units from the calibration data.

Attempted Measurements of the Fluorescence Quantum Yield of a Humic Substance by Steady State Thermal Lensing Spectrometry

Dissolved humic substances have been studied for their fluorescence properties (4,8,22,49,107). Fluorescence intensities among samples of differing origin are of interest because they may be correlated generally with the content of oxygen bearing functional groups (107) and potentially to the photochemical activity of different water samples (24). In practice, the conventional measurement of absolute fluorescence intensities of these materials involves careful calibration proceedures to account for Rayleigh and Tyndall scattering in the samples, and variation in the response of instrumentation (22).

Photothermal spectroscopy presents an interesting potential alternative to spectrofluorimetry. In particular, thermal lensing is of interest because it is readily adaptable to the direct measurement of integrated luminescence quantum yields (108). Quantum yields are evaluated by comparing the intensity of the photothermal signals observed in the presence of a fluorescing sample to that of a non-luminescent standard. The simplest case is to consider that the sample and reference standard are matched with respect to absorbance at a given excitation power and wavelength. In the case of the standard, all of the absorbed excitation energy is converted to heat by non-radiative processes. Fluorescence processes occuring in the sample essentially subtract from this maximum thermal yield that would be observed. The photothermal signal observed from the sample, therefore is diminished relative to the standard substance, and is directly relatable to the yield of fluorescence.

Theoretical Section

The theory and measurement of quantum yields by thermal lensing was first reported by Brannon and Magde (108). In this section, their theory is summarised and extended to measurements obtained in steady state experiments.

It is possible to write an energy balance for the absorption processes occurring in a fluorescing sample excited in a laser thermal lens experiment :

$$P_l = P_{th} + P_f + P_t \qquad (5\text{-}1)$$

that is, the power of the excitation (laser) beam is equal to the sum of the power transmitted by the sample, P_t, the power emitted as fluorescence, P_f, and the power degraded to heat, P_{th}. Scattering for this case is assumed to be negligible.

The quantum yield for fluorescence is written, by definition :

$$\varphi_f = \frac{P_f}{P_f + P_{th}} \cdot \frac{\nu_l}{\langle \nu_f \rangle} \qquad (5\text{-}2)$$

where $\langle \nu_f \rangle$ is the mean emission frequency of the sample fluorescence and ν_l is the laser excitation frequency. The ratio of frequencies $\frac{\nu_l}{\langle \nu_f \rangle}$ accounts for the emission

Stoke shift.

From the definitions of transmittance and (fractional) absorption (109) :

$$T = \frac{P_t}{P_l} \; ; \; \alpha = 1 - T \qquad (5\text{-}3)$$

one directly arrives at the relation:

$$P_f = \alpha P_l - P_{th}$$

Substitution of this result into equation (5-1) yields :

$$\varphi_f = \frac{\nu_l}{\langle \nu_f \rangle} \cdot \left(1 - \frac{P_{th}}{\alpha P_l} \right)$$

In the discussion that follows, we make the experimentally warranted assumption that the samples studies are optically dilute. From the definitions of absorbance, transmittance and absorption (105) :

$$T = \frac{P_t}{P_0} = e^{-2.303A} \qquad (5\text{-}6)$$

but since

$$\alpha = 1 - T = 1 - e^{-2.303A} \qquad (5\text{-}6a)$$

then for small α: $\alpha \sim 2.303A$

This assumption is made in the remainder of this development.

A comparison method of measurement may be set up which inherently compares the yield of fluorescence of the sample, φ_f, to the thermal yield of a standard. The thermal yield is defined as :

$$\varphi = \frac{P_{th}^{r}}{AP_{l}^{r}} \equiv 1 \qquad (5\text{-}7)$$

For the non-fluorescent standard, $\varphi_{th} \equiv 1$, because all of the absorbed photons are dissipated as heat to the medium. Consequently, dividing (5-7) by (5-5) gives :

$$\varphi_{f} = \frac{\nu_{l}}{\langle\nu_{f}\rangle} \cdot \left[1 - \frac{A^{r}P^{r}P_{th}^{s}}{A^{s}P^{s}P_{th}^{r}} \right] \qquad (5\text{-}8)$$

where the superscripts S and R refer to the fluorescent sample and non-luminescent standard, respectively.

The application of equation (5-8) to experimental conditions is the point of departure of this work from that of Brannon and Magde (107). In their experiments, sample excitation and detection was carried out in a transient mode. In this work, the quantum yield measurement was adapted to the steady-state thermal lens technique.

Equation (5-8) is simplified if thermal lens signals are measured for absorbance matched conditions with constant beam power and excitation wavelength. In that case :

$$\varphi_{f} = \frac{\nu_{l}}{\langle\nu_{f}\rangle} \left[1 - \frac{P_{th}^{s}}{P_{th}^{r}} \right] \qquad (5\text{-}9)$$

The expressions relating P_{th} to thermal lens responses are directly obtainable from the thermal lens response equation (Chapter 3, equations 3-48 to 3-49) at steady state. Assuming very dilute solutions, the thermal lens response is linear in absorbed power :

$$\frac{\Delta I}{I_\infty} = -\frac{(dn/dT)P_{th}}{\lambda_l K} \qquad (5\text{-}10)$$

If all of the absorbed radiation is converted to heat in (5-10) then $P_{th} = 2.303 P_l A$ (for small A). For the fluorescent sample, however :

$$P_{th} = 2.303 A P_l - P_f \qquad (5\text{-}11)$$

For optically dilute samples, the power loss due to fluorescence is linear in P_l :

$$P_f = 2.303 F A P_l \qquad (5\text{-}12)$$

where F is the fractional loss in the beam power due to fluorescence.

The F factor may be interpreted as :

$$F = \frac{\langle v_f \rangle}{v_l} \cdot \varphi_f \qquad (5\text{-}13)$$

that is, F, the loss in the beam power due to fluorescence is due to the yield of fluorescence photons, multiplied by the fractional loss in power due to energy loss (via the mean emission Stoke shift).

The thermal lens signal at steady state in the presence of fluorescence may thus be obtained from equations 5-10 and 5-11 as :

$$\frac{\Delta I}{I_\infty} = -\frac{2303 (dn/dT) P_l (1 - F) A}{\lambda_l K} \qquad (5\text{-}14)$$

Equations 5-10 and 5-14 indicate that φ_f may be evaluated experimentally from a comparison of the slopes of the calibration curves obtained in a steady state LTL experiment. For the sample and reference compounds, the slopes are :

$$m^s = -\frac{2.303(dn/dT)P_1(1-F)}{\lambda_1 K} \qquad (5\text{-}15)$$

$$m^r = -\frac{2.303(dn/dT)P_1}{\lambda_1 K} \qquad (5\text{-}16)$$

so that

$$\varphi_f = \frac{\nu_f}{\langle\nu_f\rangle}\left[1 - \frac{m^s}{m^r}\right] \qquad (5\text{-}17)$$

Equation 5-16 applies subject to the assumption that the samples were run in the same solvent with the same excitation power and wavelength, and under the same excitation/detection geometries. These conditions are easily met experimentally.

The thermal lens technique has been applied in this work to the measurement of an integrated fluorescence yield for Armadale fulvic acid - the well characterised humic substance standard.

The thermal lens method is interesting from two points of view. Armadale fulvic is known to yield steady state fluorescence for excitation in 3 ranges of wavelength: (a) in the near UV (340 - 370 nm) ; (b) in the quartz region. The emission observed at 460-480 nm and is characteristic of humic substances as a class. (c) at 450-470 nm with emission at approximately 520 nm. This second emission is considerally weaker than the 460-480 nm fluorescence .In this work both thermal lensing and conventional fluorimetry have been implemented in assessing the quantum yields of the material. With excitation at 458 nm , the use of the thermal lens technique has permitted the measurement of a component of resonance fluorescence (of the 460-480 nm emission), which is inaccessible with conventional techniques .

Results

The method adopted in the measurement of φ_f for Armadale fulvic acid was based on equation 6-16 . The thermal lens spectrometer was calibrated using standard $CoSO_4(aq)$ solutions of known absorbance. m^r was obtained from the plots of $\frac{\Delta I}{I_\infty}$ vs absorbance at 458 nm . Samples of Armadale fulvic acid (AFA) were next evaluated and a second plot of $\frac{\Delta I}{I_\infty}$ vs absorbance was prepared, the slope of the second calibration curve yielding m^s. The mean emission wavelength for AFA was taken to be 480 nm . φ_f was then directly determined from equation 5-16 . The results are reported in Table 11 .

Plots of typical experimental calibration curves are shown in Figures 49-50. The data of Figure 49a were recorded at low power (P=5-6 mW) while data of Figure 49b were recorded at 50-60 mW, and reduced FA concentrations. In the case of the low power experiments , the absorbances of all the samples run were verified directly by spectrophotometry . The lower concentration experiments required the assumption of calculated values for sample absorbances (based on

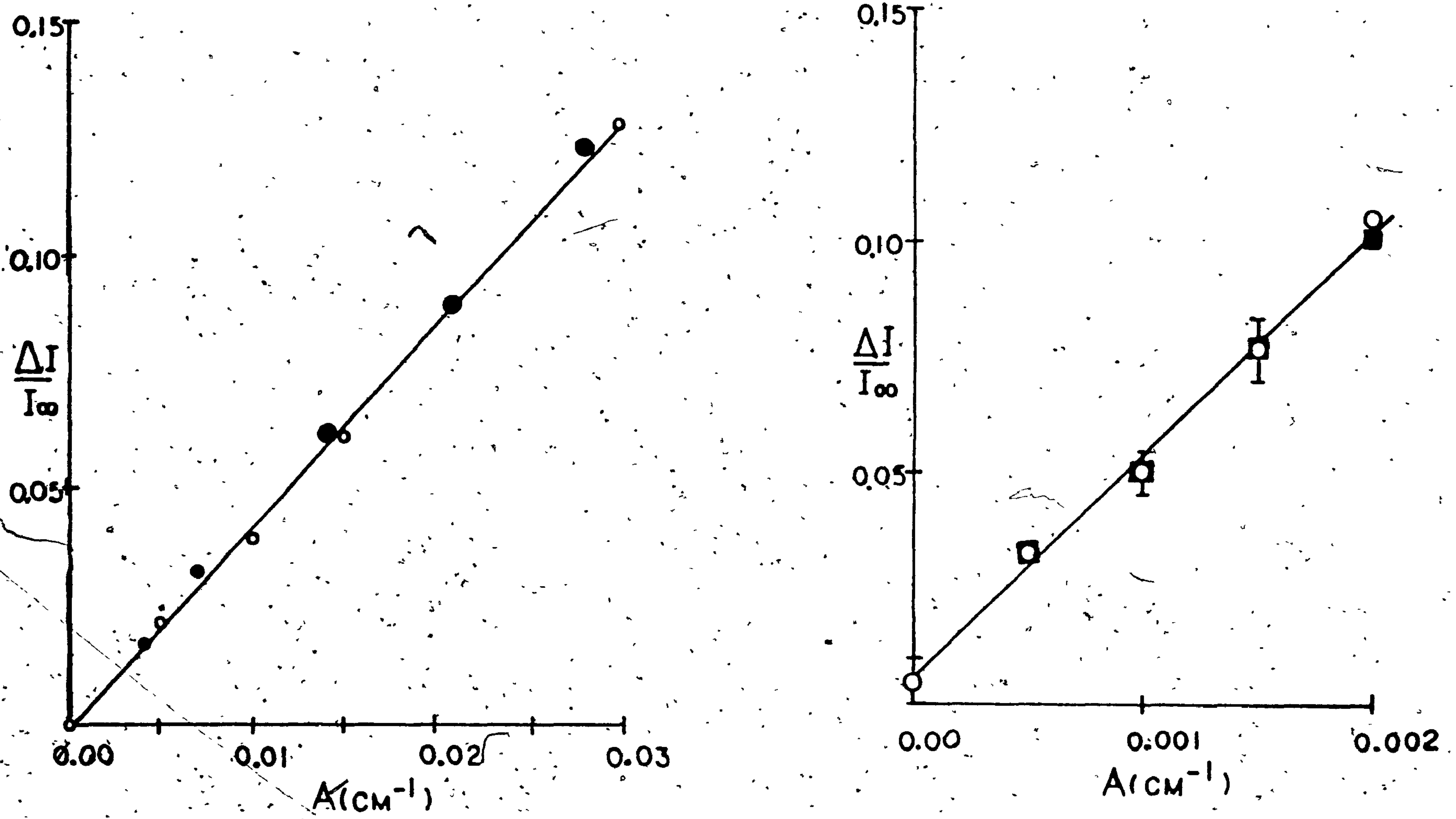

Figure 49 : (a) Quantum yield data for FA at pH 7 and 7 mW of laser power . λ_{ex} = 458 nm ; ● = $CoSO_4$(aq); ○ = FA (pH 7) (b) Quantum yield data for FA at pH 7 and 60 mW of laser power . λ_{ex} = 458 nm ; ○ = $CoSO_4$(aq) ; ■ = FA (pH 7)

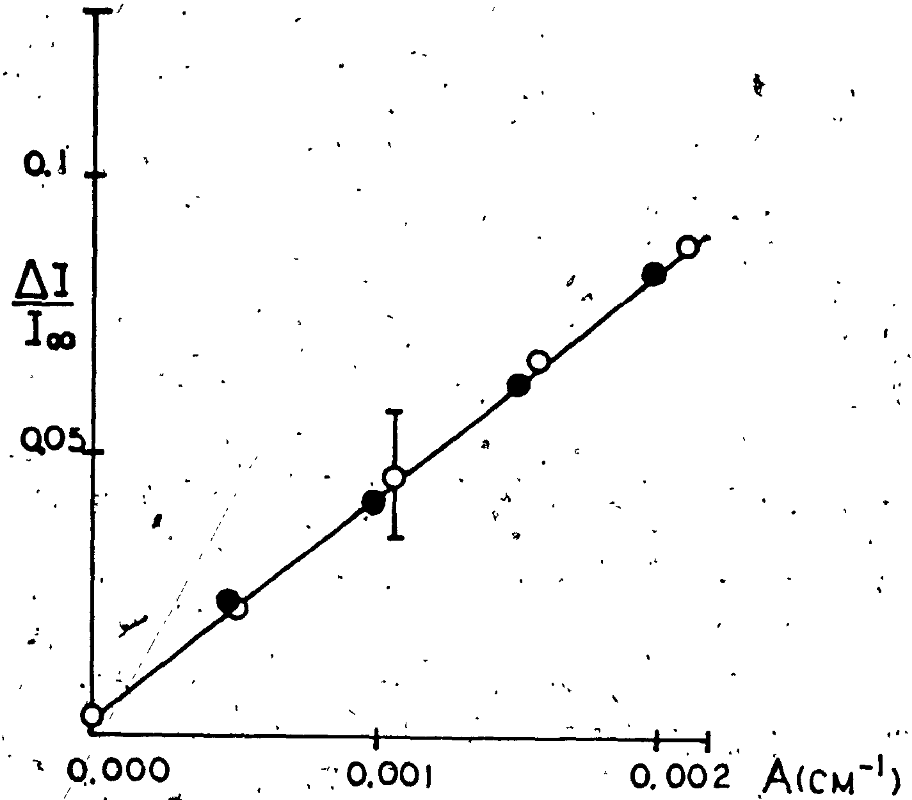

Figure 50 : Quantum yield data for FA at pH 2 and 60 mW of laser power : λ ex = 458 nm ; ● = CoSO4(aq) ; ○ = FA (pH 2)

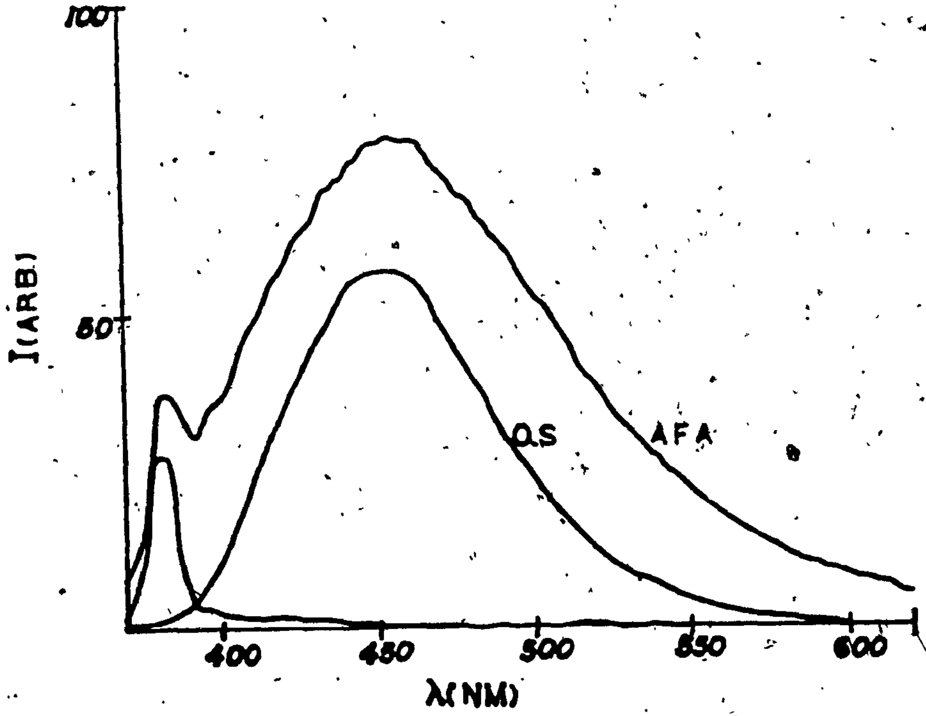

Figure 51 : Fluorescence spectra of absorbance matched samples of quinine sulfate (1 x 10^{-5} M in H_2SO_4, 0.1 N) and FA (10 ppm; pH 2.6) excited at 350 nm . The gain factor is 0.1 for QS and 30 for FA .

Table 11

Quantum Yield Data

pH	A range	φ_f	P(mW)
2.0	0 -.002	0.00 ± 0.014	50
7.0	0 -.002	- .01 ± 0.03	60
7.0	0 - .03		7

measured absorptivities of concentrated (100 mg/l) stock solutions). Both sets of measurements yielded equivalent results. The data in Figures 49 and 50 ,and Table 11 clearly indicate that the yield of fluorescence is less than the instrumental error (1-2 %) . Essentially no difference is observable between the slopes of the calibration curves reported.

These data were considered surprising in view of the ubiquitous nature of humic substance fluorescence in natural waters (22).

A number of checks were made on potential error sources in the experiment . Contaminations by metal ions (bound to the AFA) are a common cause of the strong quenching of humic substance fluorescence, was first considered. This possibility was investigated by changing the quality of the solvent (from double deionised to Nanopure H_2O with an ionic conductivity of 13 M Ω-cm) . No difference was observed with the change of solvent. Elevating the FA concentration and running samples in Nanopure H_2O made no change nor did maintenance of low pH conditions which minimise metal ion binding (at the cost of a relatively small acid quenching effect (4) (Figure 50).

An another error source considered was sample absorbance. Stock solutions of fulvic acid were checked routinely for their stability with respect to absorbance properties and showed no effective variation over the storage period. For dilute (thermal lens) samples , the pH was adjusted several hours before running the experiment in some runs and immediately prior to analysis in others. No difference was observed between these two preparation proceedures. Nor could any effect be traced to absorption errors from bulk light scattering - samples filtered through 0.45 um membranes and absorbance matched to $CoSO_4$ showed no enhanced or diminished thermal lens effect relative to $Co^{2+}(aq)$.

Instrumental factors were carefully monitored in the course of each experiment. Adequate warmup time (30 min) was ensured for the laser systems . Excitation power was monitored for each sample using a Coherent model 210 power meter. Samples were run in a staggered order to minimize the biasing effects of any instrumental drifts . In all cases , the calibration curves were linear (R= 0.999) with an instrumental error of 0.001-2 units of $\frac{\Delta I}{I_\infty}$.

Photochemical reactions occurring in the irradiated sample were considered as a possible explanation for the low luminescence yield. No evidence for cumulative photodecomposition of the sample was observed. Increases or decreases in the thermal lens signals over time within a single sample would have been required in order to explain the results: no evidence of this behavior was observed. Furthermore, a tenfold reduction in excitation power, accompanied by an equivalent increase in FA concentration would have been sufficient to at least partially offset any effect. None were observed , as can be seen from the results of Figure 49.

It is clear that the results otained in these experiments point to a low fluorescence yield for Armadale fulvic acid , at least for the emission excited at 458nm .

In order to confirm ~~this~~ finding and to determine an upper limit for the range of fluorescence yields, a conventional φ_f measurement was evaluated for the major FA emission excited at 355 nm. The measurement was carried out on a conventional spectrofluorimeter, calibrated with 1 x 10^{-5} M quinine sulfate in 0.1N H_2SO_4(100). Measurements of the fluorescence emitted from a absorbance matched AFA solution (10 ppm , pH 2.6) under identical optical geometry and conditions indicated that the emission intensity was over two orders of magnitude less than the quinine sulfate standard (Figure 51) . Since both solutions fluoresced within the linear range of intensity vs concentration, the measurement confirms that the quantum yield for the strongest fluorescence process in aqueous solution is less than 0.01. This is not inconsistent with the results obtained photothermally at 458 nm .

In conclusion , it appears that the low fluorescence yields of humic substances (insofar as they resemble Armadale fulvic acid) make photothermal techniques inapplicable to the measurement of the fluorescence of natural water samples. The measurement limitation on the LTL technique is set by the instrumental precision (1% in the case of the present instrumentation). Fluorimetry on the one hand is readily capable of detecting very low levels of emission because the measurements essentially based on signal intensities relative to a zero background. Thermal lensing on the other hand relies on the measurement of a difference in two relatively strong responses.

Consequently, it appears that the main contribution of thermal lensing to natural water analysis, will lie in the area of weak absorption measurements. The very low emission yields of humic materials prevent the direct measurement of fluorescence by photothermal comparison techniques.

Photothermal Measurement of Weakly Absorbing Natural Materials in the Prescence of Light Scattering

In the analysis of the dissolved organic material contained in natural water samples, a primary barrier to direct optical measurement has been the problem of light scattering. The problem arises from several distinct sources (1, 4) including : (a) scattering from large particles (> 0.46 um) (b) inorganic colloidal particles and (c) colloidal organic materials. These scattering materials present an operational interference in absorption spectrophotometry because of the reliance of these methods on the direct measurement of light intensities transmitted from the sample. Because removal of the scatters may cause a displacement of the sample equilibrium relative to environmental conditions, a method requiring minimum perturbation of the sample relative to the natural state is desirable. Such a method would be insensitive to scattering produced by particulates and yet highly sensitive to the organic material of interest.

These requirements are met in principle by photothermal spectroscopy, which is capable of yielding absorbance measurements without explicitly relying on measurement of the attenuation of a light beam transmitted by the sample. Thermal lensing spectrometry, in particular, is attractive as an analytical technique because of its high sensitivity and relative experimental simplicity (83). Enhancement factors of 10-100 times the sensitivity of conventional methods are readily achievable (83) in water, which has relatively poor thermooptic properties. The instrumentation involved is easily calibrated to yield signal intensities directly in terms of absorbance. Thermal lensing has the additional advantage of being potentially insensitive to light scattering. This advantage of the method arises from the fact that signal measurement relies on thermally induced refractive index gradients in the sample. These gradients arise from the deposition of heat in the sample by non-radiative decay processes following light absorption. Extraneous light scattering yields no contribution to the thermal yield and consequently, no signal interference.

Thermal lens absorption measurements will be insensitive to scattering insofar as light scattering does not appreciably diminish the power level of the excitation beam forming the thermal lens. This situation is described in steady state experiments by the thermal lens response :

$$\frac{\Delta I}{I_\infty} = - \frac{(dn/dT)P_{th}}{\lambda_1 K}$$

where P_{th} is the power degraded to heat in the sample.

The full expression for P_{th} is given by Whinnery (84)

$$P_{th} = \frac{P_1 \alpha}{\alpha + \alpha_s}\left(1 - e^{-(\alpha + \alpha_s)l}\right) \qquad (5\text{–}18)$$

where α and α_s are the extinction coefficients for absorption and scattering processes, respectively.

For optically thin samples in the absence of scattering, P_{th} = 2.303PA (where P is the laser power. see approximations made in the previous section - equation 5-6). At sufficiently high levels of scattering, however, the attenuation of the excitation beam occurs with a corresponding loss in thermal lens sensitivity. Equation 5-17 then describes the situation.

The experiments reported in this section had as their objective, the examination of this issue. The experimental approach adopted was to record calibration curves of instrument response vs concentration for a dissolved humic substance in the presence and absence of large quantities of light scattering material. The resulting data were examined for linearity of the thermal lens response, detection limit, and uniformity of response for humic material in the presence and absence of scattering.

A set of early results is reported in Figure 52. These were obtained on the LTL I spectrometer with mode-matched optical alignment. In general, high excitation power was required to maintain reasonable signal enhancement factors (E = 10-20), a requirement which was eventually satisfied by adopting the mode-mismatched detection geometry (Chapter 4).

Initial results yielded analytically useful calibration curves of $\frac{\Delta I}{I_\infty}$ vs absorbance over the range of calculated absorbances from 0-5 x 10^{-3} cm^{-1}, for Armadale fulvic acid (AFA) in the absence of light scattering. These values

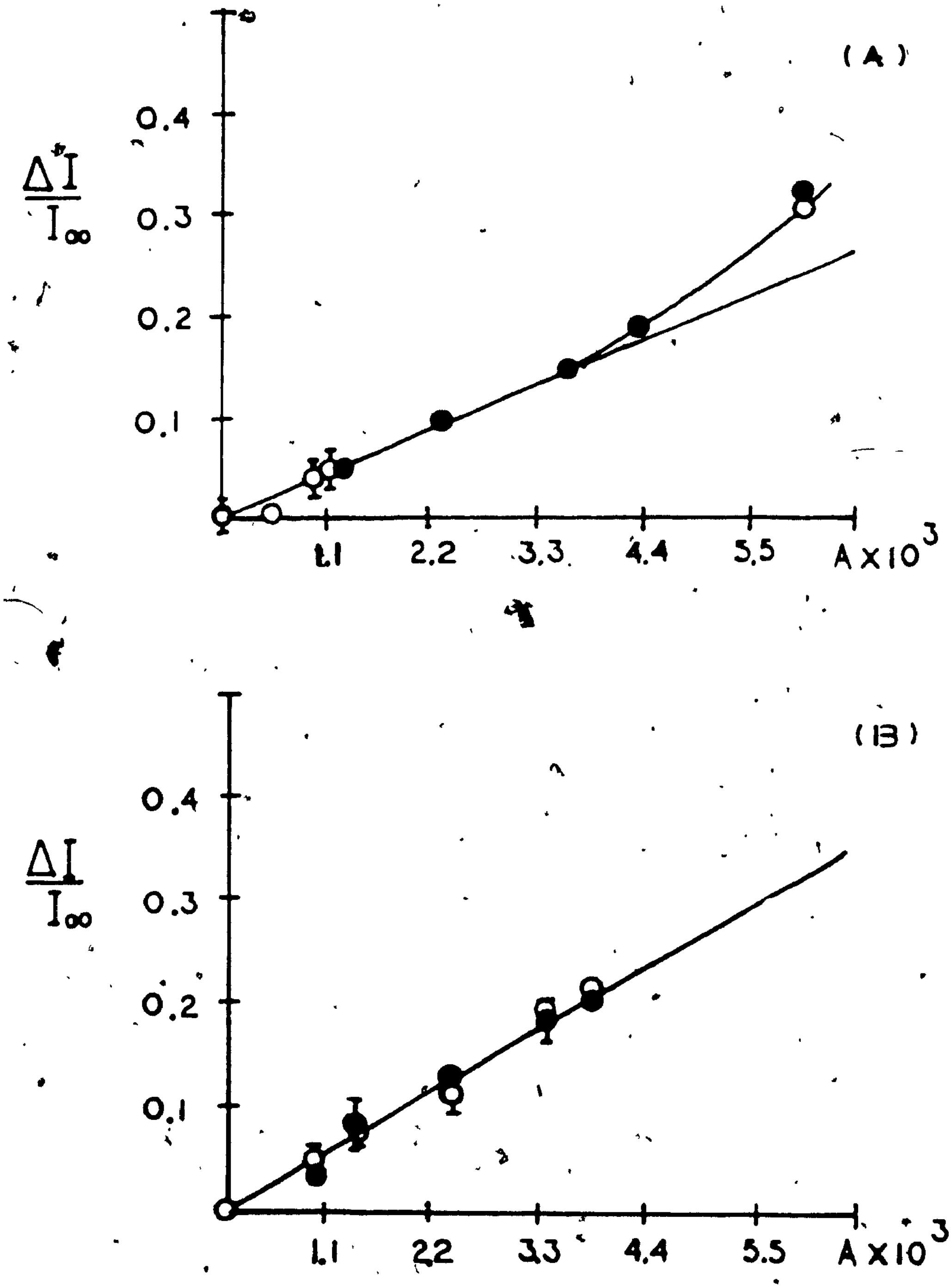

Figure 52 : Calibration curves of $\frac{\Delta I}{I_\infty}$ vs absorbance (calculated) for fulvic acid at pH 7.4 and 488 nm excitation (a) P = 120 mW ; E = 22 (b) P = 165 mW ; E = 19 ; ○ = FA + .01-0.2 % wt Si02 ; ● = FA with no Si02 .

correspond to AFA concentrations of < 3 mg/l. In mode-matched experiments, at absorbances above 5×10^{-3} cm^{-1}, the photothermal signal saturated, requiring a fitting of calibration data to a parabolic distribution as dictated by theory (19,20). The data obtained as in Figure 52 indicate that the upper limit of linearity for the technique is about 5×10^{-3} cm^{-1}, corresponding to a DOC level of about 2-3 ppm. This range is representative of the lower range of freshwater organic carbon concentrations (1). The detection limit obtained in the absence of scattering was an AFA concentration of 50-100 ppb at 488 nm (A = 0.0001-2 cm^{-1}).

Calibration data were next recorded in the presence of added bulk scatterers. Calibration curves were run on AFA in the presence of 0.01% and 0.025% wt SiO_2 (Figure 52). No loss of signal linearity was observed at low AFA containing 0.025% wt SiO_2. Samples of AFA containing no scatterers were run in paralell with the samples containing SiO_2, under the same conditions of pH and instrumental alignment. No difference in response was observed for samples run under identical conditions.

These results indicate that the thermal lens measurements are insensitive to light scattering effects, in this regime of particle concentrations. This, in turn indicates that the presence of the suspended particulates does not measurably attenuate the excitation beam in the cell. It is also clear that there is no loss of absorption due to removal of the FA from solution by adsorption on the particle surfaces. Further indications of the robustness of the TL measurement to scattering is indicated by the fact that some of the SiO_2 particles suspended in the sample actually settled out of the solution prior to the signal measurement. As well, the % wt of particles added to different samples was not rigidly controlled. Neither of these variations in scattering levels was sufficient to destroy the signal linearity with AFA concentration.

It should be noted that the concentration level of particles present in these experiments was in a regime which would easily play havoc with a conventional absorption measurement, even if the spectrophotometric sensitivity were adequate. Even at much lower levels of suspended particles, scattering still presents major problems for spectrophotometric measurements on unfiltered samples.

Some later measurements carried out on a series of natural organic carbon samples illustrated the effect quite clearly. The samples had been prepared by resin extraction and freeze drying (see experimental section). Unfiltered solutions of the dissolved materials contained varying quantities of suspended insoluble material. A series of these unfiltered stock solutions was absorbance matched by conventional spectrophotometry to the transmission standard, $CuSO_4$, diluted, and analysed by thermal lensing. The calibration curves of $\frac{\Delta I}{I_\infty}$ vs conventional absorbance are reported in Figure 54 for excitation of some of the samples at 600 nm. In theory, the entire set should have yielded a series of response curves coincident with the response obtained for the absorbance standard, Cu^{2+} because the calculated absorbance of all solutions was the same. In practice, the presence of light scatterers in the samples caused large errors in the absorbance measured spectrophotometrically. The slopes of the calibration curves for the organic matter samples were often much lower then the absorbance standard, because the calculated absorbances were greatly overestimated in the presence of light scattering.

The results obtained from the LTL I prototype were not the best achievable in terms of detection limit. With later instrumental developments, signal linearity and precision were improved (Chapter 4) by nearly an order of magnitude. The current version of the spectrometer is capable of detecting AFA concentrations as low as 10 ppb at 458 nm, which is nearly two orders of magnitude below the seawater range (0.5 - 1 mg /l) of DOC levels (1). The later version of the instrument used the mode-mismatched optical configuration and required 50-60 mW of excitation power. The signal enhancement under these conditions is typically about 25. Concentration sensitivity at 600 nm is reduced by an order of magnitude relative to 458 nm, because of the reduced absorptivity of humic samples at longer wavelengths. The absorbance detection limit, is, however, the same, for the conditions given.

In conclusion, these results demonstrate that thermal lensing is capable of distinguishing absorption from light scattering at very high ratios of scattering to absorbance. The technique is highly sensitive in the visible and is capable of yielding organic carbon detection limits in the seawater range. The most rudimentary forms of sample pretreatment are eliminated so that in situ absorbance measurements may be made directly on environmental samples. Consequently, thermal lensing could potentially displace conventional spectrophotometry as a routine method of analysis in this area.

Photothermal Measurements of E4/E6 ratios at Natural Water Levels

In the study of humic materials of terrestrial origin, visible absorption spectrometry has provided an indirect means of evaluating the physical and structural properties of isolated soil fractions (105). The solution phase absorption spectra of dissolved soil extracts are typically broad and featureless. However, the slope of the absorption spectra (as A/λ) have been shown to be relatable to such sample properties as particle size and molecular weight range. The spectral "slope " is estimated in terms of an absorptivity quotient (arbitrarily defined as the ratio between the sample absorptivities at 465 and 665 nm (105)) which varies from values of about 3-3.5 for (chernozem) humic acids to values of 6-8.5 for soil fulvic acids (105).

The measurement of E4/E6 ratios is potentially interesting to natural water analysis for several reasons. The general correlation that exists between the carbon content of a given material and its E4/E6 ratio (105) suggest that this parameter might be useful in optical determinations of the dissolved organic carbon content of a given water sample. In addition, all of the structural information provided by the ratios is potentially available at the low concentrations of humic materials present at natural water levels. The main barrier to the evaluation of E4/E6 ratios has been the lack of sensitivity of absorption methods for humic substances in the visible (1). This condition, however, is potentially removed by sensitive photothermal measurement methods such as thermal lensing, as suggested by the results already reported in this chapter.

The experiments discussed in this section had, as their object the measurement and interpretation of a series of E4/E6 ratios for samples isolated from different aquatic environments, using the thermal lens technique. The intention was to demonstrate the applicability of E4/E6 measurements to natural water analysis, and to advance some interpretations relevent to the sample properties.

Nature of the Samples Studied

The sample set studied in this work incorporated materials originating from two general environments (Figure 53): (a) Sandy low carbon creeks. The surrounding land is agricultural with tobacco as the main crop. The organic carbon content of the soil is less than 2 %. Typical examples are the Venison, Diedrich and Big Creek samples. (b) water bodies whose organic carbon content originated via runoff from soils derived from bedrock. Soils consist of fine clayey glacial tills or, in the southern sampling areas, as coarse loamy tills. The organic carbon content of the soil is about 5 %. The soil is poorly drained in areas giving rise to swamps and muskeg areas (Wylde Lake) with high carbon content. The surrounding land is mainly agricultural. Some examples of materials originating from this environment

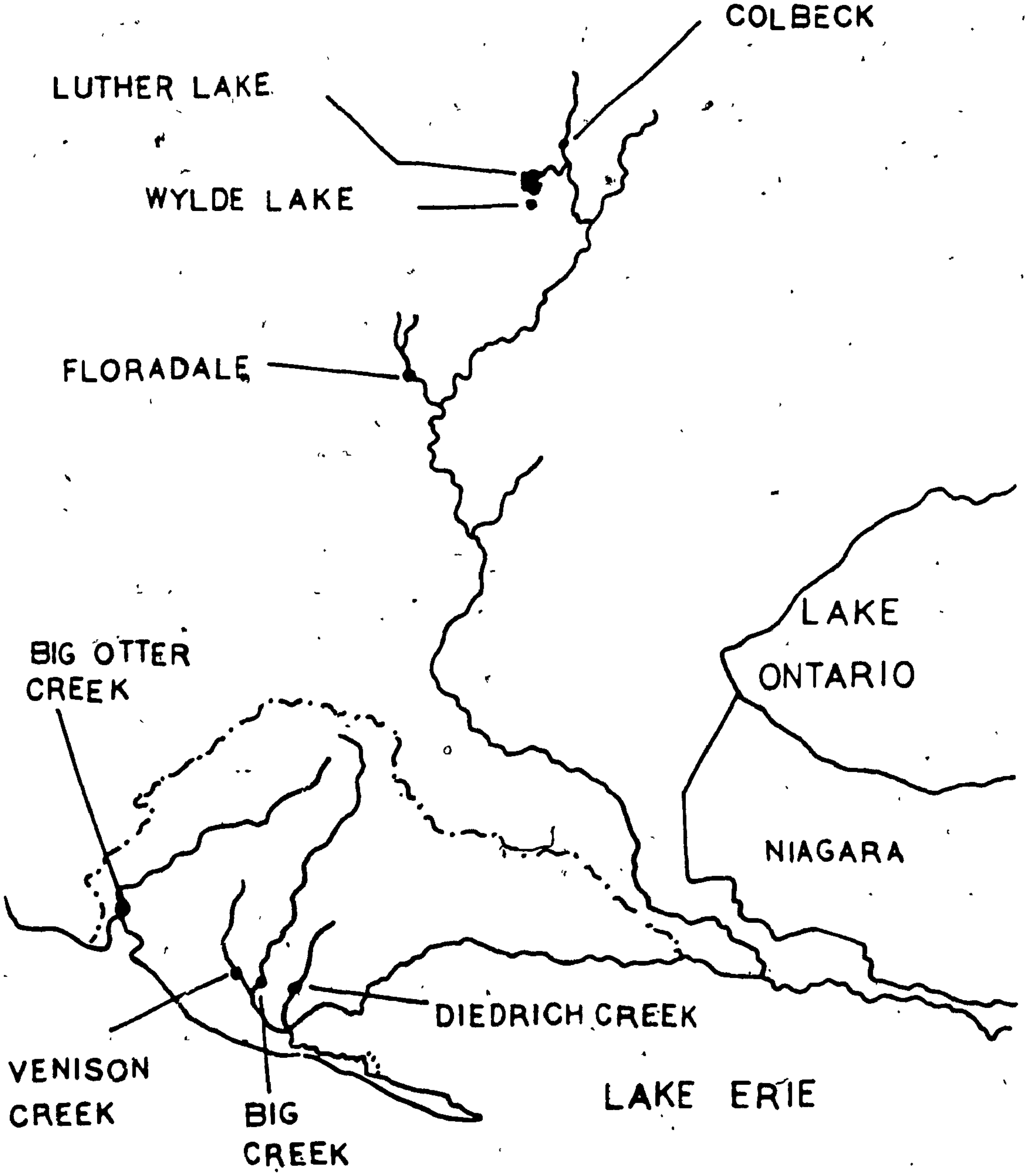

Figure 53 : Map of Sampling Sites for Natural Organic Materials

include the Floradale, Colbeck, Wylde Lake and Luther Lake samples. In addition to these materials, Armadale fulvic acid has been included as a standard since its behavior in thermal lensing is well established on the basis of this chapter's earlier results, and because as a soil derived material, its comparison with the extracted freshwater materials proves useful.

Absorptiometric and Thermal Lens Measurements and Some Interpretations

In order to obtain a qualitative picture of the absorption properties of the materials studied, conventional visible absorption spectra were run on the samples. The visible spectra of the materials are typical of humic substances consisting essentially of broad, featureless absorption profiles which increase monotonically with decreasing wavelength (4,21).

It is clear from the spectra of these samples that their absorptivities are generally low in the visible, especially as long wavelengths are approached. While the ash content of the samples has not been determined, concentrated stock solutions of these materials contain visible quantities of suspended insoluble material, the presence of which directly interferes with conventional absorbance measurements, by producing a background of light scattering as already discussed. At natural water levels, where the DOC range is from 5-30 ppm, for fresh water samples, the upper limit of

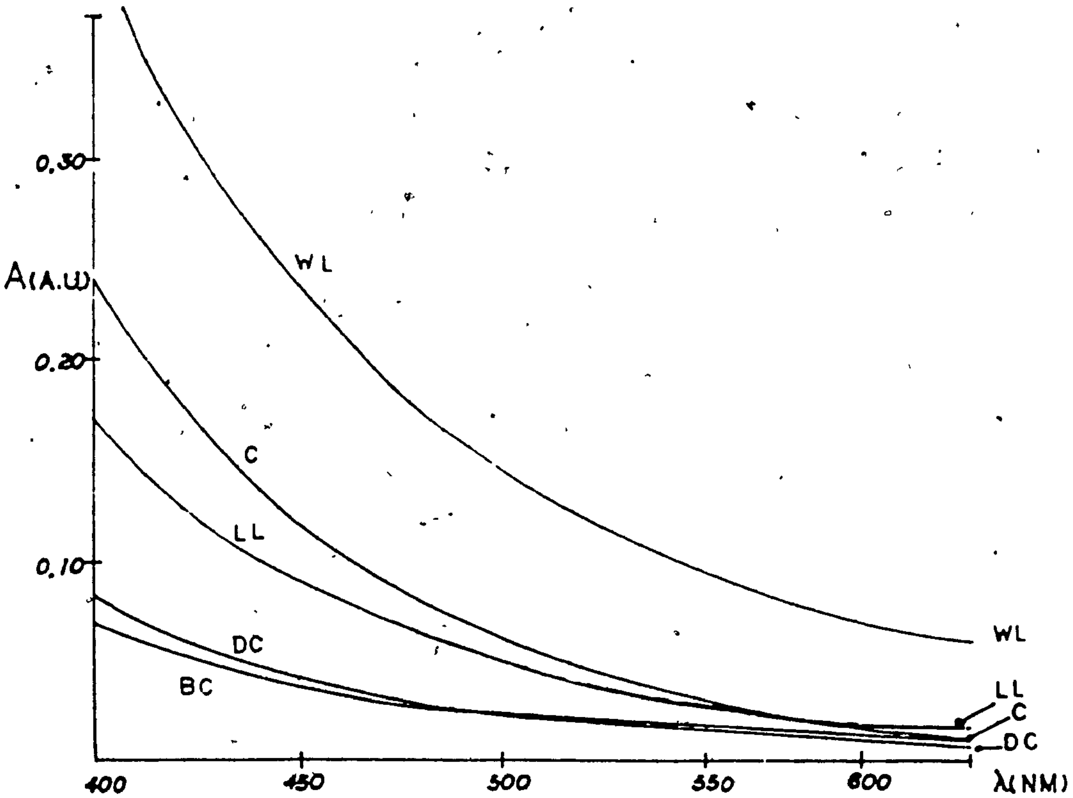

Figure 54: Visible absorption spectra of selected samples of natural organic material. Samples were unfiltered. Sample concentrations were as follows: WL 300 ppm; DC 450 ppm; LL 200 ppm; C 350 ppm; BC 350 ppm.

absorbance is about 0.01 cm^{-1} at 600 nm. This level is effectively at the limit of quantitation of most absorption spectrophotometers. The presence of scattering materials in the samples makes the conventional absorbance measurement impossible without the filtration of samples prior to analysis, and consequent sample perturbation. These considerations warrant the use of a sensitive photothermal technique such as thermal lensing because of its high sensitivity and demonstrated immunity to light scattering.

E4/E6 measurements (carried out on concentrated stock solutions of the materials) are reported in Table 13. The absorptivity data were recorded at 458 nm and 600 nm as opposed to the "classical" choice of 465/665 nm (for this reason the values of the ratios reported here differ somewhat from the absolute values reported in the literature).The choice of these wavelengths was based on the availability of excitation wavelengths from the laser source, so that comparisons could be made between the two methodologies.

Thermal lens measurements were made on the materials in dilute solution at dissolved organic carbon levels of 500 ug-10 mg/l. These values are representative of the lower limit of organic carbon concentrations found in fresh waters. Beer 's law behaviour of the samples was verified at 600 nm by measuring the thermal lens response as a function of the sample concentration. At low absorbances, the thermal lens signal as $\frac{\Delta I}{I_{\infty}}$ is known to be a linear function of sample absorbance. In practice, we have observed <u>linear</u> instrument responses over the range from A = 0-0.002 cm^{-1} at 55 mW of

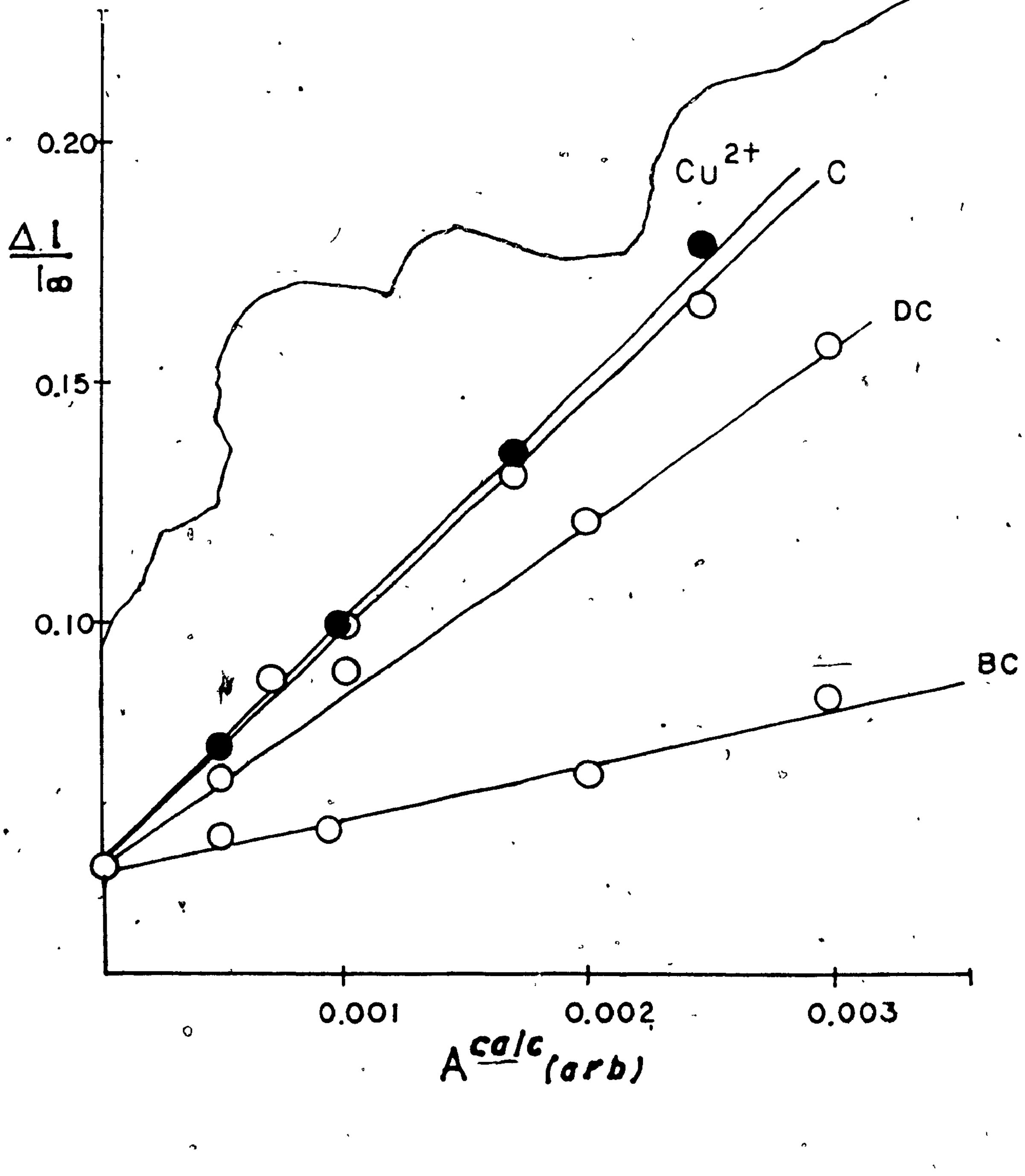

Figure 55 : Calibration curves of thermal lens response as $\Delta I / I_\infty$ vs calculated absorbance for selected samples of natural organic material . P = 55 mW ; λ = 600 nm .

laser power. Non-linearities in response above this value result from saturation of the photothermal signal rather than deviation from Beer's Law(83,84). At 458 nm. the linearity of the calibration curves was confirmed with Armadale fulvic acid. There is no evidence of any chemical deviation from Beer's law over the range of absorbances studied.

Absorptivity data for the materials as measured by thermal lensing are reported in Table 13. A comparison of the conventional values with those obtained by thermal lensing indicates the extent to which light scattering affects the conventionally measured E4/E6 ratio, especially among the low carbon samples. The error in the spectrophotometric data impedes any attempt to correlate absorbance with carbon content of the samples, especially at longer wavelengths. By contrast, the thermal lens technique yields absorbance measurements which are essentially immune to light scattering, since only absorbed radiation contributes to the photothermal signal.

The Beer's law behavior observed within a single sample is typical of the results of other workers (21,111,112). In particular, Buffle (21) has mentioned the measurement of dissolved organic carbon levels by conventional UV absorption spectrophotometry, and has reported a linear relationship between A at 285 nm and DOC, for data obtained within a single sample. A variation was observed for samples of different origins, with the slope of the A vs DOC line

Table 12

Elemental Analysis Data

Sample	%C	%H	%N	%S
Wylde Lake	25.44	6.20	8.0	0.43
Luther Lake	32.32	6.76	11.29	0.38
Colbeck	32.14	6.17	7.36	0.46
Big Creek	7.52	7.28	19.11	0.34
Venison Creek	4.72	6.91	17.98	0.42
Diedrich Creek	10.56	6.38	19.37	0.54
Floradale	20.89	6.53	11.90	0.40
Armadale FA	49.5	4.5	0.8	-

Table 13

Absorptivity Data

Sample	E4/E6 (conv)	E4 (LTL) $(g/l)^{-1}cm^{-1}$	E6 (LTL) $(g/l)^{-1}cm^{-1}$
Wylde Lake	3.70	0.987 ± .076	0.228 ± .01
Luther Lake	4.25	0.341 ± .011	0.0614 ± .0055
Colbeck	5.64	0.434 ± .020	0.0639 ± .0020
Big Creek	2.39	0.046 ± .005	0.00793 ± .0003
Venison Creek	-	0.043 ± .002	0.0064 ± .0004
Diedrich Creek	5.32	0.081 ± .010	0.012 ± .0033
Floradale	-	0.221 ± .0106	0.0325 ± .0028
Armadale	5.26	3.14 ± .18	.8 -

dependent on the nature of the sample studied. Those results suggested that absorbance measurements provide a straightforeward means of measuring humic substance concentrations for samples obtained from a common origin. No interpretation was advanced (in that work) to explain the differences in the absorptivities of the samples in terms of differences in the composition or physical properties of the materials.

In this work, the most striking feature of the results obtained is a quadratic relationship which emerges between the sample absorptivity and elemental carbon contemt, for samples posessing the same E4/E6 ratio (Figures 56,57).

For a fixed value of the E4/E6 ratio, the sample absorptivity was plotted against the carbon content, in wt %, as determined by elemental analysis (Table 12). The absorptivities were evaluated in $(g/l)^{-1}$ from the known (gravimetric) concentration of material in the sample. The resulting data, at constant E4/E6 appeared to obey a distribution of the form :

$$a_s = a(\%C) + b(\%C)^2 \qquad (5\text{-}18)$$

where %C is the % carbon composition, a_s is the absorptivity measured for the sample and a and b are regression coefficients. The profiles obtained at 458 nm and 600 nm exhibited the same parabolic relationship in all cases.(The parabolic relationships were obtained by plotting $a_s/\%C$ vs %C and fitting a least squares line to the points.)

It is interesting to note that chemical deviations from Beer's Law take on a nonlinear form when dimer species and

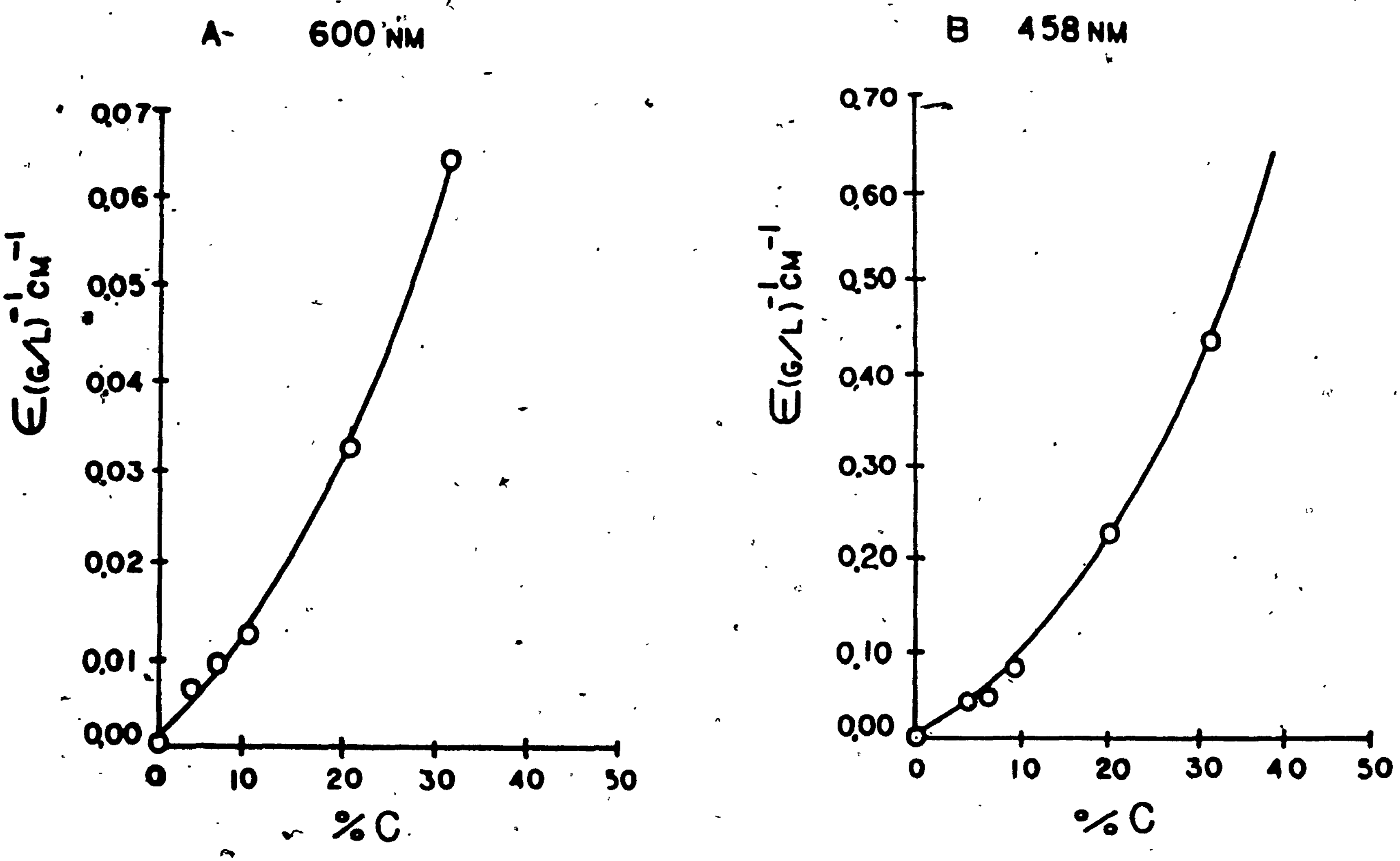

Figure 56 : Absorptivity vs %C relationships for samples with high E4/E6 ratios (E4/E6 = 6.7 ± 0.1)

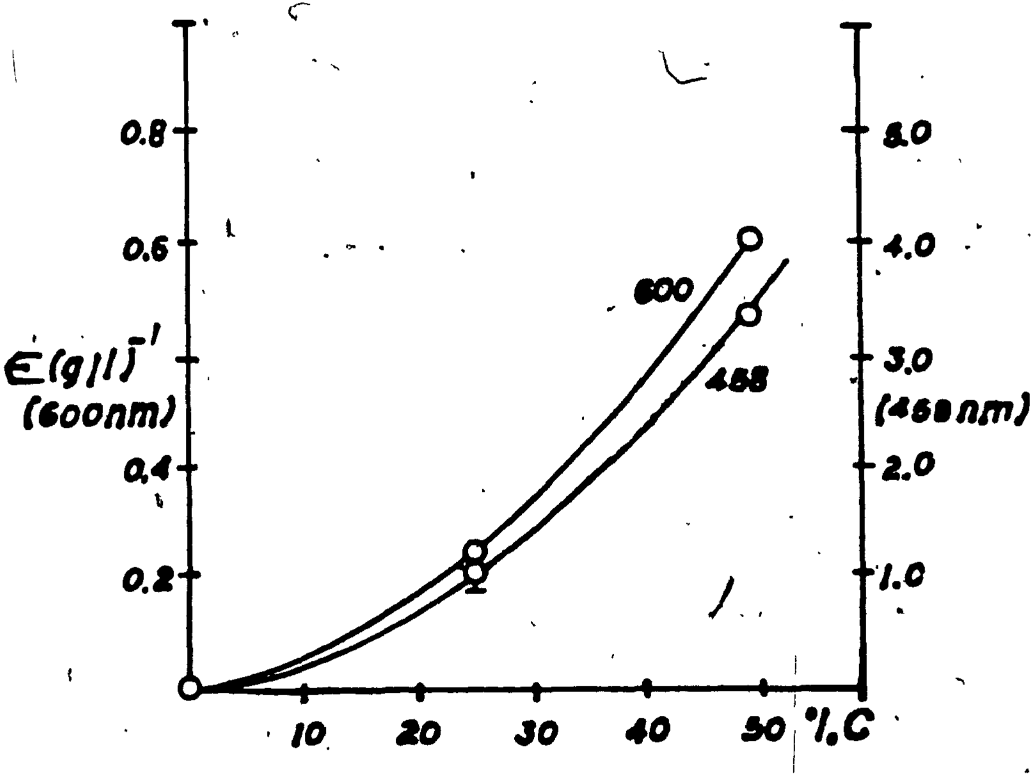

Figure 57: Absorptivity vs %C relationship for samples with low E4/E6 ratio (E4/E6 = 4.4± 0.2)

donor-acceptor complexes form from the absorbing chromophores (113). The polymer model for FA photophysics put forth in Chapter 2 might provide an explanation of the quadratic variation of sample absorptivity with increasing elemental carbon content.

If these dimerisation processes are occurring for the samples studied here, then the sample absorbance could be written as :

$$A_s = A_m + A_d \qquad (5\text{-}19)$$

where A_m is the absorbance contribution due to the monomeric chromophores and A_d is the contribution due to the dimers. The following dimerisation reaction could be considered to be taking place :

$$2M \rightleftharpoons M_2$$

with equilibrium constant $K_d = [M_2] / [M]^2$. If Beer's law is written for each species separately then :

$$A_s = a_m[M] + a_d[M_2] \qquad (5\text{-}20)$$

where l = 1 cm and a_m, a_d are the absorption coefficients for monomer, dimer . The sample absorbance can be written as :

$$A_s = A_m[M] + K_d a_d[M]^2 \qquad (5\text{-}20a)$$

The next step is to consider a total concentration of absorbing chromophores, C, where $C = [M] + 2[M_2]$ at any time. For a system at equilibrium, the concentration of absorbing monomeric chromophores is $(1 - \alpha_d)C$ where α_d is the fraction of initial chromophores that have dimerised. For small degress of dimerisation α_d is effectively constant. Equation 5-20 becomes :

$$A_s = a_m(1 - \alpha_d)C + a_dK_d(1 - \alpha_d)^2C^2 \qquad (5\text{-}12)$$

Finally, if C is directly proportiional to %C, then the above expression yields a quadratic relationship between the measured absorbance and the carbon content.

Experimentally, we measure :

$$A_s = a_sC_sl \qquad (5\text{-}22)$$

where C_s is the sample concentration in g/l. Evaluation of a_s gives :

$$a_s = A_s/C_s = (a_m(1 - \alpha_d)C + a_dK_d(1 - \alpha_d)^2C^2)/C_s \qquad (5\text{-}23)$$

If $C_s = 1$ g/l in the above equation, then a quadratic relationship between a_s and %C is predicted by the model.

The parabolic relationship is valid if K_d and α_d are small. This in turn requires a_d to be large relative to a_m, if the second order term is to be observed at all. The model predicts that the curvature in the a_s vs %C plots arises from intraparticle chromophore interactions. The Beer's Law behavior observed for the materials over the range of particle concentrations studied excludes the possibility of interparticle chromophore interactions.

If the donor-acceptor model for chromophore interactions is valid , then the dimer component should be strongly red shifted relative to the monomer and dominate at the longest wavelengths . If the dimer species forms from a monomer which absorbs in the blue end of the visible , then formation of the dimer states should produce a red shift in the absorption spectrum with the second order " b " term dominating in the red. This behavior is observed for the low E4/E6 materials. (Table 14). For the high E4/E6 samples, the a_s vs %C plots obtained at 600 nm showed less curvature than the profiles obtained at 458 nm . This would arise if the dimer components had their absorption maxima in the blue and low absorptivities in the red . The dominance of the dimer species at 458 nm suggests that the parent monomer states absorbed in the near UV (in the range 350-400 nm, as is typical for the benzene carboxylic functions present in humic materials (21).

The dimer/donor-acceptor model seems to provide some general interpretations of the optical properties observed. The features of the natural samples examined in this work appear to fall into two classes : " riverine " material with low visible absorbance (and high E4/E6), and material resembling soil humic material (Wylde Lake) with high visible absorbance (and low E4/E6). In general, low E4/E6 ratios are indicative of high molecular weight, elevated carbon content and relatively low oxygen content of the materials (105). As the carbon content and the

Table 14

Parabolic Fitting Parameters

E4/E6	**Wavelength**	**a**	**b**	**R**
6.7 ± 0.1	600 nm	7.5×10^{-4}	3.94×10^{-5}	0.999
6.7 ± 0.1	458 nm	4.2×10^{-3}	2.9×10^{-4}	0.996
			(not including Venison Creek)	
4.4 ± 0.2	600 nm	2.1×10^{-4}	3.3×10^{-4}	0.999
4.4 ± 0.2	458 nm	0.002	0.00137	0.994
			(includes origin)	

*Note : units are as follows: a: $(g/l)^{-1}cm^{-1}/\%C$

b: $(g/l)^{-1}cm^{-1}/(\%C)^2$

molecular weight increase, the visible absorbance of the material increases. According to the model proposed here, the visible absorbance should increase due to an increasing contribution of dimer states, which results in an enhanced curvature of the a_s vs %C plots, as observed. For the low E4/E6 ratios, the second order term always makes a large contribution to the total value of a_s. On the other hand, at high E4/E6 ratios, the molecular weight of the particles is lower so that the number of chromophores per particle is automatically lower. The " b " term in the a_s vs %C plots is always an order of magnitude less than the " a " term possibly indicating that the monomer components dominate the contributions to a_s. The parent monomer states probably lie in the near UV which is consistent with lighter, less conjugated material. The model proposed here lends to a general interpretation of the E4/E6 ratio, as being a parameter that depends on the chromophore density (as chromophores / particle) of a given humic material. Insofar as they relate to the chromophore density of the material, properties such as carbon content, oxygen content, molecular weight, acidity, etc. will be related to the E4/E6 ratio.

The interpretation advanced by Chen, Senesi, and Schnitzer (105), to explain the E4/E6 ratio was based on the observation that the derivative of the absorption spectrum had a $1 / \lambda^4$ wavelength dependence. A mechanism based on light scattering appeared to be consistent with this finding. In later work, Underdown found that the relationship persisted, even in photoacoustically recorded spectra where light scattering was not expected to contribute (4). He concluded that the observed spectral " slopes " could not be explicitly due to scattering effects. The present work showing the insensitivity of photothermal signals to light scattering strengthens this evidence. It also provides an explanation for the variation of the E4/E6 ratio with particle size and molecular weight, which is not based on light scattering.

It should be emphasised that the model presented here is of a speculative nature and would require a more complete study of the sample properties for verification. More work is required in relating properties of the sample such as molecular weight, particle size, O, and free radical content to the observed photothermal signals. NMR determinations of the aromatic content of the samples would be especially illuminating. A larger variety of humic substances (including soil humic acids) should be examined, providing a complete range of E4/E6 values for testing of the model.

In conclusion, the present work establishes the feasibility of measuring E4/E6 ratios of humic substances in freshwater samples, providing both sufficient sensitivity and rejection of light scattering. The method is clearly useful for measuring humic substance concentrations from samples derived from a single source. Further work will be required to firmly establish the method for the study of samples of widely differing origins.

References

1. J. Buffle in **Metal Ions in Biological Systems** Helmut Siegel , Ed. Marcel Dekker Inc , New York and Basel (1984) Chapter 6 .
2. C.H. Langford , D.S. Gamble, A.W. Underdown and S. Lee in **Aquatic and Terrestrial Humic Materials** ,R.F. Christman and E.T. Gjessing , Eds. , Ann Arbor Science Publishers, Ann Arbor , M.I. , U.S.A. , (1983) , Chapter 4.
3. S. Lee,Ph.D. Thesis , Carleton University , Ottawa , 1981.
4. A.W. Underdown, Ph.D., Thesis , Carleton University , Ottawa, 1982.
5. A.W. Underdown , C.H. Langford and D.S. Gamble , **Can. J. Soil Sci.** 61 469 (1984) .
6. A.W. Underdown , C.H. Langford , D.S. Gamble , **Environ. Sci. Technol.** 19 , 132 (1985).
7. D. Gamble and M. Schnitzer in **Trace Metals and Metal Organic Interactions in Natural Waters** P.S. Singer , Ed., Ann Arbor Science Publishers Inc . Ann Arbor , M.I. , U.S.A. (1973) p265.
8. O.C. Zafiriou , R.G. Zepp , R.G. Zika and J. Joussot-Dubien, **Environ. Sci. Technol.** 18 ,358A (1984) .
9. N. Senesi and M. Schnitzer in **Environmental Biogeochemistry and Geomicrobiology Vol 2: The Terrestrial Environment** , W.E. Krumbein , Ed. Ann Arbor Science , Ann Arbor , M.I. , U.S.A. , p 467 (1978).

10. R.G. Zepp , N.L. Wolfe , G.L. Baughmann , R.C. Hollis , **Nature** 267, 421 (1977) .

11. R.G. Zepp , G.L. Baughman , P.F. Schlotzhauer , **Chemosphere** 10 , 9 (1981).

12. R.M. Baxter and J.H. Carey , **Nature** 306 , 575 (1983).

13. T. Mill , D.G. Hendry and H. Richardson , **Science** 207 , 886 (1980) .

14. R.G. Zepp , N.L. Wolfe , J.A. Gordon and R.C. Fincher , **J. Agric. Food Chem.** 24 , 727 (1976) .

15. W.M. Draper and D.G. Crosby , **J.Agric. Food Chem.** 32 , 231 (1984) .

16. J.M. Wolfe , T.H. Halmans , H.B. Van der Heijde, **Chemosphere** 10 , 59 (1981).

17. E.H. Hansen and M. Schnitzer , **Anal. Chim. Acta.** 46, 247 (1969) .

18. D.S. Gamble , **Can. J. Chem** , 50 , 2680 (1972) .

19. J. Buffle , P. Deladoey and W. Haerdi , **Anal. Chim. Acta** 101, 339 (1978).

20. A.W. Underdown , C.H. Langford , D.S. Gamble , **Anal. Chem** . 53 , 2139-40 (1981).

21. J. Buffle , P. Deladoey , J. Zumstein and W. Haerdi , **Schweiz. Z. Hydrol.** , 44 , 327 (1982).

22. J. Weber , M. Ewald , C. Belin , and P. Berger , **Environmental Sci. Technol.** , 17 , 501 (1983).

23. A.M. Fischer , T. Mill , D.S. Kliger , D. Tse , **I.H.S.S. Symposium Proc.** , Birmingham , U.K. , July 23-28 (1984).

24. A.M. Fischer , D.S. Kliger, J.S. Winterle and T. Mill, **Chemosphere** 14, 1299-306 (1985).

25. J.P. Gordon , R.C.C. Leite , R.S. Moore , S.P.S. Porto and J.R. Whinnery , **J. Appl. Phys.** ,36 , 3 (1965).

26. C. Hu and J.R. Whinnery , **Appl. Opt.** , 12 , 72 (1973).

27. N.J. Dovichi and J.M. Harris , **Anal. Chem.** , 52 , 695A (1980) .

28. M. Schnitzer in **Short Course in Environmental Geochemistry** , Mineralogical Association of Canada, May 1984. Chapter 10, pp 237 - 267.

29. G.S. Foote , **Chem. Revs.** 1 , 104 (1968) .

30. J.L. Roberts , D.T. Sawyer , J.A.C.S. 103, 712 (1981).

31. J.R. Bolton , A. Iononye and A.R. McIntosh , Abstracts , 10th D.O.E. Solar Photochem. Conf. , Niagara-on-the-Lake, Ontario , Canada , June 8-12 , 1986 p 115 .

32. T.D. Waite and F.M.M. Morel , **Environ. Sci. Technol.** , 18, 860 (1984).

33. E.L. Russel , A.J. Twarowski , D.S. Kliger , E. Switkes , **Chem. Phys.** 22 , 167 (1977) .

34. K.B. Roach , MSc. Thesis , Concordia University , Montreal , 1983 .

35. J.G. Dick, **Analytical Chemistry,** R.E. Kreiger Publishing Co., Huntingdon, N.Y., 1978. p 640.

36. A.C. Boccara, D. Fournier and J. Badoz, **Appl. Phys. Lett.** 36, 130 (1980).

37. J. Pawliszyn, M.F. Weber, M.J. Dignam, A. Mandelis, R.D. Venter, and S.M. Park, **Anal. Chem.** 58, 239, (1986).

38. M. Pileni , **Chem. Phys. Lett.** 54 , 363 (1978) .

39. P.Rentzepis and R.P. Jones , **J. Chem. Phys.** 59 , 766 (1973).

40. G.A. Kenney-Wallace and C.D. Jonah, **Chem. Phys. Lett.** 39, 596 (1976).

41. L.I. Grossweiner and H.I. Joschek , **J.A.C.S.** 88 , 3261 (1966).

42. G. Grabner , G. Kohler , J. Zechner and N. Getoff , **J. Chem. Phys.** 84 , 3000 (1980) .

43. National Bureau of Standards Publ. # 69. , U.S.A.

44. M.S. Matheson in **The Solvated Electron** (A.C.S. Symposium Volume) , R.F. Gould , Ed. (**Advances in Chemistry Series** , A.C.S. Press , Washington , 1965)

45. G. Dobson and L.I. Grossweiner , **Trans. Faraday Society** 61 , 708 (1965) .

46. E.J. Hart and M. Anbar in **The Hydrated Electron** , Wiley Interscience , 1970 . p 40-41.

47. L.I. Grossweiner and H.I. Joschek **Advances in Chemistry Series 50** , A.C.S. Washington D.C. 1965 . p 279-288.

48. G. Grabner , W. Rauscher ~~, J.~~ Zechner and N. Getoff , J.C.S. Chem. Comm. 222 (1980) .

49. R.A. Saar and J.H. Weber , **Anal. Chem.** 52 , 2095 (1980).

50. R.G. Zepp , P.F. Schlotzhauer and R.M. Sink , **Environ. Sci. Technol.** 19 ,74 (1985) .

51. A.J. Lappen and R. Seitz , **Anal. Chim. Acta** 184 ,31 (1982).

52. **Sadtler Index of Ultraviolet and Visible Absorption Spectra**, Sadtler Research Laboratories, U.S.A. (1976).

53. D. Phillips and A.J. Roberts Eds. **Photophysics of Synthetic Polymers** Science. Revs. , Middlesex , England (1982) .

54. S.L. Mattes and S. Farid **Science** 226 ,917 (1984) .

55. M. Graley and A. Reiser in **Photophysics of Synthetic Polymers** pp 26-28 .

56. A. Harriman and B.W. Rockett , **J. Photochem.** 2 , 405 (1974).

57. N.S. Allen , J.P. Binkley , B.J. Parsons , G.O. Phillips and N.H. Tennant in **Photophysics of Synthetic Polymers** pp 128 - 135.

58. N.S. Allen and J.F. McKellars , **Makromol. Chemie** 179 , 523 (1978) .

59. W. Zeichmann, **Geoderma** 8 111 (1972).

60. D.H. Phillips and J.C. Chug, **J. Chem. Phys.** 50, 3297 (1969).

61. N.J. Dovichi and J.M. Harris , **Anal. Chem.** 53, 106-9 (1981).

62. M.L. Liesiecki and J.M. Drake , **Appl. Opt.** 21, 557 (1982).

63. T. Igaishi , T. Imasaka , N. Ishibashi , **Anal. Chem.** 55 , 1907 (1983).

64. A. Papoulis , **Systems and Transforms with Applications in Optics** , Mc Graw - Hill , 1968 , Chapter 1.

65. M. Born and E. Wolf, **Principles of Optics**, Pergamon Press, N.Y. 1965. pp 459-464.

66. S.J. Sheldon , L.V. Knight and J.M. Thirne , **Appl. Opt.** 21 , 1663 (1982).

67. F.P. Incropera and D.P. De Witt , **Introduction to Heat Transfer** , J. Wiley and Sons , 1985 . pp 44-46 .

68. I. Stakgold, **Green's Functions and Boundary Value Problems**, Wiley Interscience, N.Y., 1979.

69. M. Greenberg, **Applications of Green's Functions in Science and Engineering**, Prentice Hall, Englewood Cliffs, N.J. 1971.

70. P.M. Morse and H. Feshbach , **Methods of Theoretical Physics**, Mc Graw-Hill , 1953, Chapter 7 (Vol. I).

71. P. M. Morse and H. Feshbach , Ibid. Chapter 11 (Vol II).

72. A. Papoulis , Ibid. Chapter 2.

73. S. Stearns , **Digital Signal Analysis** , Hayden Book Co. , 1975, Chapter 3, p 27.

74. I. Stakgold , Ibid. p 200.

75. P.M. Morse and H. Feshbach , Ibid Chapter 7 , p 860-862.

76. P.M. Morse and H. Feshbach , Ibid. Chapter 7

77. Yudell Luke in **N.B.S. Mathematical Tables** , National Bureau of Standards Applied Mathematics Series. , 1970. p 486.

78. I. Kreyszig , **Advanced Engineering Mathematics** , 4th ed., J. Wiley and Sons , 1979 p A54-60.

79. E. Jahnke and E. Emde, **Tables if Functions** ,Teubner, Berlin , 1939. p 1-8.

80. A. Yariv , **Introduction to Optical Electronics** , Holt Rhinehart and Winston, N.Y., 1971. Chapter 2.

81. A.E. Siegman , **Introduction to Lasers and Masers**, Mc Graw-Hill, N.Y., 1971, Chapter 8.

82. M.E. Long, R.L. Swofford, A.C Albrecht, **Science** 26,183 (1976).

83. N.J. Dovichi and J.M. Harris , **Anal. Chem.** 53, 699A (1980).

85. J.R. Whinnery , **Acc. Chem. Res.** 10, 225 (1977).

86. K. Nakanishi, T. Imasaka, N. Ishibashi, **Anal. Chem. 54**, 2039 (1982).

87. H. Fang, and R.L. Swofford in **Ultrasensitive Laser Spectroscopy** , Academic Press, N.Y., 1983. pp 175-232.

88. T. Berthoud, N.Delorme and P. Mauchien, **Anal. Chem.** 57, 1217 (1985).

89. A. Papoulis, Ibid. Chapter 9.

90. J. Alfheim , MSc. Thesis , Concordia University , Montreal, 1985.

91. D.R. Scifres, W. Streifer and R.D. Burnham, **I.E.E.E. J. Quantum Elec.**, QE-15, 917 (1979).

92. K. Mori, T. Imasaka, N. Ishibashi , **Anal. Chem. 54** , 2034 (1982).

93. K.L. Jansen and J.M. Harris,**Anal. Chem.** 57, 1698 (1985).

94. F. Villamagna, D.K. Sharma, and C.H. Langford , **Can. J. Spectros.** 28, 181(1983).

95. J.A. Alfheim and C.H. Langford , **Anal. Chem.** 57, 861 (1985).

96. Reticon Corporation ,Sunnyvale, Calif., publication no. 18220.

97. J.D. Winefordner and G.L. Long, **Anal. Chem.** 55, 712-724A (1983).

98. J.S. Bendat and A.G. Piersol , **Engineering Applications of Correlation and Spectral Analysis** , Wiley Interscience, New York (1980).

99. C.E. Buffet and M.D. Morris , **Appl. Spec.** 37, 455 (1983).

100. S.W. McGeorge , PhD Thesis, McGill University, Montreal, 1985.

101. Design and Construction: D. Gutzman, Chemistry Dept., Concordia Univ., Montreal.

102. S. Stearns , **Digital Signal Analysis**, Chapter 5.

103. J.F. Power, E.D. Salin and C.H. Langford, to be published.

104. E.M. Thurman, R.L.Wershaw, R.L. Malcolm, D.J. Pinckney, **Organic Geochemistry** 4, 27 (1982).

105. Y. Chen, N. Senesi and M. Schnitzer, **Soil Sci. Amer. J.** 41, 32 (1977).

106. M.G. Mellon, **Analytical Absorption Spectroscopy**, J. Wiley & Sons, N.Y., 1950. pp 259-261.

107. C. Datta, K. Ghosh, S.K. Mukerjee, **J. Indian Chem. Soc.** 48, 279 (1971).

108. J.H. Brannon and D. Magde, **J. Phys. Chem.** 82, 705 (1978).

109. J.G. Dick, **Analytical Chemistry**, R.E. Kreiger Publishing Co. , Huntingdon, N.Y. 1978, pp 640.

110. J.N. Demas and G.A. Crosby, **J. Phys. Chem.** 75, 991 (1971).

111. A.L. Wilson , **J. Appl. Chem.** 9, 501 (1959).

112. J.S. Matson, C.A. Smith, T.J. Jones, S.M. Gerchakov and B.D. Epstein ,**Limnol. Oceanograph.** 19 530 (1974).

113. H.H. Bauer, G.D. Christian and J.E. O'Reilly. **Instrumental Analysis** , Allyn & Bacon, Boston, 1978. pp 172 - 175.

Appendix A

LTL I was equipped with a low cost data acquisition interface with 8 bit resolution and a 30 KHz conversion rate. The interface was designed for a SOL 20 microcomputer (Technology Corp.), an 8080 based system. Data transfers took place via an eight bit paralell I/O port. A description of the operation of the interface is summarised in this appendix along with a discussion of the design.

The analog signal from the Reticon RC301 support circuitry consisted of a series of voltage spikes with the amplitude of each spike proportional to the photocurrent integrated by a particular photodiode. The signal was recovered from the train of pulses by means of a set of active filters. A diagram of the filter stages is shown in Figure 58. The first stage consisted of an inverting RC filter with a corner frequency of 100 KHz. The array clock frequency was adjusted to 100 KHz as well. The purpose of the first stage was to partially filter the signal although the output was attentuated. The attenuated, partially filtered signal was amplified by a factor of 30 in the second stage to compensate for losses in the first stage. The second stage consisted of an inverting differential amplifier with variable gain and offset. The output of the second stage had a peak amplitude of 5-9 v, so that it was level matched to the analog-to-digital converter. However, it still contained residual spikes i.e. the carrier frequency was still present. The third stage consisted of an active high Q notch filter which was tuned to the frequency of the readout clock since the carrier had a major harmonic component at the clock frequency. This stage reduced the carrier signal level by a factor of about 10. The final stage consisted of a second RC inverting filter which had a variable (selectable) bandpass. This stage was optional and was used for additional smoothing of the residual clock signal, optical interference patterns in the array signal, or noise.

It is clear that this technique of signal processing was a compromise method due to the frequency spectrum of the signal. The carrier signal in this system approximated to a regular train of delta functions so that there were two major ranges of frequency to the carrier: the frequency of the readout clock pulse train and higher order harmonics associated with the narrow pulses. A lowpass filter designed to attenuate the clock frequency attenuated the image signal which carried the information. If the time constant of the filter is decreased to admit higher frequencies, appreciable discharge of the filter capacitors takes place during the period of the clock, so that a large residual carrier component remains in the recovered signal. The obvious solution was to increase the duty cycle of the signal by means of a sample-and-hold circuit, as was achieved by means of the RC100B motherboard system (LTL II). For initial setup and evaluation of LTL I, the system of tuned filters was, however, satisfactory.

Analog-to-digital conversion circuits were based on the ADC 0800, a low cost, readily available, successive approximations converter. The conversion time of an individual device was 50 microseconds. For maximum conversion speed, two ADC 0800's were run in paralell, with the analog signal applied to both inputs simultaneously. The converters were read out 31 microseconds apart to increase the number of data points recorded per scan. The readout process and intiation of new conversions was controlled by means of a set of Read latches which were toggled by output pulses from the I/O lines of the SOL 20. The latches changed state on the rising edge of the input pulse. When the latch output was driven high, the output data lines on the corresponding converter were enabled and the result of the conversion was read into the SOL 20. Otherwise the data lines were in the high impedance state. At the end of a readout cycle, a level change on the I/O line triggered a monostable circuit, the output of which initiated a new conversion. The timing relationships are summarised in Figure 59.

The program written to control acquisition by this interface was written in 8080 Assembler. A flow chart and listing of the acquisition program are reported on pages 240 and 241 . The sequence of events was as follows. Initially, the program set up two " mask " bytes to control the interface. When output to the SOL I/O port, Mask #1 pulsed the inputs to both read latches high, while Mask 2 reset the read latch input levels. Masks 1 and 2 were each stored in 8 bit general purpose registers. The storage address for the input data was set up in a double precision register, the lower 8 bits of which were used to count the number of bytes input to the system. The program enabled the array clock, which was supplied by means of a set of counters (see schematic, Figure 59). As the array clock was enabled, a Start pulse was supplied. A timed delay of 2 msec followed. The purpose of this sequence was to establish an accurate and reproducible integration interval for the array, before data acquisition , since the device was integrating photocurrent for an indeterminate period prior to execution of the routine. Once the preset delay was over, the read latches were initialised : Latch 1 was clocked into the **set** condition. A second scan of the array was next initiated. The program than entered the acquisition loop, consisting of two half cycles. On the first half cycle, Latch 1 reset, initiating a new conversion in ADC1, while Latch 2 set, enbling the data lines on ADC2. Data were read from ADC2 on this half cycle. On the second half cycle, Latch 2 reset, initiating a new conversion in ADC2, while Latch 1 set, enabling a readout of ADC1. A new conversions was started and data were read into the SCL every 31 microseconds. The speed limitations of the program were set by the relatively large number of I/O accesses contained in the loop. Once the acquisition was complete, the routine jumped to an infinite loop which repetively scanned the array, giving the user a continuous display of the output.

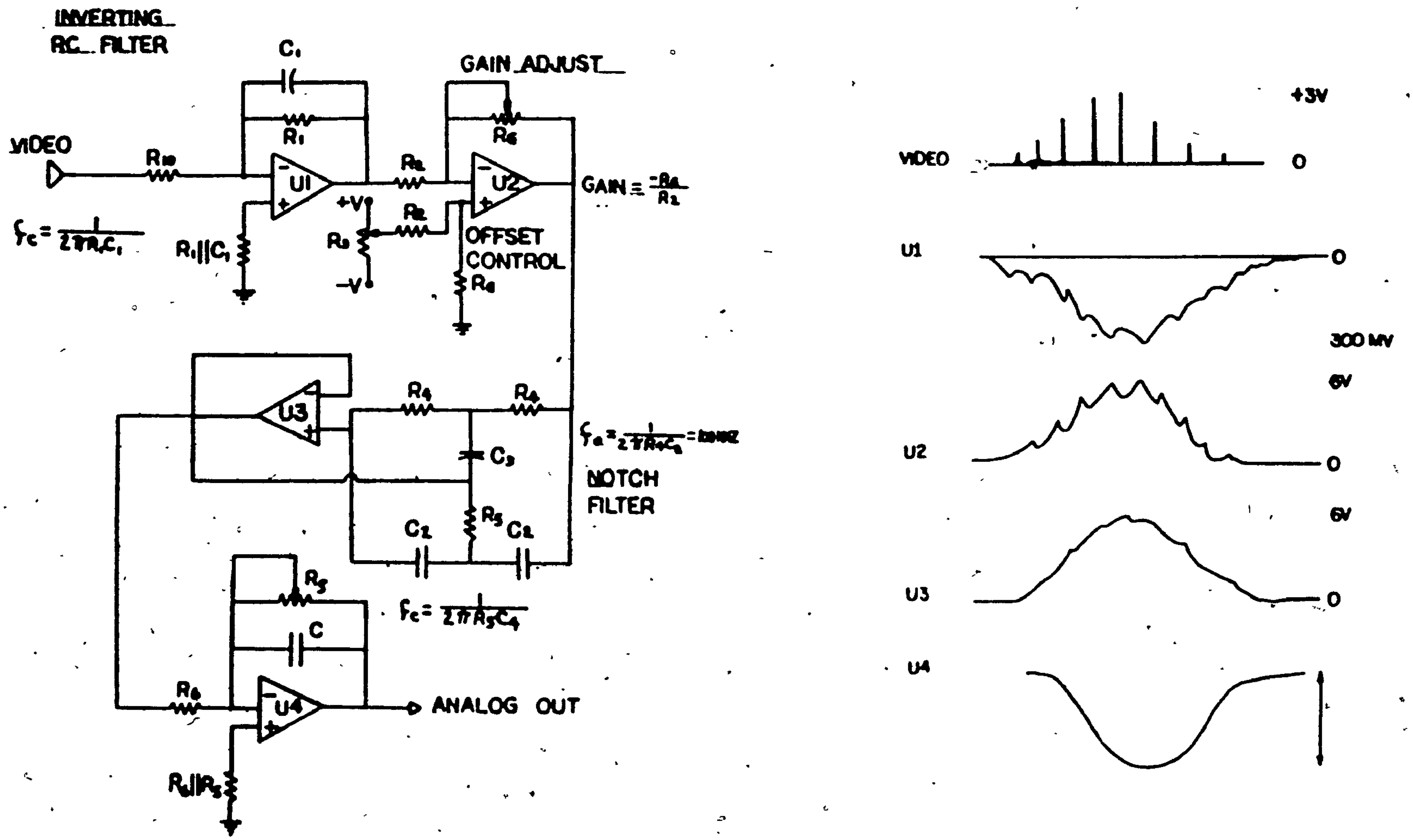

Figure 58 : Schematic of the system of tuned filters used in LTL I digital interface.

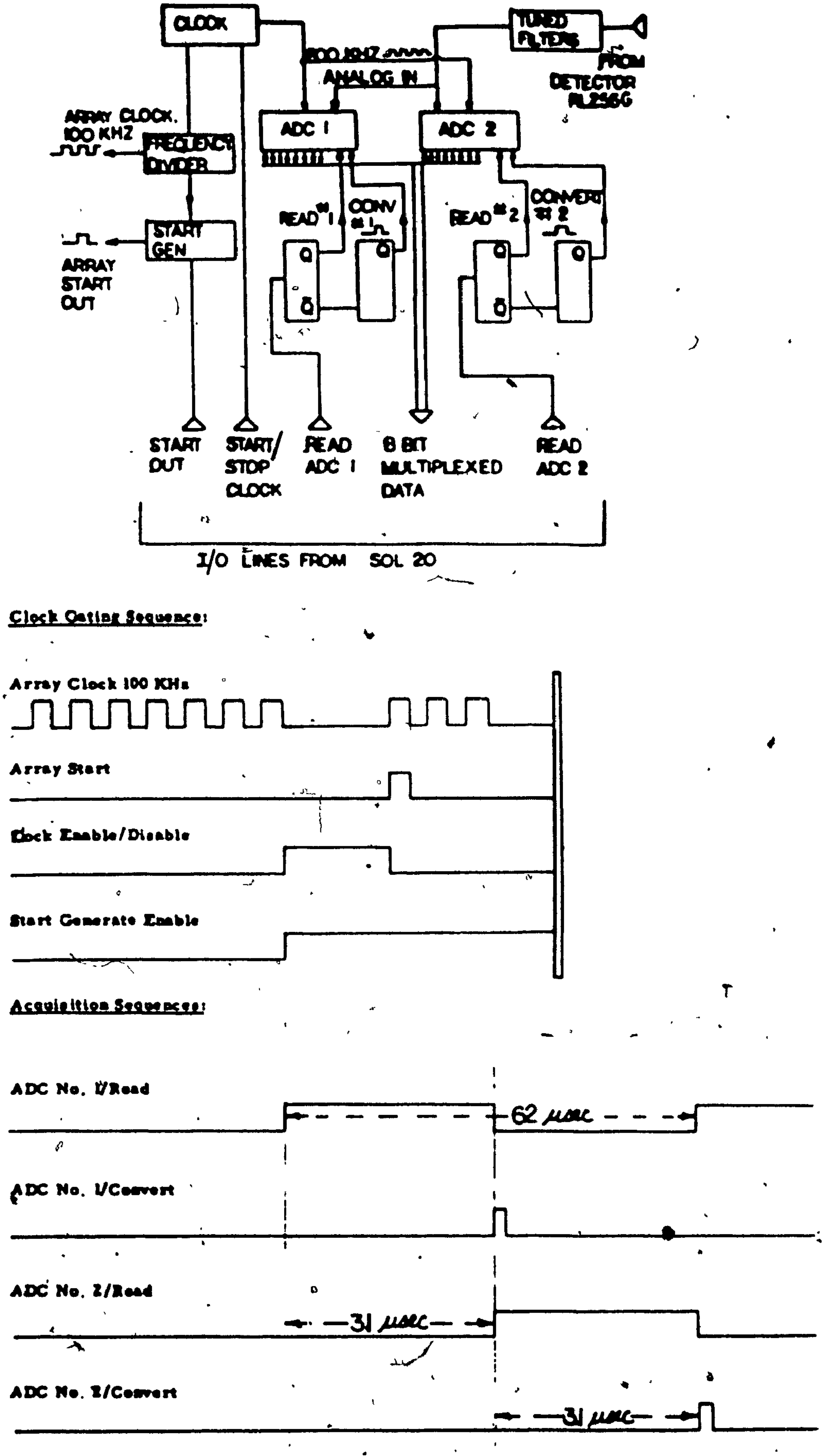

* All levels are TTL

Figure 59 : Schematic and timing relationships for LTL I digital interface.

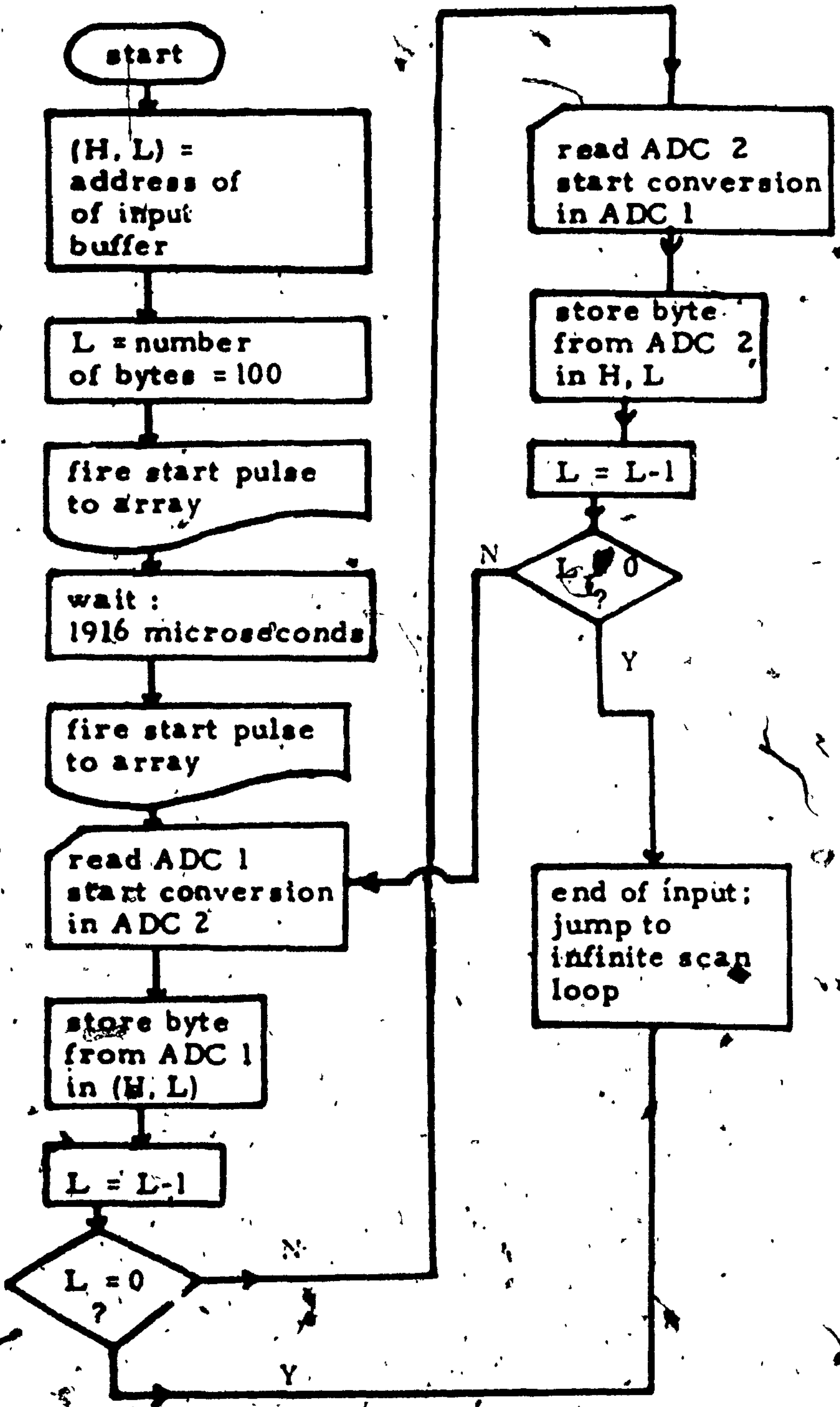

Flowchart of Input Routine : LTL I

Listings of Programs for Acquisition: LTL I Interface

DISP

Program to Supply a Continuous Display to the RL128/256G

```
LOC     LABEL     INSTRUCTION    COMMENTS

0500              JMP START      Get in
0503    GO        XRA A          Drive START low
0504              OUT PORT       (PORT = FD, paralell)
0506    WAIT      MVI D,255      keep START in low
                                 state for 1916
                                 microsec.
0508              DCR D
0509              JNZ WAIT
050C    START     MVI B,04       Set up integration
                                 time
050E    LOOP      MVI D,FF       Set up D count for
                                 delay of 1916
                                 microsec.
0510    HOLD      DCR D
0511              JNZ HOLD
0514              MVI A,02       disable array clock
                                 by driving 2¹ high
                                 and loop until total
                                 integration time is
                                 up
0516              OUT PORT
0518              DCR B
0519              JNZ LOOP

051C              XRA A
051D              OUT PORT       enable clock

051F              MVI A,01       fire Start pulse
0521              OUT PORT       to array

0523              XTHL           wait for 18 microsec.
0524              XTHL           to stabilise

0525              JMP GO         go back
```

INSOL
Program for Data Acquisition

```
LOC     LABEL      INSTRUCTION    COMMENTS

0700               MVI C,1C       ADC select pattern
0702               LXI H,00FF     count & first buffer
                                  address
0705               MVI A,11       fire Start pulse and
0707               OUT PORT       set up read line
                                  (PORT = FD)
0709               MVI B,04        set up scan
                                  integration time
070B               MVI E,02       set up subloop
070d    AGAIN      MVI D,FF       basic wait loop of
070F    WAIT       DCR D          1916 microsec.
0710               JNZ WAIT       loop
0713               DCR E
0714               JNZ AGAIN      subloop
0717               MVI A,1A       enable READ; set up
0719               OUT PORT       ADC logic and disable
071B               DCR B          clock until end of
                                  integration

071C    LOOP       MVI D,FF       wait 1916 microsec.
071E    NXT        DCR D          and keep going
071F               JNZ NXT        until end
0722               DCR B          of integration
0723               JNZ LOOP       period

0726               MVI A,11       enable clock; fire
0728               OUT PORT       start pulse and
072A               MVI B,10       enable READ line
                                  pattern to restore
                                  ADC logic.

072C    INP        MOV A,C        first time around
072D               OUT PORT       loop will read ADC1
072F               IN PORT        and restart ADC2.
                                  Second time around
                                  does vice versa.

0731               MOV M,A        move to memory

0732               MOV A,B        restore ADC logic
0733               OUT PORT
0735               DCR L          check byte count
                                  and last storage
                                  location.
0736               JNZ INP
0739               JMP DISP       restore display if
                                  end.
```

Appendix B

The material contained in this appendix outlines the configuration of Tecmar data acquisition circuitry, the design details of the interface circuit which links the Reticon motherboard to the Tecmar system, and the data acquisition program using this interface.

The Tecmar Labmaster system used in this application consists of a motherboard and a daughterboard. The motherboard contains a variety of timers, paralell ports, DAC's and interrupt generating circuits to interface to the IBM PC. The daughterboard contains the A to D conversion module (DT 5712), and an analog multiplexer (to allow the conversion of data from multiple sources).

For slower speed operation, the Tecmar motherboard is set up as ab I/O mapped device so that it is accessed by the 8088 I/O instructions. For maximum conversion speed, the Tecmar motherboard is configured as a memory mapped device which is accessed by the higher speed memory reference instructions of the 8088. In the design of LTL II, maximum speed of data acquisition was desired, so that the memory mapped configuration was selected. All options for the Labmaster are selected by means of a series of switches and jumpers contained on both the mother and daughter boards. A detailed listing of these switch settings is reported in Tables 15, and 16. The motherboard occupies memory locations COOO:0000 - OOOF in the IBM PC used in LTL II. The following options were selected for the daughterboard module: single ended inputs on the A to D converter, with unipolar, 12 bit binary outputs. The gain on the converter was fixed at unity. The input range selected for the analog signal was unipolar: 0 - +10v. The strobing of the channels of the analog multiplexer was suppressed by software: only channel 0 was converted. Software also enabled the **External Start Conversion** channel of the ADC so that the clock pulses from the array system initiated conversions automatically.

Data from the array motherboard (RC100B) were channelled to the Tecmar system via the Signal Interface described in Chapter 4. A schematic of the interface is included in Figure 60. The function of the various components was as follows: U1 is an inverting amplifier with optional offset control supplied by a voltage divider at the non-inverting input. The design uses Motorola MC1455 internally compensated operational amplifiers for U1 and 2. The output level of the RC100B signal was 0 to -3.0v. the purpose of U1 is to invert and level match the motherboard signal to the ADC. The Video signal from the motherboard is supplied to the inverting input of U1 via pin P2N of the RC100B.

The purpose of U3 and U4 is to gate the array clock train into the **External Start Conversion** channel of the Tecmar system. The array clock line is ANDed to the output of latch U3. U3 is held at reset via pin J2-8 of the Tecmar motherboard, until driven high under software control. The **Start** line of the RC100B motherboard is connected to the input of the U3 latch. When software enables J2-8 the U3 latch is enabled. The next **Start** pulse supplied by the array is latched, and drives the Q output high. The high state of the latch enables U4, which gates the clock train into the **External Start Conversion** channel of the Tecmar module (J2-3).

The software used to control the interface was written in 8088. A flowchart and program listing of the data acquisition routine are reported on pages 247 and 249 . Averaging of the signals was also carried out at this level. Communication with the keyboard and loading of data files to disk was achieved by means of DOS function calls (DOS 1.1).

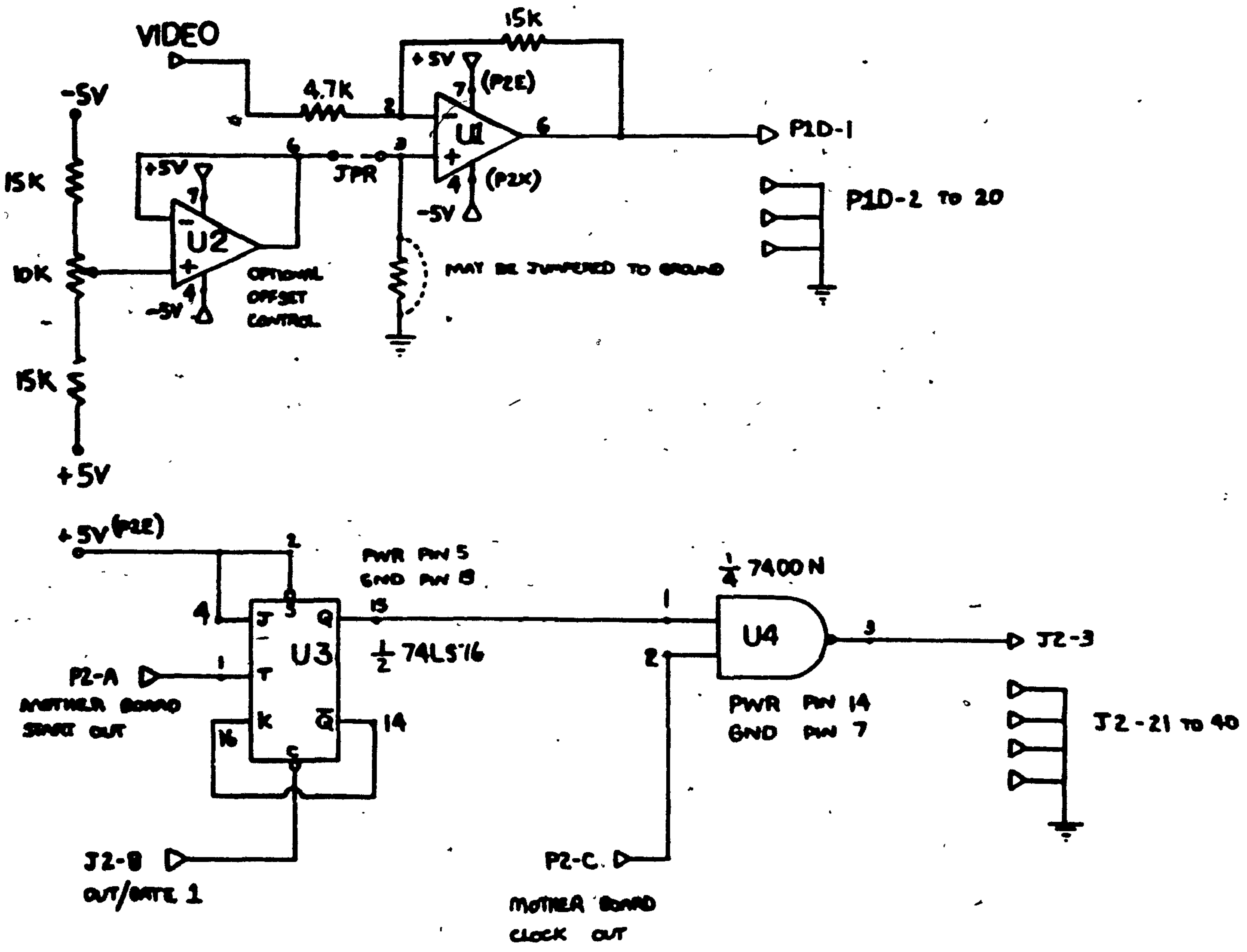

Figure 60 : Schematic diagram of the signal interface for LTI II.

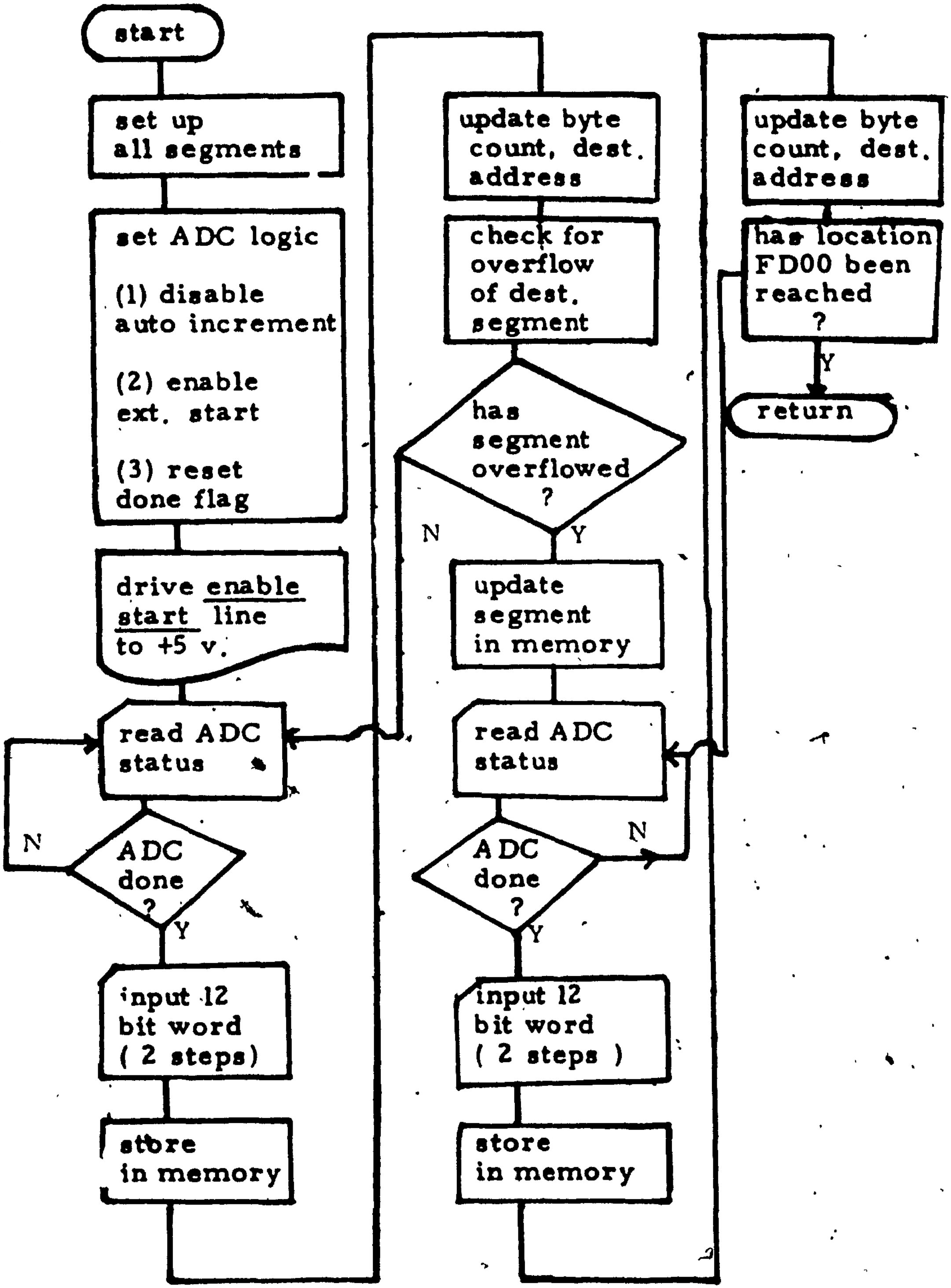

Flowchart of Input Routine : LTL II

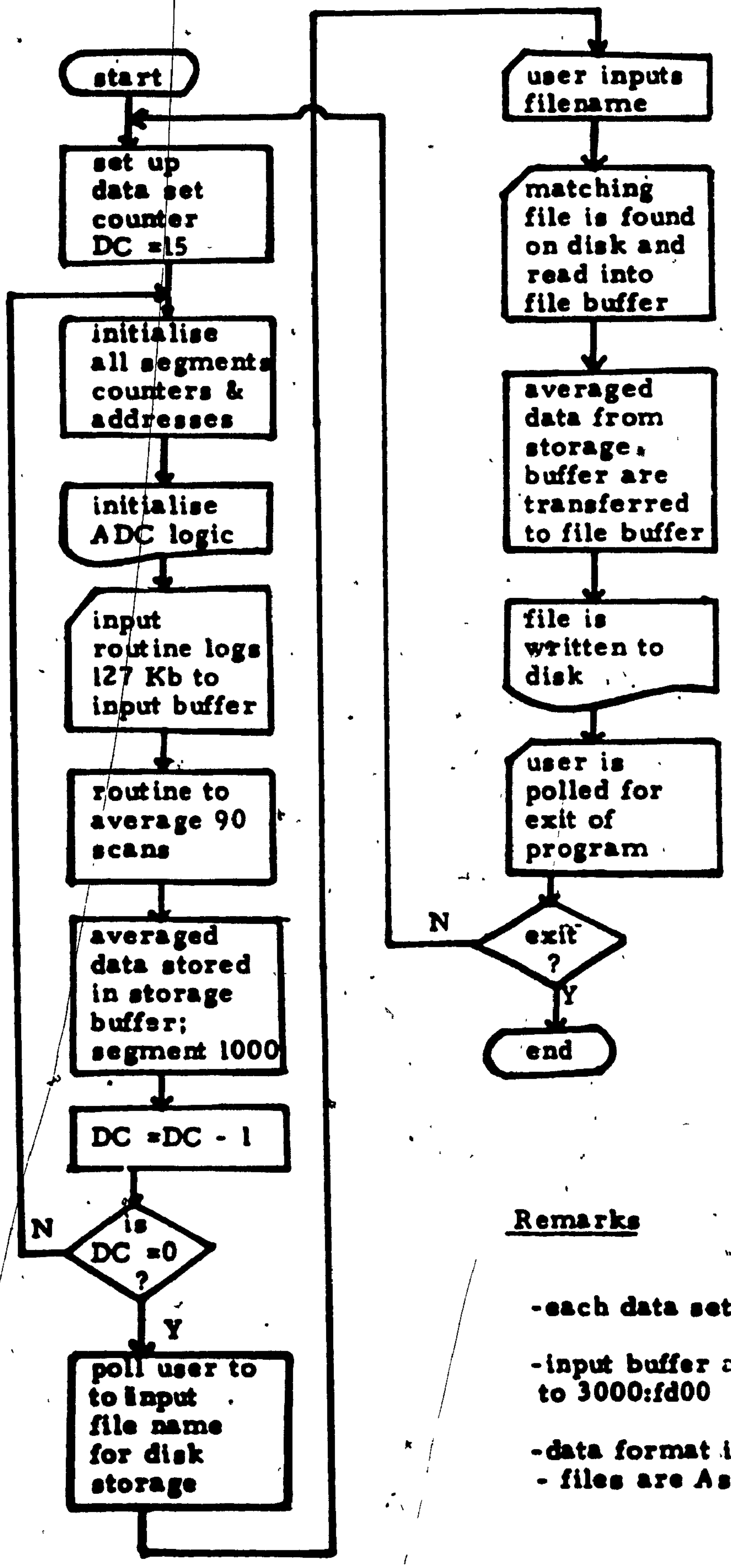

Remarks

-each data set is 256 words in length

-input buffer address : 2000:0000
to 3000:fd00

-data format is 12 bit binary
- files are Asyst compatible

Machine Level Routine for Data Acquisition

```
3000:FD00 B80030     MOV   AX,3000        entry point
3000:FD03 8ED8       MOV   DS,AX           set up data segment
3000:FD05 C606CDFD10 MOV   B,[FDCD],10
3000:FD0A 90         NOP
3000:FD0B 90         NOP
3000:FD0C 90         NOP
3000:FD0D 90         NOP
3000:FD0E 90         NOP
3000:FD0F C606FFFF0F MOV   B,[FFFF],0F
3000:FD14 90         NOP
3000:FD15 90         NOP
3000:FD16 B800C0     MOV   AX,C000     set up Labmaster segment =C000
3000:FD19 8ED8       MOV   DS,AX
3000:FD1B B80020     MOV   AX,2000      set up data storage segment = 2000
3000:FD1E 8EC0       MOV   ES,AX         destination data stored starting at
3000:FD20 BF0000     MOV   DI,0000
3000:FD23 BE0500     MOV   SI,0005     source data from          2000:0000
3000:FD26 BB0400     MOV   BX,0004
3000:FD29 B0FF       MOV   AL,FF                  C000:0005 ( MS byte )
3000:FD2B A20900     MOV   [0009],AL   reset all gates to '0  state
3000:FD2E B084       MOV   AL,84      disable autoincrement of analog
3000:FD30 A20400     MOV   [0004],AL                          multiplexer
3000:FD33 B000       MOV   AL,00
3000:FD35 A20500     MOV   [0005],AL   reset Done flag
3000:FD38 A00500     MOV   AL,[0005]  disable internal start conversion
3000:FD3B B001       MOV   AL,01
3000:FD3D A20900     MOV   [0009],AL    set analog channel to  0'
3000:FD40 B002       MOV   AL,02
3000:FD42 A20800     MOV   [0008],AL     load timer and drive output high
3000:FD45 B0E9       MOV   AL,E9
3000:FD47 A20900     MOV   [0009],AL
3000:FD4A FC         CLD              clear direction flag
3000:FD4B 8A07       MOV   AL,[BX]
3000:FD4D 2480       AND   AL,80      check done flag
3000:FD4F 74FA       JZ    FD4B
3000:FD51 A4         MOVSB
3000:FD52 A4         MOVSB            input sequence
3000:FD53 BE0500     MOV   SI,0005
3000:FD56 B90000     MOV   CX,0000
3000:FD59 31F9       XOR   CX,DI    check for end of input segment
3000:FD5B 75EE       JNZ   FD4B
3000:FD5D B80030     MOV   AX,3000    if ES overflowed update to 3000
3000:FD60 8EC0       MOV   ES,AX
3000:FD62 8A07       MOV   AL,[BX]
3000:FD64 2480       AND   AL,80
3000:FD66 74FA       JZ    FD62     repeat input sequence as above
3000:FD68 A4         MOVSB
3000:FD69 A4         MOVSB
```

```
3000:FD6A BE0500   MOV SI,0005
3000:FD6D B900FD   MOV CX,FD00      check for end of data buffer
3000:FD70 31F9     XOR CX,DI
3000:FD72 75EE     JNZ FD62         continue until end
3000:FD74 BF0000   MOV DI,0000
3000:FD77 B91002   MOV CX,0210      .number of points per scan =0210
3000:FD7A BA0000   MOV DX,0000       clear overflow in extension register
3000:FD7D B80010   MOV AX,1000
3000:FD80 8EC0     MOV ES,AX
3000:FD82 B80020   MOV AX,2000      set up source pointer to 2000
3000:FD85 8ED8     MOV DS,AX
3000:FD87 F8       CLC               clear carry
3000:FD88 BB0000   MOV BX,0000
3000:FD8B 8A07     MOV AL,[BX]     point to start of data  ( diode N scan 1 )
3000:FD8D 43       INC BX            add contents of 1st mem. loc. to AL
3000:FD8E 80270F   AND B,[BX],OF
3000:FD91 8A27     MOV AH,[BX]        point to MS and add to AH
3000:FD93 81C32004 ADD BX,0420
3000:FD97 80270F   AND B,[BX];OF
3000:FD9A 4B       DEC BX             add next point and check carry
3000:FD9B 0307     ADD AX,[BX]
3000:FD9D 7301     JNC FDA0
3000:FD9F 42       INC DX       if carry, increment extension register
3000:FDA0 43       INC BX            point to next scan, diode N
3000:FDA1 81C32004 ADD BX,0420
3000:FDA5 73F0     JNC FD97         check for overflow and loop back
3000:FDA7 2E       SEG CS                                   if not overflow
3000:FDA8 80270F   AND B,[BX],OF
3000:FDAB 4B       DEC BX             if overflow, update segment to 3000
3000:FDAC 2E       SEG CS             add results of next scan
3000:FDAD 0307     ADD AX,[BX]
3000:FDAF 7301     JNC FDB2           check carry
3000:FDB1 42       INC DX           point to MS byte, next scan
3000:FDB2 43       INC BX
3000:FDB3 81C32004 ADD BX,0420
3000:FDB7 81FB5F77 CMP BX,775F
3000:FDBB 7EEA     JLE FDA7          loop back if not end
3000:FDBD BB5B00   MOV BX,005B       divisor goes into BX
3000:FDC0 F7F3     DIV AX,BX        divide partial sum in AX by BX
3000:FDC2 81FA8000 CMP DX,0080
3000:FDC6 7E01     JLE FDC9         check remainder
3000:FDC8 40       INC AX
3000:FDC9 26       SEG ES
3000:FDCA 8985002C MOV [DI+2000],AX point to storage buffer : 1000:1000
```

```
3000:FDCE 90            NOP
3000:FDCF 90            NOP
3000:FDD0 90            NOP
3000:FDD1 90            NOP
3000:FDD2 90            NOP
3000:FDD3 81C70200      ADD  DI,0002  increment storage address
3000:FDD7 89FB          MOV  BX,DI
3000:FDD9 3E            SEG  DS
3000:FDDA 43            INC  BX
3000:FDDB B80000        MOV  AX,0000
3000:FDDE BA0000        MOV  DX,0000   clear partial sum
3000:FDE1 E2B4          LOOP FD97     loop back to next point in scan
3000:FDE3 2E            SEG  CS
3000:FDE4 FE0EFFFF      DEC  B,[FFFF]
3000:FDE8 2E            SEG  CS
3000:FDE9 803EFFFF00    CMP  B,[FFFF],00
3000:FDEE 7424          JZ   FE14
3000:FDF0 2E            SEG  CS       check to see if last data set logged
3000:FDF1 8006CDFD02    ADD  B,[FDCD],02
3000:FDF6 90            NOP
3000:FDF7 90            NOP
3000:FDF8 90            NOP    if not last scan user is polled for next input
3000:FDF9 90            NOP
3000:FDFA 90            NOP    get message, display on screen
3000:FDFB 90            NOP
3000:FDFC B80030        MOV AX,3000
3000:FDFF 8ED8          MOV DS,AX
3000:FE01 BAF0FF        MOV DX,FFF0
3000:FE04 B80009        MOV AX,0900
3000:FE07 CD21          INT 21
3000:FE09 BAF4FF        MOV DX,FFF4
3000:FE0C B8000A        MOV AX,0A00 user inputs a character
3000:FE0F CD21          INT 21
3000:FE11 E902FF        JMP FD16
3000:FE14 B80030        MOV AX,3000  if last data set logged output user
3000:FE17 8ED8          MOV DS,AX
3000:FE19 BAC0FF        MOV DX,FFC0  message to screen :'input filename
3000:FE1C B80009        MOV AX,0900
3000:FE1F CD21          INT 21
3000:FE21 C6067FFFAA MOV B,[FF7F],AA
3000:FE26 C60679FFAA MOV B,[FF79],AA       set up file control block
3000:FE2B BA7FFF        MOV DX,FF7F
3000:FE2E B8000A        MOV AX,0A00
3000:FE31 CD21          INT 21
3000:FE35 C60680FF00 MOV B,[FF80],00 user writes filename into file
3000:FE38 BA80FF        MOV DX,FF80
                                     control block directly via DOS

                                     function call
```

```
3000:FE3B B8000F     MOV  AX,0F00   disk file is opened under DOS 1.1
3000:FE3E CD21       INT  21
3000:FE40 C606A0FF00 MOV  B,[FFA0],00
3000:FE45 C606A1FF00 MOV  B,[FFA1],00
3000:FE4A C6068FFF1E MOV  B,[FF8F],1E
3000:FE4F B80020     MOV  AX,2000
3000:FE52 8ED8       MOV  DS,AX  file is read into memory under DOS 1.1
3000:FE54 BA0010     MOV  DX,1000
3000:FE57 B8001A     MOV  AX,1A00                  load at 2000:1000
3000:FE5A CD21       INT  21
3000:FE5C B80030     MOV  AX,3000
3000:FE5F 8ED8       MOV  DS,AX
3000:FE61 BA80FF     MOV  DX,FF80
3000:FE64 B80014     MOV  AX,1400
3000:FE67 CD21       INT  21
3000:FE69 B80020     MOV  AX,2000
3000:FE6C 8EC0       MOV  ES,AX
3000:FE6E B80010     MOV  AX,1000   ES =2000  dest. segment
3000:FE71 8ED8       MOV  DS,AX
3000:FE73 BB0F00     MOV  BX,000F   DS =1000
3000:FE76 BE0010     MOV  SI,1000
3000:FE79 BF8010     MOV  DI,1080
3000:FE7C B9FD01     MOV  CX,01FD   move data from storage buffer
3000:FE7F FC         CLD              at 1000:1000 to file
3000:FE80 A4         MOVSB
3000:FE81 E2FD       LOOP FE80   buffer at 2000:1080 ( copied as ASYST
3000:FE83 4B         DEC  BX              memory image file)
3000:FE84 81F30000   XOR  BX,0000
3000:FE88 75F2       JNZ  FE7C
3000:FE8A 90         NOP
3000:FE8B B80030     MOV  AX,3000
3000:FE8E 8ED8       MOV  DS,AX
3000:FE90 C606A0FF00 MOV  B,[FFA0],00
3000:FE95 90         NOP
3000:FE96 BA80FF     MOV  DX,FF80
3000:FE99 B80015     MOV  AX,1500
3000:FE9C CD21       INT  21               read file to disk
3000:FE9E BA80FF     MOV  DX,FF80
3000:FEA1 B80010     MOV  AX,1000
3000:FEA4 CD21       INT  21
3000:FEA6 BA00FF     MOV  DX,FF00
3000:FEA9 B80009     MOV  AX,0900          user message to exit
3000:FEAC CD21       INT  21
3000:FEAE BA30FF     MOV  DX,FF30
3000:FEB1 B8000A     MOV  AX,0A00  user inputs response character
3000:FEB4 CD21       INT  21
3000:FEB6 A052FF     MOV  AL,[FF52]
3000:FEB9 3479       XOR  AL,79
3000:FEBB 7405       JZ   FEC2             check for  y
3000:FEBD EA00FD0030 JMP  3000:FD00
3000:FEC2 CB         RET  L                exit if yes
```

```
3000:FFA0  01 00 00 00 00 00 00 00-00 00 00 00 00 00 00 00   ................
3000:FFB0  00 00 00 00 00 00 00 00-00 00 00 00 00 00 00 00   ................
3000:FFC0  0D 0A 49 4E 50 55 54 20-46 49 4C 45 4E 41 4D 45   ..INPUT FILENAME
3000:FFD0  2E 45 58 54 20 3A 20 24-00 00 00 00 00 00 00 00   .EXT : $........
3000:FFE0  00 00 00 00 00 00 00 00-00 00 00 00 00 00 00 00   ................
3000:FFF0  59 59 59 24 07 00 0D 00-00 00 00 00 00 00 00 00   YYY$............
3000:0000  00 00 00 00 00 00 00 00-00 00 00 00 00 00 00 00   ................
3000:0010  00 00 00 00 00 00 00 00-00 00 00 00 00 00 00 00   ................
```

Keyboard Buffer - Input

Message Buffer

```
3000:FF50  00 00 00 00 00 00 00 00-00 00 00 00 00 00 00 00   ................
3000:FF60  00 00 00 00 00 00 00 00-00 00 00 00 00 00 00 00   ................
3000:FF70  00 00 00 00 00 00 00 00-00 AA 00 00 00 00 00 AA   .........*.....*
3000:FF80  01 73 61 6D 70 6C 65 20-20 74 72 79 00 00 80 1E   .sample  try....
3000:FF90  80 1E 00 00 21 00 37 09-01 0A 01 11 01 07 00 00   ....!.7.........
3000:FFA0  01 00 00 00 00 00 00 00-00 00 00 00 00 00 00 00   ................
3000:FFB0  00 00 00 00 00 00 00 00-00 00 00 00 00 00 00 00   ................
3000:FFC0  0D 0A 49 4E 50 55 54 20-46 49 4C 45 4E 41 4D 45   ..INPUT FILENAME
```

File Control Block

Message Buffer

```
3000:FED0  00 00 00 00 00 00 00 00-00 00 00 00 00 00 00 00   ................
3000:FEE0  00 00 00 00 00 00 00 00-00 00 00 00 00 00 00 00   ................
3000:FEF0  59 80 06 CD FE 02 90 90-90 90 90 90 B8 00 30 8E   Y..M.......8.0.
3000:FF00  0A 0D 54 4F 20 45 58 49-54 20 45 4E 54 45 52 20   ..TO EXIT ENTER
3000:FF10  20 59 20 3A 20 24 20 E0-59 E0 3A 20 24 00 00 00    Y : $ `Y : $...
3000:FF20  00 00 00 00 00 00 00 00-00 00 00 00 00 00 00 00   ................
3000:FF30  FF 01 79 0D 00 00 00 00-00 00 00 00 00 00 00 00   ..y.............
3000:FF40  06 06 A0 FF 00 00 00 00-00 00 00 00 00 00 00 00   P. .............
```

Message Buffer

Table 15
Jumpering of Labmaster Daughter Board: DT5712

Jumper	Pins	Contact (c) or No Contact (nc)	Feature Selected
JSD	1S - 2S	c	slct single ended input
	3S - 4S	c	
	5S - 6S	c	
JAD	5A - 6A	c	set by mfgr
	13A - 14A	c	slct/unipolar input
JCD	4C - 16C	c	normal opn.
	16C - 17C	c	suppr/ovrlap
	5C - 17C	c	suppr/free run
	14G - 15C	nc	suppr/diff inp.
	19C - 20C	c	suppr/free run
	8C - 9C	c	slct/ext conv.
JFD	3F - 4F	nc	suppr/free run
Capacitor	dwg.	nc	gain < 10
Rext	dwg.	nc	gain = 1
JDD	13D - 14D	c	slct/ 12 bit binary
	16D - 17D	c	slct/ 12 bit binary
	19D - 20D	c	slct/ 12 bit binary
	10D - 22D	c	slct/ 12 bit binary
	12D - 24D	c	slct/ 12 bit binary

Table 16
Jumpering of Labmaster Mother Board

Jumper	Pins	Contact (c) or No Contact (nc)	Feature Selected
J1	P3 - P4	c	timer outputs (cabled to Reticon/ signal interface)
J3	all pins	nc	unused paralell port
J4	all pins	nc	DAC outputs
J5	P1 - 5	c	select memory mapped I/O
	P3 - 4	c	"
	P7 - 8	c	"
	P6 - 2	nc	"
J7	all pins	nc	disconnect all timers from interrupts
J8	P1 - 2 P4 -5	c c	paralell port configured for normal use
J9	all pins	nc	no interrupts used
Board Address Switches	Reg 1 Reg 2 Reg 3	address C0000	select memory location for board (mem. mapped conf.)